

The **Journal of the Serbian Chemical Society** (formerly Glasnik Hemijskog društva Beograd), one volume (12 issues) per year, publishes articles from the fields of chemistry. The **Journal** is financially supported by the **Ministry of Education, Science and Technological Development of the Republic of Serbia**.

Articles published in the **Journal** are indexed in **Clarivate Analytics products: Science Citation Index-ExpandedTM** – accessed via **Web of Science[®]** and **Journal Citation Reports[®]**.

Impact Factor announced 2020: **1.097**; **5-year Impact Factor**: **1.023**.

Articles appearing in the **Journal** are also abstracted by: **Scopus**, **Chemical Abstracts Plus (CAplusSM)**, **Directory of Open Access Journals**, **Referativnii Zhurnal (VINITI)**, **RSC Analytical Abstracts**, **EuroPub**, **Pro Quest** and **Asian Digital Library**.

Publisher:

Serbian Chemical Society, Karnegijeva 4/III, P. O. Box 36, 1120 Belgrade 35, Serbia
tel./fax: +381-11-3370-467, E-mails: **Society** – shd@shd.org.rs; **Journal** – jscs@shd.org.rs
Home Pages: **Society** – <http://www.shd.org.rs/>; **Journal** – <http://www.shd.org.rs/JSCS/>
Contents, Abstracts and full papers (from Vol 64, No. 1, 1999) are available in the electronic form at the Web Site of the **Journal** (<http://www.shd.org.rs/JSCS/>).

Internet Service:

Former Editors:

Nikola A. Pušin (1930–1947), **Aleksandar M. Leko** (1948–1954),
Panta S. Tutundžić (1955–1961), **Miloš K. Mladenović** (1962–1964),
Đorđe M. Dimitrijević (1965–1969), **Aleksandar R. Despić** (1969–1975),
Slobodan V. Ribnikar (1975–1985), **Dragutin M. Dražić** (1986–2006).

Editor-in-Chief:

BRANISLAV Ž. NIKOLIĆ, Serbian Chemical Society (E-mail: jscs-ed@shd.org.rs)

Deputy Editor:

DUŠAN SLADIĆ, Faculty of Chemistry, University of Belgrade

Sub editors:

Organic Chemistry

DEJAN OPSENICA, Institute of Chemistry, Technology and Metallurgy, University of Belgrade

Biochemistry and

Biotechnology

JANOS CSANÁDI, Faculty of Science, University of Novi Sad

Inorganic Chemistry

OLGICA NEDIĆ, INEP – Institute for the Application of Nuclear Energy, University of Belgrade

Theoretical Chemistry

MILOŠ ĐURAN, Serbian Chemical Society

Physical Chemistry

IVAN JURANIĆ, Serbian Chemical Society

Electrochemistry

LJILJANA DAMJANOVIĆ-VASILJIĆ, Faculty of Physical Chemistry, University of Belgrade

Analytical Chemistry

SNEŽANA GOJKOVIĆ, Faculty of Technology and Metallurgy, University of Belgrade

Polymers

SLAVICA RAŽIĆ, Faculty of Pharmacy, University of Belgrade

Thermodynamics

BRANKO DUNJIĆ, Faculty of Technology and Metallurgy, University of Belgrade

Chemical Engineering

MIRJANA KIJEVCANIN, Faculty of Technology and Metallurgy, University of Belgrade

TATJANA KALUĐEROVIĆ RADOIČIĆ, Faculty of Technology and Metallurgy, University of Belgrade

Materials

RADA PETROVIĆ, Faculty of Technology and Metallurgy, University of Belgrade

Metallic Materials and

Metallurgy

NENAD RADOVIĆ, Faculty of Technology and Metallurgy, University of Belgrade

Environmental and

Geochemistry

VESNA ANTIĆ, Faculty of Agriculture, University of Belgrade

History of and

Education in Chemistry

DRAGICA TRIVIĆ, Faculty of Chemistry, University of Belgrade

English Language

LYNNE KATSIKAS, Serbian Chemical Society

Editors:

VLATKA VAJS, Serbian Chemical Society

JASMINA NIKOLIĆ, Faculty of Technology and Metallurgy, University of Belgrade

Technical Editors:

VLADIMIR PANIĆ, ALEKSANDAR DEKANSKI, VUK FILIPOVIĆ, Institute of Chemistry, Technology and Metallurgy, University of Belgrade

Journal Manager &

Web Master:

ALEKSANDAR DEKANSKI, Institute of Chemistry, Technology and Metallurgy, University of Belgrade

Office:

VERA ČUŠIĆ, Serbian Chemical Society

Editorial Board

From abroad: **R. Adžić**, Brookhaven National Laboratory (USA); **A. Casini**, University of Groningen (The Netherlands); **G. Cobb**, Baylor University (USA); **D. Douglas**, University of British Columbia (Canada); **G. Inzelt**, Etvos Lorand University (Hungary); **N. Katsaros**, NCSR “Demokritos”, Institute of Physical Chemistry (Greece); **J. Kenny**, University of Perugia (Italy); **Ya. I. Korenman**, Voronezh Academy of Technology (Russian Federation); **M. D. Lechner**, University of Osnabrueck (Germany); **S. Macura**, Mayo Clinic (USA); **M. Spiteller**, INFU, Technical University Dortmund (Germany); **M. Stratakis**, University of Crete (Greece); **M. Swart**, University de Girona (Cataluna, Spain); **G. Vunjak-Novaković**, Columbia University (USA); **P. Worsfold**, University of Plymouth (UK); **J. Zagal**, Universidad de Santiago de Chile (Chile).

From Serbia: **B. Abramović**, **V. Antić**, **V. Bešković**, **J. Csanádi**, **Lj. Damjanović-Vasiljić**, **A. Dekanski**, **V. Dondur**, **B. Dunjić**, **M. Đuran**, **S. Gojković**, **I. Gutman**, **B. Jovančičević**, **I. Juranić**, **L. Katsikas**, **M. Kijevcanin**, **V. Leovac**, **S. Milonjić**, **V.B. Mišković-Stanković**, **O. Nedić**, **B. Nikolić**, **J. Nikolić**, **D. Opsenica**, **V. Panić**, **M. Petkovska**, **R. Petrović**, **I. Popović**, **B. Radak**, **T. Kaluderović Radiočić**, **N. Radović**, **S. Ražić**, **D. Sladić**, **S. Sovilj**, **S. Šerbanović**, **B. Šolaja**, **Ž. Tešić**, **D. Trivić**, **V. Vajs**.

Subscription: The annual subscription rate is **150.00 €** including postage (surface mail) and handling. For Society members from abroad rate is **50.00 €**. For the proforma invoice with the instruction for bank payment contact the Society Office (E-mail: shd@shd.org.rs) or see JSCS Web Site: <http://www.shd.org.rs/JSCS/>, option Subscription.

Godišnja pretplata: Za članove SHD: **2.500,00 RSD**, za penzionere i studente: **1000,00 RSD**, a za ostale: **3.500,00 RSD**; za organizacije i ustanove: **16.000,00 RSD**. Uplate se vrše na tekući račun Društva: **205-13815-62**, poziv na broj **320**, sa naznakom “pretplata za JSCS”.

Nota: Radovi čiji su svi autori članovi SHD prioritarno se publikuju.

Odlukom Odbora za hemiju Republičkog fonda za nauku Srbije, br. 66788/1 od 22.11.1990. godine, koja je kasnije potvrđena odlukom Saveta Fonda, časopis je uvršten u kategoriju međunarodnih časopisa (**M-23**). Takođe, aktom Ministarstva za nauku i tehnologiju Republike Srbije, 413-00-247/2000-01 od 15.06.2000. godine, ovaj časopis je proglašen za publikaciju od posebnog interesa za nauku. **Impact Factor** časopisa objavljen 2020. godine iznosi **1,097**, a petogodišnji **Impact Factor 1,023**.

INSTRUCTIONS FOR AUTHORS (2021)

GENERAL

The *Journal of the Serbian Chemical Society* (the *Journal* in further text) is an international journal publishing papers from all fields of chemistry and related disciplines. Twelve issues are published annually. The Editorial Board expects the editors, reviewers, and authors to respect the well-known standard of professional ethics.

Types of Contributions

Original scientific papers	(up to 15 typewritten pages, including Figures, Tables and References) report original research which must not have been previously published.
Short communications	(up to 8 pages) report unpublished preliminary results of sufficient importance to merit rapid publication.
Notes	(up to 5 pages) report unpublished results of short, but complete, original research
Authors' reviews	(up to 40 pages) present an overview of the author's current research with comparison to data of other scientists working in the field
Reviews ^a	(up to 40 pages) present a concise and critical survey of a specific research area. Generally, these are prepared at the invitation of the Editor
Surveys	(about 25 pages) communicate a short review of a specific research area.
Book and Web site reviews	(1 - 2 pages)
Extended abstracts	(about 4 pages) of Lectures given at meetings of the Serbian Chemical Society Divisions
Letters to the Editor	report miscellaneous topics directed directly to the Editor

^aGenerally, Authors' reviews, Reviews and Surveys are prepared at the invitation of the Editor.

Submission of manuscripts

Manuscripts should be submitted using the **OnLine Submission Form**, available on the JSCS Web Site (<http://www.shd-pub.org.rs/index.php/JSCS>). The manuscript must be uploaded as a Word.doc or .rtf file, with tables and figures (including the corresponding captions – above Tables and below Figures), placed within the text to follow the paragraph in which they were mentioned for the first time.

Please note that **Full Names** (First Name, Last Name), **Full Affiliation** and **Country** (from drop down menu) of **ALL OF AUTHORS** (written in accordance with English spelling rules - the first letter capitalized) must be entered in the manuscript Submission Form (Step 3). Manuscript Title, authors' names and affiliations, as well as the Abstract, **WILL APPEAR** in the article listing, as well as in **BIBLIOGRAPHIC DATABASES (WoS, SCOPUS...)**, in the form and in the order entered in the author details

Graphical abstract

Graphical abstract is a one-image file containing the main depiction of the authors work and/or conclusion and must be supplied along with the manuscript. It must enable readers to quickly gain the main message of the paper and to encourage browsing, help readers identify which papers are most relevant to their research interests. Authors must provide an image that clearly represents the research described in the paper. The most relevant figure from the work, which summarizes the content, can also be submitted. The image should be submitted as a separate file in **Online Submission Form - Step 2**.

Specifications: The graphical abstract should have a clear start and end, reading from top to bottom or left to right. Please omit unnecessary distractions as much as possible.

- **Image size:** minimum of 500×800 pixels (W×H) and a minimum resolution of 300 dpi. If a larger image is sent, then please use the same ratio: 16 wide × 9 high. Please note that your image will be scaled proportionally to fit in the available window in TOC; a 150×240 pixel rectangle. Please be sure that the quality of an image cannot be increased by changing the resolution from lower to higher, but only by rescanning or exporting the image with a higher resolution, which can be set in usual "settings" option.
- **Font:** Please use Calibri and Symbol font with a large enough font size, so it is readable even from the image of a smaller size (150 × 240 px) in TOC.
- **File type:** JPG and PNG only.

No additional text, outline or synopsis should be included. Please do not use white space or any heading within the image.

Cover Letter

Manuscripts must be accompanied by a cover letter (strictly uploaded in **Online Submission Step 2**) in which the type of the submitted manuscript and a warranty as given below are given. The Author(s) has(have) to warranty that the manuscript submitted to the *Journal* for review is original, has been written by the stated author(s) and has not been published elsewhere; is currently not being considered for publication by any other journal and will not be submitted for such a review while under review by the *Journal*; the manuscript contains no libellous or other unlawful statements and does not contain any materials that violate any personal or proprietary rights of any other person or entity. All manuscripts will be acknowledged on receipt (by e-mail).

Illustrations

Illustrations (Figs, schemes, photos...) in TIF or EPS format (JPG format is acceptable for colour and greyscale photos, only), must be additionally uploaded (Online Submission Step 2) as a separate file or one archived (.zip, .rar or .arj) file. Figures and/or Schemes should be prepared according to the **Artwork Instructions** - http://www.shd.org.rs/JSCS/jscs-pdf/Artwork_Instructions.pdf!

For any difficulties and questions related to **OnLine Submission Form** - <https://www.shd-pub.org.rs/index.php/JSCS/submission/wizard>, please refer to **User Guide** - <https://openjournal-systems.com/ojs-3-user-guide/>, Chapter **Submitting an Article** - <https://openjournal-systems.com/ojs-3-user-guide/submitting-an-article/>. If difficulties still persist, please contact JSCS Editorial Office at JSCS@shd.org.rs

A manuscript not prepared according to these instructions will be returned for resubmission without being assigned a reference number.

Conflict-of-Interest Statement*: Public trust in the peer review process and the credibility of published articles depend in part on how well a conflict of interest is handled during writing, peer review, and editorial decision making. A conflict of interest exists when an author (or the author's institution), reviewer, or editor has financial or personal relationships that inappropriately influence (bias) his or her actions (such relationships are also known as dual commitments, competing interests, or competing loyalties). These relationships vary from those with negligible potential to those with great potential to influence judgment, and not all relationships represent true conflict of interest. The potential for a conflict of interest can exist whether or not an individual believes that the relationship affects his or her scientific judgment. Financial relationships (such as employment, consultancies, stock ownership, honoraria, paid expert testimony) are the most easily identifiable conflicts of interest and the most likely to undermine the credibility of the journal, the authors, and of science itself. However, conflicts can occur for other reasons, such as personal relationships, academic competition, and intellectual passion.

Informed Consent Statement*: Patients have a right to privacy that should not be infringed without informed consent. Identifying information, including patients' names, initials, or hospital numbers, should not be published in written descriptions, photographs, and pedigrees unless the information is essential for scientific purposes and the patient (or parent or guardian) gives written informed consent for publication. Informed consent for this purpose requires that a patient who is identifiable be shown the manuscript to be published. Authors should identify Individuals who provide writing assistance and disclose the funding source for this assistance. Identifying details should be omitted if they are not essential. Complete anonymity is difficult to achieve, however, and informed consent should be obtained if there is any doubt. For example, masking the eye region in photographs of patients is inadequate protection of anonymity. If identifying characteristics are altered to protect anonymity, such as in genetic pedigrees, authors should provide assurance that alterations do not distort scientific meaning and editors should so note. The requirement for informed consent should be included in the journal's instructions for authors. When informed consent has been obtained it should be indicated in the published article.

Human and Animal Rights Statement* When reporting experiments on human subjects, authors should indicate whether the procedures followed were in accordance with the ethical standards of the responsible committee on human experimentation (institutional and national) and with the Helsinki Declaration of 1975, as revised in 2000 (5). If doubt exists whether the research was conducted in accordance with the Helsinki Declaration, the authors must explain the rationale for their approach, and demonstrate that the institutional review body explicitly approved the doubtful aspects of the study. When reporting experiments on animals, authors should be asked to indicate whether the institutional and national guide for the care and use of laboratory animals was followed.

*International Committee of Medical Journal Editors ("Uniform Requirements for Manuscripts Submitted to Biomedical Journals"), February 2006

PROCEDURE

All contributions will be peer reviewed and only those deemed worthy and suitable will be accepted for publication. The Editor has the final decision. To facilitate the reviewing process, authors are encouraged to suggest up to three persons competent to review their manuscript. Such suggestions will be taken into consideration but not always accepted. If authors would prefer a specific person not be a reviewer, this should be announced. The Cover Letter must be accompanied by these suggestions. Manuscripts requiring revision should be returned according to the requirement of the Editor, within 60 days upon reception of the reviewing comments by e-mail.

The *Journal* maintains its policy and takes the liberty of correcting the English as well as false content of manuscripts **provisionally accepted** for publication in the first stage of reviewing process. In this second stage of manuscript preparation by JSCS Editorial Office, the author(s) may be required to supply some **additional clarifications and corrections**. This procedure will be executed during copyediting actions, with a demand to author(s) to perform corrections of unclear parts before the manuscript would be published OnLine as **finally accepted manuscript (OLF Section of the JSCS website)**. Please note that the manuscript can receive the status of **final rejection** if the author's corrections would not be satisfactory.

When finally accepted manuscript is ready for printing, the corresponding author will receive a request for proof reading, which should be performed within 2 days. Failure to do so will be taken as the authors agree with any alteration which may have occurred during the preparation of the manuscript for printing.

Accepted manuscripts of active members of the Serbian Chemical Society (all authors) have publishing priority.

MANUSCRIPT PRESENTATION

Manuscripts should be typed in English (either standard British or American English, but consistent throughout) with 1.5 spacing (12 points Times New Roman; Greek letters in the character font Symbol) in A4 format leaving 2.5 cm for margins. For Regional specific, non-standard characters that may appear in the text, save documents with Embed fonts Word option: *Save as -> (Tools) -> Save Options... -> Embed fonts in the text.*

The authors are requested to seek the assistance of competent English language expert, if necessary, to ensure their English is of a reasonable standard. The Serbian Chemical Society can provide this service in advance of submission of the manuscript. If this service is required, please contact the office of the Society by e-mail (jscs-info@shd.org.rs).

Tables, figures and/or schemes must be embedded in the main text of the manuscript and should follow the paragraph in which they are mentioned for the first time. **Tables** must be prepared with the aid of the **WORD table function**, without vertical lines. The minimum size of the font in the tables should be **10 pt**. Table columns must not be formatted using multiple spaces. Table rows must not be formatted using any returns (enter key; ↵ key) and are **limited to 12 cm width**. Tables should not be incorporated as graphical objects. **Footnotes to Tables** should follow them and are to be indicated consequently (in a single line) in superscript letters and separated by semi-column.

Table caption must be placed above corresponding Table, while **Captions of the Illustrations** (Figs. Schemes...) must follow the corresponding item. **The captions, either for Tables or Illustrations**, should make the items comprehensible without reading of the main text (but clearly referenced in), must follow numerical order (Roman for Tables, Arabic for Illustrations), and should not be provided on separate sheets or as separate files.

High resolution Illustrations (named as Fig. 1, Fig. 2... and/or Scheme 1, Scheme 2...) in **TIF or EPS format** (JPG format is acceptable for photos, only) **must be additionally uploaded as a separate files or one archived (.zip, .rar) file.**

Illustrations should be prepared according to the [ARTWORK INSTRUCTIONS](http://www.shd.org.rs/JSCS/jscs-pdf/Artwork_Instructions.pdf) - http://www.shd.org.rs/JSCS/jscs-pdf/Artwork_Instructions.pdf. !

All pages of the manuscript must be numbered continuously.

DESIGNATION OF PHYSICAL QUANTITIES AND UNITS

IUPAC recommendations for the naming of compounds should be followed. SI units, or other permissible units, should be employed. The designation of physical quantities must be in italic throughout the text (including figures, tables and equations), whereas the units and indexes (except for indexes having the meaning of physical quantities) are in upright letters. They should be in Times New Roman font. In graphs and tables, a slash should be used to separate the designation of a physical quantity from the unit

(example: p / kPa, j / mA cm², t / °C, T_0 / K, τ / h, $\ln(j$ / mA cm²)...). Designations such as: p (kPa), t [min]..., are not acceptable. However, if the full name of a physical quantity is unavoidable, it should be given in upright letters and separated from the unit by a comma (example: Pressure, kPa; Temperature, K; Current density, mA cm²...). Please do not use the axes of graphs for additional explanations; these should be mentioned in the figure captions and/or the manuscript (example: “pressure at the inlet of the system, kPa” should be avoided). The axis name should follow the direction of the axis (the name of y-axis should be rotated by 90°). Top and right axes should be avoided in diagrams, unless they are absolutely necessary.

Latin words, as well as the names of species, should be in *italic*, as for example: *i.e.*, *e.g.*, *in vivo*, *ibid*, *Calendula officinalis* L., *etc.* The branching of organic compound should also be indicated in *italic*, for example, *n*-butanol, *tert*-butanol, *etc.*

Decimal numbers must have decimal points and not commas in the text (except in the Serbian abstract), tables and axis labels in graphical presentations of results. Thousands are separated, if at all, by a comma and not a point.

Mathematical and chemical equations should be given in separate lines and must be numbered, Arabic numbers, consecutively in parenthesis at the end of the line. All equations should be embedded in the text. Complex equations (fractions, integrals, matrix...) should be prepared with the aid of the **Microsoft Equation 3.0** (or higher) or **MathType** (Do not use them to create simple equations and labels). **Using the Insert -> Equation option, integrated in MS Office 2010 and MS Office 2013, as well as insertion of equation objects within paragraph text IS NOT ALLOWED.**

ARTICLE STRUCTURE

- TITLE PAGE;
- MAIN TEXT – including Tables and Illustrations with corresponding captions;
- SUPPLEMENTARY MATERIAL (optional)

Title page

- **Title** in bold letters, should be clear and concise, preferably 12 words or less. The use of non-standard abbreviations, symbols and formulae is discouraged.
- **AUTHORS' NAMES** in capital letters with the full first name, initials of further names separated by a space and surname. Commas should separate the author's names except for the last two names when 'and' is to be used. In multi-affiliation manuscripts, the author's affiliation should be indicated by an Arabic number placed in superscript after the name and before the affiliation. Use * to denote the corresponding author(s).
- *Affiliations* should be written in *italic*. The e-mail address of the corresponding author should be given after the affiliation(s).
- *Abstract*: A one-paragraph abstract written of 150 – 200 words in an impersonal form indicating the aims of the work, the main results and conclusions should be given and clearly set off from the text. Domestic authors should also submit, on a separate page, an Abstract - Izvod, the author's name(s) and affiliation(s) in Serbian (Cyrillic letters). (Домаћи аутори морају доставити Извод (укључујући имена аутора и афилијацију) на српском језику, исписане ћирилицом, иза Захвалнице, а пре списка референци.) For authors outside Serbia, the Editorial Board will provide a Serbian translation of their English abstract.
- *Keywords*: Up to 6 keywords should be given. Do not use words appearing in the manuscript title
- **RUNNING TITLE**: A one line (maximum five words) short title in capital letters should be provided.

Main text – should have the form:

- **INTRODUCTION**,
- **EXPERIMENTAL (RESULTS AND DISCUSSION)**,
- **RESULTS AND DISCUSSION (EXPERIMENTAL)**,
- **CONCLUSIONS**,
- **NOMENCLATURE (optional) and**
- **Acknowledgements: If any.**
- **REFERENCES** (Citation of recent papers published in chemistry journals that highlight the significance of work to the general readership is encouraged.)

The sections should be arranged in a sequence generally accepted for publication in the respective fields. They subtitles should be in capital letters, centred and NOT numbered.

- The INTRODUCTION should include the aim of the research and a concise description of background information and related studies directly connected to the paper.
- The EXPERIMENTAL section should give the purity and source of all employed materials, as well as details of the instruments used. The employed methods should be described in sufficient detail to enable experienced persons to repeat them. Standard procedures should be referenced and only modifications described in detail. On no account should results be included in the experimental section.

Chemistry

Detailed information about instruments and general experimental techniques should be given in all necessary details. If special treatment for solvents or chemical purification were applied that must be emphasized.

Example: Melting points were determined on a Boetius PMHK or a Mel-Temp apparatus and were not corrected. Optical rotations were measured on a Rudolph Research Analytical automatic polarimeter, Autopol IV in dichloromethane (DCM) or methanol (MeOH) as solvent. IR spectra were recorded on a Perkin-Elmer spectrophotometer FT-IR 1725X. ¹H and ¹³C NMR spectra were recorded on a Varian Gemini-200 spectrometer (at 200 and 50 MHz, respectively), and on a Bruker Ultrashield Advance III spectrometer (at 500 and 125 MHz, respectively) employing indicated solvents (*vide infra*) using TMS as the internal standard. Chemical shifts are expressed in ppm (δ / ppm) values and coupling constants in Hz (J / Hz). ESI-MS spectra were recorded on Agilent Technologies 6210 Time-Of-Flight LC-MS instrument in positive ion mode with CH₃CN/H₂O 1/1 with 0.2 % HCOOH as the carrying solvent solution. Samples were dissolved in CH₃CN or MeOH (HPLC grade purity). The selected values were as follows: capillary voltage = 4 kV, gas temperature = 350 °C, drying gas flow 12 L min⁻¹, nebulizer pressure = 310 kPa, fragmentator voltage = 70 V. The elemental analysis was performed on the Vario EL III- C,H,N,S/O Elemental Analyzer (Elementar Analysensysteme GmbH, Hanau-Germany). Thin-layer chromatography (TLC) was performed on precoated Merck silica gel 60 F254 and RP-18 F254 plates. Column chromatography was performed on Lobar LichroPrep Si 60 (40-63 μ m), RP-18 (40-63 μ m) columns coupled to a Waters RI 401 detector, and on Biotage SP1 system with UV detector and FLASH 12+, FLASH 25+ or FLASH 40+ columns pre packed with KP-SIL [40-63 μ m, pore diameter 6 nm (60 Å)], KP-C18-HS (40-63 μ m, pore diameter 9 nm (90 Å) or KP-NH [40-63 μ m, pore diameter 10 nm (100 Å)] as adsorbent. Compounds were analyzed for purity (HPLC) using a Waters 1525 HPLC dual pump system equipped with an Alltech, Select degasser system, and dual λ 2487 UV-VIS detector. For data processing, Empower software was used (methods A and B). Methods C and D: Agilent Technologies 1260 Liquid Chromatograph equipped with Quat Pump (G1311B), Injector (G1329B) 1260 ALS, TCC 1260 (G1316A) and Detector 1260 DAD VL+ (G1315C). For data processing, LC OpenLab CDS ChemStation software was used. For details, see Supporting Information.

1. Synthesis experiments

Each paragraph describing a synthesis experiment should begin with the name of the product and any structure number assigned to the compound in the Results and Discussions section. Thereafter, the compound should be identified by its structure number. Use of standard abbreviations or unambiguous molecular formulas for reagents and solvents, and of structure numbers rather than chemical names to identify starting materials and intermediates, is encouraged.

When a new or improved synthetic method is described, the yields reported in key experimental examples, and yields used for comparison with existing methods, should represent amounts of isolated and purified products, rather than chromatographically or spectroscopically determined yields. Reactant quantities should be reported in weight and molar units and for product yields should be reported in weight units; percentage yields should only be reported for materials of demonstrated purity. When chromatography is used for product purification, both the support and solvent should be identified.

2. Microwave experiments

Reports of syntheses conducted in microwave reactors must clearly indicate whether sealed or open reaction vessels were used and must document the manufacturer and model of the reactor, the method of monitoring the reaction mixture temperature, and the temperature-time profile. Reporting a wattage rating or power setting is not an acceptable alternative to providing temperature data. Manuscripts describing work done with domestic (kitchen) microwave ovens will not be accepted except for studies where the unit is used for heating reaction mixtures at atmospheric pressure.

3. Compound characterization

The Journal upholds a high standard for compound characterization to ensure that substances being added to the chemical literature have been correctly identified and can be synthesized in known yield and purity by the reported preparation and isolation methods. For **all new** compounds, evidence adequate to establish both **identity** and **degree of purity** (homogeneity) must be provided.

Identity - Melting point. All homogeneous solid products (*e.g.* not mixtures of isomers) should be characterized by melting or decomposition points. The colors and morphologies of the products should also be noted.

Specific rotations. Specific rotations based on the equation $[\alpha]_D = (100 \alpha) / (l c)$ should be reported as unitless numbers as in the following example: $[\alpha]_D^{20}; D = -25.4$ (c 1.93, CHCl_3), where $c / \text{g mL}^{-1}$ is concentration and l / dm is path length. The units of the specific rotation, $(\text{deg mL}) / (\text{g dm})$, are implicit and are not included with the reported value.

Spectra/Spectral Data. Important IR adsorptions should be given.

For all new diamagnetic substances, NMR data should be reported (^1H , ^{13}C , and relevant heteronuclei).

^1H NMR chemical shifts should be given with two digits after the decimal point. Include the number of protons represented by the signal, signal multiplicity, and coupling constants as needed (J italicized, reported with up to one digit after the decimal). The number of bonds through which the coupling is operative, nJ , may be specified by the author if known with a high degree of certainty. ^{13}C NMR signal shifts should be rounded to the nearest 0.01 ppm unless greater precision is needed to distinguish closely spaced signals. Field strength should be noted for each spectrum, not as a comment in the general experimental section. Hydrogen multiplicity (C, CH, CH_2 , CH_3) information obtained from routine DEPT spectra should be included. If detailed signal assignments are made, the type of NOESY or COSY methods used to establish atom connectivity and spatial relationships should be identified in the Supporting Information. Copies of spectra should also be included where structure assignments of complex molecules depend heavily on NMR interpretation. Numbering system used for assignments of signals should be given in the Supporting Information with corresponding general structural formula of named derivative.

HPLC/LCMS can be substituted for biochemistry papers where the main focus is not on compound synthesis.

HRMS/elemental analysis. To support the molecular formula assignment, HRMS data accurate within 5 ppm, or combustion elemental analysis [carbon and hydrogen (and nitrogen, if present)] data accurate within 0.5 %, should be reported for new compounds. HRMS data should be given in format as is usually given for combustion analysis: calculated mass for given formula following with observed mass: (+)ESI-HRMS m/z : [molecular formula + H]⁺ calculated mass, observed mass. Example: (+)ESI-HRMS m/z : calculated for $[\text{C}_{13}\text{H}_8\text{BrCl}_2\text{N} + \text{H}^+]$ 327.92899, observed 327.92792.

NOTE: in certain cases, a crystal structure may be an acceptable substitute for HRMS/elemental analysis.

Biomacromolecules. The structures of biomacromolecules may be established by providing evidence about sequence and mass. Sequences may be inferred from the experimental order of amino acid, saccharide, or nucleotide coupling, from known sequences of templates in enzyme-mediated syntheses, or through standard sequencing techniques. Typically, a sequence will be accompanied by MS data that establish the molecular weight.

Example: Product was isolated upon column chromatography [dry flash (SiO_2 , eluent EA, EA/MeOH gradient 95/5 \rightarrow 9/1, EA/MeOH/ NH_3 gradient 18/0.5/0.5 \rightarrow 9/1/1, and flash chromatography (Biotage SP1, RP column, eluent MeOH/ H_2O gradient 75/25 \rightarrow 95/5, N-H column, eluent EA/Hex gradient 6/3 \rightarrow EA). was obtained after flash column chromatography (Biotage SP NH column, eluent hexane/EA 4:6 \rightarrow 2:6). Yield 968.4 mg (95 %). Colorless foam softens at 96-101 °C. $[\alpha]_D^{20}; D = +0.163$ ($c = 2.0 \times 10^{-3}$ g/mL, CH_2Cl_2). IR (ATR): 3376w, 2949m, 2868w, 2802w, 1731s, 1611w, 1581s, 1528m, 1452m, 1374s, 1331w, 1246s, 1171m, 1063w, 1023m, 965w, 940w, 881w, 850w, 807w, cm^{-1} . ^1H NMR (500 MHz, CDCl_3 , δ): 8.46 (*d*, 1H, $J = 5.4$, H-2'), 7.89 (*s*, 1H, $J = 2.0$, H-8'), 7.71 (*d*, 1H, $J = 8.9$, H-5'), 7.30 (*dd*, 1H, $J_1 = 8.8$, $J_2 = 2.1$, H-6'), 6.33 (*d*, 1H, $J = 5.4$, H-3'), 6.07 (*s*, HN-Boc, exchangeable with D_2O), 5.06 (*s*, 1H, H-12), 4.92-4.88 (*m*, 1H, H-7), 4.42 (*bs*, H-3), 3.45 (*s*, CH_3 -N), 3.33 (*bs*, H-9'), 3.05-2.95 (*m*, 2H, H-11'), 2.70-2.43 (*m*, 2H, H-24) and HN, exchangeable with D_2O), 2.07 (*s*, CH_3COO), 2.04 (*s*, CH_3COO), 1.42 (*s*, 9H, $(\text{CH}_3)_3\text{C-N}(\text{Boc})$), 0.88 (*s*, 3H, CH_3 -10), 0.79 (*d*, 3H, $J = 6.6$, CH_3 -20), 0.68 (*s*, 3H, CH_3 -13). ^{13}C NMR (125 MHz, CDCl_3 , δ): 170.34, 170.27, 151.80, 149.92, 148.87, 134.77, 128.36, 125.11, 121.43, 117.29, 99.98, 75.41, 70.82, 50.43, 49.66, 47.60, 47.33, 44.97, 43.30, 41.83, 41.48, 37.65, 36.35, 35.44, 34.89,

34.19, 33.23, 31.24, 28.79, 28.35, 27.25, 26.45, 25.45, 22.74, 22.63, 21.57, 21.31, 17.85, 12.15. (+)ESI-HRMS (*m/z*): calculated for [C₄₅H₆₇CIN₄O₆ + H]⁺ 795.48219, observed 795.48185. Combustion analysis for C₄₅H₆₇CIN₄O₆: Calculated. C 67.94, H 8.49, N 7.04; found C 67.72, H 8.63, N 6.75. HPLC purity: method A: RT 1.994, area 99.12 %; method C: RT 9.936, area 98.20 %.

Purity - Evidence for documenting compound purity should include one or more of the following:

- Well-resolved high field 1D ¹H NMR spectrum showing at most only trace peaks not attributable to the assigned structure and a standard 1D proton-decoupled ¹³C NMR spectrum. Copies of the spectra should be included as figures in the Supporting Information.
- Quantitative gas chromatographic analytical data for distilled or vacuum-transferred samples, or quantitative HPLC analytical data for materials isolated by column chromatography or separation from a solid support. HPLC analyses should be performed in two diverse systems. The stationary phase, solvents (HPLC), detector type, and percentage of total chromatogram integration should be reported; a copy of the chromatograms may be included as a figure in the Supporting Information.
- Electrophoretic analytical data obtained under conditions that permit observing impurities present at the 5 % level.

HRMS data may be used to support a molecular formula assignment **but cannot be used as a criterion of purity.**

4. Biological Data

Quantitative biological data are required for all tested compounds. Biological test methods must be referenced or described in sufficient detail to permit the experiments to be repeated by others. Detailed descriptions of biological methods should be placed in the experimental section. Standard compounds or established drugs should be tested in the same system for comparison. Data may be presented as numerical expressions or in graphical form; biological data for extensive series of compounds should be presented in tabular form. Tables consisting primarily of negative data will not usually be accepted; however, for purposes of documentation they may be submitted as supporting information. Active compounds obtained from combinatorial syntheses should be resynthesized and retested to verify that the biology conforms to the initial observation.

Statistical limits (statistical significance) for the biological data are usually required. If statistical limits cannot be provided, the number of determinations and some indication of the variability and reliability of the results should be given. References to statistical methods of calculation should be included. Doses and concentrations should be expressed as molar quantities (*e.g.*, mol/kg, μmol/kg, M, mM). The routes of administration of test compounds and vehicles used should be indicated, and any salt forms used (hydrochlorides, sulfates, *etc.*) should be noted. The physical state of the compound dosed (crystalline, amorphous; solution, suspension) and the formulation for dosing (micronized, jet-milled, nanoparticles) should be indicated. For those compounds found to be inactive, the highest concentration (*in vitro*) or dose level (*in vivo*) tested should be indicated.

- The RESULTS AND DISCUSSION should include concisely presented results and their significance discussed and compared to relevant literature data. The results and discussion may be combined or kept separate.
- The inclusion of a CONCLUSION section, which briefly summarizes the principal conclusions, is recommended.
- NOMENCLATURE is optional but, if the authors wish, a list of employed symbols may be included.
- REFERENCES should be numbered sequentially as they appear in the text. Please note that any reference numbers appearing in the Illustrations and/or Tables and corresponding captions must follow the numbering sequence of the paragraph in which they appear for the first time. When cited, the reference number should be superscripted in Font 12, following any punctuation mark. In the reference list, they should be in normal position followed by a full stop. Reference entry must not be formatted using Carriage returns (enter key; ↵ key) or multiple space key. The formatting of references to published work should follow the *Journal's* style as follows:

- Journals^a: A. B. Surname1, C. D. Surname2, *J. Serb. Chem. Soc.* **Vol** (Year) first page Number
(<https://doi.org/doi>)^b
- Books: A. B. Surname1, C. D. Surname2, *Name of Book*, Publisher, City, Year, pp. 100-101
(<https://doi.org/doi>)^b
- Compilations: A. B. Surname1, C. D. Surname2, in *Name of Compilation*, A. Editor1, C. Editor2, Ed(s)., Publisher, City, Year, p. 100 (<https://doi.org/doi>)^b
- Proceedings: A. B. Surname1, C. D. Surname2, in *Proceedings of Name of the Conference or Symposium*, (Year), Place of the Conference, Country, *Title of the Proceeding*, Publisher, City, Year, p. or Abstract No. 100
- Patents: A. B. Inventor1, C. D. Inventor2, (Holder), Country Code and patent number (registration year)
- Chemical Abstracts: A. B. Surname1, C. D. Surname2, *Chem. Abstr.* CA 234 567a; For non-readily available literature, the Chemical Abstracts reference should be given in square brackets: [C.A. 139/2003 357348t] after the reference
- Standards: EN ISO 250: *Name of the Standard* (Year)
- Websites: Title of the website, URL in full (date accessed)
- ^a When citing Journals, the International Library Journal abbreviation is required. Please consult, e.g., https://images.wobofknowledge.com/WOK46/help/WOS/A_abrvjt.html
- ^b doi should be replaced by doi number of the Article, for example: <http://dx.doi.org/10.2298/JSC161212085B> (as active link). If doi do not exist, provide the link to the online version of the publication.

Only the last entry in the reference list should end with a full stop.

The names of all authors should be given in the list of references; the abbreviation *et al.* may only be used in the text. The original journal title is to be retained in the case of publications published in any language other than English (please denote the language in parenthesis after the reference). Titles of publications in non-Latin alphabets should be transliterated. Russian references are to be transliterated using the following transcriptions:

ж→zh, х→kh, ц→ts, ч→ch, ш→sh, щ→shch, ы→y, ю→yu, я→ya, э→e, й→i, ь→'.

Supplementary material

Authors are encouraged to present the information and results non-essential to the understanding of their paper as SUPPLEMENTARY MATERIAL (can be uploaded in Step 4 of Online Submission). This material may include as a rule, but is not limited to, the presentation of analytical and spectral data demonstrating the identity and purity of synthesized compounds, tables containing raw data on which calculations were based, series of figures where one example would remain in the main text, etc. The Editorial Board retain the right to assign such information and results to the Supplementary material when deemed fit. Supplementary material does not appear in printed form but can be downloaded from the web site of the JSCS.

Mathematical and chemical equations should be given in separate lines and must be numbered, Arabic numbers, consecutively in parenthesis at the end of the line. All equations should be embedded in the text. Complex equations (fractions, integrals, matrix...) should be prepared with the aid of the Microsoft Equation 3.0 (or higher) or MathType (Do not use them to create simple equations and labels). Using the Insert -> Equation option, integrated in MS Office 2010 and MS Office 2013, as well as insertion of equation objects within paragraph text IS NOT ALLOWED.

Deposition of crystallographic data

Prior to submission, the crystallographic data included in a manuscript presenting such data should be deposited at the appropriate database. Crystallographic data associated with organic and metal-organic structures should be deposited at the Cambridge Crystallographic Data Centre (CCDC) by e-mail to deposit@ccdc.cam.ac.uk

Crystallographic data associated with inorganic structures should be deposited with the Fachinformationszentrum Karlsruhe (FIZ) by e-mail to crysdata@fiz-karlsruhe.de. A deposition number will then be provided, which should be added to the reference section of the manuscript.

For detailed instructions please visit the JSCS website:
<https://www.shd-pub.org.rs/index.php/JSCS/Instructions>

ARTWORK INSTRUCTIONS

JSCS accepts only **TIFF** or **EPS** formats, as well as **JPEG** format (only for colour and greyscale photographs) for electronic artwork and graphic files. **MS files** (Word, PowerPoint, Excel, Visio) **NOT acceptable**. Generally, scanned instrument data sheets should be avoided. Authors are responsible for the quality of their submitted artwork. Every single Figure or Scheme, as well as any part of the Figure (A, B, C...) should be prepared according to following instructions (every part of the figure, A, B, C..., must be submitted as an independent single graphic file):

TIFF

Virtually all common artwork and graphic creation software is capable of saving files in TIFF format. This 'option' can normally be found under 'the 'Save As...' or 'Export...' commands in the 'File' menu.

TIFF (Tagged Image File Format) is the recommended file format for bitmap, greyscale and colour images.

- Colour images should be in the RGB mode
- When supplying TIFF files, please ensure that the files are supplied at the correct resolution:
 1. Line artwork: minimum of 1000 dpi
 2. RGB image: minimum of 300 dpi
 3. Greyscale image: minimum of 300 dpi
 4. Combination artwork (line/greyscale/RGB): minimum of 500 dpi
- Images should be tightly cropped, without frame and any caption.
- If applicable please re-label artwork with a font supported by JSCS (Arial, Helvetica, Times, Symbol) and ensure it is of an appropriate font size.
- Save an image in TIFF format with LZW compression applied.
- It is recommended to remove Alpha channels before submitting TIFF files.
- It is recommended to flatten layers before submitting TIFF files.

Please be sure that quality of an image cannot be increased by changing the resolution from lower to higher, but only by rescanning or exporting the image with higher resolution, which can be set in usual "settings" facilities.

EPS

Virtually all common artwork creation software, such as Canvas, ChemDraw, CorelDraw, SigmaPlot, Origin Lab..., are capable of saving files in EPS format. This 'option' can normally be found under the 'Save As...' or 'Export...' commands in the 'File' menu.

For vector graphics, EPS (Encapsulated PostScript) files are the preferred format as long as they are provided in accordance with the following conditions:

- when they contain bitmap images, the bitmaps should be of good resolution (see instructions for TIFF files)
- when colour is involved, it should be encoded as RGB
- an 8-bit preview/header at a resolution of 72 dpi should always be included
- embed fonts should always included and only the following fonts should be used in artwork: Arial, Helvetica, Times, Symbol
- the vertical space between the parts of an illustration should be limited to the bare necessity for visual clarity
- no data should be present outside the actual illustration area
- line weights should range from 0.35 pt to 1.5 pt
- when using layers, they should be reduced to one layer before saving the image (Flatten Artwork)

JPEG

Virtually all common artwork and graphic creation software is capable of saving files in JPEG format. This 'option' can normally be found under 'the 'Save As...' or 'Export...' commands in the 'File' menu.

JPEG (Joint Photographic Experts Group) is the acceptable file format **only for colour and greyscale photographs**. JPEG can be created with respect to photo quality (low, medium, high; from 1 to 10), ensuring file sizes are kept to a minimum to aid easy file transfer. Images should have a minimum resolution of 300 dpi. Image width: minimum 3.0 cm; maximum 12.0 cm.

Please be sure that quality of an image cannot be increased by changing the resolution from lower to higher, but only by rescanning or exporting the image with higher resolution, which can be set in usual "settings" facilities.

SIZING OF ARTWORK

- JSCS aspires to have a uniform look for all artwork contained in a single article. Hence, it is important to be aware of the style of the journal.
- Figures should be submitted in black and white or, if required, colour (charged). If coloured figures or photographs are required, this must be stated in the cover letter and arrangements made for payment through the office of the Serbian Chemical Society.
- As a general rule, the lettering on an artwork should have a finished, printed size of 11 pt for normal text and no smaller than 7 pt for subscript and superscript characters. Smaller lettering will yield a text that is barely legible. This is a rule-of-thumb rather than a strict rule. There are instances where other factors in the artwork, (for example, tints and shadings) dictate a finished size of perhaps 10 pt. Lines should be of at least 1 pt thickness.
- When deciding on the size of a line art graphic, in addition to the lettering, there are several other factors to address. These all have a bearing on the reproducibility/readability of the final artwork. Tints and shadings have to be printable at the finished size. All relevant detail in the illustration, the graph symbols (squares, triangles, circles, *etc.*) and a key to the diagram (to explain the explanation of the graph symbols used) must be discernible.
- The sizing of halftones (photographs, micrographs,...) normally causes more problems than line art. It is sometimes difficult to know what an author is trying to emphasize on a photograph, so you can help us by identifying the important parts of the image, perhaps by highlighting the relevant areas on a photocopy. The best advice that can be given to graphics suppliers is not to over-reduce halftones. Attention should also be paid to magnification factors or scale bars on the artwork and they should be compared with the details inside. If a set of artwork contains more than one halftone, again please ensure that there is consistency in size between similar diagrams.

General sizing of illustrations which can be used for the Journal of the Serbian Chemical Society:

- Minimum fig. size: 30 mm width
- Small fig. size - 60 mm width
- Large fig. size - 90 mm width
- Maximum fig. size - 120 mm width

Pixel requirements (width) per print size and resolution for bitmap images:

	Image width	A	B	C
Minimal size	30 mm	354	591	1181
Small size	60 mm	709	1181	2362
Large size	90 mm	1063	1772	3543
Maximal size	120 mm	1417	2362	4724

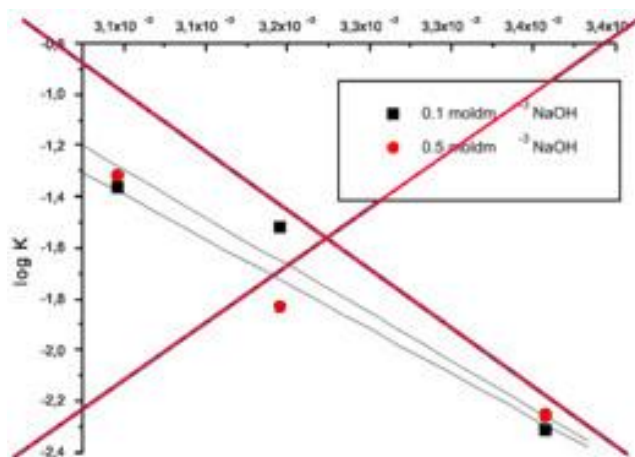
A: 300 dpi > RGB or Greyscale image

B: 500 dpi > Combination artwork (line/greyscale/RGB)

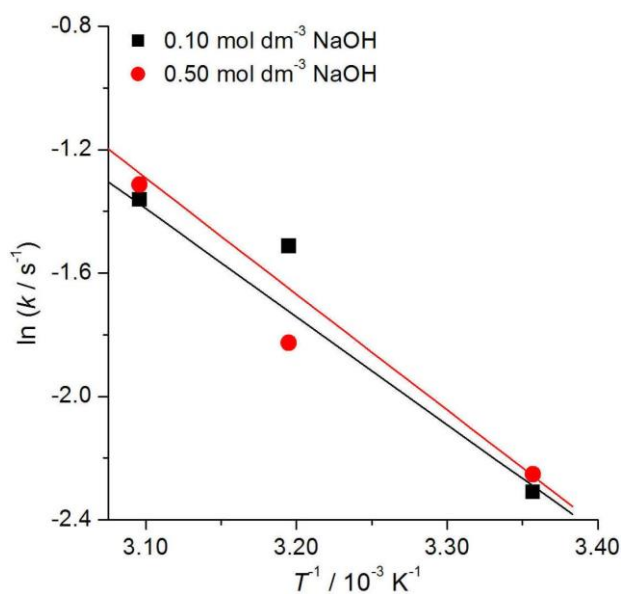
C: 1000 dpi > Line artwork

The designation of physical quantities and graphs formatting

The designation of physical quantities on figures must be in italic, whereas the units are in upright letters. They should be in Times New Roman font. In graphs a slash should be used to separate the designation of a physical quantity from the unit (example: p / kPa , $t / ^\circ\text{C}$, T_0 / K , τ / h , $\ln(j / \text{mA cm}^{-2})$...). Designations such as: p (kPa), t [min]..., are not acceptable. However, if the full name of a physical quantity is unavoidable, it should be given in upright letters and separated from the unit by a comma (example: **Pressure, kPa, Temperature, K...**). Please do not use the axes of graphs for additional explanations; these should be mentioned in the figure captions and/or the manuscript (example: “pressure at the inlet of the system, kPa” should be avoided). The axis name should follow the direction of the axis (the name of y-axis should be rotated by 90°). Top and right axes should be avoided in diagrams, unless they are absolutely necessary. Decimal numbers must have decimal points and not commas in the axis labels in graphical presentations of results. Thousands are separated, if at all, by a comma and not a point.



INCORRECT



CORRECT



CONTENTS*

Organic Chemistry

- S. Đ. Stojanović, Z. Z. Petrović and M. V. Zlatović: Amide- π interactions in active centres of superoxide dismutase 781

Biochemistry and Biotechnology

- N. Gligorijević, V. Šukalović, S. Minić, G. Miljuš, O. Nedić and A. Penezić: Physico-chemical characterisation of dihydro-alpha-lipoic acid interaction with human serum albumin by multi-spectroscopic and molecular modelling approaches 795
- I. V. Sofrenić, B. D. Anđelković, Lj. Vujisić, M. Novaković, A. Z. Knežević, M. B. Stanaković, S. M. Milosavljević and V. V. Tešević: DNA protective activity of triterpenoids isolated from medicinal mushroom *Fomitopsis betulina* 809

Physical Chemistry

- B. K. Adnađević, N. M. Cvetković and J. D. Jovanović: Kinetics of the exchange of water absorbed in silica hydrogel with ethanol: Modelling by Brouers and Sotolongo-Costa fractal kinetics 819
- A. Rahmatulloh and L. Atmadja: Correlation between silane concentration and temperature operated toward conductivity of well-synthesized chitosan-fly ash composite membrane 831

Electrochemistry

- Y. Pohorenko, R. Pshenychnyi, T. Pavlenko, A. Omel'chuk and V. Trachevskiy: Fluoride ion conductivity of solid solutions $K_xPb_{0.86-x}Sn_{1.14}F_{4-x}$ 845

Analytical Chemistry

- B. Wang, F. Jiang, X. Zuo, J. Ma and X. Ma: Benzimidazole-functionalized fluorescent probe for rapid detection of 2,4,6-trinitrophenol and Ag^+ in semiaqueous medium ... 859

Polymers

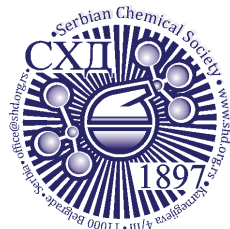
- K. A. Kololi, S. M. T. Ghomsheh, M. Noei and M. Saberi: Enhanced gas permeation performance of mixed matrix membranes containing polysulfone and modified mesoporous MCM-41 871

Materials

- A. Ivanovska, L. Pavun, B. Dojčinović and M. Kostić: Kinetic and isotherm studies for the biosorption of nickel ions by jute fabrics 885

Published by the Serbian Chemical Society
Karnegijeva 4/III, P.O. Box 36, 11120 Belgrade, Serbia
Printed by the Faculty of Technology and Metallurgy
Karnegijeva 4, P.O. Box 35-03, 11120 Belgrade, Serbia

* For colored figures in this issue please see electronic version at the Journal Home Page:
<http://www.shd.org.rs/JSCS/>



J. Serb. Chem. Soc. 86 (9) 781–793 (2021)
JSCS–5461

Amide– π interactions in active centres of superoxide dismutase

SRĐAN Đ. STOJANOVIĆ¹, ZORAN Z. PETROVIĆ² and MARIO V. ZLATOVIĆ^{3*#}

¹University of Belgrade-Institute of Chemistry, Technology and Metallurgy, Department of Chemistry, Belgrade, Serbia, ²Faculty of Mathematics, University of Belgrade, Belgrade, Serbia and ³Faculty of Chemistry, University of Belgrade, Belgrade, Serbia

(Received 21 March, revised 1 June, accepted 2 June 2021)

Abstract: In this work, the influence of amide– π interactions on stability and properties of superoxide dismutase (SOD) active centres was analysed. In the data set of 43 proteins, 5017 amide– π interactions were observed, and every active centre formed averagely about 117 interactions. Most of the interactions belonged to the backbone of proteins. The analysis of the geometry of the amide– π interactions revealed two preferred structures, parallel-displaced and T-shaped structure. The aim of this study was to investigate the energy contribution resulting from amide– π interactions, which were in the lower range of strong hydrogen bonds. The conservation patterns in the present study indicate that more than half of the residues involved in these interactions are evolutionarily conserved. The stabilization centres for these proteins showed that all residues involved in amide– π interactions were of use in locating one or more of such centres. The results presented in this work can be very useful for the understanding of contribution of amide– π interaction to the stability of SOD active centres.

Keywords: catalytic site; distribution of distances; stabilization of the SOD proteins.

INTRODUCTION

Noncovalent interactions involving aromatic rings (π -stacking, cation– π , anion– π , X–H/ π , *etc.*) play vital roles in many chemical and biochemical phenomena.^{1–3} The attractive interactions between aromatic groups of amino acids and nearby amides, in polypeptides and proteins (Ar–HN), are weakly polar and have a quadrupole–dipole nature. These interactions can be effectively modelled by the electrostatic interaction between the partial negative charge of an aromatic ring and the partial positive charge of an amide hydrogen.⁴ The strength of this

* Corresponding author. E-mail: mario@chem.bg.ac.rs

Serbian Chemical Society member.

<https://doi.org/10.2298/JSC210321042S>

interaction in vacuum (-1 to -4 kcal* mol $^{-1}$) is almost comparable with that of a conventional hydrogen bond (-2 to -7 kcal mol $^{-1}$).⁴⁻⁶ Therefore, the function and the formation of Ar–NH interactions in the protein structure are heavily dependent on the conformational consequences of stronger forces, such as the conventional hydrogen bond. On the basis of the location of the NH group in a polypeptide, the interactions between an aromatic ring and NH can be characterized as either Ar–NH(side chain) or Ar–NH(backbone). Furthermore, as the protein backbone is less flexible than the amino acid side chains, it should be simpler to target amide stacking interactions through the structure-based drug design.⁷ Additionally, the large number of intra-protein hydrogen bonds involving backbone amides means that the π -face of these functional groups is typically more accessible for the interactions with ligands.⁸

The importance of aromatic interactions in proteins were pointed out first by Burley and Petsko,⁹ in their work on interaction between phenylalanine residues. Studies by Burley and Petsko suggested the involvement of Ar–NH interactions in the stabilization of protein tertiary structures, on the basis of their spatial distribution.^{10,11} Further investigations by various research groups established the role of these interactions in the ligand recognition and the stabilization of secondary structures, mainly β -sheets and helix termini.¹²⁻¹⁵ The Diederich lab has taken the lead in increasing our understanding of these interactions and the knowledge gained from this structure-activity relationship study and the detection of the binding mode has been continuing to inspire their use in rational design.¹⁶⁻²²

The planar residues, such as His, Tyr, Asp, Arg, Pro, *etc.* are usually playing an important role at the catalytic and binding sites.²³ Furthermore, the amide groups are abundant in protein binding sites, either as part of the backbone or asparagine and/or glutamine side chains. Therefore, to explain the role of amide– π interactions in the secondary and the local structures of superoxide dismutase, as well as to improve the prediction of the amide– π interaction, 43 protein structures for the amide– π interactions between the aromatic ring of His, Phe, Trp, and Tyr and the amide group of any residue in superoxide dismutase (SOD) active centres were analysed.

EXPERIMENTAL

Dataset

For this study, the Protein Data Bank (PDB) October 5th, 2020, list of 173,420 structures was used.²⁴ The selection criteria for the superoxide dismutase to be included in the dataset were as follows: 1) the crystal structures of proteins containing E.C. Number 1.15.1.1 (superoxide dismutase) with metal were accepted; 2) the theoretical model structures and the NMR structures were not included (these structures were not accepted as it was difficult to define the accuracy of the ensemble of structures in terms of displacement, that was directly comparable to the X-ray diffraction studies); 3) the only crystal structures with the resolution of 2.0 Å

* 1 kcal = 4184 J

or better and a crystallographic R -factor of 25.0 % or lower were accepted; 4) only representatives at 30 % sequence identity were included. After assembling the dataset, several structures containing ligands and mutant amino acids were rejected, thus leaving 43 proteins that were actually used as the dataset in our analysis. The hydrogen atoms were added and optimized, where needed, using the program Reduce,²⁵ with default settings. Reduce software adds hydrogen atoms to protein and/or DNA structures in standardized geometry, optimizing them to the orientations of OH, SH, NH_3^+ , Met methyls, Asn and Gln sidechain amides, and His rings. The software determines the best hydrogen positions by selecting the best overall score from all of the possible combinations, taking into the account individual scores assigned for each individual residue and for groups containing movable protons partitioned in closed sets of local interacting networks. The PDB IDs of selected structures (protein chains) are as follows: 1ar5:A, 1cbj:A, 1d5n:A, 1hl5:A, 1ids:A, 1isa:A, 1kkc:A, 1my6:A, 1qnn:A, 1srd:A, 1to4:A, 1unf:X, 1xre:A, 1xuq:A, 1y67:A, 1yai:A, 1yso:A, 2aqn:A, 2cw2:A, 2goj:A, 2rev:A, 2w7w:A, 3ak2:A, 3ce1:A, 3dc6:A, 3evk:A, 3f7l:A, 3h1s:A, 3js4:A, 3lio:A, 3lsu:A, 3mds:A, 3pu7:A, 3tqj:A, 4br6:A, 4c7u:A, 4f2n:A, 4ffk:A, 4yet:A, 5a9g:A, 5vf9:A, 6bej:A, and 6gsc:A.

Amide- π interaction analysis

For the selection of the protein structures having various types of amide- π interactions, Discovery Studio Visualizer 2020 was used,²⁶ with some specific criteria and geometrical feature settings. Amide- π stacked interactions occur between an amide group and a π ring if the following criteria are satisfied (Fig. 1): 1) the distance between the centroid of the amide group and the π rings falls within the π - π centroid (max dist, R_{cen} ; 7 Å); 2) an atom from the each group should be within the π - π closest atom (max dist, R_{clo} ; 7 Å); 3) the angle θ between the normal of one or both groups and the centroid-centroid vector must be between 0° and \pm the stacked π -amide theta angle cut-off distance, and the angle γ between the normal to each must be between 0° and \pm the stacked π -amide gamma angle cut-off. The centroid of amide group plane was taken as the midpoint of C and N atoms. Compared to the criteria applied in the studies of small molecules found in the Cambridge Structural Database (CSD) these criteria were a bit more relaxed. The slightly looser criteria were selected because the structural variations in crystal structures of proteins are generally larger than in crystal structures of small molecules. The earlier publications confirmed π interactions as long-range interactions, having notable binding forces even at intermolecular distances of 7 Å.²⁷⁻²⁹

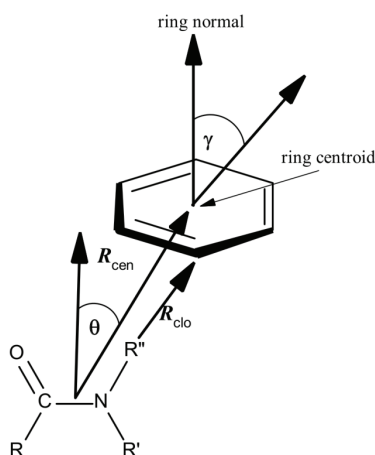


Fig. 1. Parameters for amide- π interactions: (R_{cen}) the distance between the centroid of the amide group and the π ring; (R_{clo}) the distance between π - π closest atoms from each group; (θ) the angle between the amide-centroid vector and a chosen vector on the principle axis of the aromatic ring; and (γ) the angle between the normal of each ring.

Computation of amide- π interaction energy

In order to apply *ab initio* methods in determining the energies of amide- π pairs on the desired level of theory, with the sufficient level of accuracy and still in satisfactory time frame, the calculations were performed on structurally reduced model systems.²⁹ We used formamide (**1**) as mimics for amide groups. Phenylalanine was simplified to methylbenzene (**2**), histidine to 5-methyl-1*H*-imidazole (**3**), while tryptophan and tyrosine were reduced to 3-methyl-1*H*-indole (**4**) and 4-methylphenol (**5**), respectively (Fig. 2).

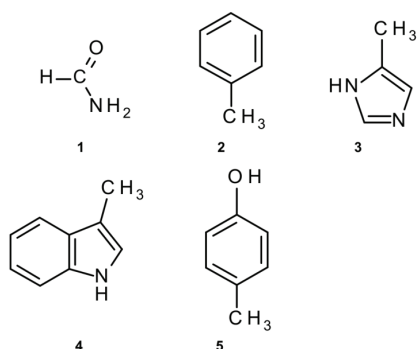


Fig. 2. Structurally reduced structures used for calculations of amide- π interaction energy: **1** instead of amide; **2** instead of Phe; **3** instead of His; **4** instead of Trp; **5** instead of Tyr.

The use of a reduced model systems in calculations of specific intramolecular interaction in large systems is a well-known and already proved methodology,³⁰ producing the results which are accurate enough, but significantly reducing the computation times and the strength needed for them. Larger models, like whole amino acids, or parts of protein chain, will complicate the calculations unnecessarily and can probably even bring in errors. Numerous interactions mechanisms are possible in a larger protein structure, and a single binding energy computation cannot always determine the accurate result, meaning which of these are present and to what amount they contribute to overall stabilization. As a result, separating the involvement of the amide- π interaction from the interacting pair, based on their energies residues involved in other noncovalent interactions, is difficult.

Ab initio calculations were performed using Jaguar from Schrödinger Suite 2018-1,³¹ using local Møller-Plesset second-order method (LMP2) method with triple zeta Dunning's correlation consistent basis set³² and ++ diffuse functions.³³ All calculations were performed in vacuum. The LMP2 method applied to the study of amide- π interactions, showed to be considerably faster than the MP2 method, while the calculated the interaction energies and the equilibrium distances were almost identical for both methods.³⁴ Several authors found that LMP2 represents an excellent method for calculation of interaction energies in proteins.^{35,36} Sometimes calculation results can be influenced largely by BSSE, so taking it into the account is mandatory, therefore the calculation times are longer. The local correlation methods (such as LMP2) not only reduce the cost of the calculations, but the local Møller-Plesset second-order method LMP2 is well known for reducing the intramolecular basis set superposition error (BSSE).³⁷⁻³⁹

Geometries of the interacting structures were optimized and their single point energies calculated using LMP2/cc-pVTZ(-f)++ level of theory. The optimized geometries of molecules were placed to match the corresponding complexes by superimposing heavy atoms onto their respective coordinates, taken from the crystal structures, and the energies of dimeric structures produced which were calculated way.

The amide- π interaction energies in dimers (amide- π pairs) were calculated as the difference between the energy of the complex and the sum of the energies of the monomers in their optimized geometries.

Computation of stabilization centres

The stabilization centres (SC) are defined as the clusters of residues which make cooperative, noncovalent long-range interactions.⁴⁰ Measured as individual interactions, the stabilization forces resulting from noncovalent long-range interactions are not very strong, but since they are cooperative by their nature they could play an important role in maintaining the overall stability of protein structures in regions where they act in a group (SC). In order to analyse SC of interaction-forming residues, we used the SCide program.⁴¹ The criteria SCide uses for determining SC are as follows: 1) two residues are in contact if there is, at least, one heavy atom-atom distance smaller than the sum of their van der Waals radii plus 1 Å; 2) a contact is recognized as “long-range” interaction if the interacting residues are, at least, ten amino acids apart; 3) two residues form a stabilization centres if they are in long-range interaction and if it is possible to select one-one residue from both flanking tetrapeptides of these two residues that make, at least, seven contacts between these two triplets.⁴¹

Computation of conservation of amino acid residues

The conservation of the amino acid residues in each protein was computed using the ConSurf server.⁴² This server computes the conservation based on the comparison of the sequence of given PDB chain with the proteins deposited in Swiss-Prot database⁴³ and finds the ones that are homologous to the PDB sequence. The number of PSI-BLAST iterations and the *E*-value cut-off used in all similarity searches were 1 and 0.001, respectively. All the sequences, that were evolutionary related to each one of the proteins in the dataset, were used in the subsequent multiple alignments. Based on these protein sequence alignments, the residues were classified into nine categories, from highly variable to highly conserved. Residues with a score of 1 are considered to be highly variable and residues with a score of 9 are considered to be highly conserved.

RESULTS AND DISCUSSION

A detailed analysis of the amide- π interactions in SOD involving backbone and side-chain groups, which are fully or partially in the active centres, is presented here. Our study was focused on the active centres, thus the amide- π interactions within the rest of the protein structures were not considered. In the dataset, there are 173,420 proteins. Using the geometrical criteria described in the Experimental section, we found 43 protein crystal structures. The analyzed protein set contains 5017 amide- π interactions. Thus, on average, every active centre forms 117 interactions. The quantification of such interactions is of great importance for a rational approach to biological systems including protein structure and function, as well as for the further development of drug design processes.

Distribution of amide- π interactions

The occurrence of different types of amide- π interactions found in the present dataset is presented in Table I. We noticed that almost all of the interactions were of backbone amide- π interactions type. These kind of interactions stabilize

tertiary and local structures and strengthen protein–ligand interactions.⁴⁴ However, although all protein structures contain side-chain amide groups (Asn, Gln and Arg) in the active centres, in our dataset those accounted for only 0.04 % of all amide– π interactions. It has been found that among the aromatic residues, the most efficient π -acceptor is the imidazole group of the histidine residue, followed by the indole group of tryptophan and the phenol moiety of tyrosine. This might be because, of all the aromatic amino acids, His occurs most frequently in both coordination spheres of active centres.²⁹

TABLE I. Frequency of occurrence of amide– π interaction-forming residues in active centres of superoxide dismutase

Residue	Amide		π	
	Number ^a	Occurrence, % ^b	Number	Occurrence, %
Backbone	5015	99.96	–	0
Side-chain				
Asn	–	0	–	0
Gln	1	0.02	–	0
Arg	1	0.02	–	0
His	–	0	1719	34.26
Phe	–	0	633	12.62
Trp	–	0	1461	29.12
Tyr	–	0	1204	24.00
Total	5017	100	5017	100

^aThe number of times a particular amino acid occurs in an appropriate interaction; ^bpercent of amino acid occurs in an appropriate interaction

A typical interface with some of the amide– π interactions involving backbone planar residues (A:Ile36:C,O;Met37:N–A:His40) and side-chain residues (A:Gln14:N–A:Tyr16) is shown in Fig. 3a and b, respectively.

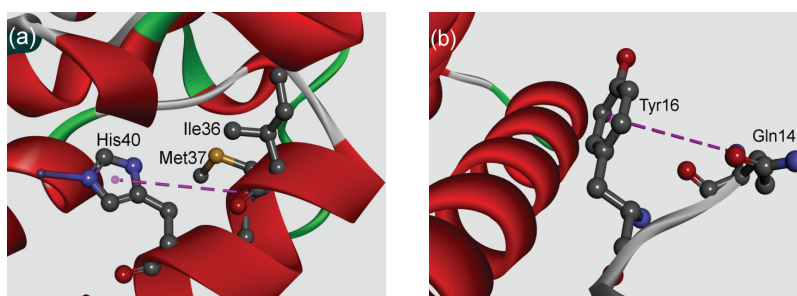


Fig. 3. Assorted examples of amide– π interactions for the MnSOD from *Aspergillus fumigatus* (PDB code 1kkc); a) backbone amide– π interaction, b) side-chain amide– π interaction. The interactions are marked with pink dashed lines.

The analysis showed that around 70 % of the total interacting residues in the dataset are involved in the formation of multiple amide– π interactions. In many

crystal structures of superoxide dismutases it is shown that a backbone amide is capable of binding with several aromatic residues. This type of interaction is marked as furcation. An illustrative example of amide- π interactions involving the presence of three aromatic groups surrounding one backbone amide is shown in Fig. 4. A backbone amide group from A:Met37-Glu38 can interact with three aromatic rings of A:His40, His42 and Trp92 simultaneously. This emphasizes the previous findings that furcation is an inherent characteristic of the superoxide dismutase.²⁹ The importance of multiple non-covalent weak interactions for the cooperativity and the governing of the multicomponent supramolecular assemblies has been already reported.⁴⁵ The another additional feature is the observed additive property of these interactions, showing an effect on the strength of the host-guest system.

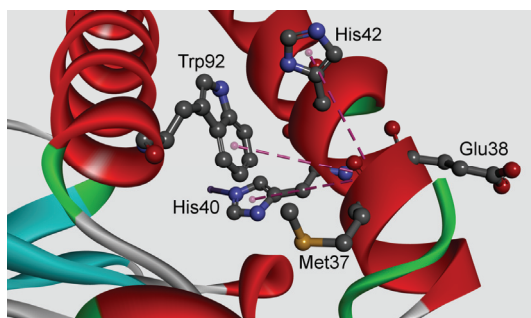


Fig. 4. Example of a multiple amide- π interaction for the MnSOD from *Aspergillus fumigatus* (PDB code 1kke); the interactions are marked with dashed lines.

Interaction geometries and energetic contribution of amide- π interactions

The frequency distribution of the distance and the angle parameters of amide- π interaction pairs were analyzed (Fig. 5). The distribution of R_{cen} , the centroid-centroid distance, for the amide- π interactions was found to be in the rather broad range of 4.5–7.0 Å (Fig. 5a), without showing a clear geometrical preference. However, a small number of interactions also occurs at distances below 4.5 Å, indicating an attractive interaction. A distribution of the R_{clo} distances shows a clear maxima of about 5 Å. This is in accordance with the centroid distances. The majority of furcated interactions exhibit longer distances than the simple non-furcated interactions, as expected.²⁹ The native structure represents the compromise of a large number of noncovalent interactions existing in proteins. The geometrical features relating two residue-types are expected to be rather broad.

The aromatic ring-amide angles were distributed between full range (0–90° range), with a preference for higher angle values (Fig. 5d). A distribution of the angles below 30° shows coplanarity, possibly due to the maximizing amide- π stacking and packing,⁴⁶ while the axial aromatic-amide pairs are more likely to have T-shaped orientation ($\gamma > 60^\circ$). In general, as the distance of the backbone amide from the aromatic residue increases, the occurrence of perpendicular

orientations increased as well. Values of the θ angle (Fig. 5c) were in good agreement with distributions of aromatic ring–amide angles. The freedom of rotation of the aromatic ring is restricted, whereas the rotamer distributions usually depend on the backbone conformation. There is no significant statistical difference in the γ angle distribution between the multiple and the single amide– π interactions. The preferred orientations are quite similar to those found in aromatic–aromatic interactions,⁴⁷ and T-shaped orientation is observed. In the parallel-stacked case, van der Waals contribution is the dominant effect and the electrostatics contribution is actually repulsive, although small in value (<1 kcal mol⁻¹). On the other hand, the van der Waals contribution in the T-shaped case is not overwhelming, and it is the attractive electrostatics contribution that results in the overall binding of ~ 2.0 kcal mol⁻¹.^{7,46}

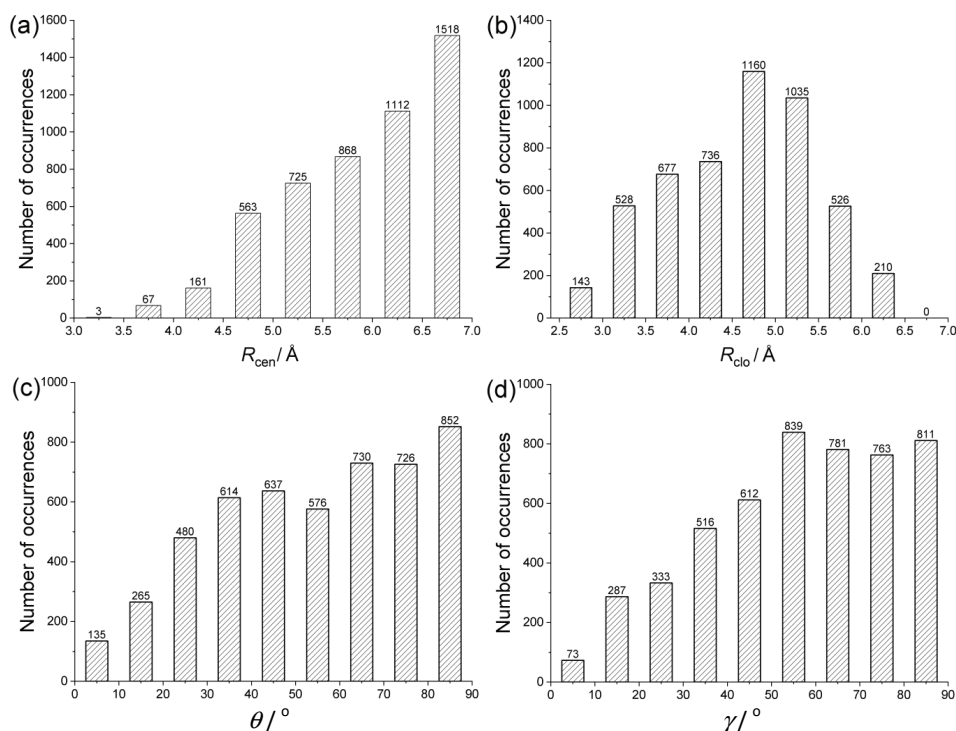


Fig. 5. Interaction geometries of amide– π interactions: a) R_{cen} distance distribution, b) R_{clo} distance distribution, c) θ angle distribution, d) γ angle distribution.

To estimate the stabilization energy of the different amide– π pairs, the energy calculations were carried out. To avoid the calculation of more than 5000 interactions, 150 structures were selected and they represent almost all of the interactions which had been found. In our database we found that the amide– π interactions energy is lower than -7 kcal mol⁻¹, and most of them have energy in the

range -1 to -4 kcal mol $^{-1}$ (Fig. 6). The energies of the weakly polar amide- π interactions examined here are in the lower range of strong hydrogen bonds (-4 to -15 kcal mol $^{-1}$), as classified by Desiraju and Steiner.⁴⁸ Thus, the amide- π interactions make a substantial impact on the conformational stability of proteins. The energy of the interaction between the aromatic ring backbone amide has a complex dependence on side chain rotamer orientations and the dynamics of the backbone.

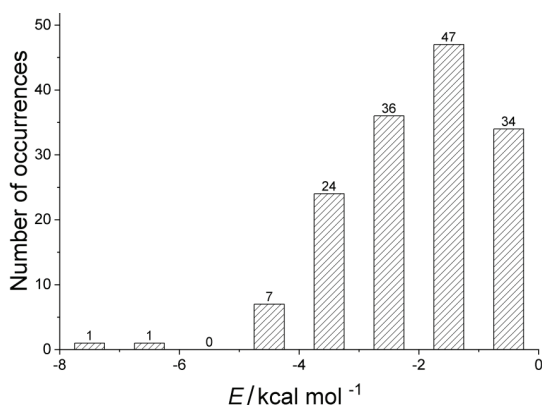


Fig. 6. Interaction energies of amide- π interactions.

Fig. 7 shows the preferred amide- π interactions of FeSOD from the thermophilic cyanobacterium *Thermosynechococcus elongatus*.

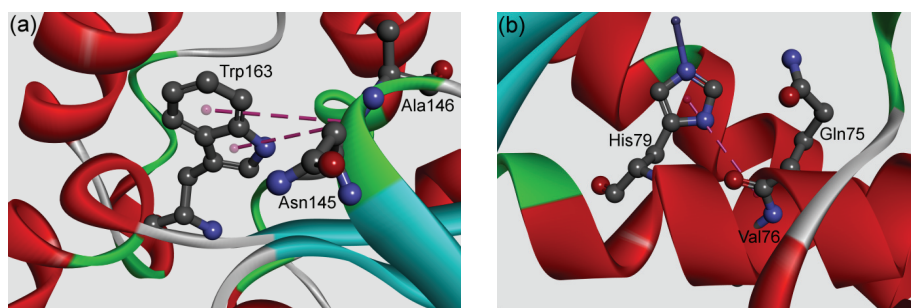


Fig. 7. Example of the structure preferred amide- π interactions of FeSOD from the *Thermosynechococcus elongatus* (PDB code 1my6): a) parallel-displaced and b) T-shaped structure. The interactions are marked with dashed lines.

The results of our *ab initio* calculations of optimized structures showed that the strongest attractive amide- π interactions exists in two preferred intermolecular structures, parallel-displaced (A:Asn145:C,O;Ala146:N—A:Trp163; $E = -7.05$ kcal mol $^{-1}$; $R_{\text{cen}} = 4.8$ Å; $R_{\text{clo}} = 2.9$ Å) and T-shaped structures (A:Gln75:C,O;Val76:N A:His79; $E = -6.89$ kcal mol $^{-1}$; $R_{\text{cen}} = 4.8$ Å; $R_{\text{clo}} = 2.8$ Å).

Stabilization centres and conservation of amino acid residues

Stabilization centres (SC) are composed of certain clusters of residues, involved in the cooperative long range interaction of proteins that regulate flexibility, rigidity and stability of the protein structures. The most frequent stabilization centre residues are usually found at buried positions and have hydrophobic or aromatic side-chains, but some polar or charged residues may also play an important role in stabilization. The stabilization centres, when compared with the rest of the residues, showed a significant difference in the composition and in the type of the linked secondary structural elements. The performed structural and sequential conservation analysis showed a higher conservation of stabilization centres over protein families.⁴⁰ The stabilization centres for all amide- π interaction forming residues in SOD active centres were computed. Considering the whole data set, 39.6 % of all stabilizing residues are involved in building the amide- π interactions. It is interesting to note that all the residues involved in amide- π interactions were included in at least one stabilization centre. These observations strongly suggest that those residues may contribute significantly to the structural stability of the studied proteins in addition to participating in amide- π interactions.

From the presented analysis, it was found that more than 69 % of amide- π interacting residues in SOD were highly conserved, with a score ≥ 6 , revealing their importance in the stability of protein structure.

CONCLUSION

The influence of amide- π interactions on the stability of SOD active centres was analysed in this research. It was found that most of the interactions occurs in the backbone of proteins. From the results it can be underlined that around 70 % of the total interacting residues in the dataset were involved in the formation of the multiple amide- π interactions. The distribution of distances for the amide- π interactions was found to be in the rather broad range of 4.5–7.0 Å, without clear geometrical preference. The amide- π interactions exists mainly in two preferred geometries, parallel-displaced and T-shaped structures. There is no significant statistical difference in the distances and the angle distribution between the multiple and the single amide- π interactions. the results suggested that the majority of the amide- π interactions showed some energy mostly in the range -1 to -4 kcal mol⁻¹. Moreover, the majority of the residues involved in amide- π interactions were evolutionarily conserved; all residues involved in amide- π interactions are included in at least one stabilization centre, thus providing an additional stabilization of the SOD proteins. The quantification of such interactions is of great importance for a rational approach to the biological systems including their protein structure and function, as well as for the further development of drug design processes.

Acknowledgement. The authors would like to thank the Ministry of Education, Science and Technological Development of Republic of Serbia (Grants No: 451-03-9/2021-14/200026, 451-03-9/2021-14/200104 and 451-03-9/2021-14/200168) for financial support.

ИЗВОД

АМИД- π ИНТЕРАКЦИЈЕ У АКТИВНОМ ЦЕНТРУ СУПЕРОКСИД-ДИСМУТАЗАСРБАН Ђ. СТОЈАНОВИЋ¹, ЗОРАН З. ПЕТРОВИЋ² и МАРИО В. ЗЛАТОВИЋ³

¹Универзитет у Београду-Институт за хемију, технологију и металургију, Београд, ²Математички факултет, Универзитет у Београду, Београд и ³Хемијски факултет, Универзитет у Београду, Београд

У овом раду је анализиран утицај амид- π интеракција на стабилност и особине активног центра супероксид-дисмутазе (SOD). Примећено је 5017 амид- π интеракција у сету података од 43 протеина, где, просечно, сваки активни центар формира 117 интеракција. Већина интеракција је укључена у основни ланац протеина. Анализа геометрије амид- π интеракција открива две приоритетне структуре, паралелно-измештен (*parallel-displaced*) и Т-облик (*T-shaped*) структуре. Ова студија има за циљ истраживање доприноса енергије амид- π интеракција чије јачине су у доњем рангу јаким водоничних веза. Преглед конзервираности показује да је више од половине остатака укључених у ове интеракције еволутивно конзервирано. Стабилизациони центри ових протеина показују да су сви остаци који чине амид- π интеракције важни у распоређивању једног или више таквих центара. Свеукупно, резултати у овом раду ће бити врло корисни за разумевање доприноса амид- π интеракција када се анализира стабилност активних центара SOD.

(Примљено 21. марта, ревидирано 1. јуна, прихваћено 2. јуна 2021)

REFERENCES

1. E. A. Meyer, R. K. Castellano, F. Diederich, *Angew. Chem., Int. Ed. Engl.* **42** (2003) 1210 (<https://doi.org/10.1002/anie.200390319>)
2. L. M. Salonen, M. Ellermann, F. Diederich, *Angew. Chem., Int. Ed. Engl.* **50** (2011) 4808 (<https://doi.org/10.1002/anie.201007560>)
3. N. Acharjee, *J. Serb. Chem. Soc.* **85** (2020) 765 (<https://doi.org/10.2298/JSC190914136A>)
4. M. Levitt, M. F. Perutz, *J. Mol. Biol.* **201** (1988) 751 ([https://doi.org/10.1016/0022-2836\(88\)90471-8](https://doi.org/10.1016/0022-2836(88)90471-8))
5. J. Cheney, B. V. Cheney, W. G. Richards, *Biochim. Biophys. Acta* **954** (1988) 137 ([https://doi.org/10.1016/0167-4838\(88\)90063-5](https://doi.org/10.1016/0167-4838(88)90063-5))
6. G. Duan, V. H. Smith, D. F. Weaver, *Chem. Phys. Lett.* **310** (1999) 323 ([https://doi.org/10.1016/S0009-2614\(99\)00804-0](https://doi.org/10.1016/S0009-2614(99)00804-0))
7. M. Harder, B. Kuhn, F. Diederich, *ChemMedChem* **8** (2013) 397 (<https://doi.org/10.1002/cmdc.201200512>)
8. S. Cotesta, M. Stahl, *J. Mol. Model.* **12** (2006) 436 (<https://doi.org/10.1007/s00894-005-0067-x>)
9. S. K. Burley, G. A. Petsko, *Science* **229** (1985) 23 (<https://doi.org/10.1126/science.3892686>)
10. S. K. Burley, G. A. Petsko, *FEBS Lett.* **203** (1986) 139 ([https://doi.org/10.1016/0014-5793\(86\)80730-x](https://doi.org/10.1016/0014-5793(86)80730-x))

11. S. K. Burley, G. A. Petsko, *Adv. Protein Chem.* **39** (1988) 125
([https://doi.org/10.1016/s0065-3233\(08\)60376-9](https://doi.org/10.1016/s0065-3233(08)60376-9))
12. T. Steiner, G. Koellner, *J. Mol. Biol.* **305** (2001) 535
(<https://doi.org/10.1006/jmbi.2000.4301>)
13. F. R. Ferreira de, M. Schapira, *MedChemComm* **8** (2017) 1970
(<https://doi.org/10.1039/c7md00381a>)
14. M. Giroud, J. Ivkovic, M. Martignoni, M. Fleuti, N. Trapp, W. Haap, A. Kuglstatler, J. Benz, B. Kuhn, T. Schirmeister, F. Diederich, *ChemMedChem* **12** (2017) 257
(<https://doi.org/10.1002/cmdc.201600563>)
15. S. Raghunathan, T. Jaganade, U. D. Priyakumar, *Biophys. Rev.* **12** (2020) 65
(<https://doi.org/10.1007/s12551-020-00620-9>)
16. M. Giroud, M. Harder, B. Kuhn, W. Haap, N. Trapp, W. B. Schweizer, T. Schirmeister, F. Diederich, *ChemMedChem* **11** (2016) 1042 (<https://doi.org/10.1002/cmdc.201600132>)
17. L. M. Salonen, M. C. Holland, P. S. Kaib, W. Haap, J. Benz, J. L. Mary, O. Kuster, W. B. Schweizer, D. W. Banner, F. Diederich, *Chemistry* **18** (2012) 213
(<https://doi.org/10.1002/chem.201102571>)
18. B. S. Lauber, L. A. Hardegger, K. A. Alam, B. A. Lund, O. Dumele, M. Harder, B. Kuhn, R. A. Engh, F. Diederich, *Chemistry* **22** (2016) 211
(<https://doi.org/10.1002/chem.201503552>)
19. V. Ehmke, E. Winkler, D. W. Banner, W. Haap, W. B. Schweizer, M. Rottmann, M. Kaiser, C. Freymond, T. Schirmeister, F. Diederich, *ChemMedChem* **8** (2013) 967
(<https://doi.org/10.1002/cmdc.201300112>)
20. G. R. De, E. Brodbeck-Persch, S. Bryson, N. B. Hentzen, M. Kaiser, E. F. Pai, R. L. Krauth-Siegel, F. Diederich, *ChemMedChem* **13** (2018) 957
(<https://doi.org/10.1002/cmdc.201800067>)
21. M. W. Krone, C. R. Travis, G. Y. Lee, H. J. Eckvahl, K. N. Houk, M. L. Waters, *J. Am. Chem. Soc.* **142** (2020) 17048 (<https://doi.org/10.1021/jacs.0c06568>)
22. K. DeFrees, M. T. Kemp, X. ElHilali-Pollard, X. Zhang, A. Mohamed, Y. Chen, A. R. Renslo, *Org. Chem. Front.* **6** (2019) 1749 (<https://doi.org/10.1039/c9qo00342h>)
23. R. Meurisse, R. Brasseur, A. Thomas, *Proteins* **54** (2004) 478
(<https://doi.org/10.1002/prot.10582>)
24. P. W. Rose, B. Beran, C. Bi, W. F. Bluhm, D. Dimitropoulos, D. S. Goodsell, A. Prlic, M. Quesada, G. B. Quinn, J. D. Westbrook, J. Young, B. Yukich, C. Zardecki, H. M. Berman, P. E. Bourne, *Nucleic Acids Res.* **39** (2011) D392
(<https://doi.org/10.1093/nar/gkq1021>)
25. J. M. Word, S. C. Lovell, J. S. Richardson, D. C. Richardson, *J. Mol. Biol.* **285** (1999) 1735 (<https://doi.org/10.1006/jmbi.1998.2401>)
26. *Accelrys Software Inc., Discovery Studio Visualizer, Release 2020*, Accelrys Software Inc., San Diego, CA, 2020
27. M. R. Jackson, R. Beahm, S. Duvvuru, C. Narasimhan, J. Wu, H. N. Wang, V. M. Philip, R. J. Hinde, E. E. Howell, *J. Phys. Chem., B* **111** (2007) 8242
(<https://doi.org/10.1021/jp0661995>)
28. V. Philip, J. Harris, R. Adams, D. Nguyen, J. Spiers, J. Baudry, E. E. Howell, R. J. Hinde, *Biochemistry* **50** (2011) 2939 (<https://doi.org/10.1021/bi200066k>)
29. V. R. Ribić, S. Đ. Stojanović, M. V. Zlatović, *Int. J. Biol. Macromol.* **106** (2018) 559
(<https://doi.org/10.1016/j.ijbiomac.2017.08.050>)

30. J. Hostaš, D. Jakubec, R. A. Laskowski, R. Gnanasekaran, J. Řezáč, J. Vondrášek, P. Hobza, *J. Chem. Theory Comput.* **11** (2015) 4086 (<http://dx.doi.org/10.1021/acs.jctc.5b00398>)
31. *Schrödinger Release 2018-I, Jaguar*, Schrödinger, LLC, New York, NY, 2018
32. T. H. Dunning, *J. Chem. Phys.* **90** (1989) 1007 (<https://doi.org/10.1063/1.456153>)
33. T. Clark, J. Chandrasekhar, G. n. W. Spitznagel, P. V. R. Schleyer, *J. Comput. Chem.* **4** (1983) 294 (<https://doi.org/10.1002/jcc.540040303>)
34. A. D. Bochevarov, E. Harder, T. F. Hughes, J. R. Greenwood, D. A. Braden, D. M. Philipp, D. Rinaldo, M. D. Halls, J. Zhang, R. A. Friesner, *Int. J. Quantum Chem.* **113** (2013) 2110 (<https://doi.org/10.1002/qua.24481>)
35. G. J. Jones, A. Robertazzi, J. A. Platts, *J. Phys. Chem., B* **117** (2013) 3315 (<https://doi.org/10.1021/jp400345s>)
36. K. E. Riley, J. A. Platts, J. Řezáč, P. Hobza, J. G. Hill, *J. Phys. Chem., A* **116** (2012) 4159 (<https://doi.org/10.1021/jp211997b>)
37. S. Saebø, W. Tong, P. Pulay, *J. Chem. Phys.* **98** (1993) 2170 (<https://doi.org/10.1063/1.464195>)
38. A. Reyes, L. Fomina, L. Rumsh, S. Fomine, *Int. J. Quantum Chem.* **104** (2005) 335 (<https://doi.org/10.1002/qua.20558>)
39. R. M. Balabin, *J. Chem. Phys.* **132** (2010) 231101 (<https://doi.org/10.1063/1.3442466>)
40. Z. Dosztányi, A. Fiser, I. Simon, *J. Mol. Biol.* **272** (1997) 597 (<https://doi.org/10.1006/jmbi.1997.1242>)
41. Z. Dosztányi, C. Magyar, G. Tusnady, I. Simon, *Bioinformatics* **19** (2003) 899 (<https://doi.org/10.1093/bioinformatics/btg110>)
42. H. Ashkenazy, E. Erez, E. Martz, T. Pupko, N. Ben-Tal, *Nucleic Acids Res.* **38** (2010) W529 (<https://doi.org/10.1093/nar/gkq399>)
43. B. Boeckmann, A. Bairoch, R. Apweiler, M. C. Blatter, A. Estreicher, E. Gasteiger, M. J. Martin, K. Michoud, C. O'Donovan, I. Phan, S. Pilbout, M. Schneider, *Nucleic Acids Res.* **31** (2003) 365 (<https://doi.org/10.1093/nar/gkg095>)
44. G. Toth, C. R. Watts, R. F. Murphy, S. Lovas, *Proteins* **43** (2001) 373 (<https://doi.org/10.1002/prot.1050>)
45. A. S. Mahadevi, G. N. Sastry, *Chem. Rev.* **116** (2016) 2775 (<https://doi.org/10.1021/cr500344e>)
46. G. B. McGaughey, M. Gagne, A. K. Rappe, *J. Biol. Chem.* **273** (1998) 15458 (<https://doi.org/10.1074/jbc.273.25.15458>)
47. B. P. Dimitrijević, S. Z. Borozan, S. Đ. Stojanović, *RSC Adv.* **2** (2012) 12963 (<https://doi.org/10.1039/C2RA21937A>)
48. G. R. Desiraju, T. Steiner, *The Weak Hydrogen Bond*, Oxford University Press, Oxford, 1999.



J. Serb. Chem. Soc. 86 (9) 795–807 (2021)
JSCS–5462

Physicochemical characterisation of dihydro- α -lipoic acid interaction with human serum albumin by multi-spectroscopic and molecular modelling approaches

NIKOLA GLIGORIJEVIĆ^{1*}, VLADIMIR ŠUKALOVIĆ², SIMEON MINIĆ^{3#},
GORAN MILJUŠ¹, OLGICA NEDIĆ^{1#} and ANA PENEZIĆ¹

¹Institute for the Application of Nuclear Energy, Department for Metabolism, University of Belgrade, Banatska 31b, 11080 Belgrade, Serbia, ²Institute of Chemistry, Technology and Metallurgy, University of Belgrade, Njegoševa 12, 11000 Belgrade, Serbia and ³Department of Biochemistry and Center of Excellence for Molecular Food Sciences, University of Belgrade – Faculty of Chemistry, Studentski Trg 12–16, 11000 Belgrade, Serbia

(Received 22 April, revised and accepted 27 May 2021)

Abstract: The binding of a popular food supplement and well-known antioxidant, dihydro- α -lipoic acid (DHLA) to human serum albumin (HSA) was characterised. The binding was monitored by several spectroscopic methods together with the molecular docking approach. HSA was able to bind DHLA with moderate affinity, $1.00 \pm 0.05 \times 10^4 \text{ M}^{-1}$. Spectroscopic data demonstrated that the preferential binding site for DHLA on HSA is IIA (Sudlow I). Both experimental and molecular docking analysis identified electrostatic (salt bridges) and hydrogen bonds as the key interactions involved in DHLA binding to HSA. Molecular docking confirmed that the Sudlow I site could accommodate DHLA and that the ligand is bound to the protein in a specific conformation. The molecular dynamic simulation showed that the formed complex is stable. Binding of DHLA does not affect the structure of the protein, but it thermally stabilises HSA. Bound DHLA had no effect on the susceptibility of HSA to trypsin digestion. Since DHLA is a commonly used food supplement, knowledge of its pharmacokinetics and pharmacodynamic properties in an organism is very important. This study further expands it by providing a detailed analysis of its interaction with HSA, the primary drug transporter in the circulation.

Keywords: spectral analysis; molecular docking; protein–ligand interaction; protein stability, protein structure.

* Corresponding author. E-mail: nikolag@inep.co.rs

Serbian Chemical Society member.

<https://doi.org/10.2298/JSC210420041G>

INTRODUCTION

Human serum albumin (HSA) is the most dominant protein in the circulation, with a concentration in the range from 35 to 50 g L⁻¹ (522 to 746 μM). It has a molecular mass of 67 kDa.¹ Structurally, HSA is composed of three homologous domains (I, II and III), each divided into two subdomains, A and B. The dominant secondary structure motif of HSA is α -helix.²

HSA has numerous essential functions in the circulation. Due to its high concentration, HSA participates in the regulation of osmotic pressure.³ Its free Cys34 thiol group (in healthy individuals 70–80 % of Cys34 thiol group is in a reduced form), makes HSA an important factor for plasma antioxidant capacity, contributing with 80 % to the total amount of plasma thiol.⁴ HSA is also a general transporter of fatty acids, ions and many drugs. The structure of HSA enables it to accommodate and bind a large variety of small molecules with moderate to high affinities. Two main binding sites for many different molecules (excluding fatty acids) are located at the IIA subdomain or Sudlow I binding site, and IIIA subdomain or Sudlow II binding site. Warfarin and ibuprofen drugs are specific ligands for Sudlow site I and Sudlow site II, respectively.⁵

Lipoic acid (LA) is a naturally occurring molecule the main sources of which are potato, broccoli and spinach. Humans can also synthesise LA in small amounts. LA is readily absorbed from foods and its oral administration as a drug is a viable therapeutic option, including the treatment of patients with Covid-19 infection.⁶ LA supplements are also commercially available, with LA concentrations of up to 600 mg per tablet. The antioxidant activity of LA is manifested through ROS scavenging, transition metal ions (*e.g.*, iron and copper) chelating, cytosolic glutathione and vitamin C level increases, and oxidative stress damage repair.⁷

Following cellular uptake, LA is reduced to dihydrolipoic acid (DHLA), which is a very potent reducing agent.⁷ LA has several beneficial effects, such as antioxidant, improvement of glycaemic control, mitigation of toxicity by heavy metal poisoning and immunomodulatory effects.^{7–9}

Although the ability of albumin to bind DHLA is well known,¹⁰ no detailed analysis of this interaction has been reported so far. In the case of bovine serum albumin (BSA), DHLA was shown to bind at the IIIA subdomain.¹¹ However, no binding experiments in the presence of a specific ligand for this site were performed. Taking into account the structural similarity of DHLA and octanoic fatty acid, it was proposed that DHLA binds to subdomain IIA,¹² but IIIA subdomain was also considered.¹¹

Considering that DHLA is a potent antioxidant used as a food supplement and that its usage can help in oxidative stress related conditions, it looked relevant to investigate its interaction with HSA, a universal transporter in the circulation. The properties of this interaction are still not fully defined in the literature. Hence, the

aim of the present study was to characterise DHLA–HSA binding, with the usage of both multi-spectroscopic and molecular modelling techniques.

EXPERIMENTAL

Materials

All chemicals used were purchased from Sigma (Burlington, MA, USA) and were of analytical grade. HSA was purchased from Sigma, (product number A-1653), and used without additional purification. A stock solution was made in 10 mM phosphate buffered saline (PBS), pH 7.4. The concentration of HSA was determined using a bicinchoninic acid (BCA) assay kit (Thermo Fisher Scientific, Waltham, MA, USA). Stock solution (5 mM) of DHLA was prepared by suspending DHLA in 10 mM PBS following the addition of a small volume of 1 M NaOH until full clarification of solution was reached.¹³ Trypsin was purchased from the Torlak Institute (Belgrade, Serbia) as a 0.25 % solution. Stock solutions of ibuprofen and warfarin were made in DMSO. In the experiments where they were used, the final DMSO concentration did not exceed 2 %. All experiments were performed in triplicate at room temperature, using 10 mM PBS, pH 7.4, unless otherwise stated. All results are presented as averaged of triplicates, and their *SD* never exceeded 5 % of the presented averages.

Analysis of HSA–DHLA complex formation by spectrofluorimetry

Determination of the binding constant (K_a) of the HSA–DHLA complex was realised by measuring the quenching of the intrinsic fluorescence emission of HSA (0.4 μ M) in the presence of increasing concentrations of DHLA (from 5 to 35 μ M) at 37 °C. Fluorescence spectra were recorded using FluoroMax®-4 spectrofluorometer (Horiba Scientific, Japan). HSA was excited at 280 nm and the emission spectra were recorded in the range from 290 to 450 nm. Each spectrum was corrected for the emission of the control that contained only DHLA at a particular concentration. The change of the emission intensity at 338 nm (HSA emission maximum) was used for the calculation of the binding constant. The emission intensity measured for HSA was first corrected for the small inner filter effect of DHLA using the equation:

$$F = F_0 10^{(A_{ex} + A_{em})/2} \quad (1)$$

where F is corrected fluorescence, F_0 is measured fluorescence, A_{ex} and A_{em} are absorbencies at excitation and emission wavelengths, which are 280 nm and 338 nm, respectively.

The binding constant between HSA and DHLA was calculated using the following equation:

$$\frac{F_0 - F}{F - F_c} = K_a c_L \quad (2)$$

where F_0 and F represent the intensities of the fluorescence emission signals of HSA in the absence and the presence of the ligand, F_c represents the fluorescence intensity of HSA completely saturated with the ligand, which was experimentally obtained by determination of the fluorescence emission intensity of the protein in the presence of 17 mM DHLA and c_L is the concentration of used ligand (DHLA).

For determination, if at the same time, dynamic (collision) and static (complex formation) types of quenching are present or only one of them, Stern–Volmer (SV) graph was plotted. From it, the SV quenching constant (K_{SV}) was calculated using the following equation:¹⁴

$$F_0/F = 1 + k_q \tau_0 c_Q = 1 + K_{SV} c_Q \quad (3)$$

where F_0 and F are the intensities of the emission signals without and in the presence of DHLA, k_q represents the biomolecule quenching rate constant, τ_0 is the average lifetime of the biomolecule without quencher (10^{-8} s), c_Q is the total concentration of quencher (DHLA). The slope from SV plot represents K_{SV} . K_{SV} was further used for the calculation of k_q .

Thermodynamic parameters of DHLA binding to HSA were calculated using the same experimental approach as for the calculation of K_a but at three different temperatures, 25, 30 and 37 °C. The calculated binding constants at three temperatures were then used to plot a van't Hoff graph. Enthalpy (ΔH) and entropy (ΔS) change were calculated from the graph applying the following equation:

$$\ln K_a = -\frac{\Delta H}{RT} + \frac{\Delta S}{R} \quad (4)$$

where T is temperature in K and R is a universal gas constant ($8.314 \text{ J mol}^{-1} \text{ K}^{-1}$). ΔH was calculated from the slope of van't Hoff graph and ΔS from the intercept.

For fluorescence emission changes, specifically originating from Tyr residues or the only Trp214 residue, synchronous fluorescence spectra were recorded on RF-6000 spectrophotometer (Shimadzu, Japan). The spectra were recorded in the range from 310 to 380 nm with $\Delta\lambda$ of 60 nm for Trp and in the range from 290 to 325 nm with $\Delta\lambda$ of 15 nm for the Tyr residues. Here, $\Delta\lambda$ represents λ of emission – λ of the excitation for each specific residue.

For the location of specific binding site(s), a competitive binding experiment was performed. To HSA, increasing concentrations of DHLA in the presence and the absence of site ligands (ibuprofen and warfarin) were added. HSA ($0.4 \mu\text{M}$) was first incubated with $0.4 \mu\text{M}$ of site specific ligands and the obtained mixture were titrated with DHLA. HSA was excited at 280 nm and emission spectra were recorded in 290–450 nm range. Calculation of HSA–DHLA affinity constants in the presence and absence of site-specific ligands was realized as already mentioned previously.

In order to confirm that DHLA binds HSA at the binding site specific of warfarin, a mixture of HSA ($0.4 \mu\text{M}$) and warfarin ($20 \mu\text{M}$) were titrated with DHLA ($10, 20, 30, 40 \mu\text{M}$). The warfarin fluorescence is enhanced in the presence of HSA and the excitation of the obtained complex was performed at 310 nm,¹⁵ while recording of emission spectra was performed in the range 340–450 nm. The obtained spectra were corrected by subtracting the emission spectra obtained in the absence of HSA.

UV-Vis analysis of the HSA–DHLA complex

UV-Vis absorption spectra of HSA ($9 \mu\text{M}$), alone and in the presence of different concentrations of DHLA ($9, 45$ and $90 \mu\text{M}$) were recorded at room temperature using a Ultrospec 2000 spectrophotometer (Pharmacia Biotech, Sweden). The spectra were recorded in the wavelength range from 250 to 300 nm. The spectrum of each mixture was corrected for the spectrum obtained for the appropriate concentration of DHLA alone. Furthermore, the UV-Vis spectrum of DHLA ($90 \mu\text{M}$) in the presence of HSA ($9 \mu\text{M}$) was recorded in the range from 300 to 450 nm and corrected for the spectrum obtained for HSA alone.

Structural analysis of HSA–DHLA complex using circular dichroism (CD) spectropolarimetry

The influence of DHLA binding on the structure of HSA was analysed using a CD-spectropolarimeter J-815 (Jasco, Japan) at room temperature by applying a scan speed of 50 nm min^{-1} . Different concentrations of DHLA were added ($6, 15$ and $30 \mu\text{M}$) to HSA ($3 \mu\text{M}$). Both HSA and DHLA stock solutions were dissolved in 10 mM phosphate buffer, pH 7.4. The tertiary protein structure was analysed by recording near-UV CD spectra in the range from

260 to 320 nm using a cell with an optical path of 10 mm, while the secondary protein structure was monitored by recording far-UV CD spectra in the range 185–260 nm using a cell with 0.5 mm optical path length. The spectra of free ligand were subtracted from the spectra of corresponding protein–ligand mixtures.

Analysis of temperature stability of HSA–DHHLA complex

Temperature stability of HSA (0.4 μM) alone and in the presence of DHHLA (40 μM) was determined by recording the reduction of fluorescence emission at 338 nm (emission peak of HSA) and at 335 nm (emission peak of HSA–DHHLA complex), using the same equipment as used in above. Reduction of protein emission was recorded in the temperature range from 37 to 87 $^{\circ}\text{C}$ with a temperature increase rate of 2 $^{\circ}\text{C min}^{-1}$. At each temperature, the mixture was allowed to equilibrate for 1 min before the measurement. The obtained spectra were corrected by subtracting the spectra of DHHLA recorded alone at each temperature. Results were fitted to sigmoid curves and from them inflexion points were obtained which represent melting temperatures of HSA (T_m).

Analysis of proteolysis of HSA by trypsin in the presence of DHHLA

For the investigation of whether DHHLA binding affects the susceptibility of HSA to trypsin proteolysis, the following experiment was performed at 37 $^{\circ}\text{C}$. To solutions containing 4 μM HSA, alone and in the presence of DHHLA (40 μM), 25 μL of 0.25 % trypsin solution was added. The final volume of reaction mixtures was 1 mL. At different time points (1, 5, 10, 20 and 30 min), 50 μL aliquots were taken from the reaction mixture and PMSF immediately added at the final concentration of 2 mM, thus stopping the reaction. Proteolytic fragments of HSA were analysed by reducing SDS-PAGE using a 12 % gel in a standard manner. The gel was stained using the Silver Stain Plus Kit (Bio-Rad, Hercules, California, USA).

Molecular docking and dynamic analysis

The methods used and the obtained results are given in the Supplement material to this paper.

RESULTS AND DISCUSSION

HSA–DHHLA complex formation

The intrinsic fluorescence of HSA is quenched in the presence of DHHLA, as shown in Fig. 1A. In addition, a small blue shift (3 nm) of the emission maximum of HSA is observed, in the presence of increasing concentrations of DHHLA. The obtained results indicate that HSA is capable of binding DHHLA and by doing so, the polarity in the vicinity of Tyr and Trp214 amino acid residues of HSA is not significantly changed. Fluorescence quenching can occur as a result of dynamic quenching (collisional) and static quenching (complex formation), whereby, both of them can be present simultaneously. To determine what applies for the present HSA–DHHLA pair, an SV graph was plotted (Fig. 1B) and from its slope, K_{SV} was determined. Since the obtained SV plot is linear ($r^2 = 0.99$), it proves that only one quenching type occurs in our tested system. K_{SV} was determined to be $0.83 \times 10^4 \text{ M}^{-1}$ and from it, the quenching rate constant of the biomolecule, k_q , was determined to be $0.83 \times 10^{12} \text{ M}^{-1}$. The obtained value of k_q is about two orders of magnitude higher than the diffusion rate of biomolecules ($10^{10} \text{ M}^{-1} \text{ s}^{-1}$),

strongly suggesting the presence of a static type of quenching or, in other words, complex formation between HSA and DHLA.¹⁶ By using Eq. (2) and the plot from Fig. 1C, K_a was determined to be $1.00 \pm 0.05 \times 10^4 \text{ M}^{-1}$, at 37 °C, showing that HSA can bind DHLA with a moderately strong affinity.

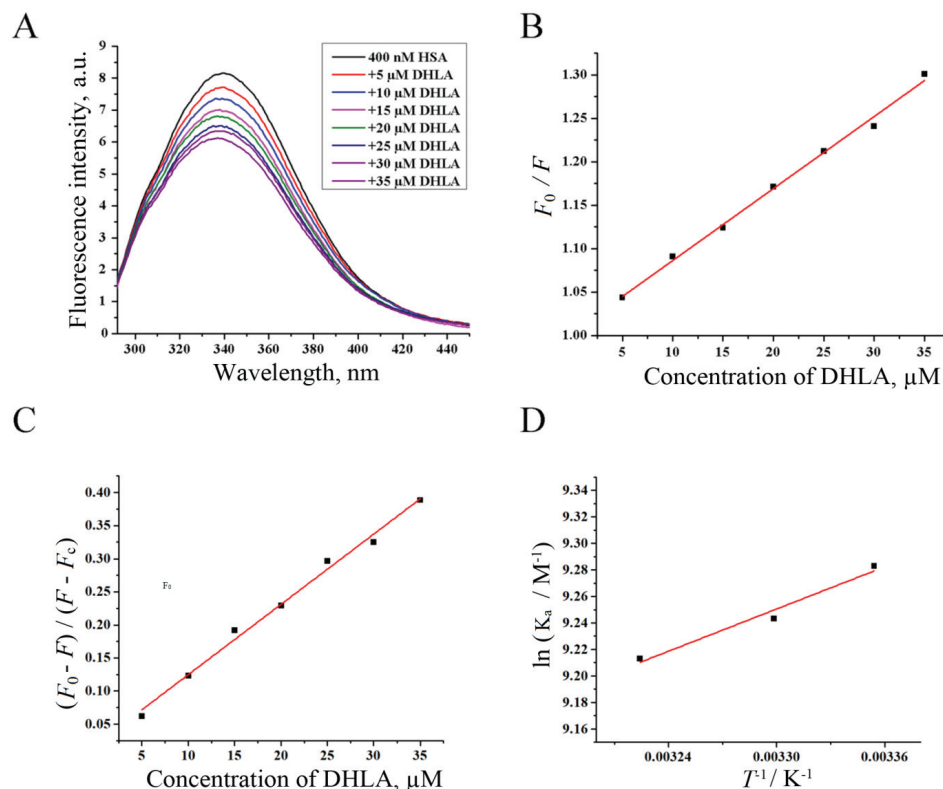


Fig. 1. Binding analysis of HSA and DHLA using spectrofluorimetry. Fluorescence emission spectra of HSA (excited at 280 nm) in the presence of increasing concentrations of DHLA (A). Stern-Volmer plot (B) and the plot used to determine the binding constant between HSA and DHLA (C) obtained using the fluorescence emission maximum of HSA at 338 nm. van't Hoff's graph, obtained by calculating the binding constants between HSA and DHLA at three different temperatures (D).

Calculation of K_a at three different temperatures showed that its value decreased as a consequence of temperature increase. This usually occurs when the static type of quenching is present since formation a complex is weaker at higher temperatures.¹⁷ This result also confirms complex formation between HSA and DHLA. From the K_a values obtained at three temperatures, thermodynamic parameters were determined using a van't Hoff plot (Fig. 1D). A negative value of ΔH was obtained, $-4.42 \text{ kJ mol}^{-1}$ and positive value of ΔS , $62.27 \text{ J mol}^{-1} \text{ K}^{-1}$.

These results indicate that electrostatic interactions are key interactions for HSA–DHLA complex formation,¹⁸ which was also confirmed by molecular dynamic analysis.

Synchronous fluorescence spectra are used to provide information about the changes in the emission of Trp and Tyr amino acid residues. HSA has only one Trp residue that is located inside the binding site of subdomain IIA (Sudlow I binding site),¹⁹ and information from synchronous spectra can provide insight into the binding site for a certain ligand. Increasing concentrations of DHLA significantly quenched emission spectrum of Trp (Fig. 2A), while quenching of emission spectrum of Tyr occurred to a very small extent (Fig. 2B). Bearing in mind the location of the only Trp residue in HSA, this result suggested that DHLA binds HSA at the subdomain IIA binding site (Sudlow I binding site).

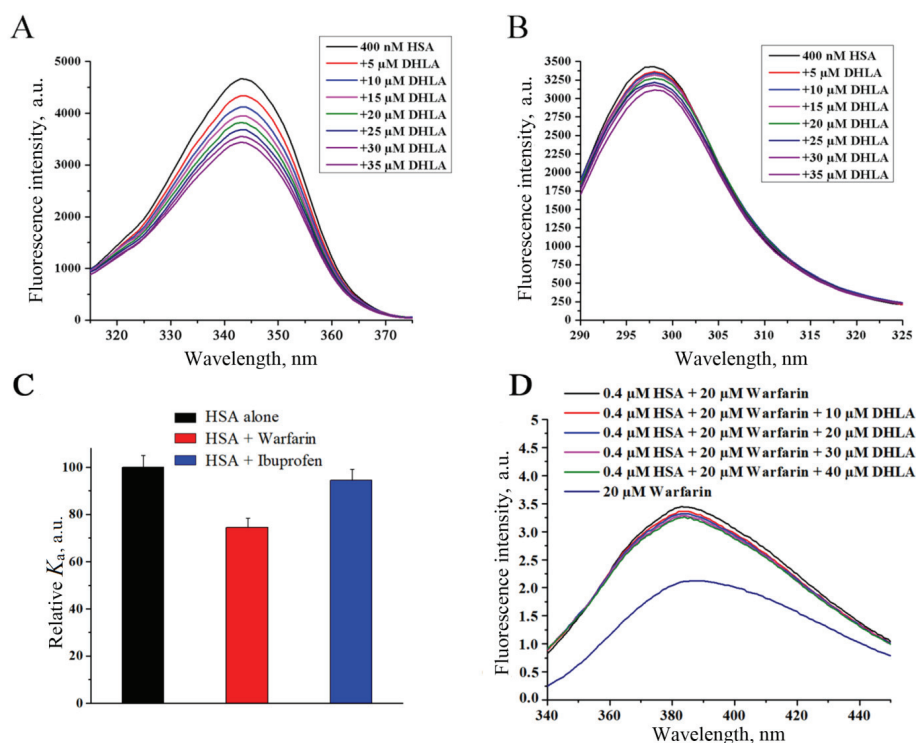


Fig. 2. Determination of a binding site of DHLA on HSA. Synchronous fluorescence spectra of HSA with $\Delta\lambda = 60$ nm for Trp (A) and $\Delta\lambda = 15$ nm for Tyr (B) in the presence of increasing concentrations of DHLA. Relative affinity constants for HSA–DHLA complex formation calculated for 0.4 μ M HSA alone and in the presence of equimolar concentrations of warfarin and ibuprofen, respectively (C). Displacement of HSA-bound warfarin by increasing concentrations of DHLA, detected by specific excitation of warfarin at 310 nm and recording its emission in the range from 340 to 450 nm (D).

For determination the binding site, DHLA was added to HSA in the presence of warfarin and ibuprofen. The affinity constant of HSA–DHLA complex in the presence of these molecules was calculated as described previously. Binding of both warfarin and ibuprofen to HSA is well characterised with affinity constants of about 10^5 M^{-1} for warfarin,²⁰ and about 10^6 M^{-1} for ibuprofen.²¹ As warfarin binds specifically to subdomain IIA binding site (Sudlow I) on HSA, while ibuprofen specifically binds to subdomain IIIA binding site (Sudlow II), they are used to block these sites in the studies that aim to locate the exact binding sites for other ligands.⁵ The obtained results, Fig. 2C, show that in the presence of warfarin, the affinity constant for the HSA–DHLA complex is reduced by almost 25 %, while ibuprofen only marginally reduced this value, about 5 %. Therefore, although the binding constant of warfarin to HSA is one order of magnitude lower than ibuprofen, the presence of warfarin has a five times more pronounced effect on the decrease of DHLA binding affinity to HSA in comparison to the presence of ibuprofen. Hence, these results show that DHLA preferentially binds at subdomain IIA on HSA.

The fluorescence intensity of warfarin increases when bound to HSA, Fig. 2D. This usually happens when a ligand binds to a protein and by doing so it becomes located in a more hydrophobic environment and thus shielded from water.²² A similar observation was noted for the binding of phycocyanobilin (PCB) to HSA, which happens at binding sites of both IIA and IB subdomains of HSA.²³ In the presence of increasing concentrations of DHLA, a reduction in the emission intensity of warfarin occurs, (Fig. 2D) indicating that DHLA displaces warfarin from its binding site, confirming that HSA binds DHLA at subdomain IIA.

The presence of aromatic amino acid residues enables proteins to absorb light in the UV region at about 280 nm and alterations in the absorption spectrum in this region may occur due to changes in the polarity of the environment that is in vicinity to these residues. The UV–Vis absorption spectrum of HSA does not change in the presence of increasing concentrations of DHLA, Fig. 3A, indicating that the binding of DHLA to HSA did not have any significant effect on the polarity or aromatic amino acids of HSA, which is in agreement with results obtained by spectrofluorimetry (Fig. 3A). The absorption spectrum of DHLA changes in the presence of HSA. Its peak is blue shifted and its intensity is reduced (Fig. 3B). Similarly, this was observed previously upon DHLA binding to fibrinogen.²⁴ Changes in the absorption spectrum of DHLA represent additional proof that the HSA–DHLA complex is being formed.

Influence of DHLA binding on the stability and structure of HSA

Often, ligand binding has effect on the protein structure, with some ligands inducing more ordered structures, others causing the protein to be more disordered,

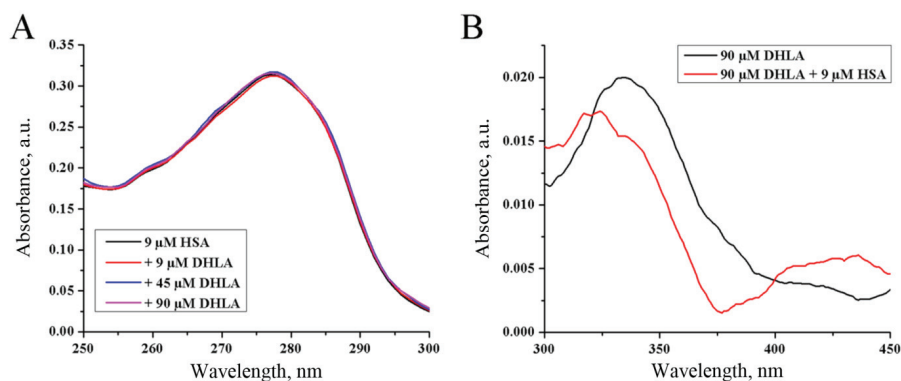


Fig. 3. The influence of complex formation on the UV-VIS absorption spectra of HSA and DHLA. UV absorption spectra of HSA alone and in the presence of increasing concentrations of DHLA (A). UV-Vis absorption spectra of DHLA alone and in the presence of HSA (B).

while some ligands have no effect. HSA has only α -helices as the secondary structure motifs. Binding of amoxicillin and PCB to HSA increases its α -helical content,²⁵ while binding of safranal and crocin decreases it.¹⁹ Far-UV CD spectra, obtained for HSA, (Fig. 4A), show a typical protein signal with α -helix as the dominant secondary structure motif. Its characteristic is a wide negative peak, ranging from 209 to 220 nm. From Fig. 4A, it can be seen that DHLA binding to HSA has no significant change in the secondary structure of HSA, even in the presence of ten times larger molar concentration of DHLA than HSA. The obtained near-UV-CD spectra for HSA alone and in the presence of all tested concentrations of DHLA are practically the same, showing that the tertiary structure of HSA upon DHLA binding is unaltered (Fig. 4B).

Besides the protein structure, other factors that affect the melting point of a protein may include the presence of bound molecules as well as their own structure. As a consequence of protein–ligand complex formation, new interactions are formed, and they may alter the temperature stability of the protein. Free HSA has a T_m of about 62 °C, while with bound fatty acids, its temperature stability increases, reaching a T_m from 64 to 72 °C.²⁶ Some ligands, such as embelin and PCB, are also able to increase the temperature stability of HSA.^{25,27} The HSA used in this study had a T_m of 68 °C. When bound to DHLA, the T_m of the HSA is increased to 70 °C (Fig. 4C). Since DHLA did not have any effect on the structure of HSA upon its binding (Figs. 4A and 4B), it seems that newly formed interactions in the HSA–DHLA complex caused additional thermal stabilisation of HSA.

Since the T_m of HSA increased in the presence of DHLA, indicating that the protein is becoming more rigid, this in turn may affect its susceptibility to proteolysis. For a protein to be proteolysed, its peptide bonds need to be exposed enough to enable their proper placement in the active site of a protease. Some ligands, such

as bilirubin for example, can make HSA more resistant to cleavage by trypsin.²⁸ From the obtained results, it seems that DHLA, although it thermally stabilises HSA, has no significant effect on HSA proteolysis by trypsin (Fig. 4D). This suggests that the binding of DHLA to HSA will not have significant (if any) effect on the half-life of this protein in circulation, regarding proteolysis. The first and the most dominant fragment of HSA resulting from its proteolysis by trypsin is the one at about 5 kDa. Other, less abundant fragments, with lower molecular masses appear later. This finding is in agreement with literature data.²⁵

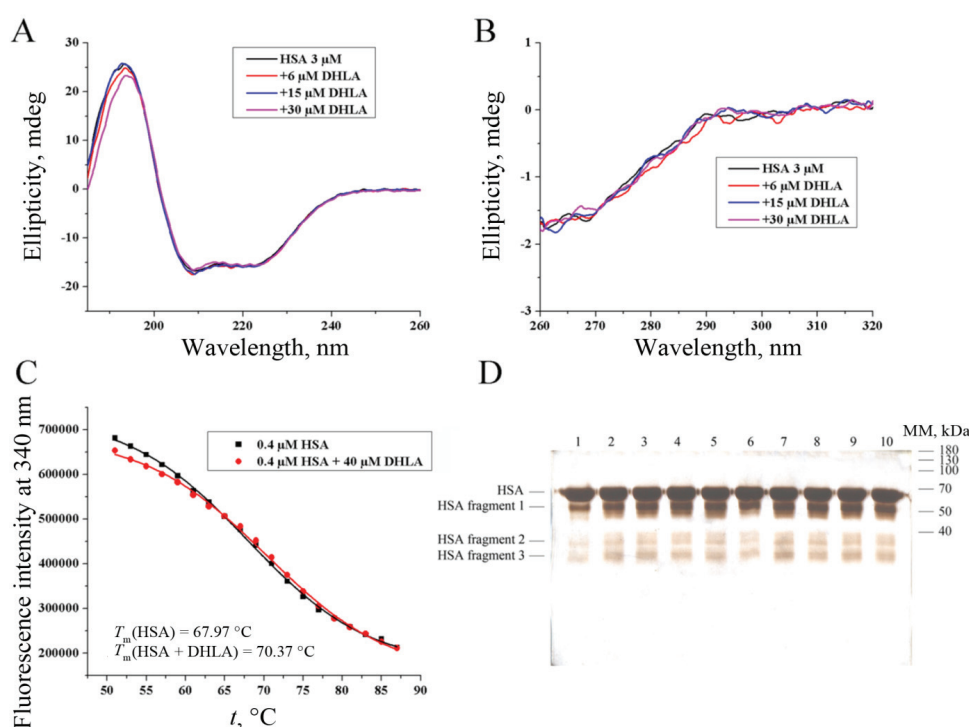


Fig. 4. Analysis of structural alterations of HSA due to DHLA binding. Far-UV CD (A) and near-UV CD (B) spectra of HSA alone and in the presence of increasing concentrations of DHLA. Temperature stability of HSA alone and in the presence of DHLA (C). Analysis of HSA digestion by trypsin in the absence (lanes 1–5, samples were taken after 1, 5, 10, 20 and 30 min of proteolysis) and in the presence of DHLA (lanes 6–10) by reducing SDS-PAGE on 12 % gel (D). MM stands for molecular weight markers.

HSA can be oxidised, and the small structural changes that arise as a consequence of this chemical modification can lead to an impairment of HSA functions, including its important ligand-binding ability.²⁹ The binding properties of HSA can also be influenced by the redox state of its free Cys34.³⁰ Considering the high concentration of HSA and its capacity to bind a large range of small

molecules, changes in its binding properties may have significant consequences on pharmacokinetic and pharmacodynamic (PKPD) properties of prescribed drugs. The ability of DHLA to protect albumin from non-enzymatic glycosylation¹⁰ and methylglyoxal modification³¹ was previously shown. Additionally, DHLA could protect Cys34 from oxidation.¹² Thus, by complex formation with HSA, DHLA can prevent the oxidation of HSA, and also preserve the antioxidative and binding properties of HSA. Considering its popular usage as a food supplement, detailed knowledge of the PKPD properties of DHLA is very important, including information on its binding proteins in the circulation.

CONCLUSIONS

The results of this paper characterise, in more detail, complex formation between DHLA and HSA, which was lacking in the literature. The obtained results showed that preferential binding on HSA of DHLA is located at sub-domain IIA (Sudlow I binding site). The ability of the Sudlow I site to bind DHLA and the stability of the formed complex was confirmed by molecular docking analysis and dynamics. The structure of HSA is not significantly altered on DHLA binding, however, HSA is stabilised. The presence of DHLA did not alter the susceptibility of HSA towards trypsin proteolysis and hence, no change of half-life of HSA in circulation due to proteolysis, is expected. These results add to the knowledge of the PKPD properties of DHLA and offer a future perspective for further studies that deal with the usage of DHLA as a food supplement.

SUPPLEMENTARY MATERIAL

Additional data are available electronically at the pages of journal website: <https://www.shd-pub.org.rs/index.php/JSCS/index>, or from the corresponding author on request.

Acknowledgement. This research was funded the Ministry of Education, Science and Technological Development of the Republic of Serbia (Grant Nos: 451-03-68/2020-14/200019, 451-03-68/2020-14/200026 and 451-03-68/2020-14/200168). There are no potential conflicts-of-interest to declare.

ИЗВОД

ФИЗИЧКО–ХЕМИЈСКА КАРАКТЕРИЗАЦИЈА ИНТЕРАКЦИЈЕ ДИХИДРО-ЛИПОИНСКЕ КИСЕЛИНЕ И АЛБУМИНА ИЗ СЕРУМА ЉУДИ ПРИМЕНОМ МУЛТИ-СПЕКТРОСКОПСКИХ МЕТОДА И МОЛЕКУЛСКОГ МОДЕЛОВАЊА

НИКОЛА ГЛИГОРИЈЕВИЋ¹, ВЛАДИМИР ШУКАЛОВИЋ², СИМЕОН МИНИЋ³, ГОРАН МИЉУШ¹,
ОЛГИЦА НЕДИЋ¹ И АНА ПЕНЕЗИЋ¹

¹Институт за примену нуклеарне енергије, Одељење за метаболизам, Универзитет у Београду, Банатска 31б, 11080 Београд, ²Институт за хемију, технологију и металургију, Универзитет у Београду, Ђеђићева 12, 11000 Београд и ³Катедра за биохемију и Центар изврсности за молекуларне науке о храни, Универзитет у Београду – Хемијски факултет, Студентски трг 12–16, 11000 Београд

У раду су описане карактеристике везивања дихидро-липоинске киселине (DHLA), познатог суплемента у исхрани и антиоксиданса, за албумин из серума људи (HSA).

Процес везивања је праћен применом већег броја спектроскопских метода и молекулским моделовањем. HSA везује DHLA умереним афинитетом, $1,00 \pm 0,05 \times 10^4 \text{ M}^{-1}$. Спектроскопски резултати су показали да је везујуће место IIA (Sudlow I) главно место везивања DHLA за HSA. Експериментални, као и резултати молекулског моделовања, су идентификовали електростатичке (сони мостови) и водоничне везе као главне типове интеракција. Резултати молекулског моделовања су потврдили да и место Sudlow I може везати DHLA, која је у том случају у специфичној конформацији. Симулација молекулске динамике је показала да је формиран комплекс стабилан. Везивање DHLA не утиче на структуру протеина, али повећава његову термалну стабилност. Везани DHLA не утиче на подложност HSA трипсинској дигестији. Како је DHLA уобичајен суплемент у исхрани, знање о његовим фармакоконетичким и фармакодинамичким особинама је веома важно. Ово испитивање допуњује досадашња знања детаљном анализом интеракције DHLA са HSA, примарним транспортним протеином лекова у циркулацији.

(Примљено 22. априла, ревидирано и прихваћено 27. маја 2021)

REFERENCES

1. R. E. Wang, L. Tian, Y.-H. Chang, *J. Pharm. Biomed. Anal.* **63** (2012) 165 (<https://doi.org/10.1016/j.jpba.2011.12.035>)
2. A. D. McLachlan, J. E. Walker, *J. Mol. Biol.* **112** (1977) 543 ([https://doi.org/10.1016/S0022-2836\(77\)80163-0](https://doi.org/10.1016/S0022-2836(77)80163-0))
3. P. Lee, X. Wu, *Curr. Pharm. Des.* **21** (2015) 1862 (<https://doi.org/10.2174/1381612821666150302115025>)
4. I. D. Pavićević, V. B. Jovanović, M. M. Takić, A. Z. Penezić, J. M. Aćimović, L. M. Mandić, *Chem. Biol. Interact.* **224** (2014) 42 (<https://doi.org/10.1016/j.cbi.2014.10.008>)
5. M. Fasano, S. Curry, E. Terreno, M. Galliano, G. Fanali, P. Narciso, S. Notari, P. Ascenzi, *IUBMB Life* **57** (2005) 787 (<https://doi.org/10.1080/15216540500404093>)
6. R. I. Horowitz, P. R. Freeman, *Med. Hypoth. J.* **143** (2020) 109851 (<https://doi.org/10.1016/j.mehy.2020.109851>)
7. C. Zuliani, L. Baroni, in *Bioactive Nutraceuticals and Dietary Supplements in Neurological and Brain Disease*, R. R. Watson, V. R. Preedy, Eds., Elsevier Inc., Amsterdam, 2015, p. 341 (<https://doi.org/10.1016/B978-0-12-411462-3.00035-7>)
8. S. Salinthon, V. Yadav, D. N. Bourdette, D. W. Carr, *Endocrine, Metab. Immune Disord. Targets* **8** (2008) 132 (<https://doi.org/10.2174/187153008784534303>)
9. A. R. Smith, S. V. Shenvi, M. Widlansky, J. H. Suh, T. M. Hagen, *Curr. Med. Chem.* **11** (2004) 1135 (<https://doi.org/10.2174/0929867043365387>)
10. T. Kawabata, L. Packer, *Biochem. Biophys. Res. Commun.* **203** (1994) 99 (<https://doi.org/10.1006/bbrc.1994.2154>)
11. G. Suji, S. A. Khedkar, S. K. Singh, N. Kishore, E. C. Coutinho, V. M. Bhor, S. Sivakami, *Protein J.* **27** (2008) 205 (<https://doi.org/10.1007/s10930-008-9126-3>)
12. P. Atukeren, S. Aydin, E. Uslu, M. K. Gumustas, U. Cakatay, *Oxid. Med. Cell. Longev.* **3** (2010) 206 (<https://doi.org/10.4161/oxim.3.3.11786>)
13. N. Perricone, K. Nagy, F. Horváth, G. Dajkó, I. Uray, I. Zs.-Nagy, *Arch. Gerontol. Geriatr.* **29** (1999) 45 ([https://doi.org/10.1016/S0167-4943\(99\)00022-9](https://doi.org/10.1016/S0167-4943(99)00022-9))
14. J. R. Lakowicz, *Principles of Fluorescence Spectroscopy*, Springer US, New York, 2006 (<https://doi.org/10.1007/978-0-387-46312-4>)
15. J. M. Vasquez, A. Vu, J. S. Schultz, V. I. Vullev, *Biotechnol. Prog.* **25** (2009) 906 (<https://doi.org/10.1002/btpr.188>)

16. S. K. Chaturvedi, M.K. Siddiqi, P. Alam, M. Zaman, R.K. Khan, *RSC Adv.* **6** (2016) 85860 (<https://doi.org/10.1039/C6RA10487H>)
17. N. Zaidi, E. Ahmad, M. Rehan, G. Rabbani, M. R. Ajmal, Y. Zaidi, N. Subbarao, R. K. Khan, *J. Phys. Chem., B* **117** (2013) 2595 (<https://doi.org/10.1021/jp3069877>)
18. P. D. Ross, S. Subramanian, *Biochemistry* **20** (1981) 3096 (<https://doi.org/10.1021/bi00514a017>)
19. A. A. Salem, M. Lotfy, A. Amin, M. A. Ghattas, *Biochem. Biophys. Reports* **20** (2019) 100670 (<https://doi.org/10.1016/j.bbrep.2019.100670>)
20. Q. Li, W. Yang, L. Qu, H.-Y. Qi, Y. Huang, Z. Zhang, *J. Spectrosc.* **2014** (2014) Article ID 834501 (<https://doi.org/10.1155/2014/386586>)
21. A. Ploch-Jankowska, D. Pentak, *Pharmaceuticals* **13** (2020) 205 (<https://doi.org/10.3390/ph13090205>)
22. L. Liang, H.A. Tajmir-Riahi, M. Subirade, *Biomacromolecules* **9** (2008) 50 (<https://doi.org/10.1021/bm700728k>)
23. S. L. Minic, M. Milcic, D. Stanic-Vucinic, M. Radibratovic, T. G. Sotiroudis, M. R. Nikolic, T. Č. Velickovic, *RSC Adv.* **5** (2015) 61787 (<https://doi.org/10.1039/c5ra05534b>)
24. N. Gligorijević, V. Šukalović, A. Penezić, O. Nedić, *Int. J. Biol. Macromol.* **147** (2020) 319 (<https://doi.org/10.1016/j.ijbiomac.2020.01.098>)
25. M. Radibratovic, S. Minic, D. Stanic-Vucinic, M. Nikolic, M. Milcic, T. C. Velickovic, *PLoS One* **11** (2016) e0167973 (<https://doi.org/10.1371/journal.pone.0167973>)
26. B. E. Lang, K. D. Cole, *Biotechnol. Prog.* **31** (2015) 62 (<https://doi.org/10.1002/btpr.1996>)
27. D. P. Yeggoni, A. Rachamalla, R. Subramanyam, *J. Photochem. Photobiol., B* **160** (2016) 248 (<https://doi.org/10.1016/j.jphotobiol.2016.04.012>)
28. T. Sjödin, R. Hansson, I. Sjöholm, *Biochim. Biophys. Acta* **494** (1977) 61 ([https://doi.org/10.1016/0005-2795\(77\)90135-0](https://doi.org/10.1016/0005-2795(77)90135-0))
29. A. Kawakami, K. Kubota, N. Yamada, U. Tagami, K. Takehana, I. Sonaka, E. Suzuki, K. Hirayama, *FEBS J.* **273** (2006) 3346 (<https://doi.org/10.1111/j.1742-4658.2006.05341.x>)
30. K. Oettl, R. E. Stauber, *Br. J. Pharmacol.* **151** (2007) 580 (<https://doi.org/10.1038/sj.bjp.0707251>)
31. I. Sadowska-Bartosz, S. Galiniak, G. Bartosz, *Molecules* **19** (2014) 4880 (<https://doi.org/10.3390/molecules19044880>).



J. Serb. Chem. Soc. 86 (9) S158–S161 (2021)

SUPPLEMENTARY MATERIAL TO
**Physicochemical characterisation of dihydro- α -lipoic acid
interaction with human serum albumin by multi-spectroscopic
and molecular modelling approaches**

NIKOLA GLIGORIJEVIĆ^{1*}, VLADIMIR ŠUKALOVIĆ², SIMEON MINIĆ³,
GORAN MILJUŠ¹, OLGICA NEDIĆ¹ and ANA PENEZIĆ¹

¹Institute for the Application of Nuclear Energy, Department for Metabolism, University of Belgrade, Banatska 31b, 11080 Belgrade, Serbia, ²Institute of Chemistry, Technology and Metallurgy, University of Belgrade, Njegoševa 12, 11000 Belgrade, Serbia and ³Department of Biochemistry and Center of Excellence for Molecular Food Sciences, University of Belgrade – Faculty of Chemistry, Studentski Trg 12–16, 11000 Belgrade, Serbia

J. Serb. Chem. Soc. 86 (9) (2021) 795–807

Molecular docking analysis

Docking simulations were carried out with the Schrodinger Maestro Suite (Schrödinger, LLC, New York, NY, 2018) using the crystal structure of HSA complexed with warfarin,¹ (PDB code: 2BXD, obtained from the RCSB PDB database (<https://www.rcsb.org/>)). The DHLA structure was drawn in the ChemDraw program (PerkinElmer Informatics, 2017). All structures were prepared in Maestro software, using default procedures. Up to 20 different docked structures were generated with the Induced fit docking protocol.² The obtained docking structures were examined and the best structure was selected based on the number of receptor–ligand interactions and docking score.

Molecular dynamics (MD) simulations

MD simulations were performed in the Schrodinger Desmond software package.³ The docked structure selected for MD was solvated with TIP3P explicit water model and neutralised *via* counter ions. A 0.15 M KCl salt solution was added. To calculate the interactions between all atoms, OPLS 2003 force field was used. For the calculation of the long-range Coulombic interactions, the particle-mesh Ewald (PME) method was used, with a cut-off radius of 0.9 nm for the short-range van der Waals (vdW) and electrostatic interactions.

During the course of the simulation, a constant temperature of 310 K and a pressure of 1.01235 bar were maintained, using a Nose–Hoover thermostat, and the Martyna Tobias Klein method. MD simulation of 50 ns with a 2.0 fs step was

* Corresponding author. E-mail: nikolag@inep.co.rs

performed and the collected trajectory used in the MD analysis to assess the docking pose and the stability of the protein–ligand interactions.

Molecular docking and dynamics results

The binding site on subdomain IIA consists of a binding pocket placed deeply in the core of the subdomain and is formed from all six helices of the subdomain and the loop-helix residues 148–154 of subdomain IB.¹⁶ The interior of the pocket is mostly hydrophobic, apart from the two clusters of polar amino acid residues (Tyr150, His242, Arg257 and Lys195; Lys199, Arg218 and Arg222).

The results from the induced fit docking simulation showed that HSA is able to bind DHLA at subdomain IIA binding site (Fig. S-1A). The energetically most favourable conformation of the docked pose demonstrated that the main interactions are salt bridges formed by the carboxyl group of DHLA with Arg218 and Arg222 residues of HSA, followed by hydrogen bonds formed between the sulfhydryl group of DHLA and Arg257, Ser287 residues of HSA (Figs. S-1B and S-1C). Molecular docking suggested that DHLA binds at the subdomain IIA binding site in a defined conformation, thus favouring interactions with specific amino acid residues. Considering the high torsional flexibility of DHLA due to nine dihedral angles that give many possible rotamers of DHLA,⁴ the recorded change in the UV-absorption spectrum (Fig. 3B, main manuscript) could point to a DHLA-conformational shift towards rotamers that have the highest probability of binding to HSA.

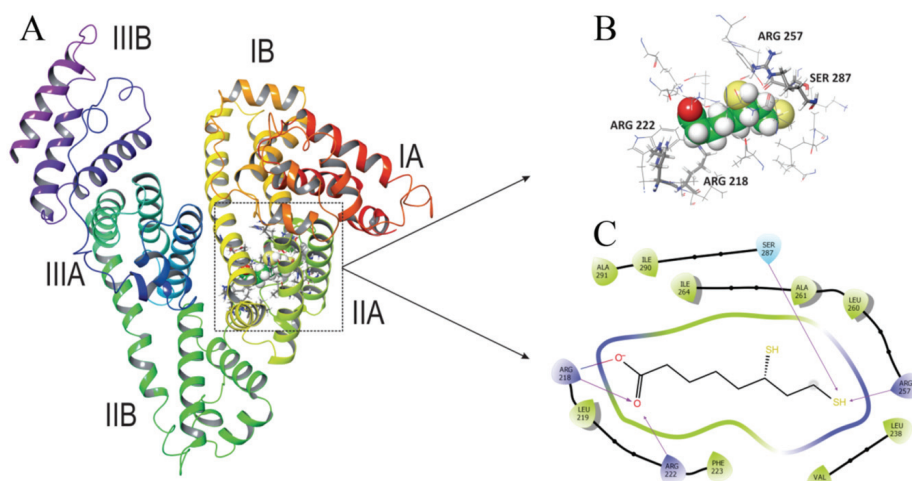


Fig. S-1. An overview of HSA with DHLA bound into subdomain IIA (A and B). The domains are colour coded and represented as secondary structure ribbons. Subdomain IIA composition and key interactions diagram (C). All amino acid residues in close contact with DHLA are displayed, with key amino acid residues marked.

For verification of docking simulation results, HSA–DHLA interactions were monitored throughout a 50 ns molecular dynamic simulation. The best conformation obtained in the molecular docking was set as the starting point for MD. The obtained MD trajectory was used to analyse both complex stability and the persistence of the main HSA–DHLA interactions over the simulation time used.

The observed *RMSD* values for HSA alone and HSA–DHLA complex show that the simulation equilibrated with the fluctuations falling within the 0.1 – 0.25 nm range. This suggests that minor conformational changes occurred during the simulation (Fig. S-2A).

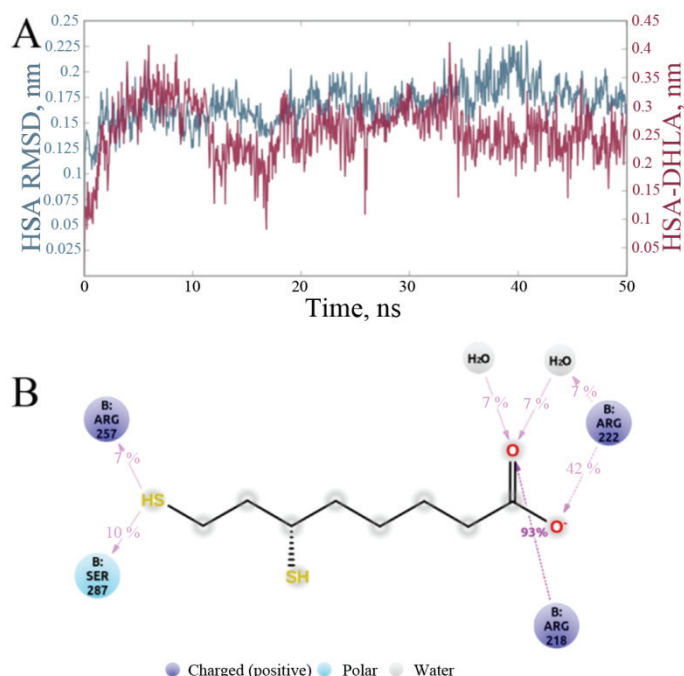


Fig. S-2. HSA and DHLA *RMSD* plot (A) and the observed key interactions during 50 ns simulation time (B).

The monitored HSA–DHLA interactions in the formed complex showed that the most important interaction is a salt bridge formed between the DHLA carboxyl group and Arg218. This interaction was present over 93 % of the simulation time, making it a key interaction for DHLA binding to HSA and it also indicates the correct orientation of DHLA inside the subdomain II binding site. The salt bridge with Arg218 is further reinforced by interaction with Arg222 (42 % of simulation time). Once DHLA is in the correct orientation in the subdomain II binding site, additional hydrogen bonds between sulfhydryl group and Ser287 and Arg257 are formed. These hydrogen bonds are maintained for 10

% (Ser287) and 7 % (Arg257) of the total simulation time (Fig. S-2B). All other observed interactions were present for less than 5 % of total simulation time (Fig. S-3).

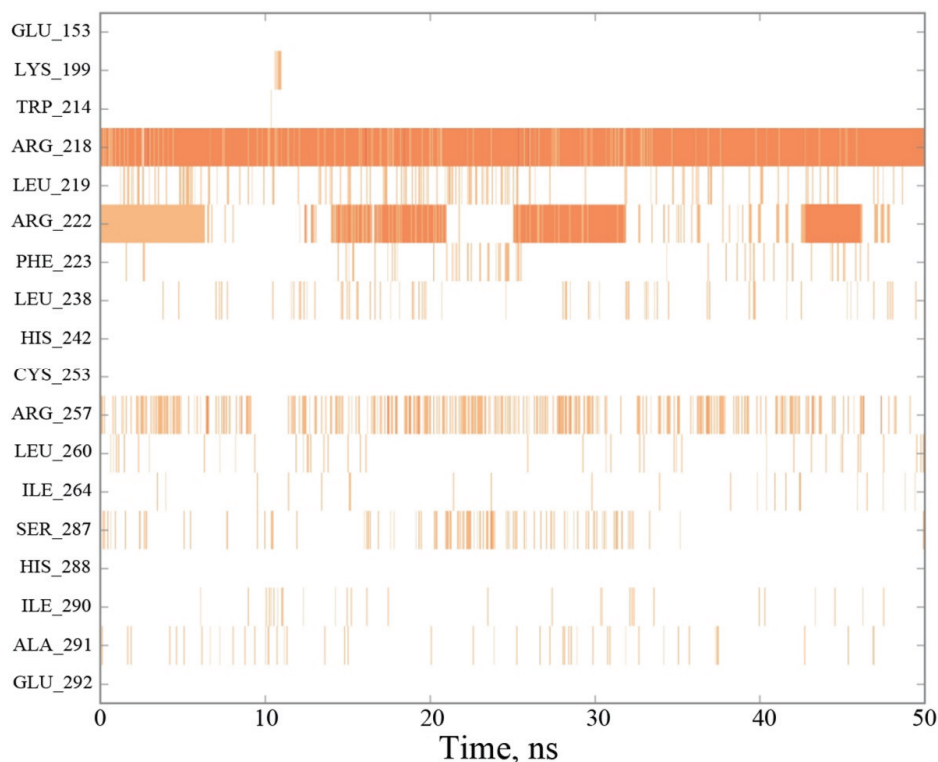


Fig. S-3. Summary of DHLA–HSA interactions observed during 50 ns simulation time. Each orange line represents one established interaction during a 1 ns time frame.

REFERENCES

1. J. Ghuman, P. A. Zunszain, I. Petitpas, A. A. Bhattacharya, M. Otagiri, S. Curry, *J. Mol. Biol.* **353** (2005) 38 (<https://doi.org/10.1016/j.jmb.2005.07.075>)
2. W. Sherman, T. Day, M. P. Jacobson, R. A. Friesner, R. Farid, *J. Med. Chem.* **49** (2006) 534 (<https://doi.org/10.1021/jm050540c>)
3. K. J. Bowers, E. Chow, H. Xu, R. O. Dror, M. P. Eastwood, B. A. Gregersen, J. L. Klepeis, I. Kolossvary, M. A. Moraes, F. D. Sacerdoti, J. K. Salmon, Y. Shan, D. E. Shaw, *Scalable Algorithms for Molecular Dynamics Simulations on Commodity Clusters*, in: *SC '06 Proc. 2006 ACM/IEEE Conf. Supercomput.*, (2006), Tampa, FL, p. 43 (<https://doi.org/10.1109/SC.2006.54>)
4. A. Vigorito, C. Calabrese, E. Paltanin, S. Melandri, A. Maris, *Phys. Chem. Chem. Phys.* **19** (2017) 496 (<https://doi.org/10.1039/c6cp05606g>).



J. Serb. Chem. Soc. 86 (9) 809–817 (2021)
JSCS–5463

DNA protective activity of triterpenoids isolated from medicinal mushroom *Fomitopsis betulina*

IVANA V. SOFRENIĆ¹, BOBAN D. ANĐELKOVIĆ^{1*}, LJUBODRAG VUJISIĆ¹,
MIROSLAV NOVAKOVIĆ², ALEKSANDAR Z. KNEŽEVIĆ³, MIROSLAVA B.
STANKOVIĆ⁴, SLOBODAN M. MILOSAVLJEVIĆ^{1,5} and VELE V. TEŠEVIĆ¹

¹University of Belgrade, Faculty of Chemistry, Studentski trg 12–16, 11000, Belgrade, Serbia, ²University of Belgrade, Institute of Chemistry, Technology and Metallurgy, National Institute of the Republic of Serbia, Studentski trg 12–16, 11000, Belgrade, Serbia, ³University of Belgrade, Faculty of Biology, Takovska 43, 11000, Belgrade, Serbia, ⁴Nuclear Facilities of Serbia, Mike Petrovića Alasa 12–14, 11351, Vinča, Serbia and ⁵Serbian Academy of Sciences and Arts, Knez Mihailova 35, 11000, Belgrade, Serbia

(Received 1 April, revised 20 May, accepted 24 May 2021)

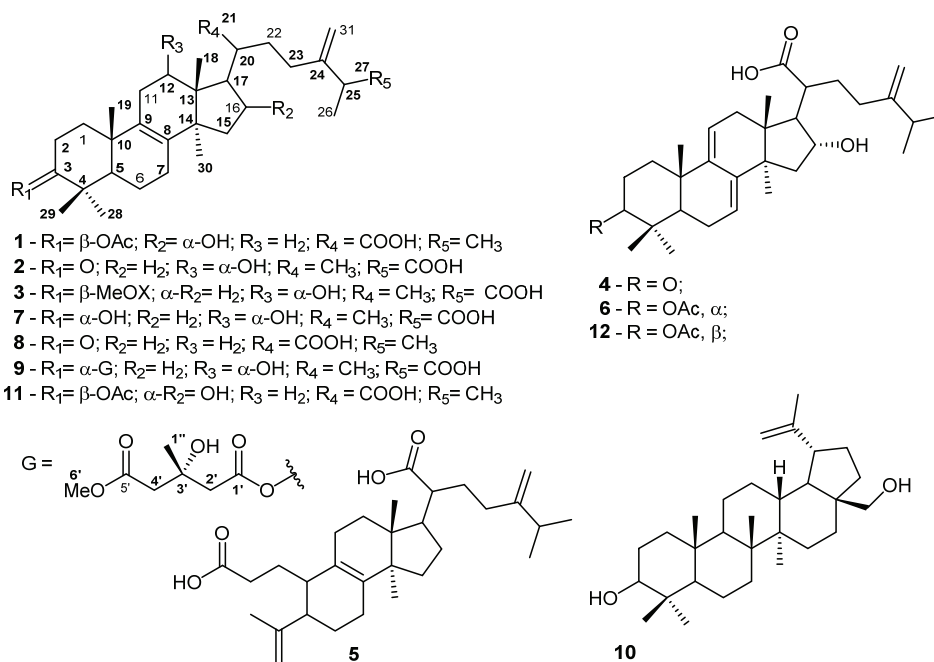
Abstract: Eleven 31-methylenlanostane triterpenoids, *i.e.*, seven 21- and four 26-oic acids, as well as a lupane triterpenoid betulin, isolated from the fruiting bodies of the mushroom *Fomitopsis betulina*, were tested for *in vitro* protective effect on chromosome aberrations in peripheral human lymphocytes using cytochalasin-B blocked micronucleus (CBMN) assay. Most of the tested compounds showed a beneficial effect by reducing DNA damage of human lymphocytes more effectively than amifostine, a radioprotective agent, used as a positive control. All the tested compounds decreased MN frequency in the concentration dependent manner, with the concentration of 2.0 $\mu\text{g mL}^{-1}$ being the most effective – with increase of the concentration the activity slightly decreases. The structure–activity relationship (SAR) studies indicated that the lanostanes containing a conjugated 7,9 (11)-diene system exhibit lower activity than Δ^8 -analogues. It was also demonstrated that the DNA protective activities within the Δ^8 -lanostane-26-oic acid group are affected by the substitution in position 3 pattern. In the Δ^8 series the oxygenation at C-12 or 16 as well as 21- or 26-oic acid functionality proved beneficial for *in vitro* protective effect on chromosomal aberrations. Betulin exhibited the lowest protective activity, but it is still comparable to that of amifostine.

Keywords: lanostane triterpenoid derivatives; CBMN assay; micronucleus; *Fomitopsis betulina*.

* Corresponding author. E-mail: aboban@chem.bg.ac.rs
<https://doi.org/10.2298/JSC210401039S>

INTRODUCTION

Lanostanes are a group of triterpenoids present in a large number of medicinal fungi such as *Ganoderma lucidum*,¹ *Gloeophyllum odoratum*² as well as other related fungi, *Poria cocos*,³ *Laetiporus sulphureus*, *Inonotus obliquus*, *Antrodia camphorate*, *Daedalea dickinsii*, *Elfvigia applamata*,⁴ *Fomitopsis pinicola*,⁵ *Fomitopsis betulina*,⁶ *etc.* Many lanostanes have shown great potential as anticancer agents owing to their cytotoxic and apoptotic effects on various cancer cell lines (Meth-A and LLC;⁷ K562,⁸ HepG2, Huh7 and Hep3B;⁴ HL-60;⁶ THP-1,⁷ *etc.*). To the best of our knowledge, *in vitro* protective effect of lanostanes on chromosomal aberrations was only tested by Mata *et al.*⁹ on some isolated from *Euphorbia conspicua*. Continuing our examination on wild growing *F. betulina* as a potential source of biologically active compounds,⁶ we now report the evaluation of DNA protective activity of the lanostanes **1–12** (Scheme 1).

Scheme 1. Tested compounds **1–12**.

The cytokinesis-block micronucleus assay (CBMN) used in this study is a standard method for determining the safety of chemicals and pharmaceuticals. The result of the assay, measuring micronuclei (MN) in cultured human and/or mammalian cells, is specifically restricted to once-divided BN cells, which can express MN.^{10,11} Binuclear cells are formed when the dividing cells are treated with cytochalasin-B (Cyt-B), a blocker of cytokinesis that strongly inhibit the

ring assembling formation by actin filaments required for the end of cytokinesis.^{10–12} The MN may originate from acentric chromosome fragments, chromosome loss or a budding process following exposure to γ -irradiation.¹³ In their study, Ye *et al.*¹⁴ showed that the MN originate from the multiple broken anaphase bridges, although whether this actually happens or not, in cytokinesis-blocked cells, remains unclear. The application of CBMN assay for the antioxidant evaluation of heterocyclic compounds is well known.^{15–18} Hitherto, the antioxidant capacity of lanostanes is questionable and depends on the applied test.^{19,20} A potential of the lanostanes as DNA protecting agents, as well as the possible mechanism of their action is discussed.

EXPERIMENTAL

Two aliquots of venous blood, 5 ml each were obtained using heparinized sterile vacutainers (Becton Dickinson, Bradford, MA). Six healthy non/smoking male volunteers who had not been exposed to chemicals, drugs or other substances gave their permission for using their blood in the experiment. A safety protocol concerning blood/born pathogen/biohazard was applied. The study complied with the code of ethics of the World Medical Association (Helsinki Declaration of 1964, as revised in 2002).²¹ The blood samples were obtained at the Medical Unit in accordance with current Health and Ethical regulations in Serbia, Law on Health Care (2005).²²

Lanostanes **1–16** were isolated and purified as described.⁶ The culture lymphocytes were treated with three concentrations (1, 2, and 4 $\mu\text{g mL}^{-1}$) of tested compounds. One cell culture served as the control and the tested chemical was not added in it. Amifostine WR-2721 (Mavigen-Biosciences, USA), 1 $\mu\text{g mL}^{-1}$, was used as a positive control and MMC (0.2 $\mu\text{g mL}^{-1}$, in phosphate buffer) as a negative control.

The treatment of binucleated (BN) cells with the examined compounds was carried out using the modified original procedure,^{23–25} applied previously applied in our laboratory.^{15,26} At least 1000 BN cells per sample were scored, registering MN according to the criteria of Countryman and Heddle²⁵ and Fenech and Morley.²³

The effects of investigated complexes on cell proliferation were estimated by the cytokinesis-block proliferation index (CBPI), calculated as suggested by Surralles and others.^{27,28} CBPI was calculated as:

$$CBPI = [(MI + 2MII + 3(MIII + MIV))]/N \quad (1)$$

where *MI–MIV* represent the number of cells with 1 to 4 nuclei, respectively, and *M* is the number of cells scored. For the analysis of MNi, only binucleated cells with well-preserved cytoplasm were scored (under a light microscope with a 40 and 100 magnification). The criteria for selection of BN cells and the identification of MNi given in the HUMAN project website (<http://www.humn.org>) were followed.¹¹ The number of BN cells with 1, 2, 3 or more MN were classified then. The data for each treatment were expressed as the frequency of MN per 1000 BN cells.

The statistical analysis was performed using Origin software package version 7.0. The statistical significance of difference between the data pairs was evaluated by analysis of variance (One-way ANOVA) followed by the Tukey test. Statistical difference was considered significant at $p < 0.01$.

RESULTS AND DISCUSSION

The tested compounds were isolated in our previous research.⁶ The identification was based on 1D and 2D NMR and HRESIMS spectra and their comparison with the literature data (for NMR data see Supplementary material to this paper, Tables S-I–S-IV). Tested compounds were: pachymic acid (**1**),²⁹ polyporenic acid G (**2**),⁶ polyporenic acid F (**3**),⁶ polyporenic acid C (**4**),³⁰ piptolinic acid B (**5**),⁸ 3-*epi*-dehydropachymic acid (**6**),⁸ polyporenic acid A (**7**),³¹ fomeficinic acid A (**8**),³² 12 α -hydroxy-3 α -(3'-hydroxy-4'-methoxycarbonyl-3'-methylbutyryloxy)-24-methyl lanosta-8,24(31)-dien-26-oic acid (**9**),³¹ betulin (**10**),³² 3 α -(acetyloxy)-16 α -hydroxy-24-methylene-lanost-8-en-21-oic acid (**11**)³³ and dehydropachymic acid (**12**).³⁴

All the compounds tested displayed a beneficial effect on the control lymphocyte cells giving a significant decrease of the frequency of MN in comparison with the control cell cultures (Fig. 1). According to the cytokinesis-block proliferation index (*CBPI*), routinely used to determine cytotoxicity of examined compounds in the *in vitro* MN test,²³ the tested compounds did not show any statistically significant decrease. The comparable *CBPI* values for the investigated compounds and tests with positive or negative control suggested an inhibitory effect on the lymphocyte cell proliferation of tested compounds (Table S-V, Supplementary material). The treatment of lymphocyte cells culture was carried out with mitomycin C (MMC), a clastogenic agent that has been used to study the susceptibility of cell to chromosomal damage and cytotoxic effects.¹⁴ MMC is capable of inducing chromosome aberrations *in vitro*,³⁵ DNA damage and MN.³⁶

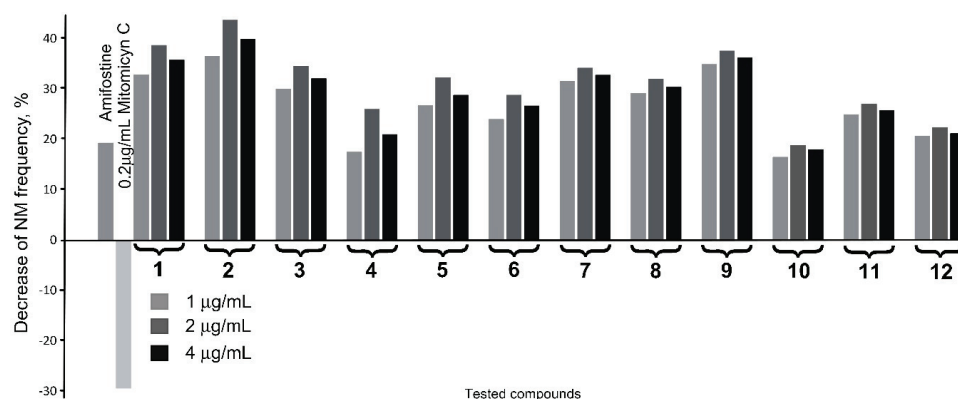


Fig. 1. Decrease of MN frequency in computation to the control (see Table S-V, Supplementary material), effected by lanostane triterpenes **1-12**.

During this experiment, we analyzed 126,000 BN cells. Our results provide the evidence of the protective effect of the all tested lanostanes on cytogenetic potential and the reduction of damage on human lymphocytes treated *in vitro*. It

was also found that the tested compounds reduced the frequency of MN in concentration dependent manner, with the medium concentration of $2.0 \mu\text{g mL}^{-1}$ being the most effective (Fig. 1).

Since MN expression is dependent on cell division, the quantification of cell proliferation and cell death is the best way to obtain reliable results is evaluation of cell kinetics and MN frequencies. Among the tested compounds at concentrations of 1, 2, and $4 \mu\text{g mL}^{-1}$, compound **2** exhibits the most prominent effect of decreasing the ($p < 0.01$) frequency of MN by 37, 44 and 40 %, respectively, when compared with the control cell cultures. A somewhat smaller effect was shown for compounds **1**, **3** and **9** at the same concentrations, decreasing the ($p < 0.01$) frequency of MN by 33, 39, 36; 30, 35, 32; 35, 38 and 36 %, respectively, when compared with the control cell cultures (Table S-V, Supplementary material). The compounds **4**, **10** and **12** at all tested concentrations caused decrease of the MN frequency in the range similar to that of amifostine, a radioprotective compound. Owing to selective action of amifostine on healthy tissues and its anti-mutagenic and anti-carcinogenic properties, it was used as a drug on oncology patients, against the damaging effects of radiation and chemotherapy.³⁷ All the compounds tested showed the highest activity at the concentration of $2 \mu\text{g mL}^{-1}$ – with an increase of the concentration the activity slightly decreases, which was not the case with the previously studied jatrophanes and sesquiterpene lactones (Krstić *et al.*¹⁷ and Cvetković *et al.*¹⁸, respectively). The typical DNA protective activity of natural products is mostly attributed to their antioxidative potential.^{15–18} The cytotoxic and antioxidant activity of nine lanostane-type triterpenes, isolated from *P. cocos*, were examined previously by Zhou *et al.*²⁰ They tested the ability of scavenging free oxygen radicals and inhibition of oxidation using 2,2-diphenyl-1-picrylhydrazyl (DPPH) radical test. In comparison to the vitamin E used as a positive control, the compounds tested did not show antioxidant activity with $p < 0.05$ that may be considered statistically significant. On the other hand, Sekiya *et al.*¹⁹ carried out the free radical-induced lyses using 2,2-azo-bis(2-amidinopropane) dihydrochloride (AAPH) of human red blood cells, in order to investigate anti-hemolytic activity of triterpenes isolated from Hoelen, scleroderma of *P. cocos*. They found that lanostane triterpene carboxylic acids isolated from the methanol extract of Hoelen, *i.e.*, pachymic acid, poly-porenic acid, 3-epidehydrotumulolic acid, 3β -hydroxylanosta-7,9(11), 24-trien-21-oic acid and 3-O-acetyl-16- α -hydroxytrametenolic acid, exhibited inhibitory activities against AAPH-induced lyses of red blood cells. Whereas in the first study,²⁰ stable free radicals were used. In the second investigation free radicals were induced by AAPH thermal decomposition in aqueous conditions. Sekiya *et al.*¹⁹ measured AAPH-induced hemolysis at 540 nm which, according to Nuruki *et al.*³⁸ was not the optimal wavelength, because AAPH oxidizes the oxygenated hemoglobin to methemoglobin and absorbance at 540 nm does not correctly ref-

lect the amount of released hemoglobin by AAPH-induced hemolysis. Thus, the absorbance at 523 nm correctly reflects the amount of released hemoglobin regardless of the status of hemoglobin (isosbestic point).³⁸

Generally, the compounds **4**, **6** and **12** containing a conjugated 7,9 (11)-diene system exhibited lower activity than the Δ^8 -analogues **1–3**, **7–9** and **11**. At the same time, compared to Δ^8 -lanostanes,⁶ the conjugated 7,9 (11)-diene system has a positive effect on cytotoxicity to HL 60 cells.⁶ It was also shown that the DNA protective activities within the Δ^8 -lanostane-26-oic acid group (**2**, **3**, **7** and **9**) (Fig. 1) are affected by the substitution in position 3 pattern. Thus, 3-keto lanostane **2**, showed slightly higher activity than those bearing 3-hydroxy (**7**) or 3-*O*-acyl substituents (**3** and **9**). Moreover, in the Δ^8 -lanostane-21-oic acid series (**1** and **11**), the DNA protection activity was dependent on the configuration at C-3. Lanostane **1** with the acetoxy group in 3 β -position revealed significantly higher activity than the epimeric 3 α -acetoxy lanostane **11** (Fig. 1). It should be noted that the compound **1** also exhibited higher cytotoxic activity in comparison with **11**.⁶

In the Δ^8 series the oxygenation at C-12 or 16 as well as 21- or 26-oic acid functionality were shown beneficial for *in vitro* protective effect on chromosomal aberrations. The smallest activity among the tested compounds was observed for compound **10**, botulin. This pentacyclic compound, lacking these functionalities, decreased the frequency of MN to the same extent as amifostine. Compound **5** has an open (3,4-*seco*) A ring and the rest of the skeleton is the same as in compound **8**. Both compounds have shown the same effect on NB cells so the scission of ring A showed no activity effect.

The above results indicate that the mechanism of action, as DNA protective agents, is not based on the antioxidant potential of tested compounds. Some other biochemical process, regulated by enzymes, should be considered as the mechanism of their action. Zhang *et al.*³⁹ tested inhibitory effects of triterpene inotodiol, the constituent of the fungus *I. obliquus*, commonly known as “chaga” on HeLa cells migration, invasion and induction of apoptosis. The results of Western blot analysis demonstrated that inotodiol could activate p53 and p21 proteins expression. The p 53 protein is crucial in the regulation of the cell cycle and, depending on the level of DNA damage, stops the G1 phase and activates repair mechanisms, increasing the expression of p21, or conduct cell into apoptosis. Protein p21, the cyclin-dependent kinase inhibitor located downstream of p53 gene, is closely related to tumor inhibition.⁴⁴⁰

We believe that tested lanostanes have similar regulatory mechanism on cell cycle regulating the p53 exertion however, this needs further investigation.

CONCLUSION

This paper presents a study of the influence of twelve triterpenes on cytogenetic potential and reduction of damage on human lymphocytes treated *in vitro*.

According to the cytokinesis-block proliferation index (CBPI), all the compounds tested exerted a significant decrease of the MN frequency in comparison with the control cell cultures. At the same time, the tested compounds did not show statistically significant cytotoxicity. The highest DNA protective activity was at concentration of 2 $\mu\text{g mL}^{-1}$, whereas at the higher concentration (4 $\mu\text{g mL}^{-1}$), the activity slightly decreased. The best results were obtained with poly-porenic acid G (2), Δ^8 -lanostane-26-oic acid with 3-keto group. The oxygenation at C-12 or 16 as well as 21- or 26-oic acid functionality were beneficial for *in vitro* protective effect on chromosomal aberrations. The comparison of our results with the literature data indicated the tested lanostanes effects on cell cycle regulating the p53 exertion which require further investigation.

SUPPLEMENTARY MATERIAL

Additional data are available electronically at the pages of journal website: <https://www.shd-pub.org.rs/index.php/JSCS/index>, or from the corresponding author on request.

Acknowledgement: The authors acknowledge their gratitude to the Ministry of Education, Science and Technological Development of Republic of Serbia for financial support (Contract numbers: 451-03-9/2021-14/ 200168, 451-03-9/2021-14/200026 and 451-03-9/2021-14/200178).

ИЗВОД

ДНК ПРОТЕКТИВНА АКТИВНОСТ ТРИТЕРПЕНА ИЗОЛОВАНИХ ИЗ МЕДИЦИНСКЕ ГЉИВЕ *Fomitopsis betulina*

ИВАНА В. СОФРЕНИЋ¹, БОБАН Д. АНЂЕЛКОВИЋ¹, ЉУБОДРАГ В. ВУЛИСИЋ¹, МИРОСЛАВ М. НОВАКОВИЋ², АЛЕКСАНДАР З. КНЕЖЕВИЋ³, МИРОСЛАВА Б СТАНКОВИЋ⁴, СЛОБОДАН М. МИЛОСАВЉЕВИЋ^{1,5} и ВЕЛЕ В. ТЕШЕВИЋ¹

¹Универзитет у Београду-Хемијски факултет, Студентски шир 16, 11000 Београд, ²Универзитет у Београду, Институт за хемију технологију и металургију, Институт од националног значаја за Републику Србију, Његошева 12, 11000, Београд, ³Универзитет у Београду, Биолошки факултет, Таковска 43, 11000, Београд, ⁴Нуклеарни објекти Србије, Мике Пећковића Аласа 12-14, 11351, Винча и ⁵Српска академија наука и уметности, Кнез Михајлова 35, 11000, Београд

Једанаест 31-метиланостанских тритерпеноида, то јест седам 21- и четири 26-ланостанских киселина, као и лупански тритерпеноид бетулин изолованих из плодоносних тела гљиве *Fomitopsis betulina* тестирани су *in vitro* на заштитни ефекат на аберације хромозома у периферним хуманим лимфоцитима. Примењен је тест мерења учесталости микронуклеуса индукованих применом инхибитора цитокинезе, цитохалазина Б. Испитивања су показала да већина тестираних једињења показује значајан протективни ефекат на ДНК хуманих лимфоцита, већи него комерцијални радиопротективни агенс аминофостин. У опсегу концентрација 1, 2 и 4 $\mu\text{g mL}^{-1}$ сва испитивана једињења су смањивала учесталост микронуклеуса (MN), при чему је најефикаснија била концентрација од 2,0 $\mu\text{g mL}^{-1}$. Са повећањем концентрације (4 $\mu\text{g mL}^{-1}$) активност се благо смањује. Студије односа структуре и активности (SAR) показале су да ланостани који садрже конјуговани 7,9-(11)-диенски систем имају нижу активност од 8-аналога. Такође је пока-

зано да на заштитне активности ДНК унутар групе 8-ланостан-26-киселина утиче супституција у положају 3. У 8-серији присуство кисеоничних функција на С-12 или С-16, као и С-21 или С-26 карбоксилних група повећава *in vitro* протективни ефекат на на ДНК хуманих лимфоцита. Међу испитиваним једињењима тритерпен бетулин (лупанска серија) је показао најмањи протективни ефекат сличан са протективним ефектом амифостина.

(Примљено 1. априла, ревидирано 20. маја, прихваћено 24. маја 2021)

REFERENCES

1. U. Grienke, J. Mihaly-Bison, D. Schuster, T. Afonyushkin, M. Binder, S. H. Guan, C. R. Cheng, G. Wolber, H. Stuppner, D. A. Guo, V. N. Bochkov, J. M. Rollinger, *Bioorg. Med. Chem.* **19** (2011) 6779 (<https://doi.org/10.1016/j.bmc.2011.09.039>)
2. U. Grienke, J. Zwirchmayr, U. Peintner, E. Urban, M. Zehl, M. Schmidtke, J. M. Rollinger, *Planta Med.* **85** (2019) 195 (<https://doi.org/10.1055/a-0690-9236>)
3. S. R. Lee, S. Lee, E. Moon, H.-J. Park, H. B. Park, K. H. Kim, *Bioorg. Chem.* **70** (2017) 94 (<https://doi.org/10.1016/j.bioorg.2016.11.012>)
4. J.-L. Ríos, I. Andújar, M.-C. Recio, R.-M. Giner *J. Nat. Prod.* **75** (2012) 2016 (<https://doi.org/10.1021/np300412h>)
5. U. Grienke, P. A. Foster, J. Zwirchmayr, A. Tahir, J.M. Rollinger, E. Mikros, *Sci. Rep.* **9** (2019) 11113 (<https://doi.org/10.1038/s41598-019-47434-8>)
6. I. Sofrenic, B. Anđelković, N. Todorović, T. Stanojković, Lj. Vujisić, M. Novaković, S. Milosavljević, V. Tešević, *Phytochemistry* **181** (2021) 112580 (<https://doi.org/10.1016/j.phytochem.2020.112580>)
7. B. S. Min, J. J. Gao, N Nakamura, M. Hattori, *Chem. Pharm. Bull.* **48** (2000) 1026 (<https://doi.org/10.1248/cpb.48.1026>)
8. Z. Tohtahon, J. Xue, J. Han, Y. Liu, H. Hua, T. Yuan, *Phytochemistry* **143** (2017) 98 (<https://doi.org/10.1016/j.phytochem.2017.07.013>)
9. R. C. S. Mata, D. I. M. D. de Mendonça, L. Vieira, A. F. dos Santos, L. A. da Silva, J. F. Gaspar, C. Martins, J. Rueff, A. E. G. Sant'Ana, *J. Braz. Chem. Soc.* **22** (2011) 35 (<https://doi.org/10.1590/S0103-50532011001000008>)
10. M. Fenech, *Mutat. Res.* **455** (2000) 81 ([https://doi.org/10.1016/S0027-5107\(00\)00065-8](https://doi.org/10.1016/S0027-5107(00)00065-8))
11. M. Fenech, W. P. Chang, M. Kirsch-Volders, N. Holland, S. Bonassi, E. Zeiger, *Mutat. Res.* **534** (2003) 65 ([https://doi.org/10.1016/S1383-5718\(02\)00249-8](https://doi.org/10.1016/S1383-5718(02)00249-8))
12. S. B. Carter, *Nature* **213** (1967) 261 (<https://doi.org/10.1038/213261a0>)
13. T. Haaf, E. Raderschall, G. Reddy, D. C. Ward, C. M. Radding, E. I. Golub, *J. Cell Biol.* **144** (1999) 11 (<https://doi.org/10.1083/jcb.144.1.11>)
14. C. J. Ye, Z. Sharpe, S. Alemara, S. Mackenzie, G. Liu, B. Abdallah S. Horne, S. Regan H. H. Heng, *Genes* **10** (2019) 366 (<https://doi.org/10.3390/genes10050366>)
15. I. Vučković, V. Vajs, M. Stanković, V. Tešević, S. Milosavljević, *Chem. Biodivers.* **7** (2010) 698 (<https://doi.org/10.1002/cbdv.200900067>)
16. D. Godevac, V. Tesevic, V. Vajs, S. Milosavljevic, M. Stankovic, *Mini-Rev. Med. Chem.* **13** (2013) 431 (<https://doi.org/10.2174/138955713804999856>)
17. G. Krstić, M. Jadrnin, M. Stanković, I. Aljančić, Lj. Vujisić, B. Mandić, V. Tešević, *Nat. Prod. Commun.* **14** (2019) 1 (<https://doi.org/10.1177/1934578X19848168>)
18. M. Cvetkovic, I. Djordjevic, M. Jadrnin, M. Stankovic, B. Mandic, S. Milosavljevic, Lj. Vujisic, *Nat. Prod. Res.* (<https://doi.org/10.1080/14786419.2019.1687470>)
19. N. Sekiya, H. Goto, Y. Shimada, Y. Endo, I. Sakakibara, K. Terasawa, *Phytother. Res.* **17** (2003) 160 (<https://doi.org/10.1002/ptr.1097>)

20. L. Zhou, Y. Zhang, L. A. Gapter, H. Ling, R. Agarwal, K. Ng, *Chem. Pharm. Bull.* **56** (2008) 1459 (<https://doi.org/10.1248/cpb.56.1459>)
21. Declaration of Helsinki – Ethical Principles for Medical Research Involving Human Subjects. *World Medical Association*, 9th July 2018 (<https://www.wma.net/policies-post/wma-declaration-of-helsinki-ethical-principles-for-medical-research-involving-human-subjects/>) (March 30th, 2021)
22. Law on Health Care, *Official Gazette of the Republic of Serbia*, 2005;107:112 (<http://www.pravno-informacioni-sistem.rs/SlGlasnikPortal/viewdoc?uuiid=d32f9cf4-1f75-4259-a40b-039099bc8eb5®actid=424598&doctype=reg>) (March 30th, 2021)
23. M. Fenech, A. A. Morley, *Mutat. Res.* **147** (1985) 29 ([https://doi.org/10.1016/0165-1161\(85\)90015-9](https://doi.org/10.1016/0165-1161(85)90015-9))
24. M. Fenech, A. A. Morley, *Mutat. Res.* **161** (1986) 193 ([https://doi.org/10.1016/0027-5107\(86\)90010-2](https://doi.org/10.1016/0027-5107(86)90010-2))
25. P. I. Countryman, J. A. Heddle, *Mutat. Res.* **41** (1976) 321 ([https://doi.org/10.1016/0027-5107\(76\)90105-6](https://doi.org/10.1016/0027-5107(76)90105-6))
26. M. Stanković, V. Tešević, V. Vajs, N. Todorović, S. Milosavljević, D. Gođevac, *Planta Med.* **74** (2008) 730 ([10.1055/s-2008-1074521](https://doi.org/10.1055/s-2008-1074521))
27. J. Surrallés, N. Xamena, A. Creus, J. Catalan, H. Norppa, R. Marcos, *Mutat. Res.* **341** (1995) 169 ([https://doi.org/10.1016/0165-1218\(95\)90007-1](https://doi.org/10.1016/0165-1218(95)90007-1))
28. J. Surrallés, A.T. Natarajan, *Mutat. Res.* **392** (1997) 165 ([https://doi.org/10.1016/S0165-1218\(97\)00054-2](https://doi.org/10.1016/S0165-1218(97)00054-2))
29. K.-H. Lai, M.-C. Lu, Y.-C. Du, M. El-Shazly, T.-Y. Wu, Y.-M. Hsu, A. Henz, J.-C. Yang, A. Backlund, F.-R. Chang, Y.-C. Wu, *J. Nat. Prod.* **79** (2016) 2805 (<https://doi.org/10.1021/acs.jnatprod.6b00575>)
30. H. K. Wangun, A. Berg, W. Hertel, A. Nkengfack, C. Hertweck, *J. Antibiot.* **57** (2004) 755 (<https://doi.org/10.7164/antibiotics.57.755>)
31. T. Kamo, M. Asanoma, H. Shibata, M. Hirota, *J. Nat. Prod.* **66** (2003) 1104 (<https://doi.org/10.1021/np0300479>)
32. Z. Alresly, U. Lindequist, M. Lalk, A. Porzel, N. Arnold, L. Wessjohann, *Rec. Nat. Prod.* **10** (2016) 103 (<https://www.acgpubs.org/doc/2018080518045712-RNP-1410-220.pdf>)
33. X.-R. Peng, H.-G. Su, J.-H. Liu, Y.-J. Huang, X.-Z. Yang, Z.-R. Li, L. Zhou, M.-H. Qiu, *J. Agric. Food Chem.* **67** (2019) 10330 (<https://doi.org/10.1021/acs.jafc.9b04530>)
34. T. Shingu, T. Tai, A. Akahori, *Phytochemistry* **31** (1992) 2548 ([https://doi.org/10.1016/0031-9422\(92\)83325-S](https://doi.org/10.1016/0031-9422(92)83325-S))
35. T. Roncada, V. E. P. Vicentini, M. S. Mantovani, *Toxicol. in Vitro* **18** (2004) 617 (<https://doi.org/10.1016/j.tiv.2004.02.007>)
36. M. R. Camelo, S. G. F. Kehdy, E. C. Salas, T. P. M. Lopes, *Molecules* **13** (2008) 1759 (<https://doi.org/10.3390/molecules13081759>)
37. D. J. Grdina, Y. Kataoka, J. S. Murley, *Drug Metab. Drug Interact.* **16** (2000) 237 (<https://doi.org/10.1515/DMDI.2000.16.4.237>)
38. Y. Nuruki, H. Matsumoto, M. Tsukada, H. Tsukahara, T. Takajo, K. Tsuchida, K. Anzai, *Chem. Pharm. Bull.* **69** (2021) 67 (<https://doi.org/10.1248/cpb.c20-00568>)
39. Z. Sun-Donga, Y. Lianga, W. Penga, K. Pinga, L. Jic, W. Li-Taob, W. Weia, Y. Li-Pinga, Z. Xiu-Huaa, F. Yu-Jie, *Phytomedicine* **60** (2019) 152957 (<https://doi.org/10.1016/j.phymed.2019.152957>)
40. K. M. Atkins, L. L. Thomas, J. Barroso-González, L. Thomas, S. Auclair, J. Yin, H. Kang, J. H. Chung, J. D. Dikeakos, G. Thomas, *Cell Rep.* **8** (2014) 1545 (<https://doi.org/10.1016/j.celrep.2014.07.049>).

SUPPLEMENTARY MATERIAL TO
**DNA protective activity of triterpenoids isolated from medicinal
mushroom *Fomitopsis betulina***

IVANA V. SOFRENIĆ¹, BOBAN D. ANĐELKOVIĆ^{1*}, LJUBODRAG VUJISIĆ¹,
MIROSLAV NOVAKOVIĆ², ALEKSANDAR Z. KNEŽEVIĆ³, MIROSLAVA B.
STANKOVIĆ⁴, SLOBODAN M. MILOSAVLJEVIĆ^{1,5} and VELE V. TEŠEVIĆ¹

¹University of Belgrade, Faculty of Chemistry, Studentski trg 12–16, 11000, Belgrade, Serbia,

²University of Belgrade, Institute of Chemistry, Technology and Metallurgy, National Institute of the Republic of Serbia, Studentski trg 12–16, 11000, Belgrade, Serbia, ³University of Belgrade, Faculty of Biology, Takovska 43, 11000, Belgrade, Serbia, ⁴Nuclear Facilities of Serbia, Mike Petrovića Alasa 12–14, 11351, Vinča, Serbia and ⁵Serbian Academy of Sciences and Arts, Knez Mihailova 35, 11000, Belgrade, Serbia

J. Serb. Chem. Soc. 86 (9) (2021) 809–817

TABLE S-I. ¹H- (500 MHz) and ¹³C-NMR (125 MHz) Spectral Data of **1-3**

C/H	1 (MeOD-d ₄)		2 (MeOD-d ₄)		3 (MeOD-d ₄)	
	δ _C / ppm	δ _H / ppm, (J / Hz)	δ _C / ppm	δ _H / ppm, (J / Hz)	δ _C / ppm	δ _H / ppm, (J / Hz)
1	36.6	1.78, 1.28, m	37.1	1.67, 2.03, m	31.9	1.56–1.52 (2H), m
2	25.3	1.67, m	35.6	2.44, 2.61, m	24.2	1.70, 1.97, m
3	82.6	4.45, dd (9.3, 7.1)	220.6	-	79.9	4.69, dd (3.6, 2.0)
4	39.0	-	48.9	-	38.1	-
5	52.2	1.16, m	52.8	1.67, m	46.9	1.55, m
6	19.3	1.73, 1.57, m	20.7	1.69–1.65 (2H), m	19.3	1.55, 1.67, m
7	27.7	2.08, m	27.5	2.07, 2.12, m	27.3	2.11–2.08 (2H), m
8	136.2	-	133.2	-	136.4	-
9	135.7	-	137.4	-	134.6	-
10	38.3	-	38.1	-	38.1	-
11	21.7	2.05, 1.98, m	34.6	2.09, 2.68, m	34.5	2.10, 2.64, m
12	30.3	1.81, 1.47, m	73.7	4.01, d (8.0)	73.8	4.00, d (8.0)
13	47.1	-	50.8	-	50.7	-
14	49.4	-	51.0	-	50.9	-
15	43.8	2.20, 1.28, m	33.5	1.20, 1.71, m	33.4	1.17, 1.70, m
16	77.9	4.04, dd (7.9, 6.6)	29.1	1.37, 2.04, m	29.1	1.36, 2.03, m
17	57.5	2.08, m	44.0	2.24, m	44.0	2.24, m
18	17.9	0.78, s	17.2	0.67, s	17.1	0.66, s
19	19.7	1.03, s	19.0	1.11, s	19.2	1.04, s
20	49.1	2.38, dt (11.2, 2.6)	37.8	1.43, m	37.8	1.42, m
21	180.6	-	18.1	1.05, d (6.6)	18.0	1.06, d (6.6)
22	32.0	2.04, 1.75, m	35.8	1.26, 1.65, m	35.8	1.27, 1.65, m

* Corresponding author. E-mail: aboban@chem.bg.ac.rs

C/H	1 (MeOD-d ₄)		2 (MeOD-d ₄)		3 (MeOD-d ₄)	
	δ_C /ppm	δ_H /ppm, (J/Hz)	δ_C /ppm	δ_H /ppm, (J/Hz)	δ_C /ppm	δ_H /ppm, (J/Hz)
23	33.6	2.07, 1.99, m	33.1	2.04, 2.24, m	33.1	2.04, 2.24, m
24	157.0	-	151.0	-	150.9	-
25	35.2	2.27, sep (6.7)	47.1	3.12, q (7.1)	46.9	3.14, q (7.1)
26	22.4	1.04, d (6.7)	179.0	-	178.8	-
27	22.5	1.02, d (6.7)	17.1	1.26, d (7.1)	17.0	1.27, d (7.1)
28	28.6	0.90, s	27.0	1.09, s	28.3	0.90, s
29	17.1	0.91, s	21.8	1.08, s	22.2	0.97, s
30	25.6	1.13, s	25.4	1.11, s	25.4	1.12, s
31	107.5	4.76, 4.73, brs	111.1	4.89, 4.93 brs	111.2	4.90, 4.93, d (2.0)
3-						
1'	173.0	-			167.9	-
2'	21.3	2.03, s			169.1	-
3'					53.1	3.72, s

TABLE S-II. ¹H- (500 MHz) and ¹³C-NMR (125 MHz) Spectral Data of 4-6

C/H	4 (Pyridine-d ₅)		5 (MeOD-d ₄)		6 (CDCl ₃)	
	δ_C /ppm	δ_H /ppm, (J/Hz)	δ_C /ppm	δ_H /ppm, (J/Hz)	δ_C /ppm	δ_H /ppm, (J/Hz)
1	37.3	2.08, 1.62, m	34.1	1.74, (2H) m	30.9	1.78, 1.65, m
2	35.4	2.72, 2.31, m	30.7	2.33, 1.97, m	26.5	1.98, 1.64, m
3	215.7	-	178.4	-	76.7	3.37, brs
4	48.0	-	147.6	-	38.2	-
5	51.6	1.58, m	48.4	2.20, m	44.1	1.55, t (7.9)
6	24.4	2.11, 5.55, m	25.4	1.77, 1.57, m	23.9	2.02, (2H), m
7	121.2	2.08, m	28.1	2.00, 1.40, m	121.8	5.46, t (3.7)
8	143.4	-	140.4	-	147.0	-
9	145.2	-	131.1	-	143.0	-
10	38.0	-	41.7	-	38.3	-
11	118.2	5.32, m	22.9	2.11, 1.98, m	116.6	5.34, m
12	36.8	2.63, 2.38, m	30.4	1.75, 1.52, m	36.4	2.22, 1.86 m
13	45.6	-	45.4	-	45.4	-
14	49.9	-	51.8	-	49.6	-
15	44.9	2.41, 1.89, d (13)	31.8	1.67, 1.29, m	44.2	2.16, 1.45, m
16	76.9	4.50, dd (7.9, 6.2)	27.2	2.10, 2.05 m	77.4	4.03, dd (7.8, 0.7)
17	58.1	2.84, dd (11.0, 6.2)	48.5	2.10, m	57.3	2.13, m
18	18.1	1.02, s	16.8	0.84, s	17.7	0.61, s
19	22.5	1.10, s	23.0	0.97, s	26.5	1.08, s
20	49.2	2.92, dt (11.0, 3.0)	49.6	2.26, m	48.6	2.13, dt (11.3, 2)
21	179.5	-	180.6	-	180.1	-
22	32.0	2.61, 2.43, m	32.5	1.68, 1.62, m	31.4	2.02, 1.76, m
23	33.8	2.50, 2.36, m	33.3	2.00 (2H) m	33.3	2.10-1.94, (2H) m
24	156.6	-	156.8	-	156.4	-
25	34.6	2.25, sep (6.8)	35.2	2.24, m	34.8	2.24, m
26	22.4	0.97, d (6.8)	22.5	1.02, d (6.6)	22.4	1.00, d (6.7)
27	22.5	0.95, d (6.8)	22.4	1.03, d (6.6)	22.3	1.01, d (6.7)
28	26.2	1.09, s	114.6	4.92, 4.69, brs	28.9	0.94, s
29	22.9	1.02, s	23.6	1.78, s	23.4	0.91, s
30	26.9	1.42, s	25.8	0.99, s	23.2	0.98, s
31	107.5	4.95, 4.81, brs	107.6	4.77, 4.72 brs	107.3	4.73, 4.70, brs

1'	170.9
2'	22.8 2.05, s

TABLE S-III. ¹H- (500 MHz) and ¹³C-NMR (125 MHz) Spectral Data of 7-9

C/H	7 (CDCl ₃ / MeOD-d ₄)		8 (CDCl ₃)		9 MeOD	
	δ _C / ppm	δ _H / ppm, (J/ Hz)	δ _C / ppm	δ _H / ppm, (J/ Hz)	δ _C / ppm	δ _H / ppm, (J/ Hz)
1	29.9	1.58, 1.46, m	36.4	1.95, 1.61, m	31.7	1.74, 1.54, m
2	25.6	1.94, 1.61, m	34.8	2.56, 2.39, m	24.2	1.90, 1.78, m
3	75.8	3.41, m	217.9	-	78.6	4.97, brs
4	37.6	-	47.9	-	37.5	-
5	44.3	1.53, m	47.4	2.11, m	46.5	1.81, m
6	18.1	1.62, 1.51, m	19.6	1.61 (2H), m	18.9	1.67, 1.52, m
7	26.1	2.03, (2H) m	26.5	2.09 (2H), m	26.8	2.12 (2H), m
8	133.1	-	135.2	-	134.2	-
9	134.8	-	133.4	-	135.6	-
10	37.6	-	37.2	-	37.6	-
11	32.6	2.62, 2.09, m	21.2	2.02, (2H), m	35.1	2.76, 2.48, m
12	73.2	3.98, d (8.0)	30.6	1.64, 1.26, m	72.5	4.25, d (7.4)
13	49.6	-	44.5	-	50.5	-
14	49.6	-	49.8	-	50.6	-
15	32.1	1.65, 1.15, m	29.1	1.72, 1.43, m	33.1	1.75, 1.23, m
16	27.8	2.02, 1.35, m	27.3	2.02, 1.38, m	28.8	2.14, 1.43
17	43.0	2.08, m	51.4	1.60, m	43.6	2.67, m
18	16.3	0.62, s	16.3	0.79, s	17.3	0.77, s
19	18.8	0.98, s	18.9	1.11, s	19.4	1.03, s
20	36.2	1.41, m	47.6	2.32, m	37.4	1.50, m
21	17.7	1.02, d (6.5)	182.3	-	18.4	1.30, d (6.4)
22	34.3	1.64, 1.24, m	31.2	1.70, (2H), m	35.6	1.89, 1.50, m
23	31.8	2.20, 2.01, m	32.2	2.02, (2H), m	33.0	2.60, 2.34, m
24	149.2	-	155.4	-	151.2	-
25	45.8	3.12, q (7.0)	34.0	2.22, sep (6.9)	47.0	3.50, q (7.0)
26	177.9	-	22.1	1.01, d (6.9)	177.5	-
27	16.3	1.28, d (7.0)	22.0	1.02, d (6.9)	17.6	1.54, d (7.0)
28	28.0	0.97, s	26.4	1.09, s	28.8	1.03, s
29	22.2	0.87, s	21.5	1.06, s	27.5	0.91, s
30	24.4	1.07, s	24.6	0.91, s	25.7	1.40, s
31	110.5	4.94, 4.90, brs	107.1	4.77, 4.69, brs	110.9	4.90, 4.93, d (2.0)
3-						
1'					171.8	-
2'					46.9	3.02, 2.98, d (14.8)
3'					70.4	-
4'					46.5	3.07, 3.04, d (14.8)
5'					172.5	-
6'					51.8	3.64, s
3'-						
Me					28.9	1.67, s

TABLE S-IV. ¹H- (500 MHz) and ¹³C-NMR (125 MHz) Spectral Data of **10-12**

C/H	10 (CDCl ₃)		11 (MeOD-d ₄ : CDCl ₃ / 20 : 1)		12 (CDCl ₃)	
	δ_C / ppm	δ_H / ppm, (J / Hz)	δ_C / ppm	δ_H / ppm, (J / Hz)	δ_C / ppm	δ_H / ppm, (J / Hz)
1	39.1	1.66, 0.91, m	31.0	1.47, 1.41, m	35.5	1.83, 1.51, m
2	27.6	1.58, (2H) m	23.5	1.84, 1.62, m	24.3	1.72, 1.68, m
3	79.2	3.19, dd (11.5, 4.7)	78.1	4.67, brs	81.0	4.50, dd (11.4, 4.4)
4	38.9	-	37.0	-	37.8	-
5	55.5	0.69, d (9.6)	45.5	1.53, m	49.4	1.20, dd (11.3, 4.2)
6	18.5	1.53, 1.40, m	18.1	1.61, 1.48, m	22.9	2.07, (2H), m
7	34.4	1.40, m	26.3	2.08, 1.98, m	120.7	5.45, d (5.9)
8	41.1	-	134.1	-	141.9	-
9	50.9	1.27, 1.23, m	134.9	-	145.5	-
10	37.5	-	37.1	-	37.4	-
11	21.0	1.41, 1.21, m	20.7	2.04, 1.97, m	116.4	5.31, d (5.9)
12	25.4	1.64, 1.04, m	29.2	1.82, (2H), m	35.5	2.25, 1.98 m
13	37.4	1.65, m	46.3	-	44.8	-
14	42.9	-	48.5	-	48.8	-
15	27.3	-	42.9	2.20, 1.31, m	43.4	2.20, 1.50, m
16	29.4	1.93, 1.21, m	77.8	4.15, dd (8.7, 6.2)	76.9	4.03, dd (7.9, 6.8)
17	48.0	2.39, m	57.0	2.15, m	57.1	2.17, m
18	48.0	2.39, m	17.6	0.76, s	17.3	0.60, s
19	49.0	1.64, 1.58, m	19.1	0.98, s	22.8	0.98, s
20	150.7	-	46.5	2.49, dt (11.0, 2.3)	46.7	2.44, dt (10.6, 2.6)
21	30.0	-	179.8	-	178.7	-
22	34.2	1.86, 1.04, m	30.8	1.98, 1.84, m	30.6	1.96, 1.81, m
23	28.2	0.97, s	32.4	2.10, 2.02, m	32.4	2.08, 2.02, m
24	15.6	0.76, s	155.2	-	155.4	-
25	16.3	0.83, s	34.0	2.24, sep (7.0)	33.9	2.24, m
26	16.2	0.98, s	22.0	1.02, d (6.2)	21.9	1.02, d (6.4)
27	15.0	1.05, s	22.1	1.02, d (6.2)	22.0	1.01, d (6.4)
28	60.8	3.80, 3.33, d	27.8	0.88, s	28.2	0.88, s
29	109.8	4.68, 4.58, m	22.0	0.92, s	17.1	0.95, s
30	19.3	1.68, s	25.7	1.19, s	26.2	1.09, s
31			107.2	4.79, 4.73, brs	107.0	4.76, 4.72, brs
3-						
1'			171.1	-	171.4	-
2'			21.6	2.05, s	21.4	2.06, s

TABLE S-V. Incidence of MN, distribution of MN per cells, CBPI, and frequency of MN measurement (mean±SD) in cell cultures of human lymphocytes treated with different concentration of **1-12**

Tested compounds	c / $\mu\text{g ml}^{-1}$	Number of MN / 1000 BN cell	Contribution of BN cell with MN, %	Number of MN/BN cell	CBPI	Frequency of MN, %
Control		26.33 ± 0.28	2.15 ± 0.07	1.19 ± 0.05	1.67 ± 0.03	100
Amifos. - 1.0		21.25 ± 0.45 ^a	1.74 ± 0.09	1.22 ± 0.06	1.66 ± 0.01	80.7
MMC - 0.2		34.06 ± 0.78 ^{a,b}	2.95 ± 0.13	1.16 ± 0.03	1.69 ± 0.06	129.4
1	1.0	17.66 ± 0.63 ^{a,b,c}	1.50 ± 0.03	1.17 ± 0.03	1.71 ± 0.09	67.1
	2.0	16.14 ± 0.56 ^{a,b,c}	1.40 ± 0.03	1.15 ± 0.05	1.65 ± 0.06	61.3
	4.0	16.91 ± 0.60 ^{a,b,c}	1.50 ± 0.05	1.12 ± 0.03	1.64 ± 0.06	64.2
2	1.0	16.71 ± 0.76 ^{a,b,c}	1.42 ± 0.15	1.19 ± 0.09	1.60 ± 0.02	63.5
	2.0	14.82 ± 1.33 ^{a,b,c}	1.27 ± 0.08	1.17 ± 0.06	1.65 ± 0.03	56.3

	4.0	15.83 ± 0.79 ^{a,b,c}	1.32 ± 0.07	1.20 ± 0.03	1.66 ± 0.04	60.1
	1.0	18.43 ± 0.45 ^{a,b,c}	1.55 ± 0.04	1.19 ± 0.04	1.66 ± 0.03	70.0
3	2.0	17.22 ± 0.48 ^{a,b,c}	1.43 ± 0.02	1.20 ± 0.03	1.70 ± 0.05	65.4
	4.0	17.89 ± 0.52 ^{a,b,c}	1.57 ± 0.07	1.14 ± 0.05	1.61 ± 0.02	67.9
	1.0	21.73 ± 0.38 ^{a,c}	1.90 ± 0.04	1.14 ± 0.01	1.65 ± 0.02	82.5
4	2.0	19.48 ± 0.42 ^{a,c}	1.68 ± 0.06	1.17 ± 0.06	1.66 ± 0.03	74.0
	4.0	20.79 ± 0.27 ^{a,c}	1.59 ± 0.06	1.31 ± 0.05	1.64 ± 0.02	79.0
	1.0	19.28 ± 0.50 ^{a,c}	1.61 ± 0.06	1.20 ± 0.08	1.71 ± 0.09	73.2
5	2.0	17.83 ± 0.92 ^{a,b,c}	1.50 ± 0.06	1.19 ± 0.02	1.66 ± 0.02	67.7
	4.0	18.76 ± 0.53 ^{a,b,c}	1.68 ± 0.09	1.12 ± 0.04	1.63 ± 0.02	71.2
	1.0	20.02 ± 0.39 ^{a,c}	1.66 ± 0.09	1.21 ± 0.04	1.97 ± 0.33	76.0
6	2.0	18.75 ± 0.83 ^{a,b,c}	1.57 ± 0.04	1.20 ± 0.04	1.64 ± 0.02	71.2
	4.0	19.30 ± 0.72 ^{a,c}	1.71 ± 0.09	1.22 ± 0.04	1.63 ± 0.01	73.3
	1.0	18.01 ± 0.52 ^{a,b,c}	1.57 ± 0.03	1.13 ± 0.01	1.65 ± 0.01	68.4
7	2.0	17.33 ± 0.45 ^{a,b,c}	1.59 ± 0.11	1.10 ± 0.06	1.69 ± 0.09	65.8
	4.0	17.70 ± 0.80 ^{a,b,c}	1.53 ± 0.04	1.16 ± 0.02	1.70 ± 0.04	67.2
	1.0	18.63 ± 0.49 ^{a,b,c}	1.54 ± 0.08	1.21 ± 0.03	1.90 ± 0.09	70.8
8	2.0	17.90 ± 0.51 ^{a,b,c}	1.58 ± 0.09	1.14 ± 0.05	1.62 ± 0.01	68.0
	4.0	18.33 ± 0.57 ^{a,b,c}	1.51 ± 0.07	1.22 ± 0.03	1.72 ± 0.08	69.6
	1.0	17.13 ± 0.37 ^{a,b,c}	1.40 ± 0.05	1.21 ± 0.05	1.61 ± 0.01	65.1
9	2.0	16.42 ± 0.64 ^{a,b,c}	1.30 ± 0.05	1.26 ± 0.06	1.68 ± 0.03	62.4
	4.0	16.81 ± 0.46 ^{a,b,c}	1.42 ± 0.03	1.18 ± 0.06	1.61 ± 0.02	63.8
	1.0	22.00 ± 0.63 ^{a,c}	1.78 ± 0.07	1.22 ± 0.01	1.67 ± 0.02	83.5
10	2.0	21.37 ± 0.40 ^{a,c}	1.77 ± 0.05	1.19 ± 0.02	1.66 ± 0.03	81.2
	4.0	21.58 ± 0.45 ^{a,c}	1.79 ± 0.05	1.20 ± 0.02	1.62 ± 0.02	82.0
	1.0	19.78 ± 0.30 ^{a,c}	1.65 ± 0.01	1.13 ± 0.04	1.75 ± 0.07	75.1
11	2.0	19.23 ± 0.17 ^{a,c}	1.67 ± 0.06	1.16 ± 0.04	1.73 ± 0.08	73.0
	4.0	19.54 ± 0.70 ^{a,c}	1.64 ± 0.07	1.20 ± 0.09	1.62 ± 0.03	74.2
	1.0	20.88 ± 0.61 ^{a,c}	1.71 ± 0.12	1.22 ± 0.10	1.65 ± 0.01	79.3
12	2.0	20.44 ± 0.39 ^{a,c}	1.74 ± 0.06	1.17 ± 0.04	1.68 ± 0.03	77.6
	4.0	20.74 ± 0.73 ^{a,c}	1.73 ± 0.02	1.19 ± 0.05	1.67 ± 0.01	78.8

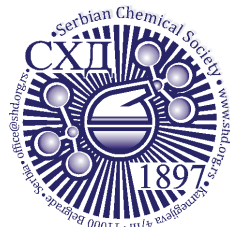
Number of MN/1000 BN cell - incidence of micronuclei in 1000 binucleated cells (examined for each concentration); Contribution of BN cell with MN: binucleated cells with micronuclei; Number of MN/BN cell incidence of micronuclei in binucleated cells; CBPI- cytokinesis-block proliferation index. Frequency of MN: incidence of MN present like share of control groups in cell cultures of human lymphocytes treated with different concentration of triterpenes

The statistical significance of difference between the data pairs was evaluated by analysis of variance (One-way ANOVA) followed by the Tukey test. Statistically difference was considered significant at $p < 0.01$.

^aCompared with control groups, statistically significant difference $p < 0.01$.

^bCompared with amifostine – WR 2721, statistically significant difference $p < 0.01$.

^cCompared with mitomycin – C, statistically significant difference $p < 0.01$. 1



J. Serb. Chem. Soc. 86 (9) 819–830 (2021)
JSCS–5464

Kinetics of the exchange of water absorbed in silica hydrogel with ethanol: Modelling by Brouers and Sotolongo–Costa fractal kinetics

BORIVOJ K. ADNAĐEVIĆ^{1*}, NEBOJŠA M. CVETKOVIĆ²
and JELENA D. JOVANOVIĆ³

¹Faculty of Physical Chemistry, University of Belgrade, Studentski Trg 12–16, P.O. Box 137, 11001 Belgrade, Serbia, ²Academy of Professional Studies South Serbia – Department of Agricultural and Food Studies, Ćirila i Metodija 1, 18400 Prokuplje, Serbia and ³Institute of General and Physical Chemistry, Studentski Trg 12–16, 11001 Belgrade, Serbia

(Received 11 January, revised 26 May, accepted 31 May 2021)

Abstract: Isothermal kinetics of the exchange of absorbed water in a silica hydrogel (SH) with ethanol was examined. The isothermal kinetic curves of absorbed water exchange with ethanol were measured at the temperatures: $T = 297, 306$ and 316 K. The rate of the exchange was analysed as a function of time. The possibility of mathematical description of the kinetics of exchange by the Brouers and Sotolongo–Costa's (BS) fractal's kinetics model was examined. Parameter values (n, τ, β) of the model and their changes with temperature were calculated. By applying the method of Ozao, it was determined that the rate limiting step of the process of exchange was the rate of exchange of the absorbed water with ethanol. Values of the fractal dimension of the SH–ethanol interphase were calculated. The dependences of the effective time-dependent rate coefficient, activation energy and pre-exponential factor on time and degree of exchange were calculated and discussed. The proposed model of the mechanism of the exchange of absorbed water with ethanol was discussed.

Keywords: silica hydrogel; solvent exchange; kinetics; fractal dimension.

INTRODUCTION

Nanoporous materials of low density, large specific surfaces and high porosity are called aerogels.¹ Due to the unique properties of silica aerogels: extreme low density, $\approx 30 \text{ kg m}^{-3}$; high porosity, $>98 \%$; low thermal conductivity, $\approx 0.01 \text{ W m}^{-1} \text{ K}^{-1}$; high surface area, $>1000 \text{ m}^2 \text{ g}^{-1}$; low refractive index, 1.01–1.10; low dielectric constant, <2 ; optical transparency, $>95 \%$; and low sound velocity, 100 m s^{-1} ,² it could be expected that they would find numerous application, such

* Corresponding author. E-mail: adnadjevic@mts.rs
<https://doi.org/10.2298/JSC210122055A>

as: excellent transparent thermal insulation materials,³ materials for acoustic barriers,⁴ catalytic support,⁵ absorption of oil,⁶ collectors,⁷ drug delivery carriers,⁸ sensors,⁹ *etc.*

The basic steps of the preparation of a silica aerogel are: formation of a silica sol in an aqueous solution, gelation of the silica sol, aging of gels, exchange of water with alcohol and supercritical drying of alcogels.¹⁰ Solvent exchange and modification (silylation) of the surfaces of the gel presents the essential processes for preserving the highly porous silica network structure during drying and obtaining aerogels with a high cumulative pore volume, high specific area, and extremely low density. Solvent exchange is a long-lasting and tedious process, because it mostly depends on the surface tension of the solvent and surface area of the gel.

Knowing the kinetics of exchange of the absorbed water from hydrogels is of extraordinary practical and scientific importance, since it enables mathematical modelling of the exchange process, which supports the design, optimization and scale-up of the processes, and development of novel technologies. To the best of our knowledge, there are no available literature data on the kinetics of the exchange of the absorbed water with a solvent. Nevertheless, there are only a few papers that investigated the exchange of absorbed water with a solvent. Rao *et al.*¹¹ investigated the effect of the solvent type (toluene, *n*-hexane, *n*-heptane) on the physico-chemical properties of silica aerogels prepared by the atmospheric pressure drying method.

The exchange of the water absorbed within a silica hydrogel with ethanol occurs at the interface between the silica hydrogel–ethanol phases. The spatial structure of the interface of the interaction is completely unknown in a dimensional and topological sense.¹² Bearing in mind the amorphous structure of a silica hydrogel, it is possible to assume that it is not ideal but disordered, irregular and non-homogeneous. Since the dimensional and topological heterogeneity of a system causes its chemical heterogeneity, the boundary surface of the interaction phase is probably also energetically heterogeneous. To describe the kinetics of processes which occur in such systems, the application of classical kinetic models, based on defined dimensional and topological properties, is not quite adequate.¹³

A fractal is an unregulated system, the disorder of which can generally be described with an innumerable value of the dimensionality of the system. A fractal object is fragmentable and can be divided into parts, with each part being a copy of the basic motif. Just for this reason, the assumption of the fractal nature of the boundary interaction surface is probably the most appropriate in describing the water absorbed–ethanol exchange kinetics, since it allows for the interaction, which occurs on the basic motif, to be reproduce on different time and duration scales.

Bearing this in mind, the present paper deals with the possibility of using a fractal kinetics model in investigating the kinetics of the exchange of water absorbed in silica hydrogel with ethanol, for the first time in the available literature.

Brouers and Sotongo–Costa fractal kinetics

In the works of Brouers and Sotongo-Costa¹⁴ and Brouers,¹⁵ the bases of fractal kinetics of chemical reactions and physicochemical processes are presented.

According to the Brouers and Sotongo-Costa (BS) fractal kinetics, the rate of chemical reaction is described by the fractional differential:

$$-\frac{dc_{n,\beta}(t)}{dt} = k_{n,\beta} [c_{n,\beta}(t)]^n \quad (1)$$

where the $c_{n,\beta}(t) / \text{g mL}^{-1}$ is the concentration of the reactant at time t , n – non-integer overall reaction order, β – fractional time index, $k_{n,\beta}(t) / \text{min}^{-\beta} \text{ mL g}^{-1}$ – effective time-dependent rate coefficient:

$$k_{n,\beta}(t) = \beta \frac{t^{\beta-1}}{\tau_{n,\beta}^\beta} \left[1 + (n-1) \left(\frac{t}{\tau_{n,\beta}} \right)^\beta \right]^{-1} \quad (2)$$

the $\tau_{n,\beta}^\beta / \text{min}^{-\beta}$ is a characteristic time of the complex kinetic, and is given by:

$$\tau_{n,\beta} = \left(c_0^{n-1} k_{n,\beta} \right)^{-\frac{1}{\beta}} \quad (3)$$

where $c_0 / \text{g mL}^{-1}$ is the initial concentration of the reactants. The solution of the differential Eq. (1) is given by:

$$c_{n,\beta}(t) = c_0 \left[1 + (n-1) \left(\frac{t}{\tau_{n,\beta}} \right)^\beta \right]^{-\frac{1}{(n-1)}} \quad (4)$$

In the case when fractal kinetics is used to describe the solvent exchange kinetics, Eq. (4) is transformed into:

$$c_{n,\beta}(t) = c_e \left\{ 1 - \left[1 + c_e (n-1) k_{n,\beta} t^\beta \right]^{-\frac{1}{(n-1)}} \right\} \quad (5)$$

where $c_e / \text{g mL}^{-1}$ is equilibrium concentration of the reactant (maximum quantity), and:

$$\tau_{n,\beta} = \left(c_e k_{n,\beta} \right)^{-\frac{1}{\beta}} \quad (6)$$

In the case when fractal kinetics is used to describe the solvent exchange kinetics, Eqs. (5) and (6) are transformed into:

$$c_{n,\beta}(t) = c_e \left\{ 1 - \left[1 + (n-1) \left(\frac{t}{\tau_{n,\beta}} \right)^\beta \right]^{\frac{1}{(n-1)}} \right\} \quad (7)$$

If the degree of exchange is defined by:

$$\alpha_{n,\beta}(t) = \frac{c_{n,\beta}(t)}{c_e} \quad (8)$$

then the conversion curve of exchange can be described by:

$$\alpha_{n,\beta}(t) = 1 - \left[1 + (n-1) \left(\frac{t}{\tau_{n,\beta}} \right)^\beta \right]^{\frac{1}{(n-1)}} \quad (9)$$

EXPERIMENTAL

The following materials were used to synthesize the silica hydrogel and to examine the kinetics of the change.

Soluble glass (sodium silicate solution), Silco 3.1, was purchased from A.D. Zeolite BSB, Probištip, North Macedonia. The chemical composition of soluble glass was as follows: silicon dioxide = 28.7 wt. %; sodium oxide = 8 wt. %; modul, $M = 3.30$; density = 1380 kg m^{-3} . For the exchange of sodium ions from a solution of soluble glass with hydrogen ions, a strong acid ion exchange resin IR-120, supplier Amberlite, USA, was used. Ammonium hydroxide and absolute ethanol 99.8 %, both *p.a.*, were purchased from Zorka Pharma, Šabac, Serbia. Distilled water was used to prepare the soluble glass solution.

Synthesis of silica hydrogels was performed according to the procedure described in detail by Rao.² In accordance with this procedure, the synthesis of silica hydrogels was carried out as follows. The soluble glass was diluted by adding distilled water to density = 1120 kg m^{-3} . The diluted soluble glass solution, at room temperature, was passed through a layer of ion exchange resin ($\phi = 2.54 \text{ cm}$, $h = 25 \text{ cm}$) at a flow rate of 1 mL min^{-1} in order to obtain the silica sol. The obtained silica sol was collected in a 250 mL beaker. Silica hydrogel was obtained by neutralisation of the silica sol ($V = 100 \text{ mL}$) with 0.4 mL of 1 M ammonium hydroxide solution. The hydrogel was formed after 15 min. In order to strengthen the silica network, the gel was left to age for 3 h at $50 \text{ }^\circ\text{C}$. After that, the gel was rinsed with water 3 times and kept in a closed vessel.

The water content in silica hydrogel, p / wt. %, was determined gravimetrically. A precise amount of the hydrogel, m_0 / g, was dried at a temperature of $T = 393 \text{ K}$, until its mass became constant, m_{TN} / g. Water content was calculated as:

$$p = 100 \frac{m_0 - m_{\text{TN}}}{m_0} \quad (10)$$

The water content in the used silica hydrogel was 91 wt. %. Determination of the degree of exchange of water absorbed on silica hydrogel with ethanol (α) was performed as follows.

In 250 mL of absolute ethanol preheated at a predetermined temperature, m / g of silica hydrogel wrapped in a meshed carrier was immersed. The reaction mixture was stirred by a magnetic stirrer at 400 rpm for a predetermined time.

The reaction mixture was sampled at predetermined time intervals in order to determine the water concentration in the reaction mixture. The water concentration exchanged, $c_{\text{H}_2\text{O}}$, in the samples, was determined by the Karl–Fischer's coulometric method. The titration was performed using a Metrohm 831 Karl–Fischer coulometer. The quantity of water exchange, q_t / g was determined by:

$$q_t = c_{\text{H}_2\text{O}} V_s \quad (11)$$

where: $c_{\text{H}_2\text{O}}$ / g mL⁻¹ is the concentration of water in the ethanol solution at time t / min, V_s / mL is the volume of the ethanol solution.

The degree of water exchange with ethanol, was calculated as:

$$\alpha = 100 \frac{q_t}{mp} \quad (12)$$

Determination of the parameters of the Brouers and Sotolongo–Costa Equation (n , τ , β) was performed by fitting the isothermal exchange conversion curves, using non-linear regression. The values of the equation parameters were determined using the OriginPro 9.0 64 Bit software. To evaluate the quality of fit, two criteria were used: the coefficient of determination, R^2 , and the reduced chi square coefficient, χ^2 .

RESULTS AND DISCUSSION

Fig. 1 shows the isothermal kinetic curves $c_{\text{H}_2\text{O}} = f(t)_T$ (Fig. 1a) and conversion curves (the dependence $\alpha = f(t)_T$, Fig. 1b) of the exchange of the absorbed water in the silica hydrogel with ethanol.

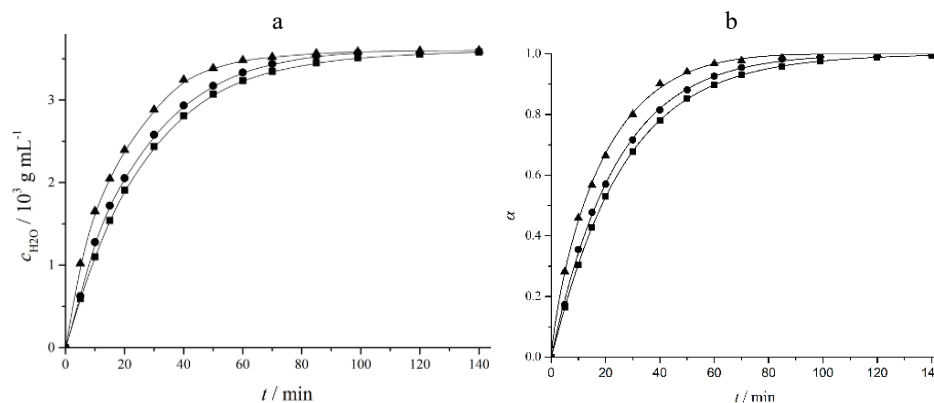


Fig. 1. Isothermal kinetic curves (a) and conversion curves (b) of the exchange of the absorbed water in ethanol–water mixtures as a function of time at: ■ 297, ● 306 and ▲ 316 K.

The kinetics and conversions curves of the water exchange have complex shapes. There are three characteristic and clearly noticeable shapes of increasing $c_{\text{H}_2\text{O}}$ with the extended exchange duration: a linear part, non-linear part and a pla-

teau. At short times of exchange, the concentration of water in ethanol increases almost linearly with extended duration of the exchange. Further increase in exchange time leads to a concave increase in $c_{\text{H}_2\text{O}}$, whereas with longer exchange time the maximum of $c_{\text{H}_2\text{O}}$ is achieved (plateau). With increasing temperature, the slope of the linear change in water concentration becomes steeper, and the equilibrium water concentration is reached sooner. The increase in the slope and the shortening of equilibration time indicates that the exchange process is thermally activated, and that the rate of exchange increases with temperature.

An attempt at determining the kinetics model of water exchange was made by analysing the shape of the curve of the exchange rate vs. time. The isothermal rate of water exchange vs. time is shown in Fig. 2.

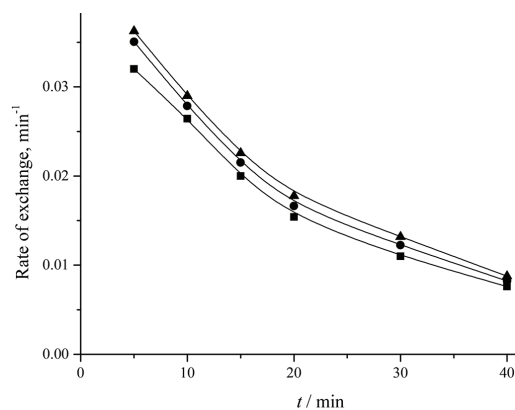


Fig. 2. Isothermal dependences of exchange rate vs. time at: ■ 297, ● 306 and ▲ 316 K.

At all the examined temperatures, the rate of exchange concavely decreases in a complex way with the time of exchange. The shape of dependence (da/dt) of the rate of exchange on time is significantly different than in cases of kinetically controlled chemical reactions (first and second order), and diffusion-controlled chemical reactions and processes, which implies a complex nature of this exchange kinetics.

With this complex dependence of the reaction rate on time in mind, and the complex structure of interface SH, the possibility of fitting isothermal conversion curves of change with the BS equation was investigated. The results of fitting the experimental conversion curves with the BS equation are shown in Fig. 1b (solid line). As shown, the experimental conversion curves, at all the investigated temperatures, are successfully fitted with the BS equation in the whole range, Fig. 1b.

The values of the BS equation parameters (n , β , τ) are given in Table I.

The values of fractal parameter n that characterizes the apparent order of the reaction are non-integer 1.05 to 0.8 and significantly deviate from the values for the reaction order of conventional chemical reactions, which confirms the fractal nature of the exchange kinetics. The parameter β varies from 1.05 to 0.82, with increasing temperature, which indicates that the mechanism of exchange does not

change with temperature, but that there is a change in the structure of the fractal interface of interaction of ethanol molecules with absorbed water on the hydrogel. The values of the characteristic time, τ , decrease with increasing temperature, which confirms the previous proposition that the specific rate of exchange increases with temperature.

TABLE I. Values of the Brouers and Sotongo-Costa fractal parameters for the isothermal kinetics

T / K	Fractal parameters	Value	$\chi^2 \times 10^6$	R^2
297	n	1.05	1.74	0.99998
	$\tau^{-1.05} / \text{min}^{-1.05}$	25.86		
	β	1.05		
306	n	0.98	0.638	0.99944
	$\tau^{-1.01} / \text{min}^{-1.01}$	23.84		
	β	1.01		
316	n	0.80	0.450	0.99955
	$\tau^{-0.82} / \text{min}^{-0.82}$	20.06		
	β	0.82		

The exchange of water absorbed on the silica hydrogel with ethanol is a heterogeneous chemical reaction which occurs continuously if there is a continuous molecular or convective diffusion of ethanol molecules to the reacting boundary surface of the hydrogel and a continuous diffusion of the altered water into the ethanol solution. In general, the rate of the exchange process is determined by the rate of the slowest stage of exchange. In the case where the rate of exchange is higher than the diffusion rate of ethanol, the kinetically limiting stage of the process is the diffusion rate of ethanol to interface. In contrast, when the rate of water exchange with ethanol is lower than the diffusion rate, the kinetically limiting stage is the rate of that exchange.

Ozao¹⁶ developed a method for determining the kinetically limiting stage of chemical reactions and physicochemical processes that can be described by fractal kinetics. According to this method, in case the kinetically limiting stage of fractal kinetics is the rate of the chemical reaction (process) at the interface, the dependence of $\ln (da/dt)$ on $\ln (1-a)$, should be linear, and the slope N of this dependence is in a functional relationship with the fractal dimension D of the interface is given as:

$$N = \frac{D}{D-1} \quad (13)$$

The isothermal dependences of $\ln (da/dt)$ on $\ln (1-a)$ are shown in Fig. 3. The dependence $\ln (da/dt)$ on $\ln (1-a)$ is linear, which indicates that the kinetically limiting stage is the rate of exchange of absorbed water with ethanol.

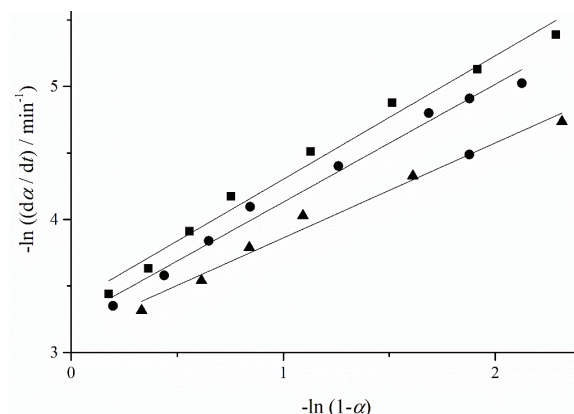


Fig. 3. Isothermal dependences of $\ln(d\alpha/dt)$ on $\ln(1-\alpha)$ at: ■ 297, ● 306 and ▲ 316 K.

The dependence of the slope and fractal dimension on temperature are given in Table II.

TABLE II. The effect of temperature on fractal dimension of the interface

T / K	N	D
297	0.93	1.93
306	0.88	1.88
316	0.71	1.71

As can be seen from Table II, an increase in the temperature of exchange leads to a decrease in the value of the fractal dimension from 1.93 to 1.71 of the interface interaction, which confirms the previously assumed assumption that a change in temperature leads to a change in the fractal structure of the interaction.

Upon knowing the isothermal values of the parameters (n , β , τ), the isothermal dependences of the effective time-dependent rate coefficient on time are calculated by Eq. (2). The isothermal dependences of the effective time-dependent rate coefficient on time are shown in Fig. 4.

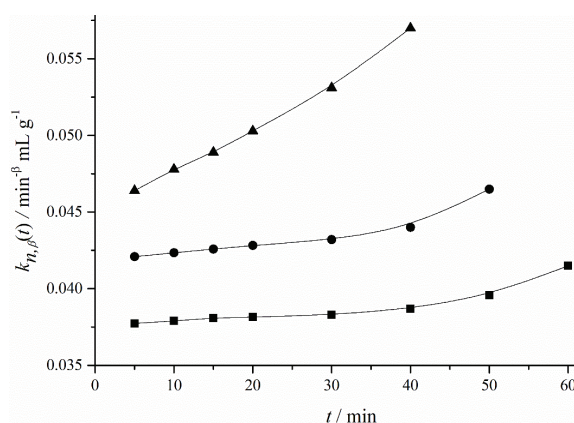


Fig. 4. Isothermal dependences of $k_{n,\beta}(t)$ on time, at: ■ 297, ● 306 and ▲ 316 K.

The effective rate coefficient of the exchange of water from silica hydrogel with ethanol is a time-dependent value. The values of the effective rate coefficient at all of the investigated temperatures, increase with the duration of the exchange process. At the defined times of exchange (isochronal conditions), the values of the effective time-dependent rate coefficient increase with temperature.

The time dependence of $k_{n,\beta}(t)$ is most likely due to the following points:

- a) the irregularities and the inhomogeneous interface in different phases of the interaction;¹⁷
- b) different rates of relaxation of the reacting species in the heterogeneous system;¹⁸
- c) the reaction rate exceeds the rate of internal rearrangement, which leads to regeneration of the distribution of reactant reactivity in disordered systems;¹⁹
- d) changing of the so-called reaction parameter, caused by the interface change during the reaction.²⁰

Bearing in mind the fractal structure of the water absorbed in silica hydrogel, it is presumed that the specific reaction rate is higher than the rate of internal rearrangement in the absorbed phase, which leads to the regeneration of the reactivity of the reactant, this being the main source of the time-dependency of k .

In fact, any exchange of a water molecule with an ethanol molecule has to lead to a structural reorganization within the absorbed phase, and due to this, the rate of internal rearrangement will change during the reaction, which will in turn change the specific reaction rate of this exchange. The increase in $k_{n,\beta}(t)$ with α indicates that the specific rate of reactivity regeneration decreases with time, since the structure of the absorbed phase is enriched with ethanol molecules

Knowing the mathematical dependence of the degree of exchange on time, the dependence of $k_{n,\beta}(t)$ on time can be transformed into dependence of $k_{n,\beta}(t)$ on the degree of exchange. The dependence of $k_{n,\beta}(t)$ on the degree of exchange is shown in Fig. 5.

At all of the examined temperatures, the $k_{n,\beta}(t)$ non-linearly increases with increasing degree of exchange. At a particular degree of exchange (isoconversional condition), the values of $k_{n,\beta}(t)$ increase with temperature in accordance with the Arrhenius equation. Thus, by applying the Arrhenius equation, the isoconversion values of the parameters of the exchange kinetics are calculated.

The isothermal dependence of E_a and $\ln A$ on the degree of exchange is presented in Fig. 6.

The values of kinetic parameters increase with α in a complex manner. This complex change of kinetic parameters with α confirms the complex fractal nature of the kinetics of exchange. The increase in the values of E_a with α indicates an enhancement of the interactions between the molecules of water in the absorbed phase with increasing degree of exchange, leading to structural changes in the absorbed phase.

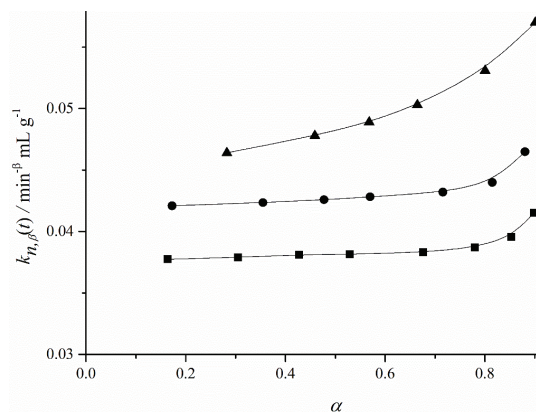


Fig. 5. Dependence of $k_{n,\beta}(t)$ on the degree of exchange at: ■ 297, ● 306 and ▲ 316 K.

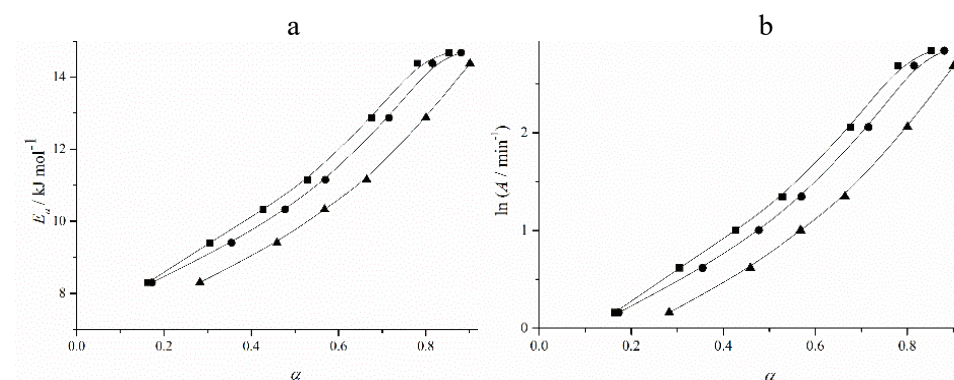


Fig. 6. Isothermal dependences of E_a on α (a) and $\ln A$ on α (b), at: ■ 297, ● 306 and ▲ 316 K.

Between the values of the kinetic parameters (E_a and $\ln A$) there is a correlation, *i.e.*, a compensation effect, which can be described by:

$$\ln A = 3.21951 + 040911E_a \quad (14)$$

The existence of a compensation effect confirms the complex nature of this kinetics, and leads to the assumption that it is the consequence of: a) the difference in the value of the effective time-dependent rate coefficient of exchange and the effective time-dependent rate coefficient of internal rearrangement in the absorbed phase; b) changes in the geometric (structural) conditions under which the process occurs.

The existence of the time-dependent values of k , E and $\ln A$ indicates that the value of the effective time-dependent rate coefficient of the exchange exceeds the rate of the internal rearrangement in the absorbed phase of the hydrogel. The increase in the value of the effective time-dependent rate coefficient of water exchange with time and degree of the exchange indicates that the effective time-dependent rate coefficient of structural transformation in the absorbed phase of

the hydrogel with the duration of the exchange and α decreases, due to the changes in the structural and aggregational properties of the absorbed water. It is confirmed with the increase in $\ln A$ with α , as seen in Fig. 6b.

CONCLUSIONS

The isothermal kinetics of the exchange of water absorbed in a hydrogel with ethanol is a kinetically complex process. The kinetics of the exchange can be completely described by the Brouers, Sotolongo-Costa fractal kinetics model. The values of the parameters of the Brouers, Sotolongo-Costa kinetic model decrease with increasing temperature of exchange. The kinetics limiting stage of the exchange process is the value of the surface area of the boundary phase of interaction. The value of the effective time-dependent rate coefficient of exchange at all the temperatures increases with the duration of exchange. The effective time-dependent rate coefficient at a specific time of exchange increases with increasing temperature. The activation energy of the exchange process increases with the duration of the exchange and with the increase in the degree of exchange. The values of $\ln A$ and the activation energy are interrelated *via* a compensation effect.

Acknowledgement. The present investigations were supported by The Ministry of Education, Science and Technological Development of the Republic of Serbia, under Contract No: 451-03-9/2021-14/ 200051.

ИЗВОД

КИНЕТИКА ИЗМЕНЕ ВОДЕ АПСОРБОВАНЕ У ХИДРОГЕЛУ СИЛИЦИЈУМ-ДИОКСИДА СА ЕТАНОЛОМ: МОДЕЛОВАЊЕ BROUERS И SOTOLONGO-COSTA ФРАКТАЛНЕ КИНЕТИКЕ

БОРИВОЈ К. АДНАЂЕВИЋ¹, НЕБОЈША М. ЦВЕТКОВИЋ² И ЈЕЛЕНА Д. ЈОВАНОВИЋ³

¹Факултет за физичку хемију, Универзитет у Београду, Студентски бр 12–16, б. бр. 137, 11001 Београд, ²Академија струковних студија Јужна Србија-Одсек за пољопривредно прехрамбене студије, Бирица и Методија бр. 1, 18400 Прокуље и ³Институт за општу и физичку хемију, Студентски бр 12–16, 11001 Београд

Испитана је изотермна кинетика измене апсорбоване воде у хидрогелу на бази силицијум-диоксида (SH) са етанолом. Изотермне кинетичке криве измене воде са етанолом измерене су на температури: $T = 297, 306$ и 316 К. Анализирана је зависност брзине измене од времена. Испитана је могућност математичког описивања кинетике измене Brouers и Sotolongo-Costa (BS) моделима фракталне кинетике. Израчунате су вредности параметара (n, τ, β) модела и њихове промене са температуром. Применом Озао методе утврђено је да је брзина процеса измене лимитирана брзином измене апсорбоване воде етанолом. Израчунате су вредности фракталне димензије граничне фазе SH–етанол. Израчунате су и дискутоване промене временски зависног коефицијента брзине, енергије активације и предекспоненцијалног фактора током времена и степена измене. Разматран је предложени модел механизма измене апсорбоване воде са етанолом.

(Примљено 11. јануара, ревидирано 26. маја, прихваћено 31. маја 2021)

REFERENCES

1. A. C. Pierre, G. M. Pajonk, *Chem. Rev.* **102** (2002) 4243 (<http://dx.doi.org/10.1021/cr0101306>)
2. A. Parvathy Rao, A. Venkateswara Rao, *J. Mater. Sci.* **45** (2010) 51 (<http://dx.doi.org/10.1007/s10853-009-3888-7>)
3. V. G. Parale, K.-Y. Lee, H.-H. Park, *J. Korean Ceram. Soc.* **54** (2017) 184 (<http://dx.doi.org/10.4191/kecers.2017.54.3.12>)
4. E. Moretti, F. Merli, E. Cuce, C. Buratti, *Energy Procedia* **111** (2017) 472 (<http://dx.doi.org/10.1016/j.egypro.2017.03.209>)
5. J. E. Amonette, J. Matyáš, *Microporous Mesoporous Mater.* **250** (2017) 100 (<http://dx.doi.org/10.1016/j.micromeso.2017.04.055>)
6. A. Venkateswara Rao, N. D. Hegde, H. Hirashima, *J. Colloid Interface Sci.* **305** (2007) 124 (<http://dx.doi.org/10.1016/j.jcis.2006.09.025>)
7. S. M. Jones, *J. Sol-Gel Sci. Technol.* **40** (2006) 351 (<http://dx.doi.org/10.1007/s10971-006-7762-7>)
8. C. A. McCarthy, R. J. Ahern, K. J. Devine, A. M. Crean, *Mol. Pharm.* **15** (2018) 141 (<http://dx.doi.org/10.1021/acs.molpharmaceut.7b00778>)
9. C.-T. Wang, C.-L. Wu, I.-C. Chen, Y.-H. Huang, *Sensors Actuators, B* **107** (2005) 402 (<http://dx.doi.org/10.1016/j.snb.2004.10.034>)
10. J. L. Gurav, I.-K. Jung, H.-H. Park, E. S. Kang, D. Y. Nadargi, *J. Nanomater.* **2010** (2010) 1 (<http://dx.doi.org/10.1155/2010/409310>)
11. A. Parvathy Rao, A. Venkateswara Rao, G. M. Pajonk, P. M. Shewale, *J. Mater. Sci.* **42** (2007) 8418 (<http://dx.doi.org/10.1007/s10853-007-1788-2>)
12. J. Šesták, *J. Therm. Anal. Calorim.* **110** (2012) 5 (<http://dx.doi.org/10.1007/s10973-011-2089-1>)
13. S. Gaspard, S. Altenor, N. Passe-Coutrin, A. Ouensanga, F. Brouers, *Water Res.* **40** (2006) 3467 (<http://dx.doi.org/10.1016/j.watres.2006.07.018>)
14. F. Brouers, O. Sotolongo-Costa, *Physica, A* **368** (2006) 165 (<http://dx.doi.org/10.1016/j.physa.2005.12.062>)
15. F. Brouers, *J. Mod. Phys.* **05** (2014) 1594 (<http://dx.doi.org/10.4236/jmp.2014.516160>)
16. R. Ozao, M. Ochiai, *J. Ceram. Soc. Japan* **101** (1993) 263 (<http://dx.doi.org/10.2109/jcersj.101.263>)
17. P. Šimon, O. Zmeškal, J. Šesták, in *Thermal analysis of Micro, Nano- and Non-Crystalline Materials. Hot Topics in Thermal Analysis and Calorimetry, Vol. 9*, J. Šesták., P. Šimon, Eds., Springer, Dordrecht, 2012, pp. 247–255 (http://dx.doi.org/10.1007/978-90-481-3150-1_12)
18. W. Siebrand, T. A. Wildman, *Acc. Chem. Res.* **19** (1986) 238 (<http://dx.doi.org/10.1021/ar00128a002>)
19. A. Plonka, A. Paszkiewicz, *J. Chem. Phys.* **96** (1992) 1128 (<http://dx.doi.org/10.1063/1.462199>)
20. R. Grima, S. Schnell, *Biophys. Chem.* **124** (2006) 1 (<http://dx.doi.org/10.1016/j.bpc.2006.04.019>).



J. Serb. Chem. Soc. 86 (9) 831–844 (2021)
JSCS–5465

Correlation between silane concentration and temperature operated toward conductivity of well-synthesized chitosan-fly ash composite membrane

ARIEF RAHMATULLOH^{1*} and LUKMAN ATMADJA²

¹Department of Chemical Engineering, Politeknik Negeri Malang, Indonesia and
²Department of Chemistry, Institut Teknologi Sepuluh Nopember, Surabaya, Indonesia

(Received 18 November 2020, revised 5 May, accepted 18 May 2021)

Abstract: Composite membrane is synthesized using well-synthesized chitosan as matrix crosslink with fly ash as filler and modified using 3-glycidyloxypropyltrimethoxy silane coupling agent. XRD analysis is carried out to characterize fly ash. While, FTIR characterization is conducted to determine the interaction between chitosan matrix and fly ash that has been modified using silane. The emergence of a new absorption at wave numbers 1118.64 cm^{-1} shows the interaction between silane and fly ash. In addition, the widening of OH absorption shows that hydrogen bonds are formed between the silane and chitosan. The interaction is also demonstrated by the evenly distributed hills and valleys on AFM topography analysis. Characterizing the composite membrane with TGA analysis is done to determine thermal stability. While, proton conductivity of the composite membranes are measured using EIS. The highest conductivity values are obtained with the addition of 5 % silane concentration of $2.75 \times 10^{-4}\text{ S cm}^{-1}$ at room temperature, $3.995 \times 10^{-4}\text{ S cm}^{-1}$ at $40\text{ }^\circ\text{C}$, and $3.909 \times 10^{-4}\text{ S cm}^{-1}$ at $60\text{ }^\circ\text{C}$. On the contrary, measurements at $80\text{ }^\circ\text{C}$, decomposition in all composite membranes occur. Thus, the crosslinked composite membrane chitosan–fly ash prepared by silane-crosslinking technique has potential to be applied with polymer electrolyte membrane fuel cell (PEMFC).

Keywords: proton conductivity; 3-glycidyloxypropyltrimethoxy silane; proton exchange membrane fuel cell.

INTRODUCTION

Fuel cell is an electrochemical device that works by reaction of hydrogen and oxygen producing electricity, with water as side product. It consists of two electrodes separated by a polymer membrane that serves as an electrolyte. Membranes in fuel cell applications known as polymer electrolyte membrane (PEM). Membrane PEM fuel cells become the medium which transports hydrogen ions

* Corresponding author. E-mail: arief1289@polinema.ac.id
<https://doi.org/10.2298/JSC201118043R>



produced by the reaction of the anode towards the cathode. Therefore, the cathode reaction can produce electrical energy.¹⁻³

Some of the requirements of good membranes for fuel cells are made from cheap materials resistant to high temperatures. As a result, the proton conductivity and the ability to retain water remain good. Proton conductivity in PEM that applied to the proton exchange membrane fuel cell (PEMFC) is a key component of PEMFC performance which results environmental friendly and power efficient cell for a wide range of different applications.^{1,2}

An alternative membrane material used for polymer fuel cell is chitosan. Chitosan is a well-known biopolymer waste consisting of monomer *N*-acetyl glucosamine (GlcNAc) and also D-glucosamine (GlcN). Chitosan is a hydrophilic material with well-organized chemical structure, inert, and with good conductive properties. Furthermore, chitosan level of toxicity is relatively low. Therefore, chitosan polymeric materials provide good properties for fuel cells. However, low solubility of chitosan in water is a drawback for fuel cell membranes because chitosan becomes waterless. Hence, cross-linking of chitosan with other materials is required in order to improve PEM properties.^{4,5}

In this study, chitosan was cross-linked with inorganic filler fly ash as a modification. Fly ash used was from the coal burning waste of local electric steam power plant. It belongs to class F fly ash. This type of fly ash was chosen due to its high rate of SiO₂ (>70 %) besides Al₂O₃, Fe₂O₃ and CaO. In addition, the SiO₂ played an important role in the process of the cross-linking. Other reasons of choosing class F fly ash was due to its abundant amount and low cost. Besides, the hydrophobic properties of fly ash can reduce methanol crossover when it contacts with water.⁶

Modifications using silane coupling agents on composite membrane chitosan-fly ash were carried out by varying concentrations of silane and operating temperature during conductivity measurements. Silane was chosen because it can create water-resistant bond at the interface between the inorganic filler and the organic matrix (chitosan). Silane coupling agents also have unique chemical and physical properties, not only to enhance the bond strength, but also to prevent debonding at the interface during aging and composite membrane usage. Silane agent can also form a stable bond between two surfaces and increase the thermal stability of the composite membrane.⁷ 3-Glycidyloxypropyltrimethoxy silane (KH-560) was used in this study. This type of silane was selected because epoxy groups from silane can react with free amine group of chitosan and bind strongly with fly ash.^{8,9} Furthermore, at interface, silane can not only form a strong bond but also be more resistant to the presence of water that can destruct composite membrane's structure. In addition, polysiloxane backbone framework enables hydrogen bonds by water. Moreover, from the previous study, it is known that modifications using this type of silane can produce better conductivity than Naf-

ion 117.^{7,9} Therefore, modifications using this coupling agents can increase the conductivity properties of the fuel cell membranes. In addition, it also has a good performance at high temperatures in a PEMFC application.

EXPERIMENTAL

Materials

Composite membranes used in this study were synthesized from shrimp shell waste. While, type F fly ash waste was from local electric steam power plant which is stable at room temperature and characterized by XRD analysis (the dissolution is conducted by DMF). Other chemicals, with purity pro analysis, included were NaOH solution (98 % purity degree, Merck); CH₃COOH (97 % purity degree, Merck); concentrated HCl (98 % purity degree, Merck), distilled water, demineralized aqua, concentrated H₂SO₄ (98 % purity degree, Merck), dimethylformamide (DMF) (98 % purity degree, Merck); 3-glycidyloxypropyltrimethoxy silane (98 % purity degree, Merck).

Instrumentation

This study used several tools to do some experiments such as electric heater, thermometer, pH indicators, cotton fabrics, Buchner funnel, erlenmeyer, petri dish, condenser, magnetic stirrer, a hundred mesh sieve, glass beaker, stirrer ultrasonic, Fourier transform infrared (FTIR) 8400 Shimadzu, atomic force microscopy (AFM) of Bruker and electrochemical impedance spectroscopy (EIS) of Autolab with FRA32M module, X-Ray Diffraction (XRD) of PanAnalytical Expert Pro, Thermogravimetric Analysis (TGA) of Mettler Toledo.

Synthesis of chitosan

Isolation of chitin. The following are the deproteinization steps done in the process of experiment. First, shrimp shell powder was dissolved in 3.5 % NaOH. Next, the mixture was stirred using a magnetic stirrer at 65 °C. Then, the precipitate was separated using a sieve fabric and Buchner funnel. The formed precipitate was washed using distilled water until its pH became neutral and dried in a vacuum oven at a temperature of 100 °C.⁷ After that, ninhydrin test was conducted by giving 10 droplets of 0.1 % ninhydrin solution in the sample solution. Then, it was heated gently for 1–2 min and cooled. The solution changed into purple when the samples still contained proteins.^{5,10} Next step is demineralization phase. In the demineralization phase, the precipitation result of deproteinization process was mixed with 1 M HCl solution. The mixture was stirred using a magnetic stirrer. Then, precipitate was separated using a sieve fabric and Buchner funnel. Next, precipitate was washed using demineralized aqua (aqua DM) until its pH became neutral and dried in a vacuum oven at 100 °C.^{5,10,11}

Transformation chitin into chitosan. To transform chitin into chitosan, precipitation result of demineralization process was mixed with 60 % NaOH solution and heated at a temperature of 120 °C. After that, the precipitate was separated with sieve fabric and Buchner funnel. Then, precipitate was washed with distilled water until its pH became neutral and dried in a vacuum oven at 100 °C. The result of this process was a form of powder called chitosan polymer. Fourier transform infrared (FTIR) was also used in this process to determine deacetylation of chitin into chitosan.¹¹

Fly ash modification using silane coupling agent

In this phase, a total of 1.9 grams of class F fly ash and 0.1 gram of 3-glycidyloxypropyltrimethoxy silane were dissolved in 20 ml of dimethylformamide (DMF) at room temperature and stirred using a magnetic stirrer for 6 h. Then, the homogenized solution was heated using

a vacuum oven at a temperature of 60 °C for 24 h. After that, it was heated again at 100 °C for 1 h and at a temperature of 120 °C for 2 h. The material isolated in this process was in the form of powder. Next, the powder was saturated in 1 M HCl solution at a temperature of 80 °C for 24 h to allow hydrolysis and condensation of the powder. When the step was done, the powder was dried at the room temperature for 24 h. The dry powder was a modified fly ash with silane coupling agent 5 %, and referred to silane concentration 10 and 15 %, they were also modified implementing the same procedure.^{6,9,12} While, XRD analysis was conducted to characterize the fly ash using $\lambda = 1.5418 \text{ \AA}$ radiation.

Variation of concentration

In this phase, 1.5 g of chitosan were dissolved in 2 % of acetic acid. The solution was heated at a temperature of 80 °C. On the other hand, the amount of fly ash with concentration of silane 0, 5, 10 and 15 %, were dissolved in 2 % of acetic acid solution and homogenized with ultrasonic for 30 min. Then, both materials were mixed and stirred at a temperature of 80 °C. After that, the mixture was treated with ultrasonic for 30 min, left for 30 min, and treated again with ultrasonic for 30 min. After the process of degasification, the mixture was flattened on a glass plate, and dried at room temperature for 48 h. Finally, the membrane was soaked in a solution of 2 M H₂SO₄ for 24 h and washed with aqua DM and dried at room temperature for 24 h.^{9,13}

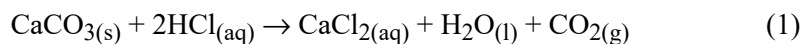
Variation of temperature operating system

Composite membrane chitosan–fly ash with 3-glycidylxypropyltrimethoxy silane concentration of 0, 5, 10 and 15 %, was respectively performed at variation of temperature 40, 60 and 80 °C in the conductivity measurement using EIS.

RESULTS AND DISCUSSION

Isolation of chitin

There were three phases in the isolation of chitin from shrimp shell powder, namely preparation phase, deproteination, and demineralization. The preparation phase was started by grinding shrimp shells using ball mill, and then smoothing it by using 100 mesh sifter. In the deproteination phase, protein was eliminated from shrimp shell powder. The results of this treatment were light brown dry powder that was protein-free. The loss of protein in the process of deproteination was also analysed by ninhydrin test to identify free amino group on the amino acid, peptide or protein in the sample. Ninhydrin is a soft oxidizer that produce a purple dye when it reacts to free amino in the sample. Hidrindantin compound was formed by reacting ninhydrin compound and the carbonyl group of free amino. Furthermore, ninhydrin reacted with hidrindantin and ammonia molecules to form Rheumann's purple and water molecules by heating treatment.¹⁴ Based on the tests, the chitin product contained no protein. Demineralization process was carried out to eliminate minerals that were physically bounded to chitin. The purpose of deproteination and demineralization was to obtain pure intermediate product in order to produce high quality and quantity of chitin at international standard level (chitin with no protein and mineral).¹⁰ Demineralization process was conducted by extracting protein-free powder in 1 M HCl solution:



The presence of frothy bubbles at the time of the addition of HCl was an indicator of the demineralization process. As a result, lighter brown dry powder with a finer texture called chitin was achieved.

Transformation chitin into chitosan

The phase of transforming chitin into chitosan is called deacetylation. In this phase, termination of the bond between carbon and nitrogen in the acetyl group into the amine group occurred. 60 % NaOH was used to break the bond between the acetyl group and nitrogen, resulting the amine group. Deacetylation took place at a temperature of 120 °C for 4 h. Consequently, the reaction occurred quickly and the greater acetyl group was substituted into the amine group.⁵ The mechanism of chitin transformation into chitosan can be seen in Fig. 1.

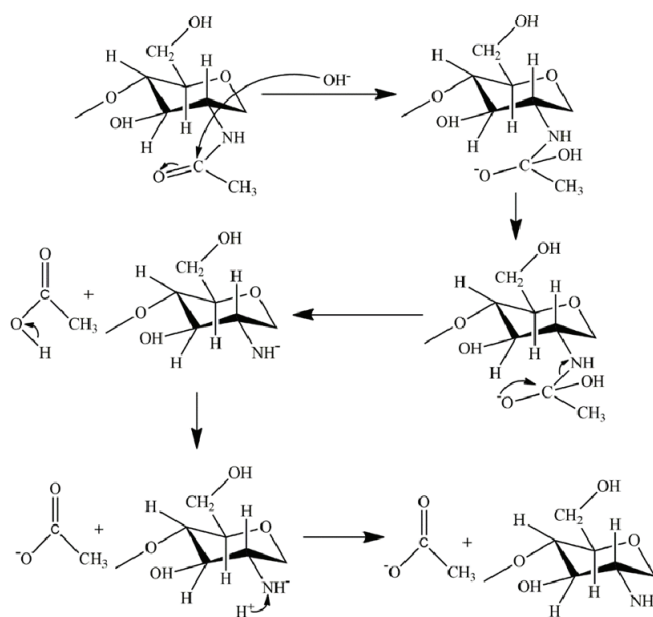


Fig. 1. Transformation mechanism of chitin into chitosan.^{5,15}

The result of the deacetylation process was pure white fine powder called chitosan. Identification using infrared spectroscopy was performed to determine the success of the transformation process of chitin into chitosan and notify that there were specific functional groups on chitin and chitosan. FTIR spectra of chitin and chitosan can be seen in Fig. 2. While, various FTIR absorption of the chitin and chitosan can be seen in Table I.

In Table I and Fig. 2, it can be seen that FTIR spectra of chitin has wide absorption pattern in 3436.91 cm^{-1} absorption peak. This absorption indicates the

presence of OH vibration. Vibration of stretching N–H appears at the absorption peak of 3109.04 cm^{-1} . Another absorption which belongs to aliphatic C–H stretching arises at 2893.02 cm^{-1} . The stretching vibration of N–H arises at 3109.04 cm^{-1} . Another absorption which arises at 2893.02 cm^{-1} indicates the aliphatic stretching of C–H bond. This absorption converges on the OH stretching band. The same condition can be seen on N–H stretching. The stretching vibration of C=O appears at 1658.67 cm^{-1} absorption peak. While the bending vibration of N–H bond arises at 1550.62 cm^{-1} absorption peak. The C–N vibration appears at 1380.94 cm^{-1} . The C–O vibration appears at both absorption peaks of 1072.35 and 1114.78 cm^{-1} . The absorption peak of 2923.88 cm^{-1} indicates the presence of CH_3 vibration. The aforementioned vibrations show the distinctive character of chitin which has the amide groups.

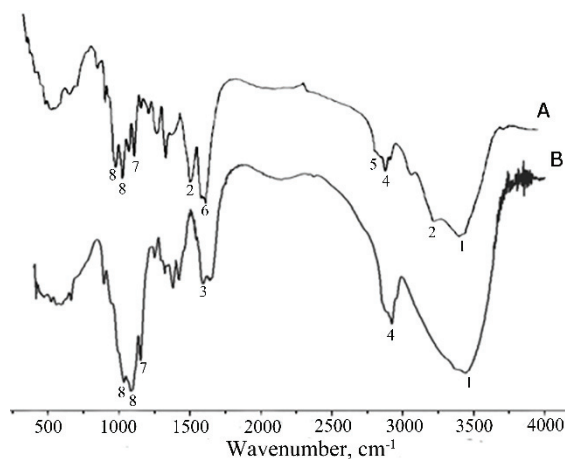


Fig. 2. Spectra FTIR of chitin (A) and chitosan (B).

TABLE I. Wavenumbers (cm^{-1}) of chitin and chitosan FTIR absorption

No.	Vibration type	Compound	
		Chitin	Chitosan
1	OH	3436.91	3446.56
2	N–H ($-\text{NHCOCH}_3$)	3109.04; 1550.62	–
3	N–H ($-\text{NH}_2$)	–	1589.23
4	$-\text{CH}_3$	2923.88	2921.96
5	$-\text{CH}_2-$	2893.02	–
6	C=O	1658.67	–
7	C–N	1380.94	1380.94
8	C–O	–1072.35; 1114.78	1083.92; 1151.42

The spectra of chitosan as the transformed product of chitin also has the OH vibration at 3446.56 cm^{-1} absorption peak. While the stretching vibration of N–H bond arises at $3300\text{--}3250\text{ cm}^{-1}$ absorption peak. However, the stretching vibrat-

ion of N–H bond does not appear on the spectra due to a shift in the vibrational OH. As a result, it overlaps the vibrational of N–H stretching of the amine group. On the chitosan spectra, a new absorption does appear at 1589.23 cm^{-1} which indicates the presence of vibrational of N–H ($-\text{NH}_2$) bending. This absorption is the distinctive characteristic of chitosan. This reveals the substitution of acetyl groups to amine groups during the deacetylation process. This is reinforced by the decrease of the absorption peak intensity from 2923.88 to 2921.96 cm^{-1} which shows the vibrational stretching of the C–H group. The absorption peak of 1421.44 and 1380.94 cm^{-1} are the vibrational of C–H bending and C–N, respectively. The vibration of C–O bond appears at 1083.92 and 1151.42 cm^{-1} . Based on the analysis degree of deacetylation of the chitosan, deacetylation degree is obtained at 86.311% . This indicates that the obtained chitosan has good properties because it has a degree of deacetylation values above 70% .

Modified fly ash using silane coupling agents

The initial stage of fly ash modification utilizing silane was achieved by adding up silane at different concentration (0; 5; 10; 15 %) to fly ash. The added epoxy group was directly proportional with the silane concentration. Then, the mixture was dissolved in dimethylformamide (DMF) and stirred to form homogeneous solution. In the initial stage, hydrolysis reaction occurred between silane and water in fly ash (2.033 mass %). The reaction formed silanol and methanol as byproducts. The next step was the condensation polymerization process conducted by heating the solution in an oven. In this process, the monomers incorporated each other to form polymer by releasing water molecules. Thus, an oxane bond was formed among silanes to provide multimolecular structure. Moreover, the mixture was heated at a temperature of $100\text{ }^\circ\text{C}$ for 1 h and $120\text{ }^\circ\text{C}$ for 2 h. This treatment was intended in order that the silane could coordinate with the fly ash surface by forming hydrogen bonds and releasing water molecules. As a result, polysiloxane network was formed between fly ash filler and silane. The final process was soaking the generated powder in 1 M HCl solution aimed to dissolve the compounds in fly ash besides SiO_2 . The compounds are Al_2O_3 ; Fe_2O_3 ; CaO , which were dissolved in acid. This process also aimed to form strong polysiloxane network between fly ash and silane. In addition, the process could spread the network further from the surface. Another aim of HCl treatment is to make the surface area of fly ash become wider. As consequence, the working area of fly ash become bigger. This fact is confirmed with Sarbak and co-workers, who modified fly ash with HCl. Their study revealed that fly ash treated with HCl has the widest surface area. The epoxy group from silane coupling agent was broken off to form hydrogen bond with amine group from chitosan. As a result, the structure of composite membrane became rougher and was directly proportional to the concentration of the added silane. Moreover, the

existence of polysiloxane network indicated that the modifications were successfully carried out.^{6,16,17} The result of fly ash characterization using XRD can be seen in Fig. 3.

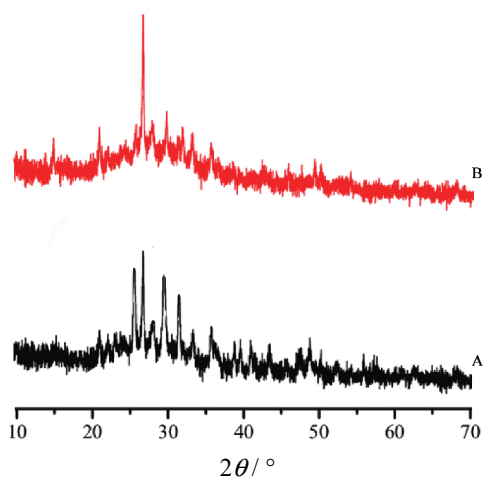


Fig. 3 XRD analysis of raw fly ash (A) and modified fly ash (B).

Fig. 3 illustrates that the XRD analysis of raw fly ash has main crystalline phases which are quartz and mullite (Fig 3A). The quartz crystalline appears at 28° and belongs to silica (SiO_2). The intensity of quartz crystalline indicates that silica has the highest rate in term of content of fly ash. While mullite appears at $26\text{--}28^\circ$ and $30\text{--}32^\circ$ appertains to alumina (Al_2O_3). In addition, the existence of hematite and lime occurs in amorphous forms at 34 and 37° , respectively. These amorphous forms belong to Fe_2O_3 and Calcium Oxide (CaO). While the modified fly ash has one crystalline phase, namely quartz with higher intensity at 28° . The higher intensity of quartz crystalline results from interaction with silane coupling agent forming polysiloxane network. The absence of mullite (Al_2O_3), hematite (Fe_2O_3) and lime (CaO) at the XRD patterns is due to the HCl treatment on fly ash. The acid dissolve the compounds of Al_2O_3 ; Fe_2O_3 ; CaO . Dana and co-workers amplified those statements by declaring that the XRD patterns of fly ash is dominated by the presence of large proportion of silica in the form of quartz crystalline. Furthermore, mullite representing alumina is the second large proportion in XRD patterns of fly ash. The hematite and CaO are also found in XRD patterns with very low intensity.¹⁸

Preparation of composite membrane chitosan-fly ash

Composite membranes were made from chitosan with fly ash integration. Fly ash was modified with various silane concentrations of 0, 5, 10 and 15 %. The ratio of chitosan and modified fly ash at the composite membrane was 70:30. The literature^{13,16} stated that this ratio of fly ash filler reached the amount of chito-

san matrix. The presence of acetic acid on this process becomes important because it can dissolve chitosan and modify fly ash perfectly. As a result, it can form fine composite. Another goal of acetic acid treatment is to make the chitosan good proton conductor. When chitosan is dissolved in acetic acid and printed in sheet form then, H^+ and CH_3COO^- of acetic acid are dispersed in the chitosan solvent and can be mobilized under an electric field. If it contains more H^+ which move in the membrane, it will become good proton conductor. While, in the modified fly ash solution, an ultrasonic treatment was carried out to make collision among molecules and produce homogeneous mixture that mixed with chitosan solution. Then, the mixed solution was heated at $80\text{ }^\circ\text{C}$ and stirred using a magnetic stirrer to form homogeneous solution. Hence, a perfect interaction can be formed between the two materials. Moreover, the solution was treated with ultrasonic for 30 min, left for 30 min and treated with ultrasonic again for 30 min. This repeated ultrasonic treatment is intended for maximum interaction between the chitosan matrix and modified fly ash. In addition, it can also turn the solution into a gel form. After the gel was formed, it was placed on a flat and clean glass for membrane printing process. Then, the molded membrane was dried at room temperature for 48 h to remove the residual acetic acid. Next, the dry membrane was immersed in 2 M sulfuric acid solution, this immersion was intended to make a cross-linking process between chitosan matrix and modified fly ash. As a result, the interaction between them is optimal. Another aim of sulfuric acid treatment was to change the chitosan matrix to become polycationic. Thus the amine group in chitosan can donate its electrons. The generated composite membrane was in the form of brownish yellow plastic sheets with various concentration of silane as shown in Fig. 4. It can be seen that the chitosan–fly ash composite membrane with silane concentration of 0 % (Fig. 4A) has darker brownish yellow membrane surface than the others. The pure fly ash filler reacts successfully with chitosan to makes the color of chitosan on the membrane less dominant. 5 % silane concentration found in fly ash filler (Fig. 4B) makes the color of the membrane brighter and the surface of the membrane more plastic

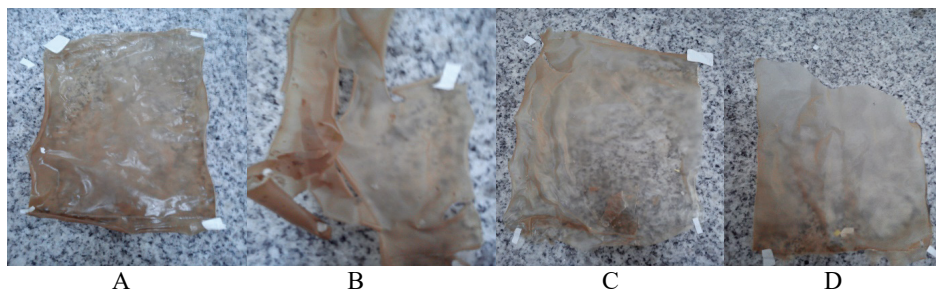


Fig. 4. Chitosan–fly ash composite membrane with: A – 0; B – 5; C – 10 and D – 15 % silane concentration.

than composite chitosan–fly ash with no silane. When the silane concentration in composite membrane is 10 % (Fig. 4C), the color of the membrane is brighter and more plastic than the membrane with a concentration of 5 and 0 % silane. As a result, the composite membrane with concentration of 10 % silane is not easily damaged when immersed in water. On the other hand, the composite membrane with concentration of 15 % silane (Fig. 4D) has the brightest color of membrane surface and the most plastic among the others. In addition, it is more resistant to the presence of water.^{9,16}

Variation of concentrations

The measurements of proton conductivity at room temperature by using the EIS is shown in Table II. The table illustrates the addition of silane concentration effect on membrane conductivity. Composite membrane – 5 % silane has the highest conductivity among the others, because the added amount of silane is suitable to the strong binding amine group of chitosan and form a polysiloxane network with fly ash. Meanwhile, on composite membrane – 10 % silane and composite membrane – 15 % silane, the hydrogen bonds between the silane and chitosan as well as the polysiloxane network become saturated. Consequently, it cannot facilitate proton conduction optimally. As a result, the proton conductivity decreases. On the system, chitosan–fly ash composite membrane which is modified with silane coupling agent, have two factors that influence proton conductivity. These two factors are: *i*) the presence of polysiloxane network which can form a water-bound membrane layer to facilitate proton hopping. The proton hopping mechanism is the mechanism of transferring proton across the membrane which determines the conductivity of membrane; *ii*) a strong hydrogen bond formed between the amine groups in chitosan and the epoxy on the silane ensures a high proton conduction.^{4,19}

This fact is confirmed by Lin and co-workers, who modified sulfonated poly (ether ketone ether arylene) containing a carboxyl group (SPAEEK-C) using 3-glycidyloxypropyltrimethoxy silane coupling agent. Their study revealed that in general, the conductivity of composite membrane declined along with the rise of 3-glycidyloxypropyltrimethoxy silane concentration. This condition is associated with low water absorption and ion exchange. Even, for 10 % concentration of 3-glycidyloxypropyltrimethoxy silane, the conductivity value is lower than pure SPAEEK-C. The appropriate polysiloxane network is formed by the addition of 5 % 3-glycidyloxypropyltrimethoxy silane concentration. Then, the addition of 5 % 3-glycidyloxypropyltrimethoxy silane concentration on composite membrane leads to high conductivity values. Then, the high amount of sulfonic acid, causes the occurrence of high proton conduction. On the other hand, the back chain of polysiloxane and the $-\text{CH}_2\text{CH}_2\text{O}-$ linkage can form a water-bound membrane layer to facilitate proton hopping.⁹

TABLE II. Proton conductivity value of composite membrane chitosan - fly ash with various silane concentrations at room temperature

Silane concentration, %	R / Ω	L / cm	A / cm^2	$\sigma \times 10^4 / \text{S.cm}^{-1}$
0	119.100	0.024	1	2.01
5	112.790	0.031	1	2.75
10	99.425	0.012	1	1.21
15	99.335	0.021	1	2.11

Variation of temperature operating system

The conductivity measurement of composite membrane using EIS at various temperatures is shown in Fig. 5. It shows that the operating temperature affects the performance of the composite membrane. At the same temperature with different silane concentrations, generally the conductivity value of the composite membrane is lower than it is at room temperature.

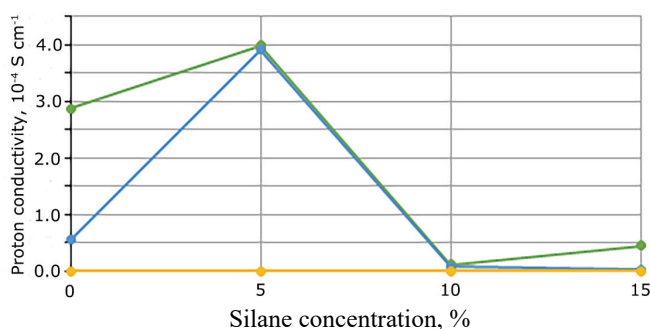


Fig. 5. Proton conductivity values of composite membrane chitosan - fly ash with various silane concentrations at various temperatures: ● 40, ● 60 and ● 80 °C.

At the same concentration with different temperatures, in general, the conductivity value decline. It is interesting that the value conductivity of composite membrane with – 5 % silane increases and it is relatively stable against temperature changes. This is related to strong interaction that is formed between silane and chitosan as well as to secure silane and fly ash cross-linking.

Fig. 5 also illustrates that at a temperature of 80 °C all membranes have no conductivity values because the membranes are shattered and dissolved at that temperature. The destruction of the membranes at high temperature are due to the broken linkage of hydrogen bonds as well as to the polysiloxane network formed between the chitosan matrix and fly ash filler with or without silane. As consequence, whether with or without the silane coupling agent, the composite membranes are decomposed. This fact indicates that the composite membranes cannot work at temperature of 80 °C. The chitosan–fly ash composite membranes with silane coupling agent has an operating temperature limit of 60 °C. However, the membranes can be utilized for proton exchange membrane fuel cell applications.

Sopian and co-workers reinforced this fact by revealing that the minimum condition for a membrane to be utilized in the proton exchange membrane fuel cell application is the membrane operated at 60 °C.¹

CONCLUSIONS

The interactions between chitosan–fly ash with silane can be confirmed in the FTIR spectra with the widening of OH absorption and the emergence of new absorption at wave number 1118.64 cm⁻¹. In the XRD analysis, the interaction between fly ash and silane coupling agent can be confirmed by higher intensity of SiO₂ quartz crystalline phase at modified fly ash than raw fly ash on XRD patterns. In the analysis using AFM, the interaction can be identified by the presence of hills or valleys on the surface of the composite membrane. TGA analysis shows that the composite membranes have two patterns of decomposition which occur at 220 and 270 °C. In general, the correlation of silane concentration on the membrane conductivity takes place when the concentration of silane in composite membrane increases. Such a condition, then decreases the membrane conductivity. Generally, the correlation operating temperature of the membrane conductivity is that when the operating temperature increases, it will decrease the conductivity of the membrane. Membrane, for PEMFC application, has to operate at a minimum temperature of 60 °C as a prerequisite. Hence, crosslinked composite membrane chitosan–fly ash prepared by silane-crosslinking technique has a potential for application of PEMFC because it can be operated at a temperature of 60 °C with high conductivity value and is thermally stable within the temperature range for PEMFC applications.

SUPPLEMENTARY MATERIAL

Additional data are available electronically at the pages of journal website: <https://www.shd-pub.org.rs/index.php/JSCS/index>, or from the corresponding author on request.

ИЗВОД

КОРЕЛАЦИЈА ИЗМЕЂУ КОНЦЕНТРАЦИЈЕ СИЛАНА И РАДНЕ ТЕМПЕРАТУРЕ У ЦИЉУ ПОБОЉШАЊА ПРОВОДЉИВОСТИ ХИТОЗАН–ЛЕТЕЋИ ПЕПЕО КОМПОЗИТНЕ МЕМБРАНЕ

ARIEF RAHMATULLOH¹ и LUKMAN ATMADJA¹

¹Department of Chemical Engineering, Politeknik Negeri Malang, Indonesia и ²Department of Chemistry, Institut Teknologi Sepuluh Nopember, Surabaya, Indonesia

Композитна мембрана је синтетисана коришћењем хитозана као матрице за умрежавање са летећим пепелом као пуниоцем који је модификован коришћењем 3-глицидилоксипропилтриметоксисилана. Летећи пепео је окарактерисан методом дифракције X-зрачења. Применом инфрацрвене спектроскопије са Фуријеовом трансформацијом испитивана је интеракција између матрице хитозана и летећег пепела која је модификована силианом. Појава нове траке на 1118,64 cm⁻¹ потврда је интеракције између силиана и летећег пепела. Додатно, ширење траке која потиче од ОН апсорпције указује на формирање водоничне везе између силиана и хитозана. Интеракција је такође потврђена равно-

мерном распodelom uzvišene i udolina u AFM topografskoj analizi. Karakterizacija kompozitne membrane termogravimetrijskom analizom je urađena da bi se utvrdila termalna stabilnost, a protonska provodljivost kompozitne membrane je merena pri-
menom elektrohemijske impedančne spektroskopije. Najveće vrednosti provodli-
vosti su dobiјene dodatkom 5 % silana i to $2,75 \times 10^{-4} \text{ S cm}^{-1}$ na sobnoj temperaturi,
 $3,995 \times 10^{-4} \text{ S cm}^{-1}$ na $40 \text{ }^\circ\text{C}$ i $3,909 \times 10^{-4} \text{ S cm}^{-1}$ na $60 \text{ }^\circ\text{C}$. Suprotno, pri merenima na $80 \text{ }^\circ\text{C}$
došlo je do dekompozicije svih kompozitnih membrane. Prema tome, umrežena kom-
pozitna membrana hitozan-lетећи pepeo ima potencijala za primenu u gorivim ћели-
јама са полимерним мембранама (PEMFC).

(Примљено 18. новембра 2020., ревидирано 5. маја, прихваћено 18. маја 2021)

REFERENCES

1. K. Sopian, W. R. Wan Daud, *Renew. Energy* **31** (2006) 719
(<https://dx.doi.org/10.1016/j.renene.2005.09.003>)
2. W. Lü, Z. Liu, C. Wang, Z. Mao, M. Zhang, *Chinese J. Chem. Eng.* **18** (2010) 856
([https://dx.doi.org/10.1016/S1004-9541\(09\)60139-7](https://dx.doi.org/10.1016/S1004-9541(09)60139-7))
3. Q. Tang, H. Cai, S. Yuan, X. Wang, W. Yuan, *Int. J. Hydrogen Energy* **38** (2013) 1016
(<https://dx.doi.org/10.1016/j.ijhydene.2012.10.107>)
4. V. Neburchilov, J. Martin, H. Wang, J. Zhang, *J. Power Sources* **169** (2007) 221
(<https://dx.doi.org/10.1016/j.jpowsour.2007.03.044>)
5. C. K. S. Pillai, W. Paul, C. P. Sharma, *Prog. Polym. Sci.* **34** (2009) 641
(<https://dx.doi.org/10.1016/j.progpolymsci.2009.04.001>)
6. M. Ahmaruzzaman, *Prog. Energy Combust. Sci.* **36** (2010) 327
(<https://dx.doi.org/10.1016/j.pecs.2009.11.003>)
7. Y. Xie, C. A. S. Hill, Z. Xiao, H. Militz, C. Mai, *Compos., A* **41** (2010) 806
(<https://dx.doi.org/10.1016/j.compositesa.2010.03.005>)
8. F. Tan, X. Qiao, J. Chen, H. Wang, *Int. J. Adhes. Adhes.* **26** (2006) 406
(<https://doi.org/10.1016/j.ijadhadh.2005.06.005>)
9. H. Lin, C. Zhao, W. Ma, K. Shao, H. Li, Y. Zhang, H. Na, *J. Power Sources* **195** (2010) 762
(<https://dx.doi.org/10.1016/j.jpowsour.2009.08.020>)
10. M. N. V. Ravi Kumar, *React. Funct. Polym.* **46** (2000) 1
([https://dx.doi.org/10.1016/S1381-5148\(00\)00038-9](https://dx.doi.org/10.1016/S1381-5148(00)00038-9))
11. M. Kurniasih, D. Windy Dwiasi, *Molekul* **2** (2007) 79
(<http://dx.doi.org/10.20884/1.jm.2007.2.2.36>)
12. R. Anuradha, V. Sreevidya, R. Venkatasubramani, *Asian J. Chem.* **25** (2013) 1095
(<http://dx.doi.org/10.14233/ajchem.2013.13522>)
13. M. Monroy-Barreto, J. C. Aguilar, E. Rodríguez de San Miguel, A. L. Ocampo, M. Muñoz, J. de Gyves, *J. Memb. Sci.* **344** (2009) 92
(<https://dx.doi.org/10.1016/j.memsci.2009.07.039>)
14. M. Fan, Q. Hu, K. Shen, *Carbohydr. Polym.* **78** (2009) 66
(<https://dx.doi.org/10.1016/j.carbpol.2009.03.031>)
15. M. R. Kasaai, *Carbohydr. Polym.* **71** (2008) 497
(<https://dx.doi.org/10.1016/j.carbpol.2007.07.009>)
16. Y. F. Yang, G. S. Gai, Z. F. Cai, Q. R. Chen, *J. Hazard. Mater.* **133** (2006) 276
(<https://dx.doi.org/10.1016/j.jhazmat.2005.10.028>)
17. Z. Sarbak, M. Kramer-Wachowiak, *Powder Technol.* **123** (2002) 53
([https://dx.doi.org/10.1016/S0032-5910\(01\)00431-4](https://dx.doi.org/10.1016/S0032-5910(01)00431-4))

18. K. Dana, S. Das, S. K. Das, *J. Eur. Ceram. Soc.* **24** (2004) 3169
(<https://dx.doi.org/10.1016/j.jeurceramsoc.2003.10.008>)
19. P. Pei, M. Wang, D. Chen, P. Ren, L. Zhang, *Prog. Nat. Sci. Mater. Int.* **30** (2020) 751
(<https://dx.doi.org/10.1016/j.pnsc.2020.08.015>).

SUPPLEMENTARY MATERIAL TO
**Correlation between silane concentration and temperature
operated toward conductivity of well-synthesized chitosan-fly
ash composite membrane**

ARIEF RAHMATULLOH^{1*} and LUKMAN ATMADJA²

¹Department of Chemical Engineering, Politeknik Negeri Malang, Indonesia and

²Department of Chemistry, Institut Teknologi Sepuluh Nopember, Surabaya, Indonesia

J. Serb. Chem. Soc. 86 (9) (2021) 831–844

INTERACTION BETWEEN MATRIX CHITOSAN AND FLY ASH FILLER

Fourier transform infrared (FTIR)

FTIR spectra of chitosan – fly ash composite membranes with different concentrations of silane is shown in Figure S-1. While various FTIR absorbances in the chitosan – fly ash composite membrane can be seen in Table S-1.

TABLE S-I. Various wavenumber of chitosan – fly ash composite membrane FTIR absorption with various silane concentration

No.	Vibration type	Wavenumber, cm ⁻¹	
		0 % (w/v) of silane	5, 10 and 15 % (w/v) of silane
1	–OH (broad)	3419.56	3458.13; 3463.92
2	–NH ₂	1631.67; 1529.45	1631.67; 1612.38; 1531.37; 1529.45
3	–CH ₂	2788.88	-
4	C–O	1000.99	1014.49; 1116.71; 1118.94
5	–C–N	1305.72; 1382.87	1309.58; 1380.94
6	Si–O–Si	621.04	432.03
7	Al–O (Al ₂ O ₃)	480.24	472.53
8	Si–O		457.1; 472.53

Table S-I and Fig. S-1 illustrate typical band characteristics for chitosan, the typical bands are stretching –OH bond, bending –NH₂ bond, –CH₂ bond, and stretching CO bond appearing at wave numbers 3419.56 cm, 1631.67 cm, 1529.45 cm, 2788.88 cm, and 1000.99 cm⁻¹ respectively, (see Fig. S-1A). Typical fly ash bands also appear at wave numbers 621.04 and 480.24 cm⁻¹ respectively showing the presence of Si–O–Si symmetric stretching and vibrations of

* Corresponding author. E-mail: arief1289@polinema.ac.id

aluminum oxide (see Fig. S-1A). In the Fig. 4, it can be seen that the $-OH$ absorption is getting wider. This shows an interaction between the chitosan matrix and fly ash (Fig. S-1A), and the chitosan matrix with silane coupling agent through the formed hydrogen bonds (see Fig. S-1B; S-1C and S-1D). Meanwhile, the interaction between fly ash and silane coupling agent can be seen by the altering wavenumber of the siloxane ($Si-O-Si$) absorption from 621.04 to 432.03 cm^{-1} . This condition is reinforced by the presence of strong enough bend of $Si-O$ bond which appears in the wavenumbers 457.1 and 472.53 cm^{-1} (see Fig. S-1B; S-1C and S-1D)^{1,2}.

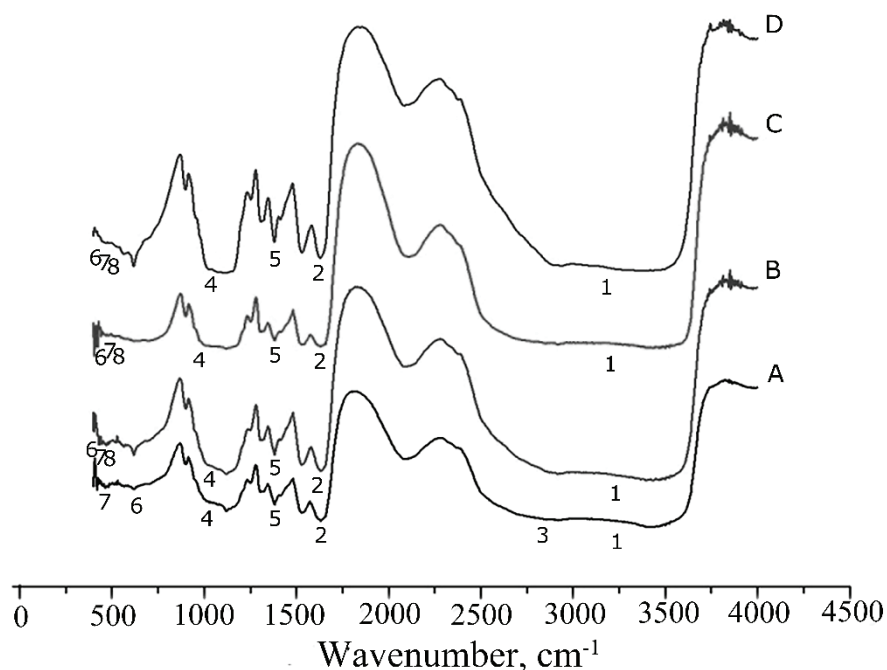


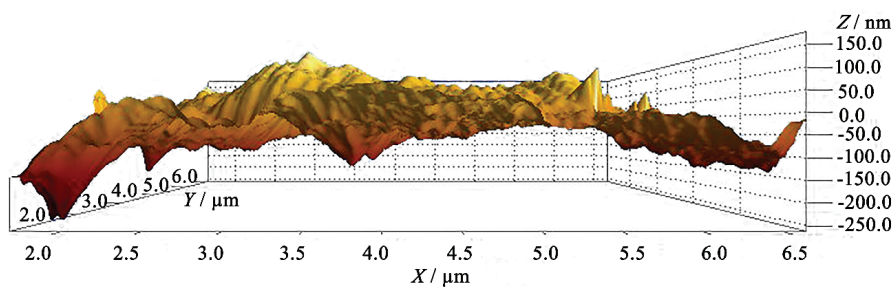
Fig. S-1. FTIR spectra composite membrane with various silane concentration variation; A - 0; B - 5; C - 10 and D - 15 %.

Atomic force microscopy (AFM)

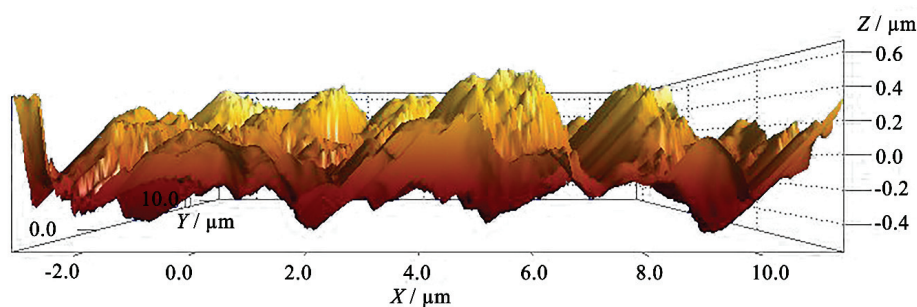
The results of analysing composite membrane chitosan–fly ash surface topography can be seen in Fig. S-2. It shows that the topography of membrane chitosan– fly ash contains hills and valleys which indicates that an interaction among chitosan, silane and fly ash occurs. The presence of silane in composite membranes causes hills and valleys become more numerous and evenly distributed. This indicates that there were strong interactions, not only between chitosan and silane but also between fly ash and silane. Nevertheless, if there is an excessive amount of silane (15 %), the hills and valleys on the surface of the

membrane is reduced noticeably because the interactions among chitosan, fly ash and silane become saturated.

A



B



C

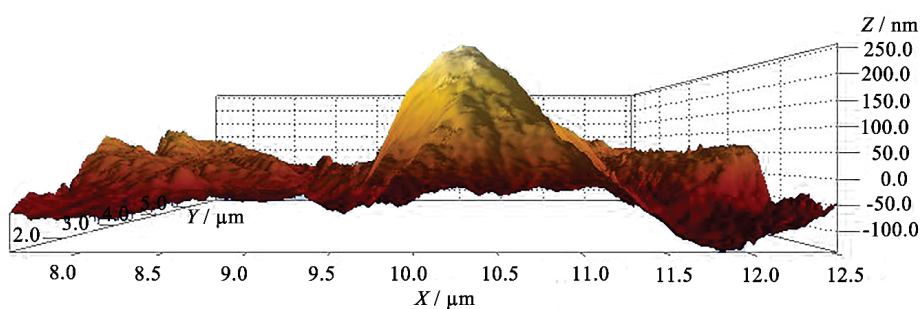


Fig. S-2. Topography analysis of composite membrane chitosan - fly ash with various silane concentrations (A) 0 % (B) 5 % (C) 15 % using AFM.

A similar study was carried out by Enescu and co-workers, who synthesized chitosan- γ -glycidoxypropyltrimethoxysilane (GPTMS) composite membrane. The results of their AFM analysis showed that pure chitosan membranes have flat membrane surface. Whereas, composite membrane of chitosan-GPTMS has rough surface topography with the appearance of hills and valleys on the surface.

Those hills and valleys emerge because of the presence of GPTMS which interacts with chitosan as a membrane matrix.³

Interface interaction among chitosan, silane and fly ash is shown in Fig. S-3. It can be seen that the compatibility between the surface of chitosan and fly ash is a key issue in determining the final membrane property and performance. While, the transitional phase is expected to occur between organic and inorganic phases to improve the interface morphology in the composite membrane. In this study, the function of organosilane of silane agent is to modify the surface of fly ash and create the desired transitional phase. Aryloxy group (RO-, R-CH₃ or CH₃CH₂) on silane can be hydrolyzed to the silanol groups (Si-OH) and to polymerized condensation as well to form oxane bond between silane with one another on the fly ash surface. After the modification, organosilane group (-CH₂-CH₂-CH₂-Si≡) interacts with SiO₂ on the surface of fly ash to form a polysiloxane network. When the modified fly ash is blended with chitosan, hydroxyl group (-OH) will interact with the amine group (NH₂) on chitosan to form hydrogen bonds. As a result, the transitional phase with good flexibility can be produced, because the hydrogen bonds can create interface between chitosan and fly ash which has compatible properties.^{1,4}

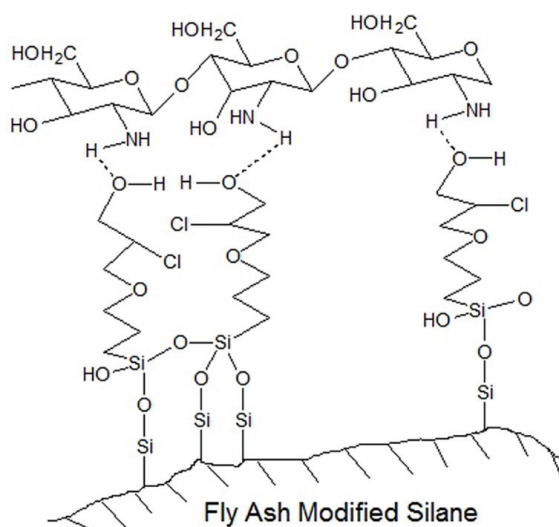


Fig. S-3. Interface interaction in composite membranes chitosan–fly ash modified silane.

TGA test was performed to find out the thermal stability of chitosan-fly ash composite membrane. The result of TGA analysis of composite membrane is shown in Fig. S-4.

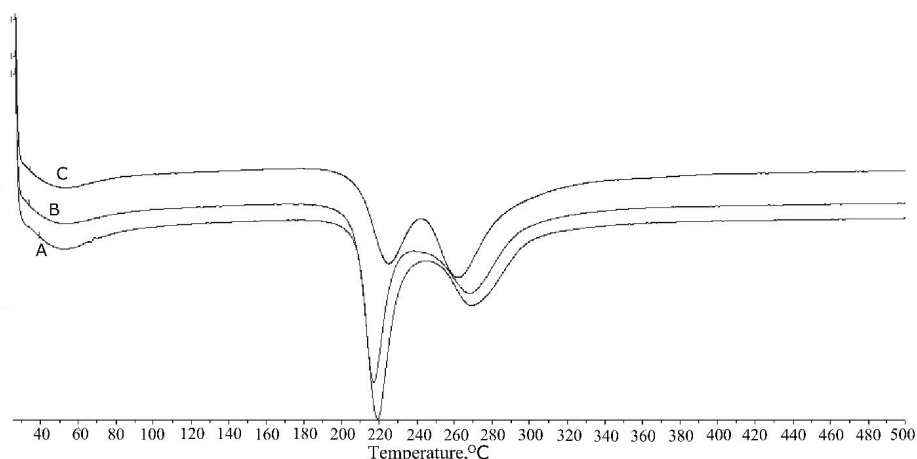


Fig. S-4. Thermogram of mass data of composite membrane chitosan – fly ash modified with silane A - 0, B – 5 and C - 15 %.

Based on Fig. S-4, it can be seen that the composite membrane of chitosan–fly ash has two decomposition patterns. The first decomposition occurs at 220°C, which is generated by the release of hydrogen bonds between the amine groups on chitosan and epoxy group on the silane for composite membranes with 5 and 15 % silane. While in composite membranes with 0% silane, first decomposition is generated by the release of hydrogen bonds between the amine groups on chitosan and silica groups on fly ash. From the figure, it also can be seen that the silane concentration in the composite membrane also affects the sharpness of the thermogram spectra. This is because the presence of silane in the composite membrane can make strong hydrogen bond between the silane and the chitosan matrix. The aforementioned fact reinforced by Zawadzki *et al.*⁵ who conducted a research on thermal analysis of chitosan in various conditions. The result of the study showed that chitosan decomposition started to take place at temperatures above 180 °C due to the broken hydrogen bonds.⁵

The second decomposition related to chitosan chain breakdown polymer due to the dehydration at high temperatures occurs at a temperature of about 270 °C. In addition, temperature of 270 °C, is also related to the elimination of the polysiloxane network formed between silane and fly ash. Thermogram spectra which is constant at temperatures above 270 °C indicates that the composite membrane has completely decomposed. The literature confirmed the second decomposition. It revealed that at a temperature of 274 °C, the decomposition is associated with polymer chain breakdown from chitosan due to the dehydration at high temperatures.⁵ Another research was conducted by Lin and co-workers¹ on thermal analysis of hybrid membrane between sulfonated poly (ketone ether arylene ether) hybrid membranes bearing a carboxyl group (SPA EK-C) utilizing

silane coupling agent (3-glycidyloxypropyltrimethoxy silane). The results of the study showed that in a temperature range of 250 – 350 °C, the decomposition is associated with the destruction of the siloxane groups in the silane.¹

REFERENCES

1. H. Lin, C. Zhao, W. Ma, K. Shao, H. Li, Y. Zhang, H. Na, *J. Power Sources* **195** (2010) 762 (<https://dx.doi.org/10.1016/j.jpowsour.2009.08.020>)
2. Y. Wen, Z. Tang, Y. Chen, Y. Gu, *Chem. Eng. J.* **175** (2011) 110 (<https://dx.doi.org/10.1016/j.cej.2011.09.066>)
3. D. Enescu, V. Hamciuc, R. Ardeleanu, M. Cristea, A. Ioanid, V. Harabagiu, B. C. Simionescu, *Carbohydr. Polym.* **76** (2009) 268 (<https://dx.doi.org/10.1016/j.carbpol.2008.10.026>)
4. H. Wu, B. Zheng, X. Zheng, J. Wang, W. Yuan, Z. Jiang, *J. Power Sources* **173** (2007) 842 (<https://dx.doi.org/10.1016/j.jpowsour.2007.08.020>)
5. J. Zawadzki, H. Kaczmarek, *Carbohydr. Polym.* **80** (2010) 394 (<https://dx.doi.org/10.1016/j.carbpol.2009.11.037>).



J. Serb. Chem. Soc. 86 (9) 845–857 (2021)
JSCS–5466

Fluoride ion conductivity of solid solutions $K_xPb_{0.86-x}Sn_{1.14}F_{4-x}$

YULIJA POHORENKO^{1*}, ROMAN PSHENYCHNYI², TAMARA PAVLENKO¹,
ANATOLIY OMEL'CHUK¹ and VOLODYMYR TRACHEVSKYI³

¹*V.I. Vernadskii Institute of General and Inorganic Chemistry of the Ukrainian NAS, 32–34 Acad. Palladina Ave., 03142 Kyiv, Ukraine,* ²*Sumy State University, Rymkogo-Korsakova st. 2, 40007 Sumy, Ukraine* and ³*G.V. Kurdyumov Institute of Metal Physics of the Ukrainian NAS, Bulvar Vernadskoho 36, 03142 Kyiv, Ukraine*

(Received 24 November 2020, revised 31 March, accepted 7 April 2021)

Abstract: The electrical conductivity of solid solutions with tetragonal syngony formed in $0.86(xKF-(1-x)PbF_2)-1.14SnF_2$ systems has been studied by ¹⁹F-NMR and impedance spectroscopy. It was found that the $Pb_{0.86}Sn_{1.14}F_4$ phase is characterized by better values of fluoride-ion conductivity than the β - $PbSnF_4$ compound. It was found that the substitution of Pb^{2+} by K^+ up to $x = 0.07$ in the structure of $Pb_{0.86}Sn_{1.14}F_4$ contributes to increase in electrical conductivity by an order of magnitude relative to the original $Pb_{0.86}Sn_{1.14}F_4$. The sample of composition $K_{0.03}Pb_{0.83}Sn_{1.14}F_{3.97}$ has the highest electrical conductivity ($\sigma_{600} = 0.38 \text{ S cm}^{-1}$, $\sigma_{330} = 0.01 \text{ S cm}^{-1}$). The fluoride anions in the synthesized samples of $K_xPb_{0.86-x}Sn_{1.14}F_{4-x}$ solid solutions occupy three structurally non-equivalent positions. It is shown that with increasing temperature, there is a redistribution of fluorine anions between positions in the anion lattice, which results in an increase in the concentration of highly mobile fluoride ions, which determine the electrical conductivity of the samples.

Keywords: solid electrolytes; lead and tin fluorides; heterovalent substitution; impedance spectroscopy; ¹⁹F-NMR spectroscopy.

INTRODUCTION

Fluoride-conducting compounds in the solid state have the potential to be used in electrochemical devices,^{1–3} such as sensors,^{4–6} ion-selective electrodes,^{7,8} primary and secondary fluoride ion batteries, *etc.*^{3,9} The effective usage of these devices depends on the right choice of electrode and electrolyte materials, the combination of which ensures rapid charge transfer by fluorine anions at the electrode–electrolyte interface. According to expert estimates, the theoretical specific energy of electrochemical power sources of this type can reach about 5 kWh dm^{-3} depending on the combination of electrode and electrolyte

*Corresponding author. E-mail: pogorenkoyulija@gmail.com
<https://doi.org/10.2298/JSC201124031P>

materials.^{10–12} Fluoride ion conducting phases with mixed ion–electronic conductivity,¹² which contain compounds of metals that are able to reversibly change the oxidation state, promise much as electrode materials. Electrolyte materials must ensure a high rate of charge (fluoride ion) transport. In view of this, much attention has been paid to the search for new compounds with high unipolar fluoride ion conductivity, with the fluoride ions retaining their composition and structure over a wide temperature range.

Complex fluorides of bivalent metals (Ca, Ba, Mg, Pb, Sn) and trivalent metals (Y, Sm, Nd, Ce, La), the lattice of which correspond to the fluorite or tysonite structural type, are attractive in this respect.^{1,13,14} The fluorides of the above elements are prone to form isovalent or aliovalent substitution solid solutions with the retention of original structural type over a wide temperature range, which contributes to increase in the concentration of defects (interstitial ions, vacancies, *etc.*) in the lattice and hence to an improvement of the conduction properties.

Aliovalent substitution solid solutions based on PbSnF_4 and BaSnF_4 fluorides are the subject of much attention. At as low as room temperature, they are characterized by high values of unipolar conductivity (10^{-2} – 10^{-5} S cm^{-1}), which is provided by fluoride anions.^{15–18} As of today, the effect of substitution of a part of the lead cations by trivalent metal cations on the conductivity of PbSnF_4 has been fairly thoroughly studied.¹⁹ For instance, it was found that when up to 20 mol. % Pb^{2+} is substituted by Ln^{3+} ($\text{Ln} = \text{Y, La, Ce, Nd, Sm, Gd}$) in the PbSnF_4 structure, the electrical conductivity of the solid solutions formed in these cases are much higher compared with original PbSnF_4 . The solid solutions containing 10.0–15.0 mol. % LnF_3 have the maximum conductivity.^{20,21}

The substitution of a part of the lead ions by potassium ions contributes to increase in electrical conductivity relative to $\beta\text{-PbSnF}_4$. The samples of the composition $\text{K}_{0.10}\text{Pb}_{0.90}\text{SnF}_{3.90}$ has the highest conductivity and the lowest conductivity activation energy in the high-temperature region ($\sigma_{573} = 0.13$ S cm^{-1}).²²

Despite the large body of accumulated experimental data on the effect of aliovalent substituents, including potassium ions, on the conduction properties of PbSnF_4 -based complex fluorides,^{15–22} the effect of different degrees of substitution of a part of the Pb^{2+} or Sn^{2+} by potassium ions on the properties of the fluoride ion conducting phases in the $\text{KF-PbF}_2\text{-SnF}_2$ system has not been unambiguously established. The effect of aliovalent substitution on the conductivity of complex lead and tin fluorides with nonstoichiometric ratio has been scantily studied. The aim of this study was to determine the effect of the substitution of Pb^{2+} or Sn^{2+} by K^+ on the electrical conductivity of the fluoride ion conducting phase $\text{Pb}_{0.86}\text{Sn}_{1.14}\text{F}_4$ with $\beta\text{-PbSnF}_4$ structure.

EXPERIMENTAL

Polycrystalline research samples were synthesized by melting together KHF_2 , PbF_2 and SnF_2 at a temperature in the range 773–823 K in an argon atmosphere. Pre-dried and ground KHF_2 , PbF_2 and SnF_2 were melted together in a platinum crucible in an argon atmosphere at 773 K, held at this temperature for 15 min and cooled with the furnace switched off (cooling rate of 3–5 K min^{-1}).

X-Ray diffraction (XRD) analysis of the synthesized samples was performed on a DRON-3M diffractometer with $\text{CuK}\alpha$ radiation in the angle range of 10–80° with a step of 0.04° and an exposure time of 3 s at each point. To interpret the diffractograms, the study of the elemental composition of the obtained samples was performed using a scanning electron microscope equipped with an energy-dispersive spectrometer AZtecOne with an X-MaxN20 detector.

The conductivity of the synthesized samples was studied by impedance spectroscopy using an Autolab electrochemical module (Ekochemie) and a frequency response analyzer in the frequency range of 10^{-1} – 10^6 Hz (at an amplitude of initial signal of 10 mV). Pressed cylindrical samples 8 mm in diameter and 2.0–3.0 mm in thickness were used for the research. Polished platinum plates served as current leads to the samples under investigation.

The temperature dependence of conductivity was studied in the range of frequencies where it is not affected by polarization and relaxation effects. The measurements were made under cooling conditions in a range of 298–773 (± 2) K after thermostating for 20–30 min in an argon atmosphere.

The electrical conductivity was calculated from the equation $\sigma = l/(sR)$, where l is the thickness of disk-shaped sample, s is contact area, R is ohmic resistance, which was determined from the results of impedance spectroscopy by the procedure described in the literature.^{19,20}

The ^{19}F -NMR spectra were recorded on a Bruker Avance 400 spectrometer (frequency 376 MHz) in the temperature range of 150–453 (± 2) K. The chemical shift (δ / ppm) was measured against a C_6F_6 standard with an accuracy of 1 ppm. The line width (at half height, ΔH) was determined in kHz with an error of not over 1 %.

RESULTS AND DISCUSSION

X-Ray phase analysis and EDS analysis

Samples of solid solutions $\text{K}_x\text{Pb}_{0.86-x}\text{Sn}_{1.14}\text{F}_{4-x}$ ($x = 0.03; 0.05; 0.07; 0.10; 0.15$) were synthesized for the research. The composition of the formed phases was monitored by energy dispersive X-ray analysis (EDS). It was found that the content of elements in the synthesized samples with increasing potassium concentration approach the amount of the actually taken salts for the synthesis (Table I).

An analysis of the results of X-ray phase studies showed that the diffraction patterns of all synthesized samples show the same reflection as for PbSnF_4 tetragonal structure (JCPDS card No. 35-1086, Fig. 1). No reflections that would indicate the presence of phases of the original components were detected. Only on the diffraction spectrum of the solid solution $\text{K}_{0.15}\text{Pb}_{0.71}\text{Sn}_{1.14}\text{F}_{3.85}$ was the formation of an additional peak at an angle of 27.39° observed, which corresponds to the KF phase.

TABLE I. Atomic content (at. %) in the solid solutions

Sample	Element			
	K	Pb	Sn	F
$K_{0.03}Pb_{0.83}Sn_{1.14}F_{3.97}$	0.61	13.54	18.70	67.15
$K_{0.05}Pb_{0.81}Sn_{1.14}F_{3.95}$	0.94	13.09	18.59	67.38
$K_{0.07}Pb_{0.79}Sn_{1.14}F_{3.93}$	1.30	12.97	19.21	66.52

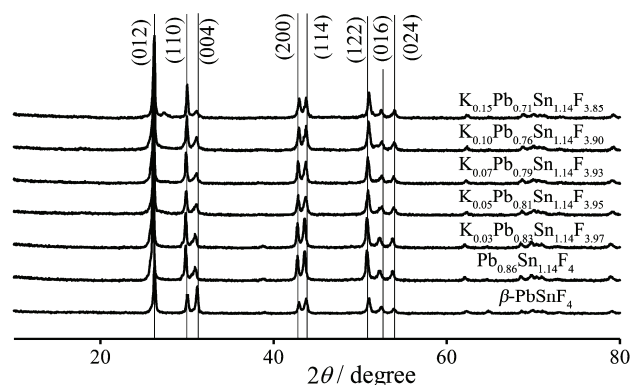


Fig. 1. X-Ray diffraction patterns of the synthesized samples.

According to the main peaks of the reference card (JCPDS card No. 35-1086), which are presented in Fig. 1, the values of the parameters of the crystal cells of the obtained solid solutions were calculated using the program UnitCell (Table II).

TABLE II. Lattice cell parameters (a , c , V) of the solid solutions $K_xPb_{0.86-x}Sn_{1.14}F_{4-x}$

Sample	a (± 0.0006) / nm	c (± 0.0023) / nm	V (± 0.060) / nm ³
β -PbSnF ₄	0.42132	1.15004	0.204147
$Pb_{0.86}Sn_{1.14}F_4$	0.42295	1.15518	0.206647
$K_{0.03}Pb_{0.83}Sn_{1.14}F_{3.97}$	0.42267	1.15608	0.206528
$K_{0.05}Pb_{0.81}Sn_{1.14}F_{3.95}$	0.42218	1.15164	0.205264
$K_{0.07}Pb_{0.79}Sn_{1.14}F_{3.93}$	0.42223	1.15103	0.205207
$K_{0.10}Pb_{0.76}Sn_{1.14}F_{3.90}$	0.42154	1.15089	0.204484
$K_{0.15}Pb_{0.71}Sn_{1.14}F_{3.85}$	0.42115	1.15097	0.204149
PbSnF ₄ (JCPDS card No. 35-1086)	0.4216	1.1407	0.20276

It is noted that when a part of the Pb^{2+} are replaced by K^+ in the structure of the initial compound $Pb_{0.86}Sn_{1.14}F_4$, the parameters of the crystal lattice decrease with increasing KF content (Table II). This effect does not contradict the Goldschmidt rule and may be a consequence of the different polarity of the K–F and Pb–F bonds, as well as the structural features of $PbSnF_4$.²³ In addition, the distances Pb–F, Sn–F and the localization sites of fluorides were calculated based on the results of an X-ray diffraction analysis of a single crystal.²⁴ These dis-

tances indicate that K^+ can occupy the position of Pb^{2+} in the crystal lattice of $PbSnF_4$ without distortion of the unit cell.

Impedance spectroscopy

An analysis of the results of impedance studies showed that in the Nyquist coordinates (Fig. 2), the impedance hodographs of all investigated samples in the high-frequency region are represented by one deformed half-ring, which transforms, on transition to the low-frequency region, into a dependence, which characterizes polarization processes at the electrolyte/blocking electrode interface.²⁵ With increasing temperature, the radius of the deformed half-rings decreases (Fig. 2), and they shift to the higher-frequency region. This nature of change in impedance diagrams is typical of polycrystalline ion-conducting electrolytes with structural and energetic nonequivalence of charge carriers, fluorine anions.²⁶

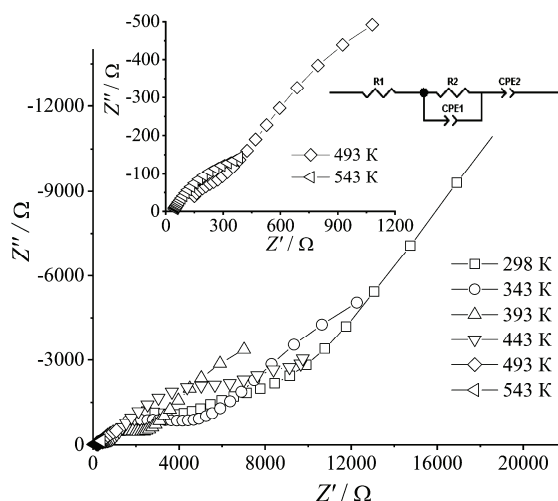


Fig. 2. Impedance hodographs and equivalent circuit of a polycrystalline sample of a $K_{0.03}Pb_{0.83}Sn_{1.14}F_{3.97}$ solid solution at different temperatures.

In all the cases the experimental complex impedance plot comprises a depressed semicircle accompanied by a straight line on the low frequency side, suggesting electrolyte–electrode polarization at the blocking electrodes. Such depression of the semicircle may originate from the presence of a distribution in relaxation times within the bulk response.^{27,28} The radius of the semicircle decreases with increasing temperature due to the increase in the conductivity of the sample. The physical model (equivalent circuit) appropriate to these plots is shown in the inset of Fig. 2.

The equivalent circuit consists of a elements R_1 , acting as the bulk resistance a blocking layer capacitance in series with the parallel combination of bulk resistance (R_2) and constant phase element (CPE_1), where CPE is generally con-

sidered as a leaky capacitor (*i.e.*, hybrid between a resistor and a capacitor). Ideally the impedance assembly for solid electrolytes related to the process of charge transport in the bulk specimen is represented by parallel combination of R_b and C_b , where R_b represents the bulk resistance and capacitance C_b arises due to the electric relaxation process.²⁹ However, in this case C_b was replaced by CPE1, which accounts for the observed depression of the semicircle, and also the non-ideal electrolyte symmetry CPE2 in the equivalent circuit accounts for the formation of inclined straight line in the low frequency region.

In the low-frequency region, resistance values associated with the polarization of near-electrode layers of solid electrolytes are recorded. As a rule, they are higher, the lower the frequency and the higher the temperature. In the frequency range of 0.1–100 kHz, frequency-independent values were recorded. They coincide with the conductivity values calculated from the values of the resistance R_2 of the equivalent circuit and the results of measurement by the bridge method at frequencies of 10–70 kHz; therefore, they were used in the analysis of plots of electrical conductivity *versus* temperature, $\sigma = l/sR_2$.

The plots of electrical conductivity *versus* temperature (Fig. 3, Table III) for all synthesized and investigated samples of solid solutions $K_xPb_{0.86-x}Sn_{1.14}F_{4-x}$ can be arbitrarily divided into two region: the low-temperature and the high-temperature regions. The transition between them is observed in the temperature range 340–430 K. Both in the high-temperature region and in the low-temperature region, these plots are satisfactorily approximated by the Arrhenius–Frenkel equation (straight line in the $\log \sigma - 1000T^{-1}$ coordinates).

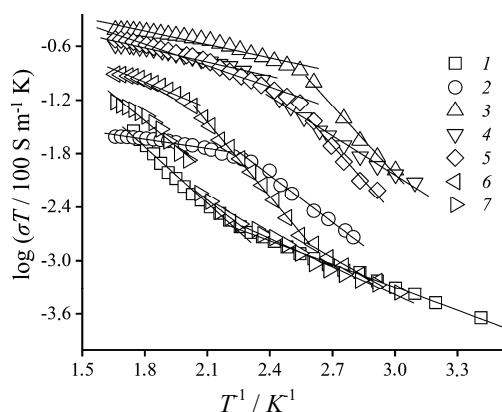


Fig. 3. Plots of electrical conductivity *versus* temperature for polycrystalline samples of $K_xPb_{0.86-x}Sn_{1.14}F_{4-x}$ solid solutions: 1: β -PbSnF₄; 2: Pb_{0.86}Sn_{1.14}F₄; 3: $x = 0.03$; 4: $x = 0.05$; 5: $x = 0.07$; 6: $x = 0.1$; 7: $x = 0.15$.

The increase in electrical conductivity in the sample Pb_{0.86}Sn_{1.14}F₄ in comparison with the sample PbSnF₄ is due to the fact that the interstitial fluorine anions (position F3) are coordinated around the cations Sn²⁺. This is evidenced by the results of the publication, which shows that the anions in position F3 (tetrahedra) are coordinated in the planes of the cationic lattice, where the cations

were Sn^{2+} .²⁴ Increasing the concentration of tin cations contributes to the increase of interstitial anions.

TABLE III. Electrical conductivity parameters of the solid solutions $\text{K}_x\text{Pb}_{0.86-x}\text{Sn}_{1.14}\text{F}_{4-x}$

Sample	$\Delta E_a (\pm 0.02) / \text{eV}$	$\log (A / \text{S cm}^{-1} \text{K}^{-1})$	$\sigma / \text{S cm}^{-1}$	T / K
$\beta\text{-PbSnF}_4$	0.36	4.19	$9.02 \cdot 10^{-4}$ (373)	298–373
	0.20	2.27	$1.88 \cdot 10^{-2}$ (573)	383–623
$\text{Pb}_{0.86}\text{Sn}_{1.14}\text{F}_4$	0.28	9.06	$2.9 \cdot 10^{-3}$ (373)	298–420
	0.18	6.67	$1.75 \cdot 10^{-2}$ (473)	430–480
	0.08	4.64	$2.41 \cdot 10^{-2}$ (573)	490–623
$\text{K}_{0.03}\text{Pb}_{0.83}\text{Sn}_{1.14}\text{F}_{3.97}$	0.49	18.24	0.12 (373)	298–370
	0.19	9.57	0.287 (473)	380–450
	0.09	7.58	0.373 (573)	460–623
$\text{K}_{0.05}\text{Pb}_{0.81}\text{Sn}_{1.14}\text{F}_{3.95}$	0.23	9.32	$2.29 \cdot 10^{-2}$ (373)	298–430
	0.14	7.92	0.25 (573)	440–623
$\text{K}_{0.07}\text{Pb}_{0.79}\text{Sn}_{1.14}\text{F}_{3.93}$	0.53	18.63	$1.93 \cdot 10^{-2}$ (373)	298–370
	0.23	10.20	0.167 (473)	380–460
	0.15	8.25	0.279 (573)	470–623
$\text{K}_{0.10}\text{Pb}_{0.76}\text{Sn}_{1.14}\text{F}_{3.90}$	0.33	9.53	$1.08 \cdot 10^{-3}$ (373)	298–400
	0.52	15.45	$2.65 \cdot 10^{-2}$ (473)	410–510
	0.17	8.51	0.11 (573)	520–623
$\text{K}_{0.15}\text{Pb}_{0.71}\text{Sn}_{1.14}\text{F}_{3.85}$	0.26	7.11	$7.85 \cdot 10^{-4}$ (373)	298–430
	0.75	19.09	$4.58 \cdot 10^{-3}$ (473)	470–540
	0.25	9.06	$4.94 \cdot 10^{-2}$ (573)	550–623

The influence of tin cations on the electrical conductivity of samples of the $\text{PbF}_2\text{-SnF}_2$ system is evidenced by the results of previous studies.³⁰ In these works, it was shown that the replacement of part of Pb^{2+} by Sn^{2+} increases the electrical conductivity and significantly reduces the activation energy.

The slight substitution ($x = 0.03$) of Pb^{2+} by K^+ in the $\text{Pb}_{0.86}\text{Sn}_{1.14}\text{F}_4$ structure causes an increase in electrical conductivity: at 600 K, its value is 0.38 S cm^{-1} and at 330 K 0.01 S cm^{-1} , which is an order of magnitude higher compared with original $\text{Pb}_{0.86}\text{Sn}_{1.14}\text{F}_4$ and two orders of magnitude higher compared to pure $\beta\text{-PbSnF}_4$ (Fig. 4A). In this case, the conductivity activation energy in the high-temperature region does not practically change (0.08 eV for original $\text{Pb}_{0.86}\text{Sn}_{1.14}\text{F}_4$ and 0.09 eV for $\text{Pb}_{0.83}\text{K}_{0.03}\text{Sn}_{1.14}\text{F}_{3.97}$ solid solution), and the total electrical conductivity increases owing to the appearance of vacancies in the anion sublattice (Fig. 4B).

When the K^+ content further increases (to $x = 0.07$), the fluoride ion conductivity of samples slightly decreases over the entire temperature range (Table III). The temperature dependence of the electrical conductivity of the solid solution of composition $\text{K}_{0.15}\text{Pb}_{0.71}\text{Sn}_{1.14}\text{F}_{3.85}$ is similar to that of $\beta\text{-PbSnF}_4$; in the high-temperature region, however, its values are somewhat higher and comparable with those of PbSnF_4 at temperatures below 490 K.

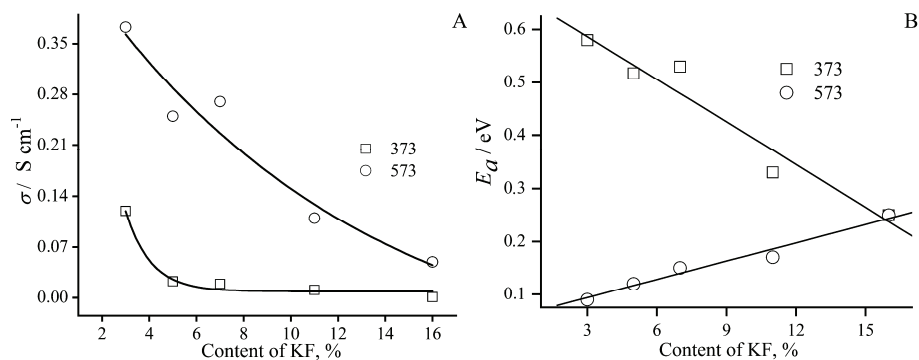


Fig. 4. Plots of electrical conductivity (A) and activation energy (B) *versus* potassium fluoride content for $K_xPb_{0.86-x}Sn_{1.14}F_{4-x}$ samples.

The electrical conductivity of the synthesized samples with the percentage of potassium ions replacing Pb^{2+} of over $x = 0.03$ decreases over the entire temperature range (Fig. 4). Unlike the compounds with purely interstitial conduction mechanism, the activation energy for $K_xPb_{0.86-x}Sn_{1.14}F_{4-x}$ solid solutions at $T > 450$ K increases with potassium fluoride content.²⁰ This may be due to the fact that the motion of fluoride ions between vacant positions requires a higher expenditure of energy than that in interstitial spaces.

NMR spectroscopy

Important information on the nature of charge carries in the system under investigation was obtained by ^{19}F -NMR spectroscopy. Typical ^{19}F -NMR spectra for, as an example, a $K_{0.03}Pb_{0.83}Sn_{1.14}F_{3.97}$ solid solution are shown in Fig. 5. The width of the spectral bands is determined by the interaction of the nuclear magnetic moments of fluorine. The appearance of the obtained spectra indicates that the fluorine anions occupy structurally different positions in the lattice.^{31,32}

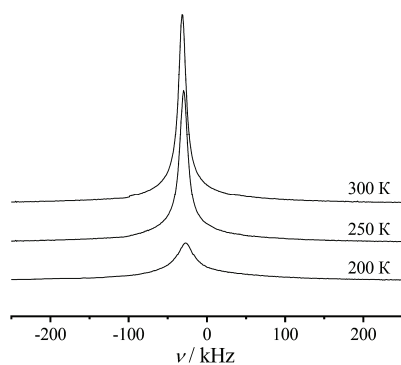


Fig. 5. ^{19}F -NMR spectra of a $K_{0.03}Pb_{0.83}Sn_{1.14}F_{3.97}$ solid solution at different temperatures.

Three position can be distinguished, F(1) in a rigid lattice with immobile anions, which are on triple axes, F(2) with locally mobile anions on the same

axes and F(3) interstitial fluorine anions. With increasing temperature, a redistribution of fluorine anions between the positions occupied by them in the lattice occurs.^{31,32} The narrow spectral component characterizing highly mobile interstitial ions becomes predominant in the integrated intensity. This anions redistribution is inherent in the overwhelming majority of fluoride ion conducting phases with fluorite and tysonite structures.³²

The transformation of the shape of the resonance band in the temperature range of 150–453 K entails a significant decrease in ΔH from 96 to 5 kHz (Fig. 6). The value of chemical shift at 150 K is ≈ 16 ppm and shifts to -31 ppm at 300 K. The chemical shift of the narrow component is sensitive to the type of structural positions occupied by ions in the diffusion process.

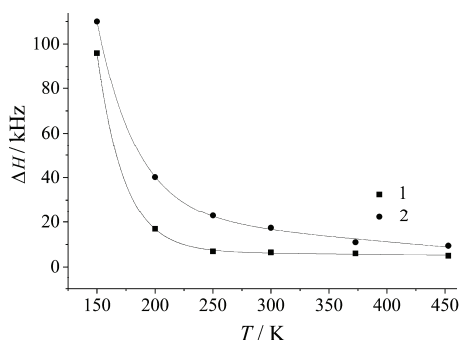


Fig. 6. Temperature dependence of the band width at half-height, $\Delta H(F)$, of the ^{19}F -NMR spectrum of a polycrystalline samples of solid solution: 1 – $\text{K}_{0.03}\text{Pb}_{0.83}\text{Sn}_{1.14}\text{F}_{3.97}$ and 2 – $\text{K}_{0.07}\text{Pb}_{0.79}\text{Sn}_{1.14}\text{F}_{3.93}$.

If the movement occurs only at positions of one type, then the chemical shifts of the “rigid” and narrow components must remain constant and should not depend on temperature. In the case when the ion visits other structural positions during diffusion, the shift of the narrow line will depend on temperature and can be represented by the average value $\langle\delta\rangle = \sum p_k \delta_k$, where p_k and δ_k are the mass coefficient and chemical shift of the k -th structural position.

The decomposition of the ^{19}F -NMR spectra of synthesized samples into components characterizing certain positions of fluorine anions in the lattice (Fig. 7) was performed according to Gabuda, *et al.*³³ and Kavun *et al.*³⁴

Since the area of the spectral components is proportional to the amount of fluorine anions, which are in one position or another, their fraction in the structure of the fluoride ion conducting phase at different temperatures can be quantitatively estimated in a first approximation. For instance, the fraction of the “highly mobile” fluorine anions that are in the interstitial spaces of the lattice (position F(3), spectral component P₃) at 150 K is not over 26 % and increases with rising temperature to 63 % at 300 K and 87 % at 453 K owing to drawing in fluoride ions from the locally mobile position F(2) and immobile position F(1) (Fig. 8). As can be seen from the presented data, up to 270 K, mainly the amount of anions that are position F(2) (the area of spectral component P₂) decreases.

The amount of fluorine anions that are in position F(1) (the area of spectral component P_1) does not practically change. At higher temperatures, they also move to interstitial positions F(3).

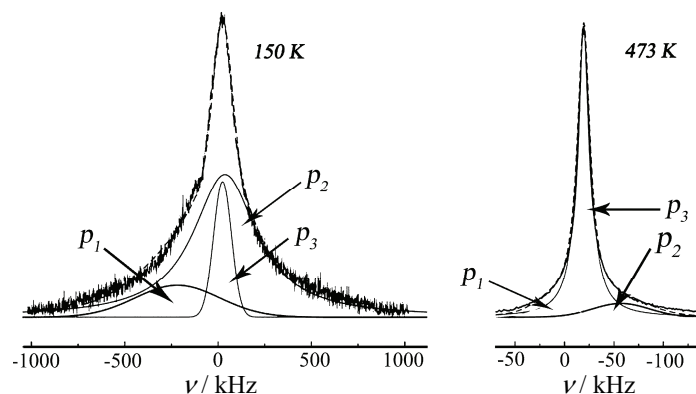


Fig. 7. Transformation of ^{19}F -NMR spectra and their components of $\text{K}_{0.03}\text{Pb}_{0.83}\text{Sn}_{1.14}\text{F}_{3.97}$ solid solutions with rising temperature.

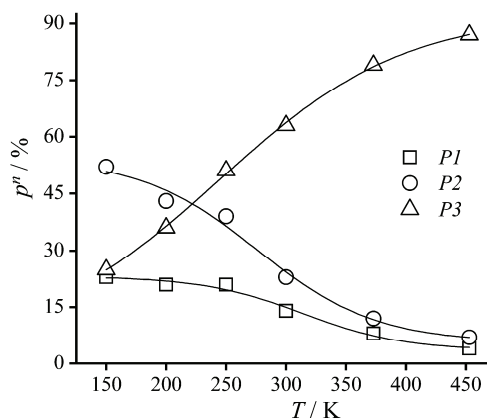


Fig. 8. Fluoride anion distribution over localization sites in the lattice of $\text{K}_{0.03}\text{Pb}_{0.83}\text{Sn}_{1.14}\text{F}_{3.97}$ at different temperatures.

The results of the NMR study agree with the trend of plots of conductivity *versus* temperature for the compounds $\text{K}_x\text{Pb}_{0.86-x}\text{Sn}_{1.14}\text{F}_{4-x}$. For instance, the $\log \sigma - 1000T^{-1}$ plots for each sample exhibit a kink in the temperature range of 370–430 K, which is characteristic of most solid electrolytes with fluorite and antiferro structures. Such dependence of electrical conductivity of temperature in the scientific literature is described as “Faraday phase transition”.³⁵ Its appearance is considered to be caused by an increase in the concentration of fluoride anions in the intermediate spaces of the crystal lattice when heated and their rate of migration.^{14,36} It is well known that in fluorine conducting the phases of fluorite and tysonite structures, the fluoride anions occupy three different positions, differing from each other by the local medium of the cation and the bond length M–F.³⁷ At a

certain temperature T_k , locally mobile fluorine anions acquire energy sufficient to overcome the energy barrier and move into the interstitial cavities. This is also largely due to the thermal fluctuations of lead and tin cations.

Approximately in this temperature range, the width at half-height of the bands in NMR spectra reaches minimum values (≈ 5 kHz), and the fluorines occupy mobile positions F(3).

CONCLUSIONS

The partial substitution of lead ions by potassium cations in the fluoride ion conducting phase of composition $\text{Pb}_{0.86}\text{Sn}_{1.14}\text{F}_4$ with a $\beta\text{-PbSnF}_4$ structure causes an increase of almost an order of magnitude in electrical conductivity relative to original $\beta\text{-PbSnF}_4$. On substitution, fluoride ion conducting phases $\text{K}_x\text{Pb}_{0.86-x}\text{Sn}_{1.14}\text{F}_{4-x}$ ($x = 0.03; 0.05; 0.07; 0.10; 0.15$) isostructural to $\beta\text{-PbSnF}_4$ are formed, the lattice of which corresponds to tetragonal syngony.

The light substitution of Pb^{2+} by potassium ions (up to $x = 0.07$ inclusive) in the fluoride ion conducting $\text{Pb}_{0.86}\text{Sn}_{1.14}\text{F}_4$ phase causes an increase in electrical conductivity over the entire studied temperature range. The sample of the composition $\text{K}_{0.03}\text{Pb}_{0.83}\text{Sn}_{1.14}\text{F}_{3.97}$ has the highest electrical conductivity ($\sigma_{600} = 0.38$ S cm^{-1} , $\sigma_{330} = 0.01$ S cm^{-1}). When the amount of substituent is further increased, the electrical conductivity in the low-temperature region decreases.

The conductivity of the synthesized solid electrolytes is provided by interstitial fluoride anions. Increasing the temperature contributes to an increase in their concentration and, as a result, in the conductivity of the solid solutions. At temperatures above 400 K, most of the fluorine ions (over 90 %) of the synthesized fluoride ion conducting phases are in highly mobile (interstitial) positions in the lattice.

Acknowledgement. This work was realized within the state project No. 0119U001824 with the financial support of MES of Ukraine.

ИЗВОД

ПРОВОДЉИВОСТ ФЛУОРИДНИХ ЈОНА ЧВРСТОГ РАСТВОРА $\text{KXPb}_{0.86}\text{-XSN}_{1.14}\text{F}_4\text{-X}$

YULIJA POHORENKO¹, ROMAN PSHENYCHNYI², TAMARA PAVLENKO¹, ANATOLIY OMEL'CHUK¹
и VOLODYMYR TRACHEVSKYI³

¹V.I. Vernadskii Institute of General and Inorganic Chemistry of the Ukrainian NAS, 32–34 Acad. Palladina Ave., 03142 Kyiv, Ukraine, ²Sumy State University, Rymkogo-Korsakova st. 2, 40007 Sumy, Ukraine и

³G.V. Kurdyumov Institute of Metal Physics of the Ukrainian NAS, Bulvar Vernadskoho 36, 03142 Kyiv, Ukraine

Електрична проводљивост чврстих раствора са тетрагоналном сингонијом, формираних у систему $0,86(x\text{KF}-(1-x)\text{PbF}_2)-1,14\text{SnF}_2$, испитивана је методом ^{19}F -спектроскопије нуклеарне магнетне резонанције (^{19}F -NMR) и спектроскопијом електрохемијске импеданције. Нађено је да је проводљивост флуоридних јона у фази $\text{Pb}_{0.86}\text{Sn}_{1.14}\text{F}_4$ боља у поређењу са једињењем $\beta\text{-PbSnF}_4$. Такође је показано да замена Pb^{2+} јонима K^+ до удела $x = 0,07$ у структури $\text{Pb}_{0.86}\text{Sn}_{1.14}\text{F}_4$ доприноси повећању електричне

проводљивости за један ред величине у односу на првобитни $\text{Pb}_{0,86}\text{Sn}_{1,14}\text{F}_4$. Узорак састава $\text{K}_{0,03}\text{Pb}_{0,83}\text{Sn}_{1,14}\text{F}_{3,97}$ поседује највећу електричну проводљивост ($\sigma_{600} = 0,38 \text{ S cm}^{-1}$, $\sigma_{330} = 0,01 \text{ S cm}^{-1}$). Флуориди у синтетисаним узорцима чврстог раствора $\text{K}_x\text{Pb}_{0,86-x}\text{Sn}_{1,14}\text{F}_{4-x}$ заузимају три структурно нееквивалентне позиције. Показано је да са повећањем температуре долази до прерасподеле флуоридних јона између места у анјонској решетци, што доводи до повећања концентрације високо покретљивих флуоридних јона, који одређују електричну проводљивост узорака.

(Примљено 24. новембра 2020, ревидирано 31. марта, прихваћено 7. априла 2021)

REFERENCES

1. V. Trnovcová, P. P. Fedorov, I. Furár, *Russ. J. Electrochem.* **45** (2009) 630 (<https://doi.org/10.1134/S1023193509060020>)
2. T. Nakajima, H. Groult, *Advanced Fluoride-Based Materials for Energy Conversion*, Elsevier, Amsterdam, 2015 (<https://doi.org/10.1016/C2013-0-18650-3>)
3. F. Gschwind, G. Rodriguez-Garcia, D. J. S. Sandbeck, A. Gross, M. Weil, M. Fichtner, N. Hörmann, *J. Fluorine Chem.* **182** (2016) 76 (<https://doi.org/10.1016/j.jfluchem.2015.12.002>)
4. J. W. Fergus, *Sensors Actuators, B* **42** (1997) 119 ([https://doi.org/10.1016/S0925-4005\(97\)00193-7](https://doi.org/10.1016/S0925-4005(97)00193-7))
5. X. Na, W. Niu, H. Li, J. Xie, *Sensors Actuators, B* **87** (2002) 222 ([https://doi.org/10.1016/S0925-4005\(02\)00238-1](https://doi.org/10.1016/S0925-4005(02)00238-1))
6. W. Moritz, S. Krause, U. Roth, J. Xie, *Anal. Chim. Acta* **437** (2001) 183
7. X. D. Wang, W. Shen, R. W. Catrall, G. L. Nyberg, J. Liesegang, *Aust. J. Chem.* **49** (1996) 897 (<https://doi.org/10.1071/CH9960897>)
8. M. Fouskaki, S. Sotiropoulou, M. Kosi, N. A. Chaniotakis, *Anal. Chim. Acta* **478** (2003) 77 ([https://doi.org/10.1016/S0003-2670\(02\)01481-2](https://doi.org/10.1016/S0003-2670(02)01481-2))
9. L. Zhang, M. A. Reddy, M. Fichtner, *Solid State Ionics* **272** (2015) 39 (<https://doi.org/10.1016/j.ssi.2014.12.010>)
10. C. B. Alcock, L. Baozhen, *Solid State Ionics* **39** (1990) 245 ([https://doi.org/10.1016/0167-2738\(90\)90403-E](https://doi.org/10.1016/0167-2738(90)90403-E))
11. C. Rongeat, M.A. Reddy, R. Witter, M. Fichtner, *J. Phys. Chem.* **117** (2013) 4943 (<https://doi.org/10.1021/jp3117825>)
12. A. Potanin, *J. Russ. Chem. Soc.* **45** (2001) 58
13. L. N. Patro, K. Hariharan, *Solid State Ionics* **239** (2013) 41 (<https://doi.org/10.1016/j.ssi.2013.03.009>)
14. N. I. Sorokin, B. P. Sobolev, *Crystallogr. Rep.* **52** (2007) 842 (<https://doi.org/10.1134/S1063774507050148>)
15. N.I. Sorokin, *Inorg. Mater.* **40** (2004) 989 (<https://doi.org/10.1023/B:INMA.0000041335.17098.d1>)
16. N. I. Sorokin, P. P. Fedorov, B. P. Sobolev, *Inorg. Mater.* **33** (1997) 1
17. A. M. Vakulenko, E. A. Ukshe, *Sov. Electrochem.* **28** (1992) 1025.
18. P. P. Fedorov, V. K. Goncharuk, I. G. Maslennikova, I. A. Telin, T. Y. Glazunova, *Russ. J. Inorg. Chem.* **61** (2016) 239 (<https://doi.org/10.1134/S0036023616020078>)
19. R. Kanno, S. Nakamura, Y. Kawamoto, *Solid State Ionics* **51** (1992) 53 ([https://doi.org/10.1016/0167-2738\(92\)90343-N](https://doi.org/10.1016/0167-2738(92)90343-N))

20. Yu. V. Pohorenko, R. M. Pshenychnyi, A. O. Omelchuk, V. V. Trachevskiy, *Solid State Ionics* **338** (2019) 80 (<https://doi.org/10.1016/j.ssi.2019.05.001>)
21. Y. V. Pogorenko, R. M. Pshenichnyi, V. I. Lutsyk, A. O. Omel'chuk, *IOP Conf. Ser.: Mater. Sci. Eng.* **175** (2017) 012039 (<https://doi.org/10.1088/1757-899X/175/1/012039>)
22. Yu. V. Pohorenko, A. A. Nahorny, R. M. Pshenychnyi, A. O. Omel'chuk, *Voprosy Khim. Khim. Tekhnol.* **5** (2019) 112 (<http://dx.doi.org/10.32434/0321-4095-2019-126-5-112-117>)
23. V. M. Goldschmidt, *Naturwissenschaften* **14** (1926) 477 (<https://doi.org/10.1007/BF01507527>)
24. Y. Ito, T. Mukoyama, H. Funatomi, S. Yoshikado, T. Takana, *Solid State Ionics* **67** (1994) 301 ([https://doi.org/10.1016/0167-2738\(94\)90021-3](https://doi.org/10.1016/0167-2738(94)90021-3))
25. A. K. Jonscher, *Nature* **267** (1977) 673 (<https://doi.org/10.1038/267673a0>)
26. J. T. S. Irvine, D. C. Sinclair, A. R. West, *Adv. Mater.* **2** (1990) 132 (<https://doi.org/10.1002/adma.19900020304>)
27. M. El Omari, J. Senegas, J. M. Réau, *Solid State Ionics* **107** (1998) 281 ([https://doi.org/10.1016/S0167-2738\(97\)00535-3](https://doi.org/10.1016/S0167-2738(97)00535-3))
28. M. M. Ahmad, K. Yamada, T. Okuda, *J. Phys. Condens. Matter.* **14** (2002) 7233 (<https://iopscience.iop.org/article/10.1088/0953-8984/14/30/312>)
29. E. Barsoukov, J. R. Macdonald, *Impedance spectroscopy emphasizing solid materials and systems*, John Wiley and Sons, Inc., Hoboken, NJ, 2005. (ISBN: 0-471-64749-7)
30. S. Vilminot, G. Perez, W. Granier, L. Cot, *Solid State Ionics* **2** (1981) 91 ([https://doi.org/10.1016/0167-2738\(81\)90004-7](https://doi.org/10.1016/0167-2738(81)90004-7))
31. M. G. Izosimova, A. I. Livshits, V. M. Buznik, P. P. Fedorov, E. A. Krivandina, B. P. Sobolev, *Sov. Phys.-Sol. State* **28** (1986) 2644.
32. V. Ya. Kavun, A. I. Ryabov, I. A. Telin, A. B. Podgorbunskii, S. L. Sinebryukhov, S. V. Gnedenkov, V.K. Goncharuk, *J. Struct. Chem.* **53** (2012) 290 (<https://doi.org/10.1134/S0022476612020126>)
33. S. P. Gabuda, Yu.V. Gagarinsky, S. A. Polishchuk, *NMR in inorganic fluorides*, Atomizdat, Moscow, 1978
34. V. Ya. Kavun, N. F. Uvarov, A. B. Slobodyuk, M. M. Polyantsev, A. S. Ulihin, E. B. Merkulov, V. K. Goncharuk, *Solid State Ionics* **330** (2019) 1 (<https://doi.org/10.1016/j.ssi.2018.12.004>)
35. D. P. Almond, A. R. West, *Solid State Ionics* **9–10** (1983) 277 ([https://doi.org/10.1016/0167-2738\(83\)90247-3](https://doi.org/10.1016/0167-2738(83)90247-3))
36. Sh. Yoshikado, Y. Ito, J. M. Réau, *Solid State Ionics* **154–155** (2002) 503 ([https://doi.org/10.1016/S0167-2738\(02\)00489-7](https://doi.org/10.1016/S0167-2738(02)00489-7))
37. C. Martineau, F. Fayon, C. Legein, J. Y. Buzaré, G. Corbel, *Chem. Mater.* **22** (2010) 1585 (<https://doi.org/10.1021/cm9030182>).



J. Serb. Chem. Soc. 86 (9) 859–870 (2021)
JSCS–5467

Benzimidazole-functionalized fluorescent probe for rapid detection of 2,4,6-trinitrophenol and Ag⁺ in semiaqueous medium

BIN WANG^{1–3}, FAN JIANG¹, XIXI ZUO¹, JING MA¹ and XIANGMEI MA^{1,2*}

¹Institute of Chemical Engineering, Anhui University of Science and Technology, Huainan, Anhui, 232001, China, ²Institute of Environment-Friendly Materials and Occupational Health of Anhui University of Science and Technology (Wuhu), Wuhu, 241003, China and ³State Key Laboratory of Mining Response and Disaster Prevention and Control in Deep Coal Mines, Anhui University of Science and Technology, Huainan 232001, China

(Received 2 July 2020, revised 6 February, accepted 8 February 2021)

Abstract: In this study, a simple fluorescent chemosensor with good fluorescence properties was synthesized, and was used to develop a sensitive and selective sensor, for the determination of 2,4,6-trinitrophenol (TNP) and Ag⁺ in THF/H₂O medium, based on the fluorescence quenching mechanism. Fluorescence quenching experiments revealed that the fluorescence intensities of the resulted probe were linear with the concentrations of TNP and Ag⁺ in the concentration range of 3.0–5.0 and 2.0–5.0 μmol dm⁻³, with the detection limit of 1.36 and 0.82 μmol dm⁻³, respectively. At the same time, accompanied with fluorescent color change under 365 nm UV light irradiation. This has demonstrated that the compound can act as a potential candidate for a “naked-eye” rapidly detector for Ag⁺ and TNP in soils and aquatic systems.

Keywords: benzimidazole; quinoline; fluorescence quenching; TNP.

INTRODUCTION

2,4,6-Trinitrophenol (TNP), a nitroaromatic explosives (NAEs) are more violent and explosive than its another analogue. It features better solubility, stronger toxicity and explosive power even at very low concentrations, that may contaminate groundwater and cause many serious diseases.^{1,2} On the other hand, silver ion, like other heavy metal ions, is widely used in industry and agriculture hence a large amount of Ag⁺ has been introduced into surface water. Because it can inactivate cellular enzymes by binding with amino, and thiol groups or by triggering oxidative damage, Ag⁺ has been recognized as one of the most hazardous heavy metal pollutants,³ with great influence on people's health and bio-

*Corresponding author. E-mail: wb6314005@126.com; 2834846807@qq.com
<https://doi.org/10.2298/JSC200702009W>

logical systems.⁴ Hence, accurate determination of trace Ag^+ and TNP in environmental samples is important for environmental monitoring. Toward this purpose, different techniques have been developed to determine NAEs including mass spectrometry,^{5,6} gas chromatography (GC),⁷ ion mobility spectrometry (IMS) and thermal neutron analysis, *etc.*^{8,9} Many conventional methods, such as flame atomic absorption, potentiometry, voltammetry and inductively coupled plasma atomic emission spectrometry, are widely used to detect Ag^+ too. Unfortunately, some detecting techniques are expensive and cannot satisfy the demand of real-time detection.¹⁰ The fluorescent detection has become popular because of its operational simplicity, high selectivity, good sensitivity, rapidity, nondestructive methodology, direct visual perception, *etc.*¹¹ In view of the above, design and synthesis of new fluorescent chemosensors for the efficient detection of TNP and Ag^+ is one of the most important research topics in environmental chemistry and biology.

Quinoline and imidazole have attracted tremendous attention because the nitrogen atom can act as a chelating site towards metal ions. The aromatic heterocyclic quinoline, as one of the most widely used organic optoelectronic functional materials, it undergoes $\pi-\pi^*$ electronic transition, and exhibits strong fluorescence.¹² Owing to the benzene ring and the imidazole ring being heterocyclic coplanar, benzimidazole presents unique electronic distribution and forms a big π -bond system, which is a well-known chromophore used in fluorescence sensing.¹³ Compared with the other nitro compounds, TNP not only has a strong electron-withdrawing ability, but also has a strong light absorption capacity at a large excitation wavelength. Based on this consideration, the benzimidazole and quinoline were combined into a molecule (BAQ) to increase the selectivity and sensitivity for detection metal ions and TNP. Furthermore, the probe showed high sensitivity and selectivity for TNP and Ag^+ in THF/ H_2O mixed solution. The extraordinary sensing properties endowed the compound with sensitive fluorometric chemosensors for the potential application of TNP and Ag^+ detection in environment system.

EXPERIMENTAL

Materials

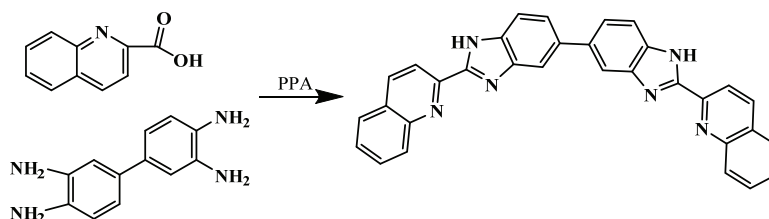
All chemicals used in this work were analytical reagent grade, purchased from Aladdin Reagent Co. Ltd. (Shanghai, China), and used without further treatment. Deionized water (18 $\text{M}\Omega$ cm) from a water purification system was used in this experiment.

Synthesis of fluorescent probe

The synthesis route of BAQ (2,2'-di(quinolin-2-yl)-1*H*,1'*H*-5,5'-bibenzo[*d*]imidazole) is shown in Scheme 1.¹⁴

Briefly, 0.0132 mol of quinoline-2-carboxylic acid and 0.006 mol of biphenyl-3,4,3',4'-tetraamine were dissolved in polyphosphate (25 mL), The mixture was refluxed for 48 h at 160 °C, the reaction was stopped by adding distilled water, and then cooled to room tem-

perature. Then, the pH value of the solution was adjusted to 9–10 with sodium hydroxide. The brown powder was collected by vacuum filtration, further purification was accomplished by recrystallization from anhydrous ethanol, melting point 183–185 °C (yield: 83.6 %).



Scheme 1. Synthetic route for probe BAQ.

Characterization

Fourier transform infrared spectroscopy (FT-IR) measurements were performed on a Bruker Vector-22 FT-IR spectrometer. Each vacuum-dried sample was ground with KBr and compressed into a pellet.

¹H-NMR spectral data were recorded on Agilent Technologies 400 spectrometer (400 MHz) with DMSO-*d*₆ as solvent and TMS as internal standard.

The fluorescence experiments were performed at room temperature with the major equipment Perkin-Elmer F-4600 spectrofluorometer.

RESULTS AND DISCUSSION

FT-IR and NMR analyses

The probe was characterized by ¹H-NMR and FT-IR spectra. In Fig. 1a, ¹H-NMR (400 MHz, DMSO-*d*₆, δ / ppm) typical peaks are observed at 7.61–7.79 (*m*, 6H), 7.95–7.85 (*m*, 4H), 8.07–8.12 (*d*, *J* = 8.1 Hz, 2H), 8.17–8.25 (*d*, *J* = 8.3 Hz, 2H), 8.50–8.63 (*m*, 4H), 13.30 (*s*, 2H). As shown in Fig. 1b, the FT-IR spectrum exhibits: –NH (3421 cm⁻¹), aromatic C–H (3060 cm⁻¹), ¹⁵C=N stretching vibration (1590 cm⁻¹), C–N (1301 and 833 cm⁻¹),^{16,17} the ring vibrations of benzimidazole and quinolin (1502, 1438, 1409, 1106 and 757 cm⁻¹).¹⁸

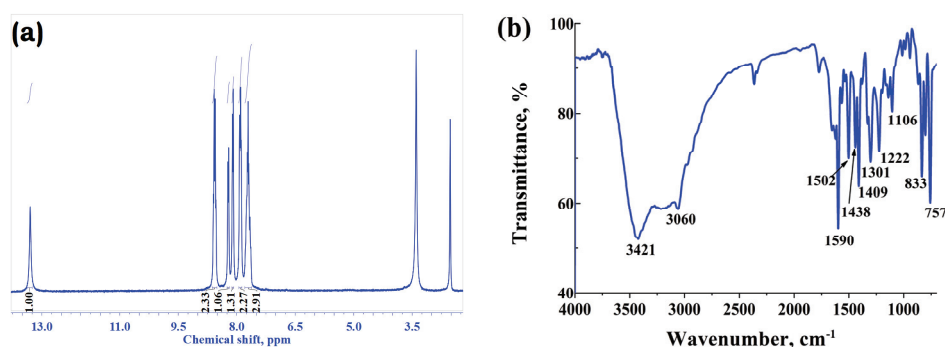


Fig. 1. ¹H-NMR (a) and FT-IR (b) spectra of the BAQ.

Fluorescence detection of TNP

Based on the better photoluminescence properties and the larger excitation wavelengths for BAQ, we investigated its sensing properties towards the potential explosive TNP. A stock solution of BAQ was prepared in THF/H₂O (1:1 volume ratio). The solutions of various NACs including trinitrotoluene (TNT), 4-nitrotoluene (4-NT), 2,6-dinitrotoluene (2,6-DNT), 2,4-dinitrotoluene (2,4-DNT), 4-nitrophenol (4-NP), 2-nitrophenol (2-NP), nitrobenzene (NB), 2-nitrotoluene (2-NT) and 2,4,6-trinitrophenol (TNP) were prepared in mixed solvent (THF/H₂O, 1:1 volume ratio). Nitroaromatic explosive (10^{-3} mol dm⁻³) was mixed separately with equal volume BAQ solution (10^{-4} mol dm⁻³), the blank sample was prepared with BAQ solution and equal volume of mixed solvent. All spectra were measured for 10 min after addition of the NAE with excitation wavelength 369 nm at room temperature, and emission was collected from 389 to 650 nm. The slit widths of the excitation and emission were both 5 nm. Fig. 2a shows that TNP caused the obvious fluorescence quenching accompanied with fluorescent color changes from light blue to turquoise under 365 nm UV lamp. The solution color did not change upon the addition of other NAEs, the apparent fluorescence emission change could be distinguished by the naked eye. These results indicate that BAQ possesses high selectivity for TNP sensing.

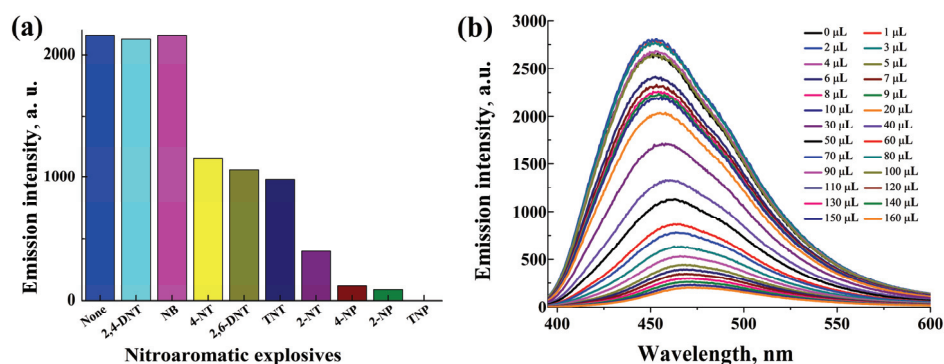


Fig. 2. Fluorescence spectra bar graph representation of the probe solution upon addition of various NAEs (a) and fluorescence spectra changes of the probe solution upon addition of different amounts of TNP (b).

To further evaluate the sensing properties of BAQ toward TNP, fluorescence quenching titration studies were carried out by progressive addition of TNP (THF/H₂O, 1:1 volume ratio). The solution of TNP (10^{-3} mol dm⁻³) was gradually titrated into 2 mL stock solution of BAQ (2 mL, 10^{-4} mol dm⁻³). As depicted in Fig. 2b, with the gradual addition of TNP, the fluorescence intensities gradually decreased. Based on the fluorescence titration results, the sensitivity of the probe to detect TNP is evaluated by the Stern–Volmer equation:

$$(I_0/I) - 1 = K_{\text{SV}}[Q] \quad (1)$$

where K_{SV} is Stern–Volmer constant indicating the sensitivity of probe; I_0 and I are the fluorescence intensities before and after the addition of TNP at 452 nm (total volume change negligible), $[Q]$ is the molar concentration of TNP. According to Stern–Volmer, the ratio of fluorescence intensity in the absence and presence of TNP displays a linear response ($R^2 = 0.988$) to the TNP concentration in the range of $3.0\text{--}5.0 \mu\text{mol dm}^{-3}$ (Fig. 3a), and the corresponding constant K_{SV} for the TNP probe was calculated as $7.07 \times 10^4 \text{ dm}^3 \text{ mol}^{-1}$. The limit of detection (LOD) was calculated to be $1.36 \mu\text{mol dm}^{-3}$, which was determined with the following equation:

$$LOD = \frac{3\delta}{D} \quad (2)$$

The δ was the standard deviation of blank measurements; D was the slope between fluorescence intensity and TNP concentration.¹⁹ The comparison between our probe and the reports has been added in the Table I, which confirmed the high sensitivities of the chemsensors.^{20–23} These results demonstrate that BAQ can be applied as a kind of probe for TNP sensing.

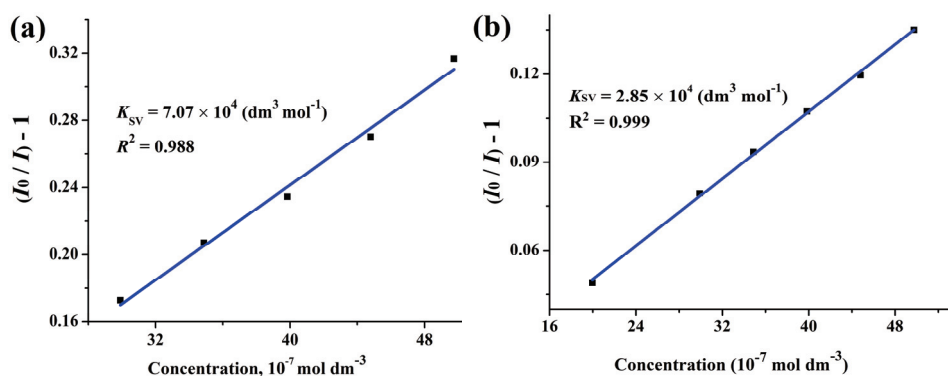
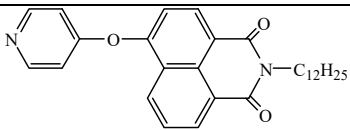
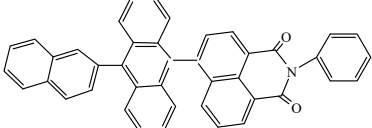
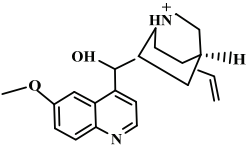


Fig. 3. The Stern–Volmer plot of BAQ for quenching of TNP (a) and Ag^+ (b).

Fluorescence detection of Ag^+

The optical properties of BAQ induced by metal ions also were studied in mixed solvent (THF/ H_2O , 1:1 volume ratio) at room temperature. The solutions of metal ions (Mg^{2+} , K^+ , Ca^{2+} , Al^{3+} , Cr^{3+} , Fe^{3+} , Co^{2+} , Cu^{2+} , Zn^{2+} and Ag^+) were prepared by the dissolution of their corresponding nitrate salts in THF/ H_2O . Each metal ion solution ($10^{-3} \text{ mol dm}^{-3}$) was mixed with equal volume of BAQ solution ($10^{-4} \text{ mol dm}^{-3}$), the blank sample was prepared with BAQ solution and equal volume of mixed solvent. All spectra were measured for 10 min after addition of the metal ion solution with excitation wavelength 369 nm at room tempe-

TABLE I. Comparison of different chemosensors for the detection of TNP

Chemosensor	Formula	LOD / $\mu\text{mol dm}^{-3}$	Reference
Gelators with pyridine		0.64	20
Nph-An derivative		470	21
Quinine sulphate		1.98	22
Carbon quantum dots		1.8	23
Benzimidazole derivatives		1.36	This work

ature, and emission was collected from 389 to 650 nm. The slit widths of the excitation and emission were both 5 nm. Fig. 4a showed the fluorescence spectra changes stimulated by Mg^{2+} , K^+ , Ca^{2+} , Al^{3+} , Cr^{3+} , Fe^{3+} , Co^{2+} , Cu^{2+} , Zn^{2+} and Ag^+ , these metal ions exhibit different degree of quenching on the fluorescence intensities. However, Ag^+ not only caused the obvious fluorescence quenching, but also were accompanied with fluorescent color change from light blue to turquoise under 365 nm UV light irradiation. Therefore, BAQ has excellent selectivity for the detection of Ag^+ .

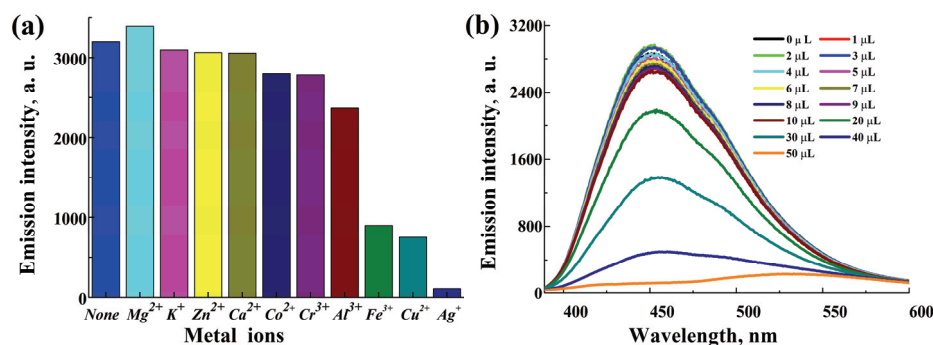


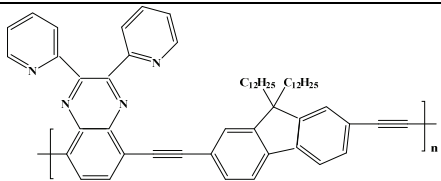
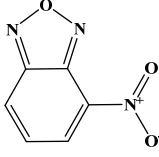
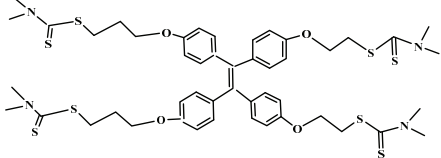
Fig. 4. Fluorescence spectra bar graph representation of the probe solution upon addition of various metal cations (a) and fluorescence spectra changes of the probe solution upon addition of different amounts of Ag^+ (b).

To further evaluate the sensing properties of BAQ toward Ag^+ , the emission spectra of BAQ titration experiments for Ag^+ were carried out. The solution of

Ag⁺ (10⁻³ mol dm⁻³) was gradually titrated into 2 mL stock solution of BAQ (10⁻⁴ mol dm⁻³). As shown in Fig. 4b, the emission intensities gradually decreased with the increasing concentrations of Ag⁺, which could be assigned to a combination effect enhanced fluorescence between Ag⁺ and BAQ.²⁴ The significant changes in fluorescence were observed from light blue to turquoise under 365 nm UV lamp. The sensitivity of the probe to detect Ag⁺ is evaluated by the Stern–Volmer equation too, the ratio of fluorescence intensity at 451 nm in the absence and presence of Ag⁺ displays a linear response to the Ag⁺ concentration in the range of (2.0–5.0 μmol dm⁻³ ($R^2 = 0.999$), with the K_{SV} value of 2.85×10^4 dm³ mol⁻¹ (as shown in Fig. 3b). The detection limit of BAQ for Ag⁺ was 0.82 μmol dm⁻³. According to the standards of the U.S. Environmental Protection Agency (EPA), the maximum content of Ag⁺ in drinking water must be limited to 0.93 μmol dm⁻³. Furthermore, the low detection limit of the chemosensor BAQ made it possible to detect the level of Ag⁺ in drinking water in normal individuals as defined.²⁵ The comparison between our probe and the reports have been added in the Table II,^{26–29} which indicated that the detection limit of BAQ is comparable or better than some similar fluorescent probes literature reported.

Job's plots experiments were carried out to elucidate the binding modes of BAQ with Ag⁺. The analysis based on keeping the total concentration of BAQ and Ag⁺ at 10⁻⁴ mol dm⁻³ and changing the molar fraction of Ag⁺ (c_{Ag^+}) from 0 to 1.0.

TABLE II. Comparison of different chemosensors for the detection of silver ion

Chemosensor	Formula	LOD / μM	Reference
Conjugated polymers		0.5	26
Gold nanoparticles (AuNPs)		1.0	27
NBD		0.65	28
TPE-4DDC		0.87	29
Benzimidazole derivative		0.82	This work

The difference in fluorescence intensity at 451 nm before (F_0) and after (F) the addition of Ag^+ was given as $(F_0 - F)$, As shown in Fig. 5a, the result shows that the $F_0 - F$ reached maximum at 451 nm at x_{Ag^+} of 0.5, indicating the formation of 1:1 complex of BAQ and Ag^+ based on the results of Job plot and the literature,³⁰ the plausible structure of $\text{Ag}^+ + \text{BAQ}$ was shown in Fig. 5b, the benzimidazole and quinoline can cooperatively participate in the binding with Ag^+ .³¹

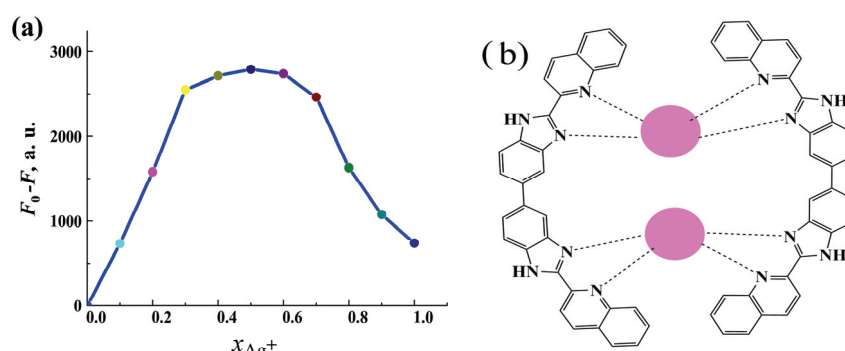


Fig. 5. Job plot of BAQ with Ag^+ complexation (a) and plausible structure of $\text{Ag}^+ + \text{BAQ}$ (b).

Sensing mechanism of BAQ with Ag^+ and TNP

The common mechanism of the fluorescence detection is the photo-induced electron transfer (PET) and Förster resonance energy transfer (FRET).³² PET includes electron move from LUMO of energized fluorophore to LUMO of quencher.³³ A productive PET can happen when the LUMO of fluorophore lie somewhat above in energy than LUMO of acceptor. We performed the theoretical research by employing the density functional theory (DFT) in Gaussian B3LYP/6-31g* basis set. The calculated HOMO–LUMO energy levels of the common NAEs and BAQ are summarized in Fig. 6a. NAEs are all electron deficient substances, the lower LUMO energy of BAQ signifies the stronger electron withdrawing ability and the higher quenching efficiency.

TNP shows the highest quenching efficiency because of the lowest LUMO among the NAEs. The result suggests that electron transfer can more easily occur from BAQ to TNP. Apart from this, the FRET could be identified by the overlap of the absorbance spectra of NAEs and the photoluminescence (PL) spectra of BAQ.³⁴ The absorption spectrum of TNP has large overlap with the PL spectrum of BAQ (Fig. 6b), which contributed to FRET from BAQ to TNP. Both the EET and FRET synergistically induce the fluorescence quenching of BAQ, resulting in the contribution of good sensing performance toward TNP, which could be the result of the formation of hydrogen binding between TNP guest and the nitrogen atoms on sensor. These could be attributed to the mechanism of electron and

resonance energy transfer processes in the complexes with the molecular interactions.^{35,36}

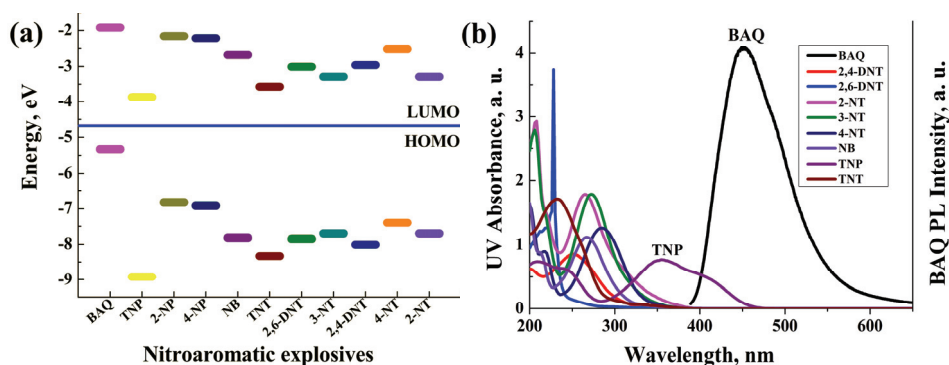


Fig. 6. Positions of the HOMO and LUMO energy levels of BAQ and various NAEs (a); spectral overlap between the PL spectrum of sensor BAQ and the absorption spectra of TNP (b).

UV-Vis absorption spectrum of BAQ (Fig. 7a) shows the typical absorption band at 216 nm (π - π transition) and 281 nm (π - π^* transition).³⁷

The UV-Vis absorbance spectrum of BAQ displayed significant change after addition of Ag^+ , the absorbance band at 281 nm decreased largely accompanied by emerging of a new absorbance band in the range of 356–407 nm with a peak at 389 nm, which proved that BAQ formed a firm binding with Ag^+ . The significant changes in the UV-Vis spectra of macrocyclic compounds and their complexes with Ag^+ suggested the formation of ground-state complexes with charge transfer process. As appeared in Fig. 7b, the absorption spectrum of Ag^+ has no overlap with excitation spectra of BAQ. So these excellent performances of BAQ for Ag^+ and TNP detection could be mainly due to different mechanisms. For Ag^+ detection, the main mechanism is based on PET. While for TNP detection, the mechanism could be FRET and PET

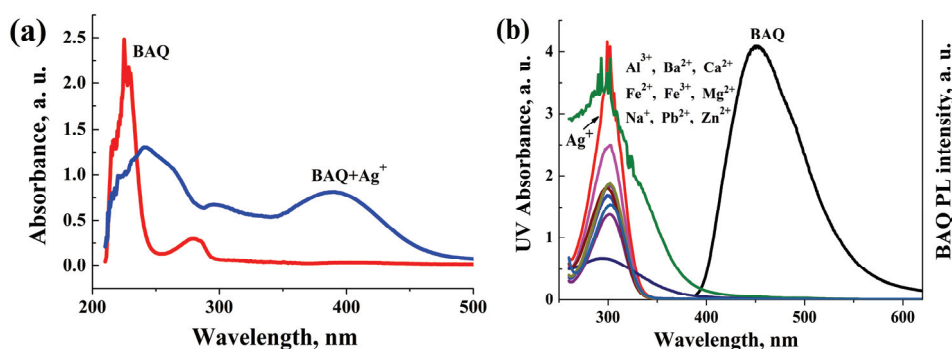


Fig. 7. The UV-Vis absorption spectra of Ag^+ and BAQ+ Ag^+ (a); spectral overlap between the PL spectrum of sensor BAQ and the absorption spectra of Ag^+ (b).

CONCLUSIONS

In summary, we report the synthesis, structural characterization, photoluminescence behavior and the sensing properties of a novel chemosensor containing benzimidazole and quinolone units (BAQ). The sensing properties of BAQ toward the potential explosive TNP and Ag^+ were investigated. The detection selectivity of the compound for TNP and Ag^+ could be visualized by naked eyes in THF/ H_2O solution, and the detection limits of TNP and Ag^+ were as low as 1.36 and 0.82 $\mu\text{mol dm}^{-3}$, respectively. At last, the detection mechanism of BAQ for Ag^+ and TNP detection were further investigated by the theoretical calculation, ultraviolet and fluorescence spectra. Based on the different detection mechanism, the BAQ exhibited different fluorescent response to Ag^+ and TNP. The results will help to design effective fluorometric sensors with benzimidazole and quinoline units in future.

Acknowledgements. This work was supported by the Funded by Research Foundation of the Institute of Environment-Friendly Materials and Occupational Health of Anhui University of Science and Technology (Wuhu) (Grant No. ALW2020YF06); the Key Research and Development Projects in Anhui Province (Grant No. 202004h07020022).

ИЗВОД

ФУНКЦИОНАЛНА ФЛУОРЕСЦЕНТНА ПРОБА НА БАЗИ БЕНЗИМИДАЗОЛА ЗА БРЗО
ОДРЕЂИВАЊЕ 2,4,6-ТРИНИТРОФЕНОЛА И Ag^+ У СМЕШИ
ТЕТРАХИДРОФУРАН–ВОДАBIN WANG^{1,2}, FAN JIANG¹, XIXI ZUO¹, JING MA¹ И XIANGMEI MA^{1,2}

¹Institute of Chemical Engineering, Anhui University of Science and Technology, Huainan, Anhui, 232001, China и ²Institute of Environment-Friendly Materials and Occupational Health of Anhui University of Science and Technology (Wuhu), Wuhu, 241003, China

У овом раду је описан новосинтетисан, једноставан и осетљив хемисензор, са добрим флуоресцентним карактеристикама, које су искоришћене за селективно одређивање 2,4,6-тринитрофенола (TNP) и Ag^+ у смеши THF/ H_2O . Интензитет флуоресценције новосинтетисаног једињења линеарно опада у опсегу концентрација TNP 3,0—5,0 $\mu\text{mol dm}^{-3}$ и Ag^+ 2,0—5,0 $\mu\text{mol dm}^{-3}$, са границом детекције од 1,36 $\mu\text{mol dm}^{-3}$ за TNP и 0,82 $\mu\text{mol dm}^{-3}$ за Ag^+ . Како под утицајем UV зрачења таласне дужине 365 nm долази до промене флуоресцентне боје, ово једињење је потенцијални кандидат за брзу детекцију Ag^+ и TNP у земљишту и воденим системима.

(Примљено 2. јула 2020, ревидирано 6. фебруара, прихваћено 8. фебруара 2021)

REFERENCES

1. M. Rong, L. Lin, X. Song, T. Zhao, Y. Zhong, J. Yan, Y. Wang, X. Chen, *Anal. Chem.* **87** (2015) 1288 ([http://refhub.elsevier.com/S0039-9140\(19\)30151-1/sbref5](http://refhub.elsevier.com/S0039-9140(19)30151-1/sbref5))
2. Y. Salinas, R. M. Máñez, M. D. Marcos, F. Sancenón, A. M. Costero, M. Parra, S. Gil, *Chem. Soc. Rev.* **41** (2012) 1261 ([http://refhub.elsevier.com/S1386-1425\(19\)30973-4/sref1](http://refhub.elsevier.com/S1386-1425(19)30973-4/sref1))

3. N. Pandeya, M. S. Mehatab, N. Fatmaa, S. Pant. *Luminescence* **205** (2019) 475 (<https://doi.org/10.1016/j.jlumin.2018.09.062>)
4. H. Y. Wang, Q. J. Lu, M. X. Li, H. Li, Y. L. Liu, H. T. Li, Y. Y. Zhang, S. H. Yao, *Anal. Chim. Acta* **1027** (2018) 121 (<https://doi.org/10.1016/j.aca.2018.03.063>)
5. L. Barron, E. Gilchrist, *Anal. Chim. Acta* **806** (2014) 27 ([http://refhub.elsevier.com/S0039-9140\(19\)30151-1/sbref7](http://refhub.elsevier.com/S0039-9140(19)30151-1/sbref7))
6. K. Badjagbo, S. Sauve, *Anal. Chem.* **84** (2012) 5731 ([http://refhub.elsevier.com/S0039-9140\(19\)30151-1/sbref8](http://refhub.elsevier.com/S0039-9140(19)30151-1/sbref8))
7. M. Berg, J. Bolotin, T. B. Hofstetter, *Anal. Chem.* **79** (2007) 2386 ([http://refhub.elsevier.com/S0039-9140\(19\)30151-1/sbref9](http://refhub.elsevier.com/S0039-9140(19)30151-1/sbref9))
8. M. Sabo, S. Matejcek, *Anal. Chem.* **84** (2012) 5327 ([http://refhub.elsevier.com/S0039-9140\(19\)30151-1/sbref14](http://refhub.elsevier.com/S0039-9140(19)30151-1/sbref14))
9. G. Vourvopoulos, P. Womble, *Talanta* **54** (2001) 459 ([http://refhub.elsevier.com/S0039-9140\(19\)30151-1/sbref15](http://refhub.elsevier.com/S0039-9140(19)30151-1/sbref15))
10. J. H. Pang, K. Z. Shen, D. F. Ren, S. N. Feng, Y. Wang, Z. H. Jiang, *J. Mater. Chem.* **1** (2013) 1465 (<https://doi.org/10.1039/C2TA00363E>)
11. Y. Fu, P. Li, J. X. Kang, X. Y. Liu, G. Y. Li, F. Ye, *Luminescence* **178** (2016) 156 (<http://dx.doi.org/10.1016/j.jlumin.2016.05.023>)
12. L. Liu, F. Dan, W. Liu, X. Lu, Y. Han, S. Xiao, H. Lan. *Sensors Actuators, B* **247** (2017) 445 (<http://dx.doi.org/10.1016/j.snb.2017.03.069>)
13. R. M. Gadirov, R. R. Valiev, L. G. Samsonova, *Chem Phys Lett.* **717** (2019) 53 (<https://doi.org/10.1016/j.cplett.2019.01.014>)
14. X. C. Han, Y. J. Xie, D. Liu, *J Membrane Sci.* **589** (2019) 117230 (<https://doi.org/10.1016/j.memsci.2019.117230>)
15. S. Khatua, S. H. Choi, J. Lee, K. Kim, Y. Do, D. G. Churchill, *Inorg. Chem.* **48** (2009) 2993 ([http://refhub.elsevier.com/S1386-1425\(16\)30586-8/rf0220](http://refhub.elsevier.com/S1386-1425(16)30586-8/rf0220))
16. S. Khatua, J. Kang, D. G. Churchill, *New J. Chem.* **34** (2010) 1163 ([http://refhub.elsevier.com/S1386-1425\(16\)30586-8/rf0230](http://refhub.elsevier.com/S1386-1425(16)30586-8/rf0230))
17. K. Wang, L. Ma, G. Liu, D. Cao, R. Guan, Z. Liu, *Dyes Pigments* **126** (2016) 104 (<http://10.1016/j.dyepig.2015.11.019>)
18. K. Wang, W. Feng, Y. Wang, D. Cao, R. Guan, X. Yu, Q. Wu, *Inorg. Chem. Commun.* **71** (2016) 102 (<http://dx.doi.org/10.1016/j.inoche.2016.07.013>)
19. L. Wang, D. Ye, D. Cao, *Spectrochim. Acta A* **90** (2012) 40 (<http://dx.doi.org/10.1016/j.saa.2012.01.017>)
20. X. Cao, N. Zhao, H. Lv, Q. Ding, A. Gao, Q. Jing, T. Yi, *Langmuir* **33** (2017) 7788 ([http://refhub.elsevier.com/S0039-9140\(19\)30151-1/sbref55](http://refhub.elsevier.com/S0039-9140(19)30151-1/sbref55))
21. H. Ma, C. He, X. Li, O. Ablikim, S. Zhang, M. Zhang, H. Ma, C. He, X. Li, O. Ablikim, S. Zhang, M. Zhang, *Sensors Actuators, B* **230** (2016) 746 ([http://refhub.elsevier.com/S1386-1425\(17\)30131-2/rf0205](http://refhub.elsevier.com/S1386-1425(17)30131-2/rf0205))
22. J. Y. Du, J. P. Liu, Y. F. Ren, C. W. Wang, F. B. Bai, H. X. Hao. *Spectrochim. Acta, A* **211** (2019) 287 (<https://doi.org/10.1016/j.saa.2018.12.014>)
23. F. Cheng, X. An, C. Zheng, S. Cao, *RSC Adv.* **113** (2015) 93360 (<https://doi.org/10.1039/C5RA19029K>)
24. G. J. Park, H. Kim, J. J. Lee, Y. S. Kim, S. Y. Lee, S. Lee, I. Noh, C. Kim, *Sensors Actuators, B* **215** (2015) 568 ([http://refhub.elsevier.com/S0040-4020\(16\)30405-7/sref33](http://refhub.elsevier.com/S0040-4020(16)30405-7/sref33))

25. Y. Tian, Y. Chen, M. Chen, Z. L. Song, B. Xiong, X. B. Zhang. *Talanta* **221** (2021) 121627 (<https://doi.org/10.1016/j.talanta.2020.121627>)
26. W. Cui, L. Y. Wang, G. Xiang, L. X. Zhou, X. N. An, D. R. Cao, *Sensors Actuators, B*, **207** (2015) 281 (<http://dx.doi.org/10.1016/j.snb.2014.10.072>)
27. B. Liu, H. Tan, Y. Chen, *Microchimica Acta* **180** (2013) 331 ([http://refhub.elsevier.com/S0925-4005\(18\)30732-9/sbref0240](http://refhub.elsevier.com/S0925-4005(18)30732-9/sbref0240))
28. Y. Fu, L. Mu, X. Zeng, J. L. Zhao, C. Redshaw, X. L. Ni, T. Yamatoc, *Dalton Trans.* **42** (2013) 3552 ([http://refhub.elsevier.com/S2214-1804\(15\)30025-8/rf0160](http://refhub.elsevier.com/S2214-1804(15)30025-8/rf0160))
29. Y. Li, H. Yu, G. Shao, F. Gan. *J. Photochem. Photobiol., A* **301** (2015) 14 (<http://dx.doi.org/10.1016/j.jphotochem.2014.12.013>)
30. C. Chen, H. Liu, B. Zhang, Y. Wang, K. Cai, Y. Tan, C. Gao, H. Liu, C. Tan, Y. Jiang, *Tetrahedron* **72** (2016) 3980 (<http://dx.doi.org/10.1016/j.tet.2016.05.020>)
31. L. L. Liu, F. J. Dan, W. J. Liu, X. Lu, Y. L. Han, S. Z. Xiao, H. C. Lan, *Sensors Actuators, B* **247** (2017) 445 (<http://dx.doi.org/10.1016/j.snb.2017.03.069>)
32. X. Hu, H. Zeng, T. Chen, H. Q. Yuan, L. Zeng, G.-M. Bao, *Sensors Actuators, B* **319** (2020) 1282829 (<http://dx.doi.org/10.1016/j.snb.2020.128282>)
33. S. Zhang, H. Wang, Y. Li, F. Y. Data, Q. Wang, L. Jiao, *Mater. Lett.* **263** (2020) 127208 (<https://doi.org/10.1016/j.matlet.2019.127208>)
34. H. Ma, F. Li, L. Yao, Y. Feng, Z. Zhang, M. Zhang, *Sensors Actuators, B* **259** (2018) 380 (<https://doi.org/10.1016/j.snb.2017.12.029>)
35. S. Zhang, H. Wang, Y. Li, F. Y. Data, Q. Wang, L. Jiao, *Mater. Lett* **263** (2020) 127208 (<https://doi.org/10.1016/j.matlet.2019.127208>)
36. F. Qiu, Y. H. Huang, Q. M. Ge, M. Liu, H. Cong, Z. Tao. *Spectrochimica Acta, A* **226** (2020) 117583. (<https://doi.org/10.1016/j.saa.2019.117583>)
37. S. Philip, P. S. Thomas, K. Mohanan. *J. Serb. Chem. Soc.* **83** (2018) 561 (<https://doi.org/10.2298/JSC180918010P>).



J. Serb. Chem. Soc. 86 (9) 871–884 (2021)
JSCS–5468

Enhanced gas permeation performance of mixed matrix membranes containing polysulfone and modified mesoporous MCM-41

KAVEH ABBASI KOLOLI¹, SEYED MOSTAFA TABATABAEI GHOMSHEH^{1*}, MAZIAR NOEI² and MASOUD SABERI³

¹Department of Chemical Engineering, Mahshahr Branch, Islamic Azad University, Mahshahr, Iran; ²Department of Chemistry, Faculty of Pharmaceutical Chemistry, Tehran Medical Sciences, Islamic Azad University, Tehran, Iran; ³Department of Chemical Engineering, Bushehr Branch, Islamic Azad University, Bushehr, Iran

(Received 19 February, revised 18 April, accepted 29 April 2021)

Abstract: The aim of this study was the development of mixed matrix membranes (MMMs) based on silica MCM-41 dispersed in polysulfone (PSf) for the separation of carbon dioxide from methane. For this purpose, MCM-41 was synthesized by a hydrothermal method and was modified with 3-aminopropyltriethoxysilane (APTES). SEM, FTIR, BET and XRD analyses were used for characterization of the modified and unmodified particles. Then, various MMMs containing PSf at different weight percents (5, 10, 15 and 20) of modified and unmodified particles were prepared and the morphology and structure of the prepared membranes were studied using SEM and XRD analyses. Regardless of the particle type, the addition of MCM-41 to PSf caused an increase in gas permeability compared to a neat PSf membrane. Adding unmodified particles to PSf matrix resulted in undesirable effects, including particle agglomeration and/or the formation of interfacial voids. The MMMs with modified MCM-41 showed relatively better separation performance compared to MMMs with unmodified MCM-41. As a result, the MMM of PSf with 20 wt. % modified MCM-41 showed a significant increase in selectivity of carbon dioxide/methane and the value of selectivity reached 25.24.

Keywords: PSf; MCM-41; surface modification; silane coupling agent; gas separation.

INTRODUCTION

Separation of carbon dioxide as an undesirable component for increasing the heating value of fuel is one of the general separation processes in the natural gas industry. Furthermore, carbon dioxide causes corrosion of process equipment in

* Corresponding author. E-mail: m.tabatabaei@mhriau.ac.ir
<https://doi.org/10.2298/JSC210219034A>

the presence of water. Therefore, the separation of carbon dioxide from methane and bringing it to an acceptable level before the distribution of natural gas is essential.¹⁻³

Polymeric membranes are widely used in natural gas separation processes. The difference in gas permeability rates is the basis of membrane processes for the separation of gases.⁴⁻⁷ Polymeric membranes have good process properties, including low energy consumption, high transport properties, and low current and constant cost. Currently, the membranes have many applications for the separation of gases, such as oxygen/nitrogen enrichment, hydrogen recycling, separation of carbon dioxide from methane or nitrogen, and separation of organic materials from the output currents.^{8,9}

Membrane technology for removal of carbon dioxide has been established since the 1980s with the rapid growth of the natural gas industry.^{10,11} Robeson reported that there is usually a reverse relationship between permeability and selectivity for neat polymer membranes.¹² To overcome this drawback of neat polymer membranes, mineral fillers with porous structure were used within the polymer matrix to improve the gas separation performance. These minerals have unique structure, surface chemistry and mechanical strength. These compounds, known as MMMs, have been extensively tested for the separation of carbon dioxide from natural gas, Flue gas and biogas.¹³⁻¹⁹

Depending on the type of nanoparticles, MMMs can significantly reduce the cost of membranes in comparison to expensive inorganic membranes.^{20,21} The presence of porous silica particles in the polymer matrix with a proper distribution leads to improvement in the mechanical strength and thermal stability of the polymer. High specific surface area, high surface adsorption of carbon dioxide, narrow and regular channels, large pore sizes with adjustable pore dimensions, high thermal and mechanical stability and simplicity of surface modification are the most important characteristics of MCM-41, which makes these nanoparticles known as the most famous member of the M41S family (MCM-41, MCM-48, MCM-50).²²⁻²⁶ It is worth mentioning that one of the most important criteria in MMMs is the achievement of good adhesion between the mineral filler and the polymer matrix. Generally, glassy polymers have good separation performance and high mechanical stability. However, the use of some polymers to fabricate a MMM due to the lack of suitable compatibility between the surface of inorganic nanoparticles and polymer matrix may have non ideal effects, such as agglomeration of the particles and formation of surface voids around the particles. These defects, which cause non selective voids in the membrane, are the most important challenges in the fabrication of an MMM.^{27,28} Sorribas *et al.* investigated the effect of adding micro-mesoporous silica ZIF-8 -MSS to the PSf matrix for the separation of carbon dioxide/methane. They reported that in the fabricated membrane, gas permeability increased and selectivity was almost

unchanged.²⁹ One of the most important points in the preparation of MMMs is the homogeneous dispersion of particles in the polymer matrix, which has a direct effect on the properties of the MMMs.³⁰ Vankelecom *et al.* improved the compatibility between the nanoparticles and the polymer matrix by modifying the outer surface of the zeolite. As a result, the prepared membrane showed better performance under optimal conditions of silane use.³¹

In the present research, silica MCM-41 was synthesized by the hydrothermal method and the solvent method (SO) was used for modifying the particles employing the APTES silane coupling agent. Modified and unmodified particles were characterized by SEM, FTIR and XRD analyses. Then, three groups of membranes, including neat PSf membrane, MMMs consisting of PSf and different content (5, 10, 15, 20 wt. %) of unmodified and APTES-modified MCM-41 were prepared, which were labelled as PSf, PSf-UMO-M_x and PSf-AP-M_x (*x* indicates the weight percentage of particles). These membranes were examined by XRD and SEM analyses. Finally, the performance of these membranes in the separation of carbon dioxide from methane was studied by gas permeability and selectivity tests.

EXPERIMENTAL

Materials

Cetyltrimethylammonium bromide (CTAB), tetraethylorthosilicate (TEOS), sodium hydroxide (NaOH), tetrahydrofuran (THF) and APTES were purchased from Merck. Anhydrous toluene was purchased from Sigma Chemical Co. Moreover, polysulfone (Udel P-1700 grade), a glassy polymer with a glass transition temperature (T_g) of 185 °C, was obtained from Amoco.

Synthesis and Functionalization of MCM-41 mesoporous silica

Synthesis of MCM-41 particles. The hydrothermal method was used to achieve MCM-41 particles with a uniform pore size distribution.^{32,33} In this method, an aqueous micellar solution containing 1 g of CTAB surfactant, 0.28 g of sodium hydroxide and 480 ml of deionised water was prepared under stirring for 1 h. Then, 5 ml of TEOS, as a silica source, was slowly added to the solution at 80 °C in an oil bath to form a white slurry solution. After 2 h stirring (500 rpm), the slurry was transferred to a glass container and was left for 24 h to be completely transformed. The slurry was filtered using a ceramic filter and washed many times with deionised water until the filtrate became neutral. Then, the resulting precipitate was dried at ambient temperature. Finally, the obtained powder was calcined at 550 °C in air for 6 h to remove the surfactant.

Functionalization of MCM-41 particles. The synthesized MCM-41 particles were silylated as follows: in the first step, 100 ml of toluene and 0.4 g of MCM-41 were mixed and this mixture was sonicated for 5 min. Then 0.4 g of APTES was dissolved in the toluene and the suspension solution was refluxed at 68 °C for 6 h under nitrogen atmosphere to form covalent bond between functional components and particle surface. After cooling, the mixture was filtered using filter paper. Finally, the excess amine was removed by Soxhlet extraction for 10 h using dichloromethane and the amine modified MCM-41 particles were dried for 6 h at room temperature under vacuum.

Fabrication of membranes

The neat membrane and MMMs were fabricated using the solution casting method. Before preparation of the membranes, PSf was degassed at 80 °C for 8 h under vacuum to remove absorbed moisture. For preparing the neat membrane with 10 wt. % PSf, 0.5 g PSf was added to 4.5 g THF and stirred at room temperature to obtain a uniform solution. Then, the preparation solution was cast on a glass plate and placed at 40 °C for 24 h to evaporate the solvent. The remaining solvent in the prepared membrane was evaporated in a vacuum oven at 85 °C for 4 h.

For fabrication of the MMMs, in the first step, due to the presence of different number of particles in the polymer matrix (5, 10, 15 and 20 wt. %), the amount of each modified and unmodified MCM-41 was dried in a vacuum oven. Then, the fillers were added to 3 g of THF and the mixture was stirred for 10 h and to increase dispersion was sonicated for 20 min. The process of stirring and sonicating were repeated twice. At the same time, a homogeneous solution containing PSf and THF was stirred in another container. Then 4–5 drops of this solution were added to the suspension and this suspension was stirred and sonicated for 20 min again in order to cover the surface of the particles. Then, the remainder of the polymeric solution was added to the suspension and this suspension was stirred and sonicated to prevent formation of particle agglomerates. Then, the mixture was stirred for 4 h at room temperature and was sonicated for 10 minutes to remove any gas bubbles before casting. The final casting on a glass plate was similar to that used for the neat PSf membrane.

Characterization

Fourier transform infrared (FTIR) spectroscopy was performed using a Thermo Avatar spectrometer in the range of 4000–400 cm^{-1} to characterize the functional groups of the particles. The morphology of unmodified and modified MCM-41 particles and membranes was investigated using a MIRRA 3 Tescan scanning electron microscope (SEM). The N_2 adsorption–desorption isotherms were collected at 77 K using Micromeritics ASAP 2020. The Surface areas and the pore size distribution were determined by the BET and BJH methods, respectively. Membranes were broken under liquid nitrogen and sputter coated with gold using Cressington HR208 (UK) high resolution sputter coater. X-Ray diffraction (XRD) patterns were determined using a X'Pert Pro, analytical X-ray diffractometer. The results were recorded using Cu $K\alpha$ radiation ($\lambda = 0.154 \text{ nm}$) in the 2θ range of 1–10° for MCM-41 and in the 2θ range of 10–90° for the neat membrane and MMMs.

Gas permeation measurements

The permeability in the neat membrane and MMMs fabricated using the constant pressure method was measured with a soap bubble flow-meter. The gas permeability device consisted of a gas permeability cell in which the membrane is placed and one side is exposed to the gas feed. The pressure on the feed side was regulated by a regulator and measured by a pressure gauge. In this study, the fabricated membranes were tested for gas permeability to methane and carbon dioxide gases with a purity of 99.99 %.

The permeability of gas i in the membrane, P_i , is obtained using Eq. (1):

$$P_i = \frac{l}{A\Delta p} \frac{dV_i}{dt} \quad (1)$$

where P_i / Barrer is the permeability of gas i (1 Barrer = $10^{-10} \text{ cm}^3_{\text{STP}} \text{ cm}^{-2} \text{ s}^{-1} \text{ cmHg}^{-1}$); V_i / cm^3 is the volume of displaced gas in the soap bubble flow-meter or volume of gas permeation in the membrane; A / cm^2 is the effective surface area of the membrane; l / cm is the thickness of the

membrane, which was measured with a micrometer; t/s is the time interval of soap bubble movement in the column and Δp is the pressure drop across the membrane, cm_{Hg} . The gas permeability in this study was determined at a pressure of 8 bar.

The ideal selectivity of gases, α_{ij} , for each membrane was obtained with Eq. (2):

$$\alpha_{ij} = \frac{P_i}{P_j} \quad (2)$$

where α_{ij} is the ideal selectivity of gas i to j and P_i and P_j are the permeability of the gases i and j , respectively.

RESULTS AND DISCUSSION

Characterization results of silica MCM-41

The particles morphology was assessed by SEM analysis. SEM images of the unmodified MCM-41 particles and the particles modified with APTES are shown in Fig. 1. Unmodified MCM-41 particles (Fig. 1a) have particle diameters of about 200 to 650 nm and a spherical shape. The modified MCM-41 particles (Fig. 1b) have diameters in the range of 200 to 650 nm and a spherical shape. As can be seen, the MCM-41 particles did not undergo structural and morphological changes after modification, and their structure was preserved.

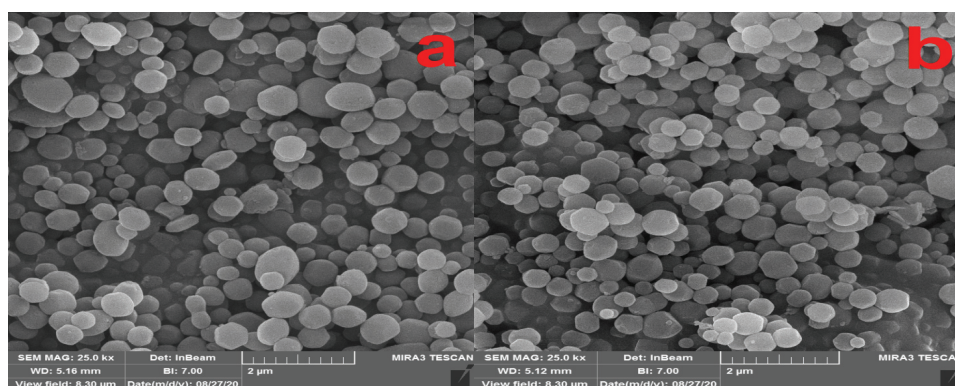


Fig. 1. SEM image of: a) unmodified and b) APTES modified MCM-41.

The infrared spectra of MCM-41 in the range $4000\text{--}400\text{ cm}^{-1}$ before and after functionalization with APTES are shown Fig. 2. The inset of the figure shows the clarification of peaks in the range of $1250\text{--}400\text{ cm}^{-1}$. As shown in Fig. 2a, for unmodified MCM-41 particles, the peaks observed in region 3402 cm^{-1} are due to O–H stretching vibrations of water molecules adsorbed on its surface as well as hydroxyl silanol groups Si–OH. The peak observed at 1626 cm^{-1} belongs to the vibrations of H_2O molecules trapped in the lattice. The main characteristic of MCM-41 particles is the presence of a silicate network. This characteristic is observed by the peaks at 460 , 950 and 1084 cm^{-1} , which belong to the Si–O–Si, Si–OH and Si–O silicate groups, respectively. As can be seen in

Fig. 2b, a new peak appeared in the 2932 cm^{-1} region after APTES functionalized the mesoporous silica particles. This peak belongs to the vibrations of C–H groups, which are caused by the substituent propyl group of APTES. The changes observed in the 1480 cm^{-1} region also indicate changes in amine bonds that occur after functionalization of the particles. Amination also changes the appearance of the peak at 3402 cm^{-1} . The above observations show that modification of particles was successfully performed by APTES using the SO method.

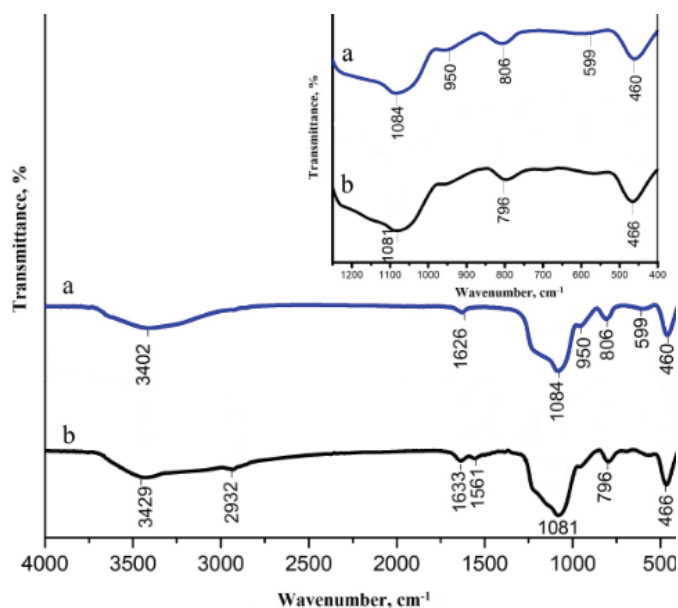


Fig. 2. FTIR spectra for the unmodified (a) and APTES modified (b) MCM-41.

The XRD spectrum for unmodified MCM-41 particles is shown in Fig. 3. The diffraction angles observed at 2θ 1.75 , 3.65 , 4.3 and 5.9° belong to the (100), (110), (200) and (210) planes, respectively. These peaks are well matched to the hexagonal P6 space array of MCM-41 particles³² and indicate the crystallinity of silica MCM-41 particles. Since MCM-41 is not crystalline at the atomic level, no reflection were observed at higher angles. The results indicate the MCM-41 particles were successfully synthesized.

The specific surface area (SBET) and average pore diameter (Pd) of unmodified and modified MCM-41 particles are presented in Table I and Fig. 4. In addition, pore diameter (D) and pore volume (v) are shown in Fig. 4. The inset of the Figure shows the pore size diameter of unmodified and modified MCM-41 particles. Nitrogen adsorption isotherms at 77 K for unmodified and modified MCM-41 both are reversible type IV adsorption isotherms corresponding to a mesoporous material. Unmodified MCM-41 particles had a specific surface area

of $1111.6 \text{ m}^2 \text{ g}^{-1}$, while after modification, the specific surface area of the particles decreased to $520.52 \text{ m}^2 \text{ g}^{-1}$ due to functionalization using APTES. The pore size distribution was computed using the BJH method.

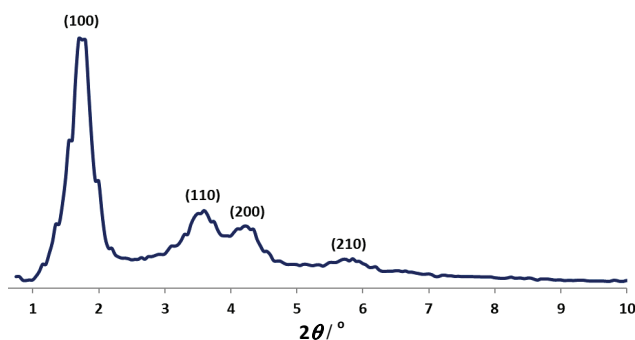


Fig. 3. XRD pattern of unmodified MCM-41.

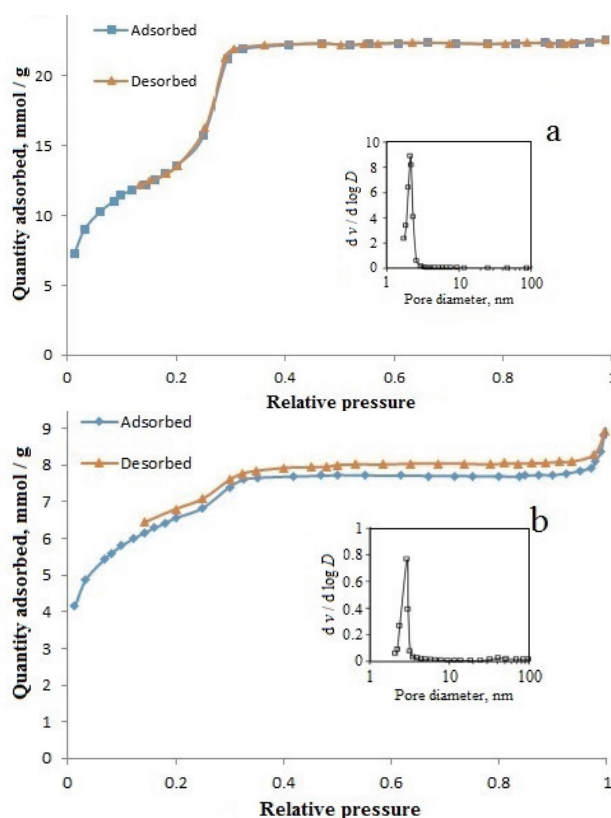


Fig. 4. BET isotherms and BJH pore size distribution for the unmodified (a) and the APTES-modified (b) MCM-41.

TABLE I. Specific surface area and average pore diameter of MCM-41 before and after modification

Type of silica MCM-41	Surface modified MCM-41 materials	$S_{\text{BET}} / \text{m}^2 \text{g}^{-1}$	D_p / nm
Unmodified MCM-41	–	1111.6	2.88
Modified MCM-41	APTES	520.52	2.61
Unmodified MCM-41 ²⁵	–	845	3.1
Modified MCM-41*	<i>n</i> -Octyldimethylmethoxysilane	528	2.3

The average pore diameter of 2.88 nm for unmodified particles was obtained. Also, it was observed that the diameter of the pores remains almost in the same range after functionalization and reach to 2.61 nm that shows the mesoporous structure was preserved. According to Table I and Fig. 4, the decrease in surface area and average pore diameter showed the presence of APTES on the surface of MCM-41.

Characterization results of mixed matrix membranes

SEM images of the cross section for neat PSf membrane and PSf-UMO-M10 MMM are shown in Fig. 5. As can be seen in Fig. 5a, the cross-sectional SEM image of the neat PSf membrane shows a homogeneously dense morphology while dispersion of the unmodified MCM-41 particles in the MMM increases the roughness of the cross section. Fig. 5b shows the agglomeration of particles and the presence of surface voids in the surface between the polymer and the particle.

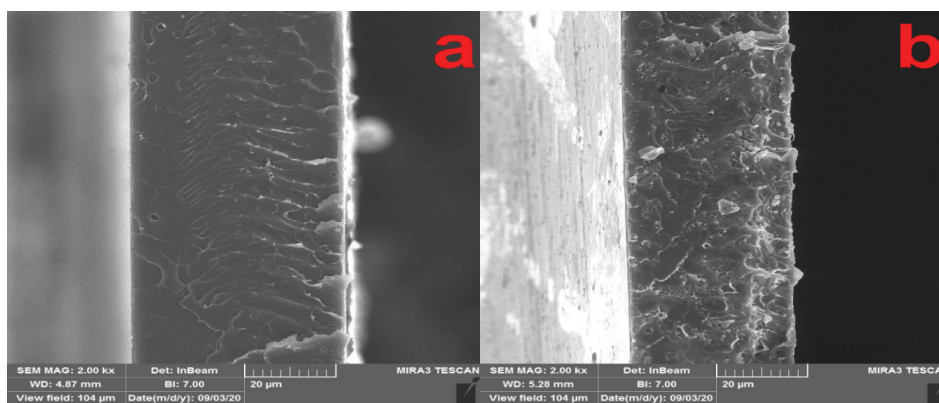


Fig. 5. SEM images of cross section of: a) neat PSf membrane and b) PSf-UMO-M10 MMM.

The results of XRD analysis for the neat PSf membrane, PSf-UMO-M10 and PSf-AP-M10 MMMs are shown in Fig. 6. As can be seen, the neat PSf membrane has an amorphous structure with a large peak at $2\theta = 18^\circ$ and a small peak around $2\theta = 44^\circ$. The XRD pattern of different MMMs shows peaks similar to those for neat PSf originating from the amorphous polymer structure. Therefore, the addition of MCM-41 silica particles to PSf did not change the diffraction pattern of PSf

membrane and the pattern characteristic and amorphous characterization of the membrane were preserved. It should be noted that crystalline phases are considered as impermeable regions and the permeability of gas from semi-crystalline polymer membranes is much lower than from amorphous polymer membranes due to the reduction of space for the diffusion of gases as a result of the winding path around the crystals.²⁸

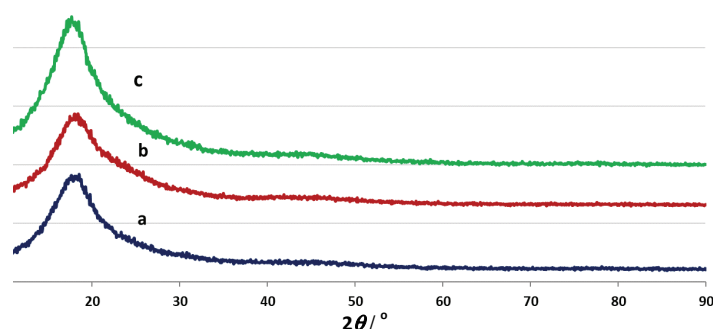


Fig. 6. XRD patterns for: a) the neat PSf, b) PSf-UMO-M10 and c) PSf-AP-M10.

Gas separation results

Gas separation properties including carbon dioxide and methane permeability and ideal selectivity of carbon dioxide/methane for neat PSf membrane and PSf-modified and unmodified MCM-41 MMMs are given in Figs. 7 and 8. In addition, the effect of the presence of different types of MCM-41 (20 wt. %) in the MMMs on the permeability and selectivity is given in Table II.

Regardless of the type of particles (modified and unmodified particles), the addition of MCM-41 to the PSf matrix increased the permeability of all MMMs in comparison to the neat PSf membrane. In general, this increase in permeability in fabricated MMMs has two main reasons: one is that the addition of filler particles increases the volume of voids in the polymer and the other is that the inherent permeability of fillers is higher than that of the polymer. On the other hand, the increase in selectivity in the MMMs fabricated of PSf and modified MCM-41 particles is due to the proper performance of APTES, which allows carbon dioxide to pass through the membrane more easily than methane.³⁴

In the PSf-unmodified MCM-41 MMM up to 10 wt. %, the selectivity increased slightly and at higher concentrations decreased (Fig. 8). The reason for this decrease in selectivity is probably related to the low quality of particles dispersion and the formation of non-selective voids in the PSf matrix. The agglomeration of unmodified particles in the polymer matrix is due to the hydroxyl–hydroxyl attraction, which causes improper particles dispersion and reduces the effect of the MCM-41 molecular sieving mechanism.²⁷

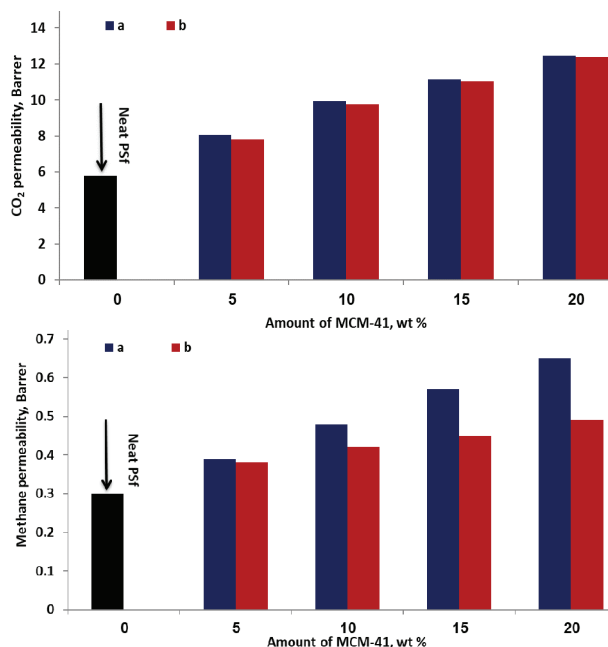


Fig. 7. Effect of: a) unmodified and b) APTES-modified MCM-41 loading on the measured permeabilities of carbon dioxide (left side) and methane (right side) through MMMs at 8 bar and room temperature.

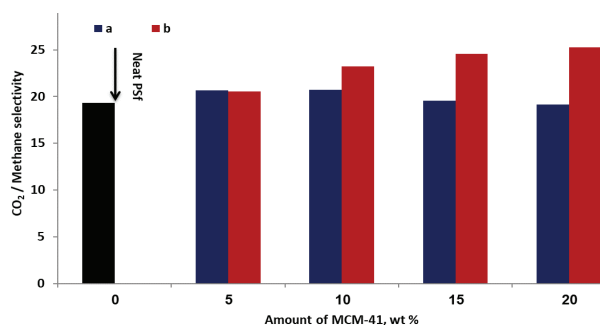


Fig. 8. Effect of: a) unmodified and b) APTES-modified MCM-41 loading on the carbon dioxide/methane selectivity for MMMs at 8 bar and room temperature.

In MMMs consisting of mineral particles dispersed in a polymer matrix, the bond between the two materials plays an important role in the performance of these membranes. A silane coupling agent can increase the adhesion between a polymer matrix and mineral fillers.³⁵ Therefore, in order to increase the adsorption capacity of carbon dioxide by the membrane, the surface of silica MCM-41 particles was modified before being placed in the polymer matrix by APTES and its effect on the separation performance of PSf-MCM-41 MMM was investigated. For APTES-

-modified particles in the PSf matrix, the polar groups of the aminopropyl bond interact with the polar sulfone groups to form new hydrogen bonds. Therefore, the addition of modified MCM-41 particles to PSf causes the particles to be homogeneously dispersed in the polymer structure and produce a MMM without defects. Under these conditions, even at high weight percentages, the particles disperse properly and increase the selectivity of MMMs.

TABLE II. Permeabilities and selectivity's of carbon dioxide and methane through the unmodified and modified MCM-41 (20 wt. %) MMMs at 8 bar and room temperature

Membrane	P_{CO_2} / Barrer	P_{methane} / Barrer	$\alpha = P_{\text{CO}_2}/P_{\text{methane}}$
PSf-UMO-M20	12.46	0.65	19.17
PES-UMO-M20 ²⁷	3.56±0.17	0.13±0.01	26.5
PSf-AP-M20	12.37	0.49	25.24
PES-APTMS-M20 ²⁷	3.44±0.16	0.1±0.01	35.6

The addition of the unmodified MCM-41 to the PSf matrix caused a significant increase in membrane permeability compared to other fabricated membranes (Fig. 7). As a result, the highest permeability was obtained for the PSf-UMO-M20 MMM, in which the permeability of carbon dioxide increased by 114.83 % compared to neat PSf membrane. The selectivity of carbon dioxide/methane in the PSf-AP-M20 MMM compared to neat PSf membrane showed a significant increase and reached 25.24 from 19.33.

CONCLUSIONS

In this work, silica MCM-41 was successfully synthesized by a hydrothermal method and a solvent method was used for modifying these particles by using an APTES silane coupling agent. Modified and unmodified particles were characterized by SEM, FTIR and XRD analyses. Then, three groups of membranes including neat PSf, MMMs consisting of PSf and different weight fractions (5, 10, 15 20 %) of modified and unmodified MCM-41 were prepared and the performance of these membranes in the separation of carbon dioxide from methane was studied by gas permeability and selectivity tests. The results show an increase in the permeability by adding MCM-41 into the PSf matrix, although depending on the modification of MCM-41 using silane coupling agent, the selectivity showed different trends. Due to the tendency of unmodified particles to form hydrogen bonds, particles agglomeration occurs in the polymer matrix at high loading that form non-selective voids. As a result, in MMMs fabricated with unmodified particles, the ideal selectivity did not change much compared to neat PSf membrane. For MMMs with modified MCM-41, the surface modification prevented the formation of hydrogen bonds between particles due to the long side chains of APTES. Moreover, APTES bonding groups have a good compatibility with the polymer matrix even at high loadings (up to 20 wt. %). Therefore, the selectivity

of carbon dioxide/methane was significantly increased compared to the MMMs comprising unmodified MCM-41.

ИЗВОД

ПОБОЉШАНЕ ПЕРФОРМАНСЕ МЕШАНИХ МАТРИЧНИХ МЕМБРАНА КОЈЕ САДРЖЕ
ПОЛИСУЛФОН И МОДИФИКОВАНИ МЕЗОПОРОЗНИ МСМ-41 ЗА
ПРОПУШТАЊЕ ГАСА

KAVEN ABBASI KOLOLI¹, SEYED MOSTAFA TABATABAEI QOMSHEH¹, MAZIAR NOEI² и MASOUD SABERI³

¹Department of Chemical Engineering, Mahshahr Branch, Islamic Azad University, Mahshahr, Iran,

²Department of Chemistry, Faculty of Pharmaceutical Chemistry, Tehran Medical Sciences, Islamic Azad University, Tehran, Iran и ³Department of Chemical Engineering, Bushehr Branch, Islamic Azad University, Bushehr, Iran

Циљ ове студије је развој мешаних матричних мембрана (MMM) на бази силицијум-диоксида МСМ-41 диспергованог у полисулфону (PSf) за одвајање угљен-диоксида од метана. У ту сврху МСМ-41 је синтетизован хидротермалном методом и модификован је са 3-аминопропилтриетоксисиланом (APTES). SEM, FTIR, BET и XRD анализе коришћене су за карактеризацију модификованих и немодификованих честица. Затим су припремљени различити MMM који садрже PSf са различитим масеним процентима (5, 10, 15 и 20 %) модификованих и немодификованих честица и проучавана је морфологија и структура припремљених мембрана помоћу SEM и XRD анализа. Без обзира на врсту честица, додавање МСМ-41 у PSf изазвало је повећање пропусности гасова у поређењу са мембраном од PSf. Додавање немодификованих честица у PSf матрицу резултирало је неидеалним ефектима, укључујући агломерацију честица и/или стварање међуфазних празнина. MMM са модификованим МСМ-41 показали су релативно боље перформансе раздвајања у поређењу са MMM са немодификованим МСМ-41. Као резултат, MMM PSf са 20 мас. % модификованог МСМ-41 показала је значајан пораст селективности угљен-диоксида/метана и вредност селективности достигла је 25,24.

(Примљено 19. фебруара, ревидирано 18. априла, прихваћено 29. априла 2021)

REFERENCES

1. J. D. Wind, *PhD Thesis*, University of Texas, Austin, TX, 2002 (<https://repositories.lib.utexas.edu/handle/2152/1048>)
2. R. E. Kesting, A. Fritzsche, *Wiley-Inter.* **36** (1993) 102 (<https://doi.org/10.1002/pi.1995.210360116>)
3. X. Guo, Z. Qiao, D. Liu, C. Zhong, *J. Mat. Chem., A* **7** (2019) 24738 (<https://doi.org/10.1039/C9TA09012F>)
4. S. E. Kentish, C. A. Scholes, G. W. Stevens, *Recent Patent Chem. Eng.* **1** (2008) 52 (<https://www.ingentaconnect.com/content/ben/cheng/2008/00000001/00000001/art00005>)
5. P. Pandey, R. Chauhan, *Prog. Polym. Sci.* **26** (2001) 853 ([https://doi.org/10.1016/S0079-6700\(01\)00009-0](https://doi.org/10.1016/S0079-6700(01)00009-0))
6. M. Saberi, *J. Serb Chem. Soc.* **86** (2021) 341 (<https://doi.org/10.2298/JSC200715046S>)
7. A. Bos, I. G. M. Punt, M. Wessling, H. Strathmann, *Sep. Purif. Technol.* **14** (1998) 27 ([https://doi.org/10.1016/S1383-5866\(98\)00057-4](https://doi.org/10.1016/S1383-5866(98)00057-4))
8. J. D. Wind, C. Staudt-Bickel, D. R. Paul, W. J. Koros, *Ind. Eng. Chem. Res.* **41** (2002) 6139 (<https://doi.org/10.1021/ie0204639>)

9. A. Brunetti, P. Bernardo, E. Drioli, G. Barbieri, Y. Yampolskii, B. Freeman, *Membr. Gas Separ.* **6** (2010) 279
10. P. Bernardo, G. Clarizia, *Eng. Trans.* **32** (2013) 1999
(<https://doi.org/10.3303/CET1332334>)
11. L. M. Robeson, *J. Membr. Sci.* **320** (2008) 390
(<https://doi.org/10.1016/j.memsci.2008.04.030>)
12. J. K. Ward, W. J. Koros, *J. Membr. Sci.* **377** (2011) 75
(<https://doi.org/10.1016/j.memsci.2011.04.010>)
13. T. W. Pechar, S. Kim, B. Vaughan, E. Marand, M. Tsapatsis, H. K. Jeong, C. J. Cornelius, *J. Membr. Sci.* **277** (2006) 195 (<https://doi.org/10.1016/j.memsci.2005.10.029>)
14. E. Karatay, H. Kalıpçılar, L. Yılmaz, *J. Membr. Sci.* **364** (2010) 75
(<https://doi.org/10.1016/j.memsci.2010.08.004>)
15. P. Jha, J. D. Way, *J. Membr. Sci.* **324** (2008) 151
(<https://doi.org/10.1016/j.memsci.2008.07.005>)
16. S. Rafiq, Z. Man, A. Maulud, N. Muhammad, S. Maitra, *Sep. Purif. Technol.* **90** (2012) 162 (<https://doi.org/10.1016/j.seppur.2012.02.031>)
17. A. M. Hillock, S. J. Miller, W. J. Koros, *J. Membr. Sci.* **314** (2008) 193
(<https://doi.org/10.1016/j.memsci.2008.01.046>)
18. M. Junaidi, C. Leo, S. Kamal, A. Ahmad, T. Chew, *Fuel Process.* **112** (2013) 1
(<https://doi.org/10.1016/j.fuproc.2013.02.014>)
19. R. Mahajan, R. Burns, M. Schaeffer, W. J. Koros, *J. Appl. Polym. Sci.* **86** (2002) 881
(<https://doi.org/10.1002/app.10998>)
20. T. T. Moore, R. Mahajan, D. Q. Vu, W. J. Koros, *AIChE J.* **50** (2004) 311
(<https://doi.org/10.1002/aic.10029>)
21. X. Liu, H. Sun, Y. Chen, Y. Yang, A. Borgna, *Microporous Mesoporous Mat.* **121** (2009) 73 (<https://doi.org/10.1016/j.micromeso.2009.01.018>)
22. M. Nekoomanesh, H. Arabi, G. Nejabat, M. Emami, G. Zohuri, *Iran. J. Polym. Sci. Tech. (Persian)*, **21** (2008) 243
23. T. L. Chew, A. L. Ahmad, S. Bhatia, *Adv. Coll. Int. Sci.* **153** (2010) 43
(<https://doi.org/10.1016/j.cis.2009.12.001>)
24. G. R. Nejabat, M. Nekoumanesh, H. Arabi, *Iran. Polym. J.* **19** (2010) 79
(<https://www.sid.ir/en/journal/ViewPaper.aspx?id=167621>)
25. T. Yasmin, K. Müller, *J. Chromat., A* **1217** (2010) 3362
(<https://doi.org/10.1016/j.chroma.2010.03.005>)
26. M. Laghaei, M. Sadeghi, B. Ghalei, M. Dinari, *Prog. Org. Coat.* **90** (2016) 163
(<https://doi.org/10.1016/j.porgcoat.2015.10.007>)
27. M. Laghaei, M. Sadeghi, B. Ghalei, M. Shahrooz, *J. Mem. Sci.* **513** (2016) 20
(<https://doi.org/10.1016/j.memsci.2016.04.039>)
28. S. Sorribas, B. Zornoza, C. Téllez, J. Coronas, *J. Membr. Sci.* **452** (2014) 184
(<https://doi.org/10.1016/j.memsci.2013.10.043>)
29. J. Yuan, S. Zhou, G. Gu, L. Wu, *J. Mat. Sci.* **40** (2005) 3927
(<https://link.springer.com/article/10.1007/s10853-005-0714-8>)
30. I. F. Vankelecom, E. Scheppers, R. Heus, J. B. Uytterhoeven, *J. Phys. Chem.* **98** (1994) 12390 (<https://doi.org/10.1021/j100098a038>)
31. Q. Cai, Z. S. Luo, W. Q. Pang, Y. W. Fan, X. H. Chen, F. Z. Cui, *J. Chem. Mater.* **13** (2001) 258 (<https://doi.org/10.1021/cm990661z>)

32. M. Janicke, C. Landry, S. Christiansen, S. Birtalan, G. Stucky, B. Chmelka, *Chem. Mat.* **11** (1999) 1342 (<https://doi.org/10.1021/cm981135v>)
33. A. Jomekian, M. Pakizeh, A. R. Shafiee, S. A. A. Mansoori, *Sep. Purif. Technol.* **80** (2011) 556 (<https://doi.org/10.1016/j.seppur.2011.06.011>)
34. T. C. Merkel, Z. He, I. Pinnau, B. D. Freeman, P. Meakin, A. J. Hill, *Macromolecules* **36** (2003) 6844 (<https://doi.org/10.1021/ma0341566>)
35. I. F. Vankelecom, S. van den Broeck, E. Merckx, H. Geerts, P. Grobet, J. B. Uytterhoeven, *J. Phys. Chem.* **100** (1996) 3753 (<https://doi.org/10.1021/jp9526511>).



J. Serb. Chem. Soc. 86 (9) 885–897 (2021)
JSCS–5469

Kinetic and isotherm studies for the biosorption of nickel ions by jute fabrics

ALEKSANDRA IVANOVSKA^{1*#}, LEPOSAVA PAVUN^{2#}, BILJANA DOJČINOVIĆ³
and MIRJANA KOSTIĆ^{4#}

¹University of Belgrade, Innovation Center of the Faculty of Technology and Metallurgy, Karnegijeva 4, 11000 Belgrade, Serbia, ²University of Belgrade, Faculty of Pharmacy, Vojvode Stepe 450, 11000 Belgrade, Serbia, ³University of Belgrade, Institute of Chemistry, Technology and Metallurgy, Njegoševa 12, 11000 Belgrade, Serbia and ⁴University of Belgrade, Faculty of Technology and Metallurgy, Karnegijeva 4, 11000 Belgrade, Serbia

(Received 19 January, revised 11 April, accepted 12 April 2021)

Abstract: Raw jute fabric was chemically modified with 1 % NaOH for 30 min, 17.5 % NaOH for 5 min or with 0.7 % NaClO₂ for 30 and 60 min to study the influence of changes in the chemical composition of the fabrics and quantity of carboxyl groups on the biosorption capacity of the fabrics for nickel ions. The effects of contact time and initial concentration of nickel ions on the biosorption capacity of the fabrics were also investigated. The obtained results revealed that the biosorption of nickel ions can be explained by the pseudo-second-order kinetic model, while the experimental isotherm data fit better with the Langmuir model. The calculated ratios between maximal biosorption capacity (6.30–12.06 mg g⁻¹) of the jute fabrics and carboxyl group quantity indicated that approximately half of the carboxyl groups of the fabrics' would be involved in binding nickel ions during biosorption. Therefore, the quantity of carboxyl groups can be used to predict the maximal biosorption capacity of jute fabrics toward nickel ions. In the case of oxidized jute fabrics, the lignin removal, and consequently increased content of cellulose and hemicelluloses, also contributed to a higher biosorption capacity.

Keywords: chemical composition; carboxyl groups; hemicelluloses; lignin; pseudo-second-order; Langmuir model.

INTRODUCTION

Industrial expansion enables the detection of numerous environmental problems and contributes to improving the quality of the environment by applying new technologies to solve existing problems. In many instances, such problems are

* Corresponding author. E-mail: aivanovska@tmf.bg.ac.rs

Serbian Chemical Society member.

<https://doi.org/10.2298/JSC210209030I>

historic pollution and the presence of heavy metals in an environment posing a specific threat since they cannot be degraded. Among other heavy metals, considerable amounts of nickel ions are present in the wastewaters generated from mining, electroplating, pigments and ceramic industries. The presence of these ions in aqueous systems at trace levels has become a worldwide health and environmental concern due to the possibility of entering the food chain.

Various physicochemical methods have already been developed for the removal of heavy metal ions from wastewaters. Some of them (such as precipitation and coagulation) are less efficient and create sludge, while others (such as ion-exchange and reverse osmosis) are effective and efficient, but expensive. Additionally, these conventional methods are found to be inappropriate or ineffective for the removal of trace metals indicating the necessity for finding alternative wastewater treatments. Nowadays, biosorption using lignocellulosic waste has received remarkable attention since it is very efficient for absorbing heavy metals present in wastewaters at trace levels, *i.e.*, below 100 mg l⁻¹.¹ Besides the mentioned advantage, biosorption using lignocellulosic waste is economically feasible (use of a low-cost resource for applications in pollutant removal), technologically simple (simple equipment; can be applied to different flow regimes), and capable of treating large volumes.² On the other hand, lignocellulosic materials are renewable, biodegradable, and environmentally friendly resources. They are widely available in many countries, can be used in different forms (powders, fibres, felts, steams), can be easily modified by different chemical treatments and grafting reactions, and possess outstanding metal-binding capacities.² After use, these biosorbents can be burned and the metals recovered (*e.g.*, for catalysis), while the lignocellulosic material as abundant and low-cost waste can be used to prepare activated carbons.

It was shown earlier that alkali and oxidative chemical modifications significantly improved the sorption^{3,4} and electrokinetic⁵ properties of jute fabrics. Moreover, such prepared jute fabrics could be successfully used as protective clothes or textile of specific behaviour in environments sensitive to electrical discharges and home textiles due to their improved dielectric properties. Taking into account the wide variety of utilizations of the fabrics, the amount of jute waste having improved sorption properties has considerably increased. Therefore, the objective of the current study was to up value jute fabric waste by its utilization as a biosorbent for wastewater treatment. Recycling in the way of producing filters for wastewaters minimizes the disposal costs of such fabrics thus contributing to “closing the loop” of their lifecycle, which is in agreement with the circular economy concept.

This study reports on the efficiency of chemically modified jute fabrics (derived as waste from other industries) for the removal of nickel ions under different experimental conditions, *i.e.*, initial nickel ion concentration and contact

time. Thereafter, the experimental data were correlated to different kinetic and adsorption isotherm models. Moreover, a correlation between the jute biosorption capacity and its molecular structure (*i.e.*, contents of cellulose and non-cellulosic components as well as quantity of COOH groups) was investigated in detail.

EXPERIMENTAL

Material

Raw jute fabric (sample denoted as RJ) was chemically modified with 1 % NaOH for 30 min (sample A1/30) or with 17.5 % NaOH for 5 min (sample A17.5/5) at room temperature. These modifications were followed by neutralization with 10 % CH₃COOH, washing with distilled water, rinsing with 0.5 % NaHCO₃, washing with distilled water, and drying at room temperature. On the other hand, oxidative modifications of raw jute fabric with 0.7 % NaClO₂ (pH 4–4.5) at boiling temperature for 30 or 60 min (samples marked as C30 and C60, respectively) were followed by washing with distilled water, rinsing with 2 % NaHSO₃, washing and drying at room temperature.

Characterization of obtained jute biosorbents

The chemical composition of raw and chemically modified jute fabrics was determined according to the modified procedure described by Soutar and Bryden.⁶

The carboxyl group quantity was determined using the calcium-acetate method.⁷ The cellulose carboxyl groups react with calcium acetate (weak acid salt), forming a salt of the cellulose and releasing an equivalent amount of the weaker acid. The cellulose should be obtained in the acidic form by replacement of its cations with hydrogen ions by the treatment of jute sample (0.5 g) with 100 mL of 0.01 M HCl solution for 1 h following by washing with distilled water. In the next step, 50 mL of distilled water and 30 mL of 0.25 M calcium acetate were added and the mixture was stirred for 2 h. Thereafter, 30 mL portions of the liquid were titrated with 0.01 M NaOH solution, using phenolphthalein as an indicator. The quantity of carboxyl groups (Q_{COOH} / mmol g⁻¹) was calculated as follows:

$$Q_{\text{COOH}} = \frac{(80/30)0.01V_{\text{NaOH}}}{m} \quad (1)$$

where: 0.01 is the NaOH concentration, mol L⁻¹, V_{NaOH} is the volume of NaOH solution used for titration mL, m is the weight of absolutely dry jute fabric, g.

Biosorption of nickel ions

Jute fabric (0.5 g) was immersed in 200 mL of NiSO₄ solution (distilled water was used as the aqueous matrix) (initial metal ion concentration: 10–30 mg L⁻¹, initial pH: 5.50 adjusted with 0.1 HCl) at room temperature and constantly shaken for 9 h. After defined times (5–540 min), the concentration of nickel ions in the aqueous solution was determined by inductively coupled plasma optical emission spectrometry, ICP-OES (iCAP 6500 Duo ICP, Thermo Fisher Scientific, Cambridge, UK). The measurements were performed at the Ni II 231.604 nm emission-line. Quality control was carried out using blank samples, matrix-matched calibration solutions, and triplicate analyses of each sample.

The biosorption of nickel ions (q / mg g⁻¹) was determined according to:

$$q = \frac{c_0 - c_t}{m} V \quad (2)$$

where: c_0 and c_t in mg L^{-1} are the nickel ion concentrations in the solution before biosorption and after a defined period of biosorption, respectively, V / L is solution volume and m / g is the mass of dry jute fabric.

Adsorption kinetics

The pseudo-first⁸ (Eq. (3)) and pseudo-second-order⁹ (Eq. (4)) kinetic models were used to investigate the biosorption mechanism of nickel ions onto jute fabrics:

$$\log (q_e - q_t) = \log q_e - \left(\frac{k_1}{2.303} \right) t \quad (3)$$

$$\frac{t}{q_t} = \frac{1}{k_2 q_e^2} + \left(\frac{1}{q_e} \right) t \quad (4)$$

where q_e and q_t in mg g^{-1} are the amounts of nickel ions adsorbed per gram adsorbent at equilibrium and at time t / min , k_1 / min^{-1} is the pseudo-first-order rate constant, while $k_2 / \text{g mg}^{-1} \text{min}^{-1}$ is the pseudo-second-order rate constant.

Adsorption isotherms

Langmuir¹⁰ (Eq. (5)) and Freundlich¹¹ (Eq. (6)) isotherm equations were applied for modelling the equilibrium adsorption data, and to assess the maximum biosorption capacities of the jute fabrics:

$$\frac{c_e}{q_e} = \left(\frac{1}{q_m K_L} \right) + \left(\frac{1}{q_m} \right) c_e \quad (5)$$

$$\ln q_e = \ln K_f + \frac{1}{n} \ln c_e \quad (6)$$

where q_e and q_m in mg g^{-1} are the equilibrium and maximal adsorbed nickel per g of adsorbent, $K_L / \text{L mg}^{-1}$ is Langmuir constant, $c_e / \text{mg L}^{-1}$ is the equilibrium nickel concentration in the solution, K_f is the Freundlich constant $/ (\text{mg g}^{-1}) (\text{L mg}^{-1})^{-1/n}$, $1/n$ is a constant related to the surface heterogeneity of the fabric.

RESULTS AND DISCUSSION

Characterization of the jute biosorbents

Chemical modifications with NaOH and NaClO₂ were performed to obtain jute fabrics with different chemical compositions and quantity of carboxyl groups. From the results given in Table I, it is clear that alkali modifications contributed to the selective removal of hemicelluloses (their content decreased to 14 and 37 %), while oxidative modifications led to selective lignin removal (its content decreased to 39 and 63 %). After both types of chemical modifications, cellulose-rich fabrics were obtained (cellulose content increased up to 22 %). Bearing in mind the aim of this investigation, *i.e.*, utilization of waste jute fabrics as biosorbents and the fact that the carboxyl groups represent potential sites for binding metal ions through ion-exchange, their contents within jute fabrics should be taken into consideration, Table I. The increased quantity of carboxyl groups (up to 58 %) in the alkali modified jute fabrics is due to the rupture of lignin–hemicellulose ester linkages, while the sodium chlorite oxidation leads to

conversion of the aldehyde cellulose groups to carboxyl groups (carboxyl group quantity increased up to 81 %), Fig. S-1 of the Supplementary material to this paper.

TABLE I. Chemical composition of jute biosorbents and quantity of COOH groups

Jute fabric	Content \pm SD, %			$Q_{\text{COOH}} / \mu\text{mol g}^{-1}$
	Hemicelluloses	Lignin	Cellulose	
RJ	21.76 \pm 0.38	13.48 \pm 0.56	60.1 \pm 1.3	207 \pm 1
A1/30	18.62 \pm 0.10	13.45 \pm 0.14	67.9 \pm 1.1	327 \pm 7
A17.5/5	13.79 \pm 0.30	12.91 \pm 0.25	73.3 \pm 1.0	284 \pm 7
C30	21.29 \pm 0.23	8.25 \pm 0.39	70.4 \pm 1.5	345 \pm 9
C60	24.93 \pm 0.19	4.96 \pm 0.08	70.1 \pm 1.4	375 \pm 3

Application of the Student's *t*-test confirmed a statistically significant difference between the hemicellulose (in the case of alkali modified jute fabrics) and lignin (in the case of oxidized jute fabrics) contents, as well as the quantity of COOH groups (Table S-I).

Biosorption of nickel ions

Based on the earlier published results,^{3,4} *i.e.*, improved sorption properties (such as moisture sorption and water retention power) of chemically modified jute fabrics, it was expected that waste of those fabrics will possess satisfactory biosorption potential towards heavy metal ions. In this section, the influence of contact time, and initial concentration of nickel ions (selected as a model ion) on the biosorption capacity of jute fabrics was analysed in detail. Moreover, the links between the chemical composition of fabrics as well as the quantity of COOH groups and the biosorption capacity of jute fabrics towards nickel ions were established.

The effect of contact time on the biosorption capacity of jute fabric (in further text: *q*) toward nickel ions ($c_0 = 15 \text{ mg L}^{-1}$) is depicted in Fig. 1. The *q* of raw jute (sample RJ) within the first hour of contact time was about 83 % of its equilibrium biosorption capacity, which is reached after a contact time of 4 h. On the other hand, chemically modified jute fabrics possess higher but slower biosorption of nickel ions. Namely, about 79–81 % of their q_e were observed within a contact time of 2 h, while the equilibriums were attained after a contact time of 7 h. More precisely, at the beginning of the biosorption process, the presence of a large number of free sites for nickel adsorption increased the q_t values (*i.e.*, a quite fast external surface adsorption occurred due to the well-shaken system).¹² However, with prolonged contact time, nickel ions travel within the jute pores, the number of free sites decreased, reducing the nickel adsorption and reaching a plateau. This behaviour could be also ascribed to nickel intra-particle diffusion inside the pores that slowed down the adsorption mainly at the end of the pro-

cess.¹³ Additionally, repulsive forces between nickel ions in solution and those adsorbed, could hinder the diffusion of nickel into the adsorbent structure by extending the contact time.¹²

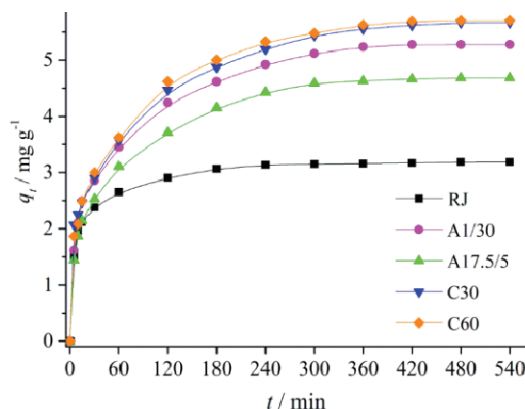


Fig. 1. Biosorption capacity (q_t) of nickel ions ($c_0 = 15 \text{ mg L}^{-1}$) onto jute fabrics as a function of contact time.

The highest content of non-cellulosic components (Table I) is the possible reason for the lowest q values of the raw jute fabric (sample RJ) since they impeded the diffusion and biosorption of nickel ions, Fig. 1. Moreover, this sample has the lowest amount of active sites, *i.e.*, the lowest quantity of COOH groups ($207 \text{ } \mu\text{mol g}^{-1}$), Fig. 2a (q_e is given in $\mu\text{mol g}^{-1}$ to compare with the quantity of COOH groups). A good linear correlation ($r = 0.983$) between the quantity of COOH groups and the equilibrium biosorption capacity of the fabrics (in further text: q_e) was observed, Fig. 2b. Namely, with increasing the quantity of COOH groups in the range 37.2–81.2 %, the q_e of chemically modified jute fabrics was improved by 47.0–78.2 %, compared to the raw jute fabric. In the

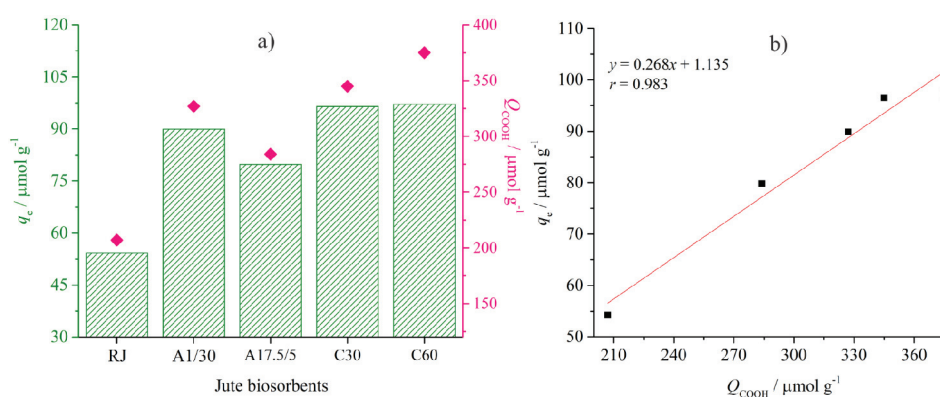


Fig. 2. a) Equilibrium biosorption capacities (q_e) of the fabrics *vs.* quantity of COOH groups (Q_{COOH}) and b) the relationship between the q_e of the fabrics and the quantity of COOH groups.

case of oxidized jute fabrics (samples C30 and C60), besides the quantity of COOH groups, the lignin removal, and consequently the increased content of available hydrophilic components (cellulose and hemicelluloses), also contributed to higher q_e , Fig. 2a.

Kinetic study

To describe the adsorption kinetic of nickel ions on the jute fabrics, the experimental data (Fig. 1) were fitted with pseudo-first and pseudo-second-order kinetic models. Their plots with the coefficients of determination (R^2) are shown in Fig. 3a and b, respectively.

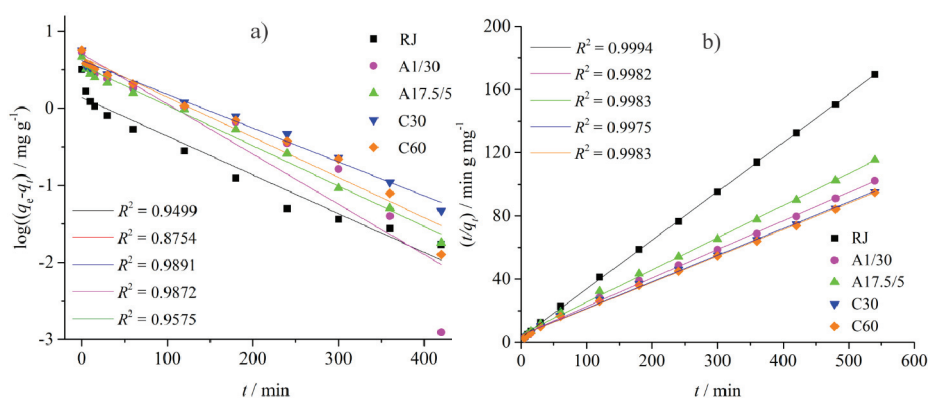


Fig 3. a) Pseudo-first and b) pseudo-second-order kinetics for the adsorption of nickel ions ($c_0 = 15 \text{ mg L}^{-1}$).

According to the obtained R^2 values (Fig. 3) and model prediction values for the $q_{e,cal}$ (Table II), it is clear that the biosorption of nickel ions on all investigated samples was fitted better by the pseudo-second-order kinetic model, with relative errors of 1.7–4.9 %, indicating that the adsorption/binding was established through sharing or exchange of electrons between the adsorbate and the adsorbent, as ionic exchanges.¹⁴ A significantly higher value of raw jute fabric pseudo-second rate constant (Table II, $k_2 = 0.034 \text{ g mg}^{-1} \text{ min}^{-1}$) than the values of chemically modified jute fabrics ($k_2 = 0.005\text{--}0.008 \text{ g mg}^{-1} \text{ min}^{-1}$) indicates that the rate of

TABLE II. Kinetic parameters obtained by the pseudo-first and pseudo-second-order kinetic models for the adsorption nickel ions ($c_0 = 15 \text{ mg L}^{-1}$) on jute fabrics

Kinetic model	Kinetic parameters	Jute fabrics				
		RJ	A1/30	A17.5/5	C30	C60
Pseudo-first	$q_{e,cal} / \text{mg g}^{-1}$	1.39	5.11	3.62	4.19	4.65
	k_1 / min^{-1}	0.012	0.015	0.012	0.010	0.012
Pseudo-second	$q_{e,cal} / \text{mg g}^{-1}$	3.24	5.53	4.90	5.93	5.98
	$k_2 / \text{g mg}^{-1} \text{ min}^{-1}$	0.034	0.008	0.008	0.007	0.005
	$q_{e,exp} / \text{mg g}^{-1}$	3.187	5.278	4.682	5.666	5.700

nickel adsorption is higher in the case of raw fabric. On the other hand, the reported lower values of k_2 for the chemically modified fabrics are the result of a slower nickel adsorption,¹⁵ as can be seen in Fig. 1.

Adsorption isotherms

Initial ion concentration is another factor affecting the biosorption potential of jute fabrics towards nickel ions. The results shown in Fig. 4 reveal that an increase in the initial concentration of nickel ions leads to a remarkable increase in the q_e of jute fabrics. This phenomenon indicated that the driving force for the adsorption of nickel ions is the concentration gradient between the aqueous phase and the solid one, which overcomes the resistance to mass transfer between the two phases; the higher the gradient, the more favoured the process.¹⁶ For example, increasing the initial ion concentration from 10 to 30 mg L⁻¹ causes an increase in raw jute fabric q_e by about 92 %. In the case of the chemically modified fabrics, the most prominent increase was observed for the oxidized ones (C30 and C60) and accounts for 160 %, while the lowest increase in q_e was observed for fabric A17.5/5. Independently of initial nickel concentration, the same trend for q_e (RJ < A17.5/5 < A1/30 < C30 < C60) was noticed.

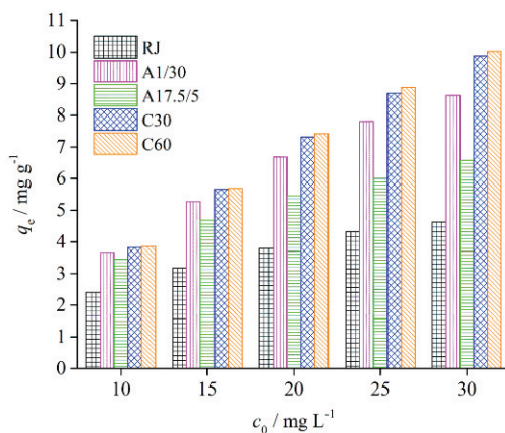


Fig. 4. Equilibrium biosorption (q_e) as a function of initial concentration nickel ions.

In order to determine the maximum biosorption capacities of the jute fabrics and to describe the adsorption behaviour of nickel ions at equilibrium, the Langmuir and Freundlich adsorption isotherms were used. The linear fit of the experimental data along with the coefficients of determination (R^2) are presented in Fig. 5. A comparison of the R^2 values reveals that the biosorption equilibrium data obtained were better fitted by the Langmuir ($R^2 > 0.9918$) than by the Freundlich ($R^2 < 0.9892$) model, implying that the adsorption process is monomolecular and occurs at homogenous active sites in the adsorbents.¹⁷ The isotherm parameters determined by fitting the experimental data (Fig. 4) with the Langmuir and Freundlich adsorption equations are listed in Table III. The maxi-

mal biosorption capacity of the fabrics, *i.e.*, q_m values obtained from Langmuir isotherm ranged from 6.30 mg g^{-1} to 12.06 mg g^{-1} .

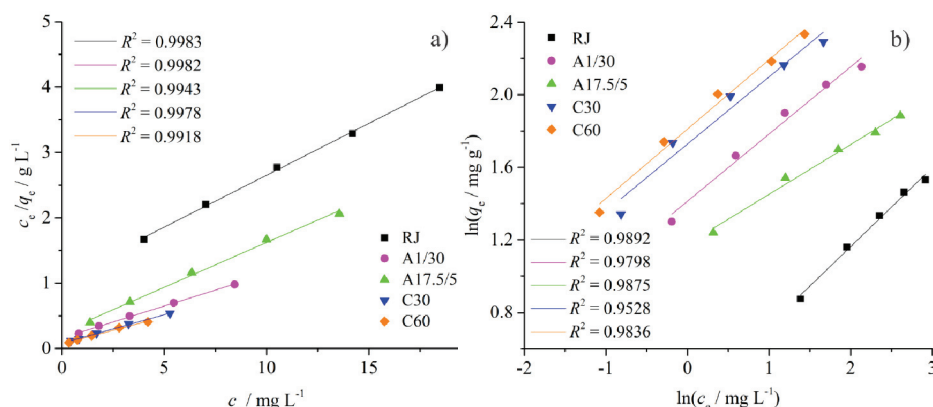


Fig. 5. a) Langmuir and b) Freundlich adsorption isotherm and the linear fit of the experimental adsorption data for nickel ions.

TABLE III. Langmuir and Freundlich isotherm parameters for the adsorption of nickel ions onto jute fabrics

Adsorption isotherm	Isotherm parameters	Jute fabrics				
		RJ	A1/30	A17.5/5	C30	C60
Langmuir	$K_L / \text{L mg}^{-1}$	0.149	0.615	0.548	1.099	1.000
	$q_m / \text{mg g}^{-1}$	6.30	10.21	7.29	11.45	12.06
Freundlich	$K_f / (\text{mg g}^{-1})(\text{L mg}^{-1})^{-1/n}$	1.34	4.11	3.24	5.63	6.11
	$1/n^a$	0.44	0.37	0.27	0.97	0.38

^aConstant related to the surface heterogeneity of the fabric

Observing in parallel the results obtained for the q_m of the samples and quantity of COOH groups (Fig. 6), a good linear correlation ($r = 0.953$) between them was found. It has to be emphasized that the ratios between the q_m and

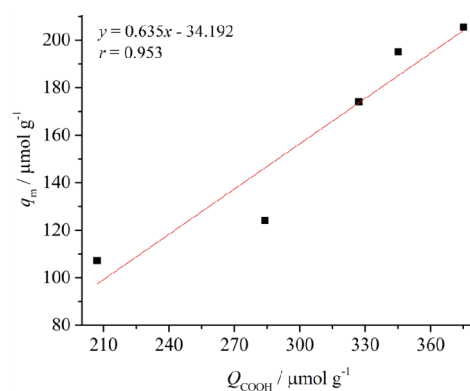


Fig. 6. Relationship between the maximal biosorption capacity of the fabrics (q_m) and the quantity of COOH groups (Q_{COOH}).

COOH group quantity are between 0.44 and 0.55, which means that approximately half of the COOH groups of the fabrics would be involved in binding nickel ions. According to the above mentioned, it can be concluded that the quantity of COOH groups can be used to predict the maximal biosorption potential of the jute fabrics towards nickel ions.

Comparison between other lignocellulosic fibres

Bearing in mind that the biosorption experimental conditions (*i.e.*, biosorbent dosage, solution pH, contact time, initial ion concentration and additional biosorbent treatments) used in the current study differ from those used in other studies (Table IV), it is very difficult to compare the results obtained for the biosorption capacities of jute fabrics with the results reported for other lignocellulosic fibres.

TABLE IV. Comparison between the biosorption potential of other lignocellulosic fibres and findings of the current study

Fibre type	Biosorbent dosage, g L ⁻¹	pH	Contact time h	c_0 mg g ⁻¹	q_{ex} mg g ⁻¹	Reference
Raw hemp felt	0.010	5.00	1	25	≈ 2.4	18
Raw hemp	0.001	5.00	24	100	65	19
Hemp modified with NaOH and citric acid					69	
Raw kenaf	0.005	4.50	24	500	41.66	20
Raw coir	0.005	6.5	2	150	2.74	21
Alkali treated coir					8.84	
Raw coir	0.020	6.5	2	350	2.51	22
Oxidized coir					4.33	
Raw coir pith	0.002	5.3	2	50	15.72	23
	0.007	4.0	1	20	2.066	24
Raw coir	0.011	N/A	1/3	5.067	0.456	25
	0.002	5.95	1/3	20	9.44	26
Raw jute	0.002	5.50	2	500	~ 11	27
Alkali modified jute					~ 12.5	
Raw Jute	0.020	5.87	2	400	3.37	28
Oxidized jute					457	
Jute dyed with CI Reactive Orange 13					357	
Raw jute	0.002	5.50	7	25	3.19	Current study
Alkali modified jute					5.28	
Oxidized jute					5.70	

In the study conducted by Shukla and Pai,²⁸ biosorption capacities of raw and oxidized jute fibres of 3.37 and 5.57 mg g⁻¹ were reported, which is very similar to those obtained in the current study (3.19 and 5.70 mg g⁻¹, respectively). However, the researchers used significantly higher initial ion concentrations, a twice higher biosorbent dosage, and a ¼ lower solution volume. Twenty times higher initial nickel concentration and 20 % higher solution volume/biosorbent dosage ratio contributed to higher biosorption capacities of raw and alkali

treated jute fabrics²⁷ than that presented in the current study. In most of the presented papers (Table IV, initial nickel concentration above 100 mg L⁻¹), the adsorption is not necessary since higher nickel concentrations can be removed by using conventional methods for wastewater treatment. On the other hand, chemically modified jute fabrics used in this investigation are efficient biosorbents for nickel ions present at trace levels in wastewaters.

CONCLUSIONS

Different alkali and oxidative modifications were applied to raw jute fabric in order to obtain jute fabrics with different chemical compositions and quantity of carboxyl groups. Such prepared fabrics were used as biosorbents for nickel ions from an aqueous solution. According to the obtained results, the biosorption of nickel ions obeys the pseudo-second-order kinetic model, while the experimental isotherm data fit better with the Langmuir model. The calculated ratios between maximal biosorption capacities of the jute fabrics (6.30–12.06 mg g⁻¹) and quantity of carboxyl groups indicated that approximately half of the fabrics' carboxyl groups would be involved in binding nickel ions during biosorption. Therefore, the carboxyl group quantity can be used to predict the maximal biosorption capacity of jute fabrics toward nickel ions. Permanent collection and reuse of jute fabric waste have promising multi positive effects on the economy as well environment, including reducing its quantity, saving energy, and its utilization as raw material for profitable innovation, which is in agreement with the circular economy concept.

SUPPLEMENTARY MATERIAL

The jute fabric chemical composition and statistical analysis are available electronically at the pages of the journal website: <https://www.shd-pub.org.rs/index.php/JSCS>, or from the corresponding author on request.

Acknowledgement. This work was supported by the Ministry of Education, Science and Technological Development of the Republic of Serbia (Contract Nos. 451-03-9/2021-14/200287, 451-03-9/2021-14/200135).

ИЗВОД

БИОСОРПЦИЈА ЈОНА НИКЛА НА ТКЕНИНАМА ОД ЈУТЕ: КИНЕТИЧКА И ИЗОТЕРМСКА ИСПИТИВАЊА

АЛЕКСАНДРА ИВАНОВСКА¹, ЛЕПОСАВА ПАВУН², БИЉАНА ДОЛЧИНОВИЋ³ и МИРЈАНА М. КОСТИЋ⁴

¹Универзитет у Београду, Иновациони центар Технолошко–металуричког факултета, Карнегијева 4, 11000 Београд, ²Универзитет у Београду, Фармацеушки факултет, Војводе Ситеве 450, 11000 Београд, ³Универзитет у Београду, Институт за хемију, технологију и металургију, Њешићева 12, 11000 Београд и ⁴Универзитет у Београду, Технолошко–металурички факултет, Карнегијева 4, 11000 Београд

Сирова тканина од јуте је хемијски модификована 1 % NaOH у току 30 min, 17,5 % NaOH у току 5 min или 0,7 % NaClO₂ у току 30 и 60 min у циљу испитивања утицаја промена хемијског састава и садржаја карбоксилних група на биосорпциони капацитет тка-

нина према јонима никла. Такође, испитиван је и утицај времена контакта тканина са раствором NiSO₄ и почетне концентрације раствора никла на биосорпциони капацитет тканина од јуте. Добијени резултати указују на то да се процес биосорпције никла може описати кинетичким моделом псеудо-другог реда, а равнотежне вредности добијене за сорпцију никла се боље слажу са Langmuir адсорпционом изотермом. Израчунати однос између максималних биосорпционих капацитета тканина од јуте (6,30–12,06 mg g⁻¹) и садржаја карбоксилних група указују на то да ће приближно половина карбоксилних група учествовати у везивању јона никла током биосорпције. Према томе, садржај карбоксилних група се може користити као индикатор максималног биосорпционог капацитета тканина од јуте према јонима никла. Код оксидисане тканине, уклањање лигнина које је праћено са повећањем садржаја целулозе и хемицелулоза је такође допринело већем биосорпционом капацитету.

(Примљено 19. јануара, ревидирано 11. априла, прихваћено 12. априла 2021)

REFERENCES

1. Z. Kovacova, S. Demcak, M. Balintova, C. Pla, *Materials* **13** (2020) 3575 (<https://doi.org/10.3390/ma13163575>)
2. G. Crini, E. Lichtfouse, *Environ. Chem. Lett.* **17** (2019) 145 (<https://doi.org/10.1007/s10311-018-0785-9>)
3. A. Ivanovska, D. Cerovic, S. Maletic, I. Jankovic Castvan, K. Asanovic, M. Kostic, *Cellulose* **26** (2019) 5133 (<https://doi.org/10.1007/s10570-019-02421-0>)
4. A. Ivanovska, D. Cerovic, N. Tadic, I. Jankovic Castvan, K. Asanovic, M. Kostic, *Ind. Crop. Prod.* **140** (2019) 111632 (<https://doi.org/10.1016/j.indcrop.2019.111632>)
5. A. Ivanovska, M. Kostić, *J. Serb. Chem. Soc.* **85** (2020) 1621 (<https://doi.org/10.2298/JSC201013069I>)
6. W. Ganer, *Textile Laboratory Manuel: Fibers*, Heywood Books, London, 1967
7. M. Knežević, A. Kramar, T. Hajnrih, M. Korica, T. Nikolić, A. Žekić, M. Kostić, *J. Nat. Fibers* (2020), in press (<https://doi.org/10.1080/15440478.2020.1745120>)
8. S. Lagergren, *Handl.* **24** (1898) 1
9. Y. S. Ho, G. McKay, *Process. Biochem.* **34** (1999) 451 ([https://doi.org/10.1016/S0032-9592\(98\)00112-5](https://doi.org/10.1016/S0032-9592(98)00112-5))
10. A Y.-S. Ho, W.-T. Chiu, C.-C. Wang, *Bioresour. Technol.* **96** (2005) 1285 (<https://doi.org/10.1016/j.biortech.2004.10.021>)
11. K.-Y. Shin, J.-Y. Hong, J. Jang, *J. Hazard. Mater.* **190** (2011) 36 (<https://doi.org/10.1016/j.jhazmat.2010.12.102>)
12. V. Rizzi, F. D'Agostino, P. Fini, P. Semeraro, P. Cosma, *Dyes Pigments* **140** (2017) 480 (<https://doi.org/10.1016/j.dyepig.2017.01.069>)
13. V. Rizzi, F. Romanazzi, J. Gubitosa, P. Fini, R. Romita, A. Agostiano, A. Petrella, P. Cosma, *Biomolecules* **9** (2019) 571 (<https://doi.org/10.3390/biom9100571>)
14. Y. S. Ho, G. Mckay, *Water. Res.* **34** (2000) 735 ([https://doi.org/10.1016/S0043-1354\(99\)00232-8](https://doi.org/10.1016/S0043-1354(99)00232-8))
15. A. Vázquez-Guerrero, R. Cortés-Martínez, R. Alfaro-Cuevas-Villanueva, E. M. Rivera-Muñoz, R. Huirache-Acuña, *Water* **13** (2021) 89 (<https://doi.org/10.3390/w13010089>)
16. P. Semeraro, P. Fini, M. D'Addabbo, V. Rizzi, P. Cosma, *Int. J. Environ. Agric. Biotechnol.* **2** (2017) 1835
17. R. Kumar, R. Kr. Sharma, *React. Funct. Polym.* **140** (2019) 82 (<https://doi.org/10.1016/j.reactfunctpolym.2019.04.014>)

18. S. Loiacono, G. Crini, G. Chanet, M. Raschetti, V. Placet, N. M. Crini, *J. Chem. Technol. Biotechnol.* **93** (2018) 2592 (<https://doi.org/10.1002/jctb.5612>)
19. G. Z. Kyzas, Z. Terzopoulou, V. Nikolaidis, E. Alexopoulou, D. N. Bikiaris, *J. Mol. Liq.* **209** (2015) 209 (<https://doi.org/10.1016/j.molliq.2015.05.060>)
20. C. M. Hasfalina, R. Z. Maryam, C. A. Luqan, M. Rashid, *J. Nat. Fibers* **7** (2010) 267 (<https://doi.org/10.1080/15440478.2010.527508>)
21. P. M. Shukla, S. R. Shukla, *Sep. Sci. Technol.* **48** (2013) 421 (<https://doi.org/10.1080/01496395.2012.691933>)
22. S. R. Shukla, R. S. Pai, A. D. Skendarkar, *Sep. Purif. Technol.* **47** (2006) 147 (<https://doi.org/10.1016/j.seppur.2005.06.014>)
23. H. Parab, S. Joshi, N. Shenoy, A. Lali, U. S. Sarma, M. Sudersanan, *Process. Biochem.* **41** (2006) 609 (<https://doi.org/10.1016/j.procbio.2005.08.006>)
24. K. Swarnalatha, S. Ayoob, *Int. J. Sust. Technol.* **9** (2016) 259 (<https://doi.org/10.1080/19397038.2016.1152323>)
25. Ch. Aravind, K. Chanakya, K. Mahindra, *Int. J. Civil Eng. Technol.* **8** (2017) 1869 (http://www.iaeme.com/MasterAdmin/uploadfolder/IJCIET_08_04_213/IJCIET_08_04_213.pdf)
26. D. Nityanandi, C. V. Subbhuraam, K. Kadirvelu, *Environ. Technol.* **27** (2006) 15 (<https://doi.org/10.1080/09593332708618621>)
27. D. Q. Melo, C. B. Vidal, A. L. da Silva, G. S. C. Raulino, A. D. de Luz, C. da Luz, P. B. A. Fachine, S. E. Mazzeto, R. F. do Nascimento, *Int. J. Civil Environ. Eng.* **15** (2015) 14 (http://ijens.org/Vol_15_I_06/155505-1506-2929-IJCEE-IJENS.pdf)
28. S. R. Shukla, R. S. Pai, *Bioresource Technol.* **96** (2005) 1430 (<https://doi.org/10.1016/j.biortech.2004.12.010>).

SUPPLEMENTARY MATERIAL TO
**Kinetic and isotherm studies for the biosorption of nickel ions by
jute fabrics**

ALEKSANDRA IVANOVSKA^{1*}, LEPOSAVA PAVUN², BILJANA DOJČINOVIĆ³
and MIRJANA KOSTIĆ⁴

¹University of Belgrade, Innovation Center of the Faculty of Technology and Metallurgy,
Karnegijeva 4, 11000 Belgrade, Serbia, ²University of Belgrade, Faculty of Pharmacy,
Vojvode Stepe 450, 11000 Belgrade, Serbia, ³University of Belgrade, Institute of Chemistry,
Technology and Metallurgy, Njegoševa 12, 11000 Belgrade, Serbia and ⁴University of
Belgrade, Faculty of Technology and Metallurgy, Karnegijeva 4, 11000 Belgrade, Serbia

J. Serb. Chem. Soc. 86 (9) (2021) 885–897

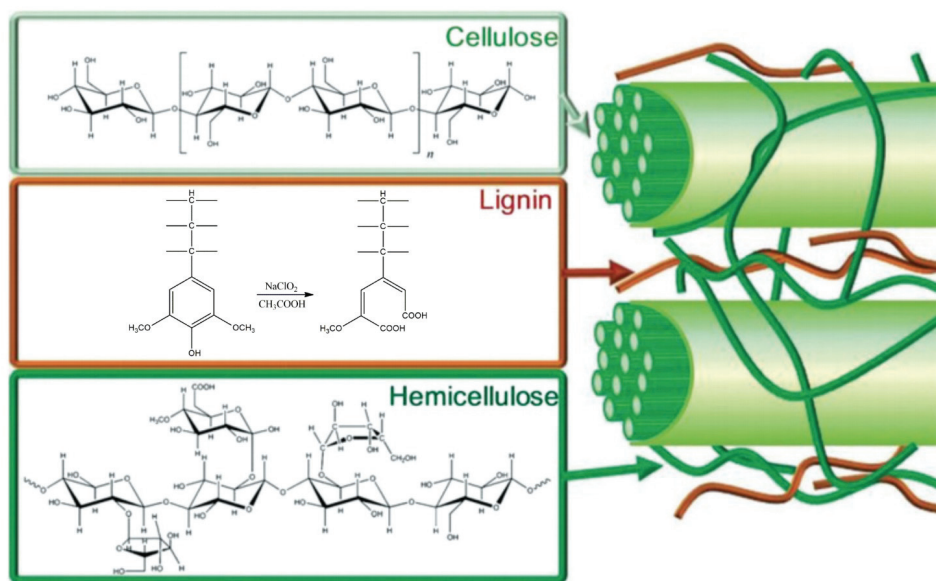


Fig. S-1. Chemical composition of jute fibres (Figure parts are taken from the literature^{1,2})

* Corresponding author. E-mail: aivanovska@tmf.bg.ac.rs

Statistical analysis

TABLE S-I. Results of *t*-test analysis by comparing the chemical composition and COOH group quantity of jute biosorbents. Values of parameter $|t|$ regarding the chemical composition of jute fabric and quantity of COOH groups ($df = n_1 + n_2 - 2 = 4$) ($n_1 = n_2 = 3$)

Jute fabrics					
RJ, A1/30	RJ, A17.5/5	A1/30, A17.5/5	RJ, C30	RJ, C60	C30, C60
Hemicellulose content, %*			Lignin content, %*		
13.89	28.72	26.75	13.21	25.86	14.30
COOH group quantity, %*			COOH group quantity, %*		
28.47	19.91	7.52	26.8	111.92	5.60

*0.001 level of significance.

REFERENCES

1. B. Sajjadi, T. Zubatiuk, D. Leszczynska, J. Leszczynski, W. Y. Chen, *Rev. Chem. Eng.* **35** (2018) 815 (<https://doi.org/10.1515/revce-2018-0003>)
2. M. A. N. Abd-Allah, L. H. Mohammad, *J. Appl. Polym. Sci.* **102** (2006) 1399 (<https://doi.org/10.1002/app.24255>).



J. Serb. Chem. Soc. 86 (9) 899 (2021)
JSCS-5470

Journal of
the Serbian
Chemical Society

ersion
lectronic

JSCS@tmf.bg.ac.rs • www.shd.org.rs/JSCS

Note
Published 17 August, 2021

Retracting Note

Paper entitled "Bioleaching of copper, zinc and gold from a polymetallic ore flotation concentrate from Čoka Marin deposit (Serbia)", by J. Avdalović *et al.* <https://doi.org/10.2298/JSC210127016A>, published on August 1, 2021 in the OnLine First sections of the Journal of the Serbian Chemical Society has been retracted and withdrawn since the authors (corresponding author) did not approve galley proof prepared by Editorial office.

Retracted manuscript was deposited in the DoiSerbia quarantine, Repository service of the National Library of Serbia: <http://doiserbia.nb.rs/issue.aspx?issueid=1981>

<https://doi.org/10.2298/JSC210817062R>